

# Imaging from Echoes: On Inverse Problems in Ultrasound

Thèse N° 9310

Présentée le 15 février 2019

à la Faculté des sciences et techniques de l'ingénieur  
Laboratoire de traitement des signaux 5  
Programme doctoral en génie électrique

pour l'obtention du grade de Docteur ès Sciences

par

**Adrien Georges Jean BESSON**

Acceptée sur proposition du jury

Prof. P. Frossard, président du jury  
Prof. J.-Ph. Thiran, Prof. Y. Wiaux, directeurs de thèse  
Prof. M. Tanter, rapporteur  
Prof. M. E. Davies, rapporteur  
Prof. M. Unser, rapporteur

2019



# Acknowledgements

I would like to express my profound gratitude to my two advisors: Jean-Philippe and Yves, without whom I would most probably be stuck in a professional life I would not really like.

Jean-Philippe, thank you for everything: your optimism, support and professional advices greatly helped me in this exciting journey. More importantly, the freedom you offered me to explore many research directions as well as the trust you put in my work were the perfect ingredients for a complete personal fulfillment.

Yves, thank you for ensuring my complete integration into your group and for the fruitful collaborations I had the chance to lead with Zhouye and Audrey. Thank you for your out-of-the box technical advices and the in-depth discussions that were always of great help for me.

I am thankful to my thesis committee: Prof. Mickael Tanter, Prof. Michael E. Davis, Prof. Michaël Unser and the jury president Prof. Pascal Frossard, for taking the time to read such a long manuscript.

During my thesis, I had the chance to work as part of the self-appointed “Ultrasound Group” of the LTS 5 with my amazing colleagues Dimitri, Marcel and Florian.

Florian, I remember the first time I met you as a supervisor for your master project and I am very glad to see the engineer you have become. Thank you for your hard work on the “py-us” framework and for your patience when reading my messy code.

Marcel, you were not only my mentor in ultrasound but also an example for me as a scientist. I am amazed by the fact that the amount of things you know is inversely proportional to your curiosity. Thank you for everything you taught me and for being such a kind person.

Last but not least, thank you Dimitri. I cannot really put in words the amount of things we have shared together. Some of them like the rushes until 6 am for conference submissions, the MATLAB license problem at 2 am the day before the demo, the discussions at 4 am in our hostel in Tokyo, will stay as memorable souvenirs. I’ve learned a lot from you both professionally and personally and part of this thesis is yours as well.

I am also grateful to you, Eric, that I consider as half “Ultrasound Group” - half LCAV. Thank you for your passion in developing super helpful python notebooks. Thank you also for leading the collaboration between LCAV and LTS 5 on the project on ultrasound localization. You managed to bring the theoretical concepts developed at LCAV in the ultrasound world, which is a huge task. I hope you all the best for your new life in Paris.

There are number of people who have made me enjoy my everyday life at LTS 5 and I want to express my gratitude to all of them. A special thanks to Rosie and Anne for managing all the administrative issues such that I was able to focus on the research side. Damien, thank

## Acknowledgements

---

you for your kindness and for the many personal discussions that we had together during after-lunch coffees. David, thank you for advices at the end of the thesis, for both the writing of the manuscript and the oral presentation.

I also had the chance to collaborate with Lucien, Matthieu, Sepand and Hanjie from Paul's team in IBM Zurich. I am thankful to all of them for their mathematical rigor that greatly helped me formalizing the mathematics of this thesis. A special thank you to Lucien and Mathieu for the in-depth discussions we had about everything. Both of you are brilliant mind and be aware that you were more than colleagues for me.

I would also like to say thank you to two people that were there for me at the beginning of my thesis to steer me in the right direction. Thank you Rafa for being my mentor on compressed sensing and optimization. You taught me the way to understand the beauty of those two topics. Thank you Olivier for your kindness, support and for your help on the ultrasound side.

I am grateful to all the students I have supervised during various master projects: Louis, Benjamin, Philippe, Saleh, Julie, Yuliang, Malo and Lucas. I've learned a lot from each of you. Thank you to Pascal and Andreas from ETHZ for the fruitful co-supervision of some of these projects. It was a real pleasure to collaborate with you.

I am thankful to all the interesting people I met at IUS, ICASSP, SPARS and BASP: the crazy CREATIS crew (Hervé, François, Didier, Barbara, Denis, Seb, Maxime, Emilia, Miaomiao), Adrian and Denis from IRIT, Ewen and Dominique from TPAC, the Langevin people (Elodie, Mafalda, Marion, David), the LCAV crew (Robin, Ivan, Gilles, Miranda, Frederike).

I am grateful to all my friends that made my stay in Lausanne enjoyable. Thank you to the CG1D - Quentin, Doc, Niels, Gol, Nono, to the people I met in Lausanne - Perreard, Romain, Safia, Milan, Fanny, Maddie, Henri, José, Charbel, Nicolas, to the Grenoble crew - Lolo, John, Hugo, Romain. A special thanks to you, Charles and Billat, for everything we've shared together in Lausanne and abroad.

I cannot end without thanking my family. I must thank my grandparents, Viviane and Jean, for teaching me their taste for adventure. I am grateful to my parents and brother, Sophie, Gerard and Valentin, for nurturing my scientific curiosity early in my childhood and for their unconditional love and support. Last but not least, I am deeply grateful to you, Keilen, for your infinite love, support, patience and encouragement.

*Lausanne, 24 Janvier 2019*

A. B.

# Abstract

Ultrasound (US) imaging is currently living a revolution. On the one hand, ultrafast US imaging, a novel way of acquiring and producing US images, has paved the way to several advanced imaging modes, e.g. shear-wave elastography, ultrafast Doppler imaging and ultrafast contrast imaging. On the other hand, the mass adoption of mobile commodity devices pushes towards portable US imaging. These new paradigms require to rethink the imaging pipeline and come with a myriad of new challenges in terms of data rate, power considerations as well as software and hardware design. In this thesis, we explore several inverse problems related to these challenges, with an emphasis on data-rate reduction for imaging and localization.

We follow the view of considering pulse-echo US imaging as a tomographic image reconstruction problem where sensor measurements can be seen as projections onto quadric surfaces. By appropriate parameterization of these surfaces, we devise efficient formulations of the measurement model associated with the image reconstruction problem and pave the way to large scale regularized US imaging.

We introduce USSR, an UltraSound Sparse Regularization framework, which exploits the measurement model in the context of convex optimization algorithms. We describe three applications, namely sparsely regularized beamforming where high-quality images are obtained with few insonifications, compressed beamforming which aims to decrease the amount of data collected per insonification, and image restoration which exploits a model of non-stationary blur to enhance already reconstructed images.

We suggest a compressive multiplexing approach for US signals. Such a technique achieves high-quality imaging with significantly fewer coaxial cables connecting the probe to the imaging system than existing methods. The compression is based on the compressive multiplexer, an analog compressed-sensing architecture, and the reconstruction relies on convex optimization algorithms. We propose two methods which exploit different low-dimensional models of US signals, namely the bandpass signal model and the pulse-stream model.

We tackle the problem of localizing strong reflectors, with potential application in non-destructive evaluation and contrast-enhanced US imaging. We suggest a threefold approach composed of a time-of-flight (TOF)-sensing step, a TOF-labeling step and a localization step, which is capable of recovering the locations of strong reflectors with significantly fewer transducer elements and less sensor measurements than existing techniques.

By exploring innovative methods for imaging and localization, this work contributes to a next generation of US imaging devices which will benefit from ultrafast US imaging to integrate advanced imaging modes into more and more compact systems.

## Acknowledgements

---

**Keywords:** Ultrasound imaging, ultrafast ultrasound imaging, inverse problem, compressed sensing, compressive sampling, convex optimization, sparsity, joint sparsity, finite rate of innovation, Euclidean distance matrices.

# Résumé

L'imagerie ultrasonore (US) vit actuellement une profonde mutation. D'une part, l'imagerie échographique ultrarapide a révolutionné la manière dont les images sont formées, ouvrant la voie à de nouveaux modes avancés d'imagerie comme l'élastographie shear wave, l'imagerie ultrarapide du flux et l'échographie ultrarapide de contraste. D'autre part, l'adoption massive des appareils mobiles a fortement poussé le développement d'une échographie de plus en plus portable. Une myriade de nouveaux défis techniques sont apparus en termes de transfert de données, de consommation électrique et de design logiciel et matériel. Cette thèse explore différents problèmes inverses liés à ces nouveaux défis, et plus particulièrement à la réduction du débit de données, pour des applications d'imagerie et de localisation.

Dans un premier temps, nous revisitons l'imagerie échographique "pulse-echo" comme un problème de reconstruction tomographique. Les mesures acquises par les transducteurs échographiques sont interprétées comme des projections sur des surfaces quadriques, dont la forme dépend de la configuration d'imagerie. Nous dérivons ensuite des formulations efficaces et sans matrice pour évaluer le modèle linéaire de mesure associé à notre problème inverse. Ces dernières, basées sur une paramétrisation des surfaces quadriques impliquées dans les projections, sont clés dans l'utilisation de méthodes itératives pour résoudre le problème inverse.

Dans un deuxième temps, nous introduisons "USSR : an UltraSound Sparse Regularization Framework", qui exploite le modèle de mesure introduit précédemment au sein d'algorithmes d'optimisation convexe, en vue de résoudre trois problèmes inverses différents. Le premier concerne la formation de voies régularisée par parcimonie dans lequel des images de haute qualité sont obtenues avec peu de transmissions. Le deuxième concerne la formation de voie compressée où l'objectif est de réduire la quantité de données acquises par transmission. Le troisième concerne la restauration d'images et exploite un modèle de flou non-stationnaire au sein d'un algorithme de recherche de maximum-a-posteriori pour améliorer la qualité d'images déjà reconstruites.

Dans un troisième temps, nous proposons un modèle de multiplexage compressé de signaux US qui permet d'obtenir des images de haute qualité avec un nombre réduit de câbles coaxiaux reliant la sonde à l'appareil d'imagerie. La compression est basée sur le "compressive multiplexer", une architecture analogique d'acquisition comprimée, et la reconstruction utilise des algorithmes d'optimisation convexe. Nous suggérons deux techniques qui explorent différents modèles basse dimension des signaux US : le modèle passe-bande et le modèle de train d'impulsions.

## Acknowledgements

---

Dans un dernier chapitre, nous abordons le problème de la localisation de réflecteurs forts, avec des applications en contrôle non-destructif et en échographie de contraste. Nous proposons une approche composée de trois étapes : la détection des temps de vol, l'assignation des temps de vol à des réflecteurs et la localisation des réflecteurs. Celle-ci est capable de localiser des réflecteurs avec un nombre significativement réduit de transducteurs échographiques et d'échantillons acquis par transducteur, comparé aux méthodes existantes.

Ainsi, en exploitant des méthodes innovantes d'imagerie et de localisation, cette thèse contribue à l'échographie de demain, qui bénéficiera de l'imagerie ultrarapide pour intégrer des modes avancés d'imagerie dans des appareils toujours plus compacts.

**Mots clés :** Imagerie ultrasonore, Imagerie échographique ultrarapide, problème inverse, acquisition comprimée, optimisation convexe, parcimonie, parcimonie jointe, finite rate of innovation, matrice des distances Euclidiennes.

# Contents

<b>Acknowledgements</b>	<b>iii</b>
<b>Abstract</b>	<b>vii</b>
<b>Résumé</b>	<b>ix</b>
<b>List of Figures</b>	<b>xiii</b>
<b>List of Tables</b>	<b>xix</b>
<b>Notations and Symbols</b>	<b>1</b>
Abbreviations . . . . .	1
Matrices . . . . .	3
Vectors . . . . .	3
Sets . . . . .	4
Functions . . . . .	4
Spaces and Norms . . . . .	5
Miscellaneous . . . . .	5
<b>1 Introductory Notes</b>	<b>7</b>
1.1 A Brief History of Ultrasound . . . . .	8
1.1.1 Early Discoveries: From Sound to Ultrasound . . . . .	8
1.1.2 Echo Ranging with Ultrasound: Everything Starts with the Titanic . . . . .	9
1.1.3 Ultrasound for Medical Imaging and Therapy . . . . .	9
1.1.4 Ultrasound Imaging in the 21st Century . . . . .	12
1.1.5 The Revolution of Ultrafast Ultrasound Imaging . . . . .	13
1.2 Several Challenges in Ultrasound imaging . . . . .	15
1.2.1 Gaining More Physical Understanding of Ultrafast Ultrasound Imaging . . . . .	15
1.2.2 High-quality Ultrafast Ultrasound Imaging with few Insonifications . . . . .	16
1.2.3 High-quality Ultrafast Ultrasound Imaging with a Reduced Number of Elements and Cables . . . . .	16
1.3 Roadmap of the Thesis . . . . .	17

<b>2</b>	<b>Basics of Ultrasound Imaging</b>	<b>21</b>
2.1	An Ultrasound Imaging System in a Nutshell . . . . .	21
2.1.1	Diagram of an Ultrasound Imaging System . . . . .	21
2.1.2	Transmission and Reception of Ultrasound Waves . . . . .	23
2.1.3	Forming Images from Echoes: Digital Ultrasound Beamforming . . . . .	25
2.1.4	Post-processing and Display . . . . .	27
2.2	Important Features of an Ultrasound System . . . . .	27
2.2.1	Radiated Field from an Ultrasound Array . . . . .	27
2.2.2	Spatial Resolution . . . . .	28
2.2.3	Speckle . . . . .	29
2.2.4	Temporal Resolution . . . . .	30
2.2.5	Attenuation in Tissues . . . . .	30
2.3	Image Formation in Ultrafast Ultrasound Imaging . . . . .	32
2.3.1	Delay-and-sum Beamforming in Ultrafast Ultrasound Imaging . . . . .	32
2.3.2	Coherent Compounding in Ultrafast Ultrasound Imaging . . . . .	34
<b>3</b>	<b>Pulse-echo Ultrasound Imaging Seen as an Inverse Problem</b>	<b>37</b>
3.1	Existing Approaches and Motivations . . . . .	38
3.2	Hail to the Pulse-echo Spatial Impulse Response Model . . . . .	39
3.2.1	Acoustical Understanding of the Spatial Impulse Response . . . . .	39
3.2.2	The Pulse-echo Spatial Impulse Response Model . . . . .	41
3.2.3	The Pulse-echo Waveform: From Pressure Fields to Echo Signals . . . . .	43
3.3	Ultrasound Imaging Seen as an Inverse Problem . . . . .	44
3.3.1	Inverse Problem at the Continuous Level . . . . .	44
3.3.2	From Continuous to Discrete Inverse Problem . . . . .	46
3.4	Measurement Model for a Single Emitter - Single Receiver Configuration . . . . .	47
3.4.1	Spatial Impulse Response of a Transducer Element . . . . .	47
3.4.2	Continuous Measurement Model in 3D . . . . .	48
3.4.3	Discretization of the Measurement Model in 3D . . . . .	54
3.4.4	Continuous Measurement Model in 2D . . . . .	55
3.4.5	Discretization of the Measurement Model in 2D . . . . .	56
3.5	Measurement Model in Diverging Wave Imaging . . . . .	57
3.5.1	Continuous Measurement Model in 3D . . . . .	57
3.5.2	Discretization of the Measurement Model in 3D . . . . .	60
3.5.3	Continuous Measurement Model in 2D . . . . .	61
3.5.4	Discretization of the Measurement Model in 2D . . . . .	65
3.6	Measurement Model in Plane-wave Imaging . . . . .	66
3.6.1	Continuous Measurement Model in 3D . . . . .	66
3.6.2	Discretization of the Measurement Model in 3D . . . . .	69
3.6.3	Continuous Measurement Model in 2D . . . . .	70
3.6.4	Discretization of the Measurement Model in 2D . . . . .	72

3.7	Adjoint of the Measurement Model: Revisiting the Delay-and-sum Algorithm from a Functional Perspective . . . . .	73
3.7.1	Derivation of the Adjoint of the Measurement Model . . . . .	73
3.7.2	A Functional Interpretation of the Delay-and-sum Algorithm . . . . .	75
<b>4</b>	<b>USSR: The UltraSound Sparse Regularization Framework</b>	<b>77</b>
4.1	A Brief Overview of Variational Regularization in Imaging . . . . .	78
4.1.1	Variational Regularization for Imaging Problems . . . . .	78
4.1.2	Proximal Gradient Methods for Convex Regularization . . . . .	79
4.2	Sparsely Regularized Beamforming for Enhanced Ultrafast Ultrasound Imaging	80
4.2.1	Motivations and Existing Approaches . . . . .	80
4.2.2	Sparse Regularization for Enhanced Ultrasound Image Reconstruction .	81
4.2.3	Experiments and Results . . . . .	82
4.3	Compressed Ultrasound Beamforming . . . . .	88
4.3.1	Motivation and Existing Approaches . . . . .	88
4.3.2	Proposed Compressed Beamforming Approach . . . . .	89
4.3.3	Experiments and Results . . . . .	91
4.4	Non-stationary Blur Modeling and Image Restoration . . . . .	96
4.4.1	Motivations and Existing Approaches . . . . .	96
4.4.2	Mathematical Modelling of Non-stationary Blur . . . . .	97
4.4.3	Evaluation Strategy of the Proposed Model of Non-stationary Blur . . . .	99
4.4.4	Proposed Image Restoration Technique . . . . .	102
4.4.5	Experiments and Results . . . . .	102
4.5	Discussion and Perspectives . . . . .	110
4.5.1	Limitations of Convex Optimization Methods in Ultrasound Imaging . .	110
4.5.2	Towards Compressed Sensing for Ultrasound Imaging . . . . .	112
4.5.3	USSR 2.0: Deep Neural Networks for Ultrasound Image Reconstruction .	113
<b>5</b>	<b>Compressive Multiplexing of Ultrasound Signals</b>	<b>115</b>
5.1	A Short Tour on Compressed Sensing . . . . .	116
5.1.1	Sensing Sparse Signals: A Novel Paradigm . . . . .	116
5.1.2	Sensing and Recovery Guarantees for Sparse Signals . . . . .	116
5.1.3	Sensing Matrices in Compressed Sensing . . . . .	119
5.2	Joint Sparsity with Partially Known Support . . . . .	120
5.2.1	Joint Sparsity: Compressed Sensing Applied to Multiple Measurement Vectors . . . . .	120
5.2.2	Recovery Methods in Joint Sparsity . . . . .	121
5.2.3	Joint Sparsity with Partially Known Support . . . . .	124
5.2.4	Experiments . . . . .	129
5.3	Low-dimensional Models of Ultrasound Signals . . . . .	131
5.3.1	The Bandpass Signal Model . . . . .	132
5.3.2	The Pulse-stream Model . . . . .	133
5.4	Compressive Multiplexing of Ultrasound Signals . . . . .	135

## Contents

---

5.4.1	Compression Module . . . . .	136
5.4.2	Reconstruction Module . . . . .	138
5.4.3	Experiments and Results . . . . .	139
5.5	Estimation of the Pulse-echo Waveform from Compressed Measurements . . . . .	143
5.5.1	Estimation of Pulse-echo Waveform as a Blind Deconvolution Problem . . . . .	144
5.5.2	Solving the Blind Deconvolution Problem . . . . .	145
5.5.3	Validation of the Algorithm . . . . .	147
5.5.4	Reconstruction of <i>In Vivo</i> Carotids from Compressed Measurements and Unknown Pulse-echo Waveform . . . . .	149
5.6	Discussion on the Proposed Compressive Multiplexing Strategy . . . . .	150
<b>6</b>	<b>Ultrasound Localization at the Rate of Innovation</b> . . . . .	<b>153</b>
6.1	Existing Approaches and Proposed Localization Method . . . . .	153
6.1.1	Existing Localization Approaches in Ultrasound Imaging . . . . .	153
6.1.2	Measurement Setup and Problem Statement . . . . .	154
6.1.3	Proposed Localization Approach . . . . .	155
6.1.4	Critical Sampling Rate of the Proposed Localization Approach . . . . .	156
6.2	Sampling Along Channels with Finite Rate of Innovation . . . . .	157
6.2.1	From Bandlimited Signal Sampling to Finite Rate of Innovation . . . . .	157
6.2.2	Proposed Finite Rate of Innovation Sampling of Ultrasound Signals . . . . .	158
6.2.3	Experiments and Results . . . . .	163
6.3	Sampling Across Channels with Euclidean Distance Matrices . . . . .	165
6.3.1	Time-of-flight Labeling with Euclidean Distance Matrices . . . . .	165
6.3.2	Pruning Methods to Reduce the Number of Combinations . . . . .	169
6.3.3	Conditions for Unique Recovery of the Time-of-flight Labeling Method . . . . .	170
6.3.4	Time-of-flight Labeling in Noisy Scenarios . . . . .	171
6.3.5	Validation of the Proposed Approach with Simulations . . . . .	171
6.4	Localization from Labeled Time-of-flights . . . . .	173
6.4.1	Multidimensional Scaling . . . . .	173
6.4.2	Multilateration . . . . .	173
6.5	Experiments and Results . . . . .	174
6.5.1	Field II Simulations . . . . .	174
6.5.2	Non-destructive Evaluation Experiment . . . . .	174
<b>7</b>	<b>Concluding Remarks</b> . . . . .	<b>177</b>
7.1	Time-reversing the Thesis . . . . .	177
7.2	Future Prospects . . . . .	179
<b>A</b>	<b>Generalized Radon Transforms</b> . . . . .	<b>181</b>
A.1	Linear Radon Transform . . . . .	181
A.1.1	Definition of the Linear Radon Transform . . . . .	181
A.1.2	Inversion of the Linear Radon Transform in 2D . . . . .	181
A.2	Generalized Radon Transform . . . . .	182

A.2.1	Definition of the Generalized Radon Transform . . . . .	182
A.2.2	The Spherical Radon Transform . . . . .	183
A.2.3	The Elliptical Radon Transform . . . . .	183
A.2.4	The Parabolic Radon Transform . . . . .	184
<b>B</b>	<b>Expression of the Parametric Equations in Ultrafast Ultrasound Imaging</b>	<b>185</b>
B.1	Parametric Equations in Diverging Wave Imaging . . . . .	185
B.1.1	3D Imaging . . . . .	185
B.1.2	2D Imaging . . . . .	186
B.2	Parametric Equations in Plane Wave Imaging . . . . .	187
B.2.1	3D Imaging . . . . .	187
B.2.2	2D Imaging . . . . .	188
<b>C</b>	<b>Proximity Operators of Several Regularization Terms</b>	<b>189</b>
C.1	Proximity Operators Associated with the $\ell_1$ -norm . . . . .	189
C.1.1	$\ell_1$ -norm in the Image Domain . . . . .	189
C.1.2	$\ell_1$ -norm in the Transform Domain . . . . .	189
C.2	Proximity Operators Associated with the $\ell_p$ -norm . . . . .	190
C.2.1	Case $p = 3/2$ . . . . .	190
C.2.2	Case $p = 4/3$ . . . . .	190
	<b>Bibliography</b>	<b>191</b>
	<b>Curriculum Vitae</b>	<b>209</b>



# List of Figures

1.1	The Curie's "quartz piézo-électrique". Obtained from [2]. . . . .	9
1.2	Image of the sonar patent filed in 1917 by Constantin Chilowsky and Paul Langevin. . . . .	10
1.3	Image of the brain ventricles with Dussik's system. Obtained from [5]. . . . .	11
1.4	Figure (a) shows a clinical examination with the Siemens Vidoson 635. Figure (b) displays the Multiscan assembly. . . . .	12
1.5	Analogy between the two steps involved in (a)-optical holography, (b)-time reversal ultrasound imaging and (c)-ultrafast ultrasound imaging. Obtained from [11] with permission. © 2014 IEEE . . . . .	14
2.1	Simplified diagram of an ultrasound system. . . . .	22
2.2	Figure (a) presents the impulse response and Figure (b) displays the frequency spectrum of the Verasonics L11-5V probe. . . . .	24
2.3	Figure (a) presents the multilayer structure of a probe and Figure (b) describes a 1D array probe with an elevation lens. Obtained from [36] with permission. . . . .	24
2.4	Examples of probes used in ultrasound imaging. Figure (a) presents a linear-array probe. Figure (b) shows a convex-array probe. Figure (c) displays a phased-array probe. . . . .	25
2.5	Sectors scanned by the different types of probes. Obtained from [34] with permission. . . . .	25
2.6	On-axis radiated field of a planar circular source of radius $a$ . Obtained from [34] with permission. . . . .	28
2.7	The leftmost figure displays the frequency spectrum of the pulse-echo waveform at different depths. The three other figures show (from left to right) the reference pulse-echo waveform and the normalized pulse-echo waveform at 3 cm and 15 cm, respectively. . . . .	32
2.8	Standard 2D ultrasound imaging configuration. . . . .	33
2.9	Conventional focused and ultrafast ultrasound imaging for a region of interest of 4 cm. In the leftmost image, 128 focused beams are used with 4 focal depths. Obtained from [11] with permission. © 2014 IEEE. . . . .	35
3.1	Geometry for a baffled piston. . . . .	39
3.2	Geometry for a pulse-echo experiment with two pistons. . . . .	41
3.3	Planar rectangular transducer element. . . . .	47

## List of Figures

---

3.4	Element directivity of a planar transducer element assuming a soft-baffle condition. . . . .	48
3.5	The leftmost figure represents an example spheroid in the particular case when $\mathbf{p} = \mathbf{q}$ . The rightmost figure displays an example prolate spheroid in the general case when $\mathbf{p} \neq \mathbf{q}$ . The light gray accounts for the part of the surface that is outside the positive half volume. . . . .	52
3.6	Coordinate system and angle convention for diverging wave imaging. . . . .	59
3.7	Standard 2D diverging-wave imaging configuration. . . . .	62
3.8	Standard 2D plane-wave imaging configuration. . . . .	70
4.1	Contrast-to-noise ratio [dB] calculated on the simulated anechoic-inclusion phantom as a function of the number of insonifications for (left)-plane wave imaging and (right)-diverging wave imaging. The orange line corresponds to the contrast-to-noise ratio of the sparsely regularized beamforming with 1 insonification and the green line is the contrast-to-noise ratio obtained with the delay-and-sum algorithm for 1 to 15 insonifications. . . . .	84
4.2	From left to right. Log-compressed B-mode images of the anechoic-inclusion phantom reconstructed with the delay-and-sum algorithm for 1 plane-wave insonification, the sparsely regularized beamforming for 1 plane-wave insonification, the delay-and-sum algorithm for 1 diverging-wave insonification, the sparsely regularized beamforming for 1 diverging-wave insonification. . . . .	85
4.3	From left to right. Log-compressed B-mode images of the point-reflector phantom reconstructed with the delay-and-sum algorithm for 1 plane-wave insonification, the sparsely regularized beamforming for 1 plane-wave insonification, the delay-and-sum algorithm for 1 diverging-wave insonification, the sparsely regularized beamforming for 1 diverging-wave insonification. . . . .	86
4.4	From left to right. Log-compressed B-mode images of a first <i>in vivo</i> carotid reconstructed with the delay-and-sum algorithm and with the sparsely regularized beamforming for 1 plane-wave insonification. Log-compressed B-mode images of a second <i>in vivo</i> carotid reconstructed with the delay-and-sum algorithm and with the sparsely regularized beamforming for 1 plane-wave insonification. . .	87
4.5	From left to right. Log-compressed B-mode images of a cross-section view of an <i>in vivo</i> carotid reconstructed with the delay-and-sum algorithm and with the sparsely regularized beamforming for 1 plane-wave insonification. Log-compressed B-mode images of a longitudinal view of an <i>in vivo</i> carotid reconstructed with the delay-and-sum algorithm and with the sparsely regularized beamforming for 1 plane-wave insonification. . . . .	87

4.6	Figures (a) and (b) display the mutual coherence against the number of measurements for the Dirac basis and the Haar basis for the uniform selection of transducer elements, the random selection of transducer elements, CMIX and CTMIX ( $D = 10$ ). Figure (c) displays the coherence for CMIX and CTMIX with mixing coefficients drawn using normal and Rademacher distributions. Figure (d) reports the coherence of CTMIX for different values of $D$ . . . . .	93
4.7	Log-compressed B-mode images of the point-reflector phantom for 1 plane-wave insonification. Figure (a) displays the log-compressed B-mode image reconstructed with the delay-and-sum algorithm. Figure (b) shows the log-compressed B-mode image reconstructed with compressed beamforming coupled with CMIX strategy with 4 % measurements. . . . .	94
4.8	Log-compressed B-mode images of the point-reflector phantom for 1 diverging-wave insonification. Figure (a) shows the log-compressed B-mode image reconstructed with the delay-and-sum algorithm. Figure (b) displays the log-compressed B-mode image reconstructed with compressed beamforming coupled with CMIX strategy with 4 % measurements. . . . .	94
4.9	Peak-signal-to-noise ratio against the number of measurements calculated on the point-reflector phantom for 1 plane-wave insonification and CTMIX, CMIX and the uniform selection of transducer elements. . . . .	95
4.10	Log-compressed B-mode images of the <i>in vivo</i> carotids for 1 plane-wave insonification. Figures (a) and (c) display the log-compressed B-mode images reconstructed with the delay-and-sum algorithm. Figures (b) and (d) show the log-compressed B-mode images reconstructed with compressed beamforming coupled with the CMIX strategy and 20 % measurements. . . . .	95
4.11	Figure (a) displays the tissue-reflectivity function of the point-reflector phantom. Figure (b) presents the corresponding log-compressed B-mode image reconstructed with the delay-and-sum algorithm. We clearly notice the spatially varying blur induced by the delay-and-sum beamforming. . . . .	96
4.12	Numerical point-reflector phantom. Figure (a) displays the phantom used in diverging-wave imaging. Figure (b) presents the phantom used in plane-wave imaging. . . . .	104
4.13	From left to right. Close-up of the log-compressed B-mode images of point reflector 1 to point reflector 8 for the diverging-wave configuration (Fig. 4.12(a)) obtained with standard delay-and-sum beamforming (top row), restored with the proposed model of non-stationary blur (middle row) and restored with the stationary point-spread-function 1 (bottom row). . . . .	105
4.14	Log-compressed B-mode image of the numerical PICMUS phantom. . . . .	106
4.15	x-axis (top row) and z-axis (bottom row) sections corresponding to the points 1 and 2 of Figure 4.14, located at $z = 14$ mm and $x = 0$ mm and 15 mm respectively, for $p = 1.5$ (2 left plots) and $p = 1.3$ (2 right plots) and for the different blur models.	107

## List of Figures

---

4.16	Figures (a-d) present the log-compressed B-mode images of the <i>in vivo</i> carotid 1. Figure (a) displays the low-resolution (LR) image reconstructed with the delay-and-sum algorithm. Figure (b) shows the high-resolution (HR) image obtained with the restoration algorithm ( $p = 1.5$ ) with the proposed model of non-stationary blur. Figures (c-d) show the HR image reconstructed with the restoration algorithm ( $p = 1.5$ ) with the stationary point-spread-functions 1 and 2. Figures (e-h) present the log-compressed B-mode images of the <i>in vivo</i> carotid 2. Figure (e) displays the LR image reconstructed with the delay-and-sum algorithm. Figure (f) shows the HR image obtained with the restoration algorithm ( $p = 1.3$ ) with the proposed model of non-stationary blur. Figures (g-h) show the HR image reconstructed with the restoration algorithm ( $p = 1.3$ ) with the stationary point-spread-functions 1 and 2. . . . .	108
4.17	Tissue (1) and blood (2) regions of the <i>in vivo</i> carotids used for the computation of the tissue-to-clutter ratio and signal-to-noise ratio. . . . .	108
4.18	Ratio of computation times between the proposed non-stationary blur evaluation strategy and the Fourier-based evaluation of stationary blur for varying grid sizes. . . . .	110
4.19	Log-compressed B-mode images of the numerical PICMUS phantom reconstructed (from left to right) with the delay-and-sum algorithm for 1 plane-wave insonification, the delay-and-sum algorithm followed by U-Net16 for 1 plane-wave insonification, the delay-and-sum algorithm followed by U-Net64 for 1 plane-wave insonification, and the delay-and-sum algorithm for 75 plane-wave insonifications. From [203]. . . . .	113
5.1	Figures (a) and (d) display the recovery probability of SA-MUSIC-PKS for varying number of measurements and size of the known support in a noiseless and noisy scenarios (SNR = 30 dB). Figures (b) and (e) present the recovery probability of SA-MUSIC-PKS, RA-ORMP-PKS and SNIHT-PKS against SA-MUSIC, RA-ORMP and SNIHT for varying number of measurements in a noiseless and noisy scenarios (SNR = 30 dB). Figures (c) and (f) present the recovery probability of SA-MUSIC-PKS, RA-ORMP-PKS and SNIHT-PKS against SA-MUSIC, RA-ORMP and SNIHT for varying ranks in a noiseless and noisy scenarios (SNR = 30 dB). . . . .	130
5.2	Recovery probability of MUSIC and MUSIC-PKS when $\text{rank}(\mathbf{X}_{(J_0)}) =  J_0 $ (Exp. 1) and when $\text{rank}(\mathbf{X}_{(J_0)}) = 1$ (Exp. 2). . . . .	132
5.3	The compressive multiplexer. . . . .	136
5.4	The ultrasound compressive multiplexer architecture. . . . .	137
5.5	Recovery performance of the proposed compressive multiplexing method on the simulated anechoic-inclusion phantom for JS-F (dashed line) and CS-PS (solid line) and for (from left to right) a 3 MHz probe with 60 % bandwidth, a 3 MHz probe with 75 % bandwidth, a 5 MHz probe with 60 % bandwidth, and a 5 MHz probe with 75 % bandwidth. . . . .	140

5.6	Log-compressed B-mode images of the numerical PICMUS phantom reconstructed (from left to right) with LS-F, CS-PS, and obtained without compression. We consider a sampling frequency of 62.5 MHz and a compression ratio of 8 for LS-F and CS-PS. . . . .	142
5.7	Log-compressed B-mode images of the <i>in vivo</i> carotid reconstructed (from left to right) with LS-F, CS-PS, and obtained without compression. We consider a sampling frequency of 62.5 MHz and a compression ratio of 8 for CS-PS and LS-F.144	144
5.8	From left to right: Pulse-echo waveform estimated on the point-reflector phantom for the first and second compression strategy; pulse-echo waveform estimated on the anechoic phantom for the first and second compression strategy.	148
5.9	Log-compressed B-mode images of the <i>in-vivo</i> carotid reconstructed (from left to right) with LS-F, CS-PS, CS-PSE and obtained without compression. We consider a sampling frequency of 62.5 MHz and a compression ratio of 8 for LS-F, CS-PS and CS-PSE. . . . .	150
6.1	Diagram of the proposed localization approach: (1) time-of-flight recovery for each channel, (2) time-of-flight matching across channels, (3) localization. . . .	155
6.2	Bipartite graph associated with the proposed localization approach. . . . .	156
6.3	The leftmost figure presents the element-raw data sampled at 20.8 MHz with overlaid pulse-stream parameters. The rightmost figure reports the recovered pulse-stream parameters (red) as well as the reference parameters (green) for $K = 10$ pulses. . . . .	163
6.4	The leftmost figure reports the signal-to-residuals ratio for an increasing number of pulse-stream parameters. The rightmost figure presents the recovered pulse-stream parameters (red) as well as the reference parameters (green) for $K = 30$ pulses. . . . .	164
6.5	Signal-to-residuals ratio as a function of the signal-to-noise ratio for 10 pulses (left figure) and 20 pulses (right plot) and several oversampling ratios. . . . .	165
6.6	Average misclassification error (10 draws) of the proposed time-of-flight labeling algorithm for different values of the signal-to-noise ratio. . . . .	172
6.7	Impact of the proposed pruning method on (left figure)-the number of combinations and (right figure)-the processing time of the time-of-flight labeling method; “No pruning” removes the already used combinations and “Max TOF” exploits the method described in Section 6.3.2. . . . .	173
6.8	The leftmost figure displays the original (orange) and noisy element-raw data (blue); The rightmost figure presents the localizations of the 15 point-reflectors recovered with the proposed approach with 3 transducer elements in receive and 5 times oversampling compared to critical sampling rate (20 iterations of Cadzow denoising for time-of-flight recovery). . . . .	175
6.9	Localization of the 7 drilled holes. The localization results are overlaid on the log-compressed B-mode image reconstructed with the delay-and-sum algorithm.176	176



## List of Tables

4.1	Characteristics of the ATL L12-5 50 mm and P4-2v probes . . . . .	83
4.2	Comparison of the proposed sparsely regularized beamforming against state-of-the-art methods on the simulated PICMUS dataset . . . . .	86
4.3	Relative timings of the main operations involved in sparsely regularized beamforming for the cyst phantom in plane-wave imaging and the point-reflector phantom in diverging-wave imaging . . . . .	88
4.4	Contrast-to-noise ratio [dB] for the three considered compressed beamforming strategies and for various numbers of measurements . . . . .	95
4.5	Characteristics of the P4-2v, L11-4v and L12-5 50mm probes . . . . .	103
4.6	Comparison of the restoration methods on the point-reflector phantom in the diverging wave experiment . . . . .	104
4.7	Comparison of the restoration methods on the point-reflector phantom in the plane-wave experiment . . . . .	105
4.8	Comparison of the restoration methods on the numerical PICMUS phantom . . . . .	107
4.9	Comparison of the restoration methods on the in vivo carotids . . . . .	109
4.10	Computation times of different blur evaluation strategies . . . . .	110
5.1	Comparison of the compressive multiplexing methods on the numerical PICMUS phantom . . . . .	142
5.2	Comparison of the compressive multiplexing methods on the in vivo carotids . . . . .	143
5.3	Comparison of the pulse-estimation methods on the simulated anechoic and point-reflector phantoms . . . . .	148
5.4	Comparison of the compressive multiplexing methods with pulse-estimation on the in vivo carotids . . . . .	149



# Notations and Symbols

## Abbreviations

cf.	confere
e.g.	exempli gratia
i.e.	id est
i.i.d.	independent identically distributed
s.t.	such that
w.r.t.	with respect to
ADC	analog-to-digital converter
AM	alternating minimization
ASIC	application-specific integrated circuit
CAD	computer-aided design
CDWC	coherent diverging wave compounding
CMIX	channel mixing
CMUX	compressive multiplexer
CNN	convolutional neural network
CNR	contrast-to-noise ratio
CoSaMP	compressive sampling matching pursuit
CPWC	coherent plane wave compounding
CR	contrast ratio
CS	compressed sensing
CS-MUSIC	compressive MUSIC
CT	computerized tomography
CTMIX	channel and time mixing
DAS	delay-and-sum
DFT	discrete Fourier transform
DNN	deep neural network
DOF	degrees of freedom
DSP	digital signal processing
DW	diverging wave
EDM	Euclidean distance matrix
EVD	eigenvalue decomposition
FISTA	fast iterative shrinkage thresholding algorithm

## Abbreviations

---

FRI	finite rate of innovation
FT	Fourier transform
FWHM	full width at half maximum
GGD	generalized Gaussian distribution
GRT	generalized Radon transform
GPU	graphical processing unit
IHT	iterative hard thresholding
IQ	in Phase-Quadrature
ISTA	iterative shrinkage thresholding algorithm
LASSO	least-absolute shrinkage and selection operator
LRT	linear Radon transform
LTl	linear time-invariant
MAP	maximum-a-posteriori
MIRF	material impulse response function
MMV	multiple measurement vectors
MRI	magnetic resonance imaging
MTF	material transfer function
MUSIC	multiple signal classification
NDE	non-destructive evaluation
NRMSE	normalized root mean square error
OMP	orthogonal matching pursuit
OSMP	orthogonal subspace matching pursuit
PDF	probability density function
PDFB	primal dual forward backward
PICMUS	plane-wave imaging challenge in medical ultrasound
PSF	point spread function
PSNR	peak-signal-to-noise ratio
PW	plane wave
PZT	lead-zirconate-titanate
RIP	restricted isometry property
SAFT	synthetic aperture focusing techniques
SAR	synthetic aperture radar
RA-ORMP	rank aware orthogonal recursive matching pursuit
RF	radio-frequency
SA	synthetic aperture
SA-MUSIC	subspace augmented MUSIC
SH	sample and hold
SMV	single measurement vector
SNIHT	simultaneous normalized iterative hard thresholding
SNR	signal-to-noise ratio
SRR	signal-to-residual ratio
SSIM	structural similarity index

SVD	singular value decomposition
TCR	tissue-to-clutter ratio
TGC	time-gain compensation
TOF	time-of-flight
TRF	tissue-reflectivity function
TV	total variation
uDGP	unassigned distance geometry problem
UFUS	ultrafast ultrasound
US	ultrasound
VLSI	very large scale integration
WKS	Whittaker-Kotelnikov-Shannon

## Matrices

$\mathbf{X}$	Matrix $\mathbf{X} \in \mathbb{K}^{M \times N}$
$\mathbf{X}_i$	$i$ -th column of the matrix $\mathbf{X}$
$\mathbf{X}_{(i)}$	$i$ -th row of the matrix $\mathbf{X}$
$X_{i,j}$	$(i, j)^{th}$ entry of the matrix $\mathbf{X}$
$\mathbf{X}_J$	Restriction of the matrix $\mathbf{X}$ to the columns indexed in $J$
$\mathbf{X}_{(J)}$	Restriction of the matrix $\mathbf{X}$ to the rows indexed in $J$
$\mathbf{X}^\top$	Transpose of the matrix $\mathbf{X}$
$\mathbf{X}^*$	Hermitian transpose of the matrix $\mathbf{X}$
$\mathbf{X}^\dagger$	Moore pseudo-inverse of the matrix $\mathbf{X}$
$\mathcal{R}(\mathbf{X})$	Span of the columns of the matrix $\mathbf{X}$
$\mathcal{N}(\mathbf{X})$	Nullspace of the matrix $\mathbf{X}$
$\det(\mathbf{X})$	Determinant of the matrix $\mathbf{X}$
$\lambda_{\max}(\mathbf{X})$	Maximum eigenvalue of the matrix $\mathbf{X}$
$\text{rank}(\mathbf{X})$	Rank of the matrix $\mathbf{X}$
$\text{spark}(\mathbf{X})$	Spark of the matrix $\mathbf{X}$
$\text{Tr}(\mathbf{X})$	Trace of the matrix $\mathbf{X}$
$\text{supp}(\mathbf{X})$	Row-support of the matrix $\mathbf{X}$
$\ \mathbf{X}\ _F$	Frobenius norm of the matrix $\mathbf{X}$
$\ \mathbf{X}\ _{0,\text{row}}$	Zero row-norm of the matrix $\mathbf{X}$
$\mathbf{X} \circ \mathbf{Y}$	Hadamard product between $\mathbf{X}$ and $\mathbf{Y}$
$\langle \mathbf{X}, \mathbf{Y} \rangle$	Frobenius Inner-product between the matrices $\mathbf{X}$ and $\mathbf{Y}$
$\text{diag}(\mathbf{X})$	Column vector formed by the diagonal elements of the matrix $\mathbf{X}$
$\mathbf{I}$	Identity matrix

## Vectors

$\mathbf{x}$	Vector $\mathbf{x} \in \mathbb{K}^N$
$x_i$	$i$ -th component of the vector $\mathbf{x}_i \in \mathbb{K}^N$

## Functions

---

$\mathbf{x}^\top$	Transpose of the vector $\mathbf{x}$
$\mathbf{x}^*$	Conjugate transpose of the vector $\mathbf{x}$
$\ \mathbf{x}\ _p$	$\ell_p$ -norm of the vector $\mathbf{x}$ , e.g. $\ \mathbf{x}\ _p = \sqrt[p]{\sum_{i=1}^n  \mathbf{x}_i ^p}$
$\text{supp}(\mathbf{x})$	Support of the vector $\mathbf{x}$
$\langle \mathbf{x}, \mathbf{y} \rangle$	Inner-product between $\mathbf{x} \in \mathbb{C}^N$ and $\mathbf{y} \in \mathbb{C}^N$ , i.e. $\langle \mathbf{x}, \mathbf{y} \rangle = \sum_{i=1}^n \mathbf{x}_i^* \mathbf{y}_i$
$\mathbf{x} * \mathbf{y}$	Discrete convolution between $\mathbf{x} \in \mathbb{C}^M$ and $\mathbf{y} \in \mathbb{C}^N$ , i.e. $(\mathbf{x} * \mathbf{y})_u = \sum_{i=\max(1, u-N+1)}^{\min(M, u)} \mathbf{x}_i \mathbf{y}_{u-i+1}$
$\text{diag}(\mathbf{x})$	Diagonal matrix formed by the vector $\mathbf{x}$
$\mathbf{1}$	Vector of all ones

## Sets

$\mathbb{N}$	natural numbers
$\mathbb{N}_+$	positive natural numbers
$\mathbb{Z}$	integers
$\mathbb{R}$	real numbers
$\mathbb{R}_+$	positive real numbers
$\mathbb{C}$	complex numbers
$\mathbb{K}$	$\mathbb{R}$ or $\mathbb{C}$
$J$	index set, $J \subset \{1, \dots, n\}$
$\bar{J}$	complement of the index set, $\bar{J} = \{1, \dots, n\} \setminus J$
$ J $	Cardinal of the index set $J$

## Functions

$\frac{\partial u}{\partial \xi}, \frac{du}{d\xi}$	Derivative of the function $u$ w.r.t the variable $\xi$
$\frac{\partial^2 u}{\partial \xi^2}, \frac{d^2 u}{d\xi^2}$	Second order derivative of $u$ w.r.t the variable $\xi$
$\nabla_\xi u$	Gradient of $u$ w.r.t the variable $\xi$ , e.g. $\nabla_\xi u = \left[ \frac{\partial u}{\partial \xi_1}, \dots, \frac{\partial u}{\partial \xi_N} \right]^\top$ in $\mathbb{R}^N$
$ \nabla_\xi u $	$u$ , $ \nabla_\xi u  = \sqrt{\langle \nabla_\xi u, \nabla_\xi u \rangle}$ for a scalar valued function
$\nabla^2 u$	Laplacian of $u$ , e.g. $\nabla^2 u = \sum_{i=1}^N \frac{\partial^2 u}{\partial^2 x_i}$ in $\mathbb{R}^N$
$u \otimes_\xi v$	Convolution of $u$ and $v$ w.r.t the variable $\xi$ , e.g. $u \otimes_\xi v = \int_{-\infty}^{+\infty} u(\xi) v(\cdot - \xi) d\xi$
$Hu, H(u)$	Linear operator acting on $u$
$\delta$	Dirac delta function
rect	Rect function, $\text{rect}(\xi) = 1$ if $\xi \in \left[-\frac{1}{2}, \frac{1}{2}\right]$ , $\text{rect}(\xi) = 0$ otherwise
sgn	Sign function, $\text{sgn}(\xi) = \pm 1$ if $\xi > 0$ , $\xi < 0$ and $\text{sgn}(0) = 0$
sinc	Sinc function, $\text{sinc}(\xi) = \frac{\sin \pi \xi}{\pi \xi}$
$\lfloor \cdot \rfloor$	Floor function, $\lfloor \xi \rfloor = \max(m \in \mathbb{Z}, m \leq \xi)$

$\mathbf{1}_A$	Indicator function on a subset $A$ , $\mathbf{1}_A(x) = 1$ if $x \in A$ , $\mathbf{1}_A(x) = 0$ otherwise
$P_A$	Projection on the set $A$

## Spaces and Norms

$L_p(\Omega)$	Banach space equipped with the norm $\ u\ _{L_p(\Omega)} = (\int_{\Omega}  u(x) ^p dx)^{1/p}$
$L_2(\Omega)$	Hilbert space of square integrable functions on $\Omega$
$\langle f, g \rangle_{L_2(\Omega)}$	Inner product on $L_2(\Omega)$ , e.g. $\langle f, g \rangle_{L_2(\Omega)} = \int_{\Omega} f(x) g(x) dx$
$l_2(\mathbb{Z})$	Space of square summable sequences

## Miscellaneous

$\Omega$	Subset of $\mathbb{R}^N$
$\partial\Omega$	Boundary of $\Omega$
$\wedge$	Cross product in $\mathbb{R}^3$
$\text{Re}(\cdot)$	Real part of, e.g., $\text{Re}(a + ib) = a$
$\text{Im}(\cdot)$	Imaginary part of, e.g. $\text{Im}(a + ib) = b$
big $O$	big $O$ notation, $x \in O(y)$ if and only if $0 \leq x_n \leq \gamma y_n$ , for all $n \geq n_0$ , $n_0 \in \mathbb{N}$ , $\gamma > 0$



# 1 Introductory Notes

Quelle que soit la cause déterminante, toutes les fois qu'un cristal hémihèdre à faces inclinées, non conducteur, se contracte, il y a formation de pôles électriques dans un certain sens; toutes les fois que ce cristal se dilate, le dégagement d'électricité a lieu en sens contraire.

---

*Comptes rendus de l'Académie des Sciences, séance du 2 août 1880*  
Pierre and Jacques Curie

In the last decade, the field of US imaging has lived a revolution driven by two main technical breakthroughs. The first one is the democratization of ultrafast ultrasound (UFUS) imaging which has completely changed the way US imaging is performed. While conventional US imaging builds an image from multiple focused beams, UFUS proposes to exploit plane wave (PW) and diverging wave (DW) insonifications. This has a significant impact on every stage of the US imaging pipeline but more specifically on image reconstruction where beamforming based on scan-lines has been replaced by fully parallel pixel-based beamforming. UFUS imaging permits to perform US imaging at a frame rate of a few kHz which paves the way to a myriad of novel clinical applications, e.g. ultrafast Doppler imaging, shear wave elastography and functional US imaging of the brain activity.

The second breakthrough is the development of portable US imaging impelled by the mass adoption of mobile commodity devices, e.g. smartphones and tablets. From a technical point of view, this requires a complete redesign of the US imaging system, in which the data would be digitized early in the acquisition process, in the head of the probe.

Hence, US imaging is living a complete mutation and many new signal processing challenges have appeared, especially on the ability to perform high-quality imaging with as few insonifications as possible. In this thesis, we study various inverse problems related to these challenges. Our goal is to provide a mathematical formalism of the physical process underlying US imaging as well as an understanding of the nature of US signals in such a way that appropriate methods are leveraged to solve these inverse problems.

In this chapter, we propose a historical introduction of US that will be useful to understand the current challenges and the motivations of the thesis, described in a second section. Finally, we briefly introduce the different chapters of this thesis. We detail the specific challenges addressed in each of them as well as the methods developed to solve the related issues.

### 1.1 A Brief History of Ultrasound

#### 1.1.1 Early Discoveries: From Sound to Ultrasound

Sound is probably as old as the Universe. It has been used by animals and later humans to communicate, locate and identify objects. Acoustics, which comes from the greek word *akouein* (to hear), is the science of sound. Ancient Greeks and Romans were deeply interested in the physics of sound waves which is reflected by the fine acoustics of antique theaters. Pythagoras, mostly known for his famous theorem, studied vibrating strings and sounds. He discovered that it was possible to produce sound with different frequencies by splitting vibrating strings.

The first writing about acoustics comes from Vitruvius, a Roman architect, who wrote in its *De Architectura* [1]:

We must choose a site in which the voice may fall smoothly, and not be returned by reflection so as to convey an indistinct meaning to the ear.

Much of early works in acoustics were related to music. Galileo, Sauveur and Taylor worked on the vibrating string and especially on the relation between the length of the string and the frequency of the emitted sound wave. This research has culminated with the work of Bernoulli who described a partial differential equation for the vibrating string.

Acoustics have made enormous advances in the 19th century, impelled by remarkable acousticians such as Tyndall, von Helmholtz, Koenig, Stokes, Bell, Edison, and Rayleigh. The contributions of the latter were fundamental with 128 publications among which the “Theory of Sound” has settled the mathematical formalism to characterize sound waves.

The use of sound as a medical imaging modality has been firstly mentioned by Hooke (1605-1703) which wrote:

There may also be a possibility of discovering the internal motions of the internal parts of bodies, whether animal, vegetable, or mineral, by the sound they make; that one may discover the works performed in the several offices and shops of a man’s body, and thereby discover what instrument or engine is out of order, what works are going on at several times, and lie still at others, and the like. I could proceed further, but methinks I can hardly forbear to blush when I consider how the most part of men will look upon this: but, yet again, I have this encouragement, not to think all these things utterly impossible.

Spallanzani (1729-1799) firstly observed US waves by studying navigation of bats in the darkness. He concluded that, in order to hunt at night, bats did not rely on their eyes but on some other sense. However, he did not conclude that that other sense was hearing. Louis

Jurine (1751-1819), a Swiss physician contemporary to Spallanzani, followed up the work of the Italian naturalist and managed to discover that this other sense was hearing.

The real breakthrough that paved the way to systems based on high-frequency sound is the discovery of the piezoelectric effect by Pierre and Jacques Curie in 1880. They discovered that certain crystals accumulate electrical potential in response to mechanical stress. To measure and illustrate such an effect, they built the “quartz piézo-électrique”, displayed in Figure 1.2, which consists of a long and narrow quartz plate, whose two larger surfaces were metalized. In order to quantify the piezoelectric effect, they used the particularities of transverse piezoelectricity in quartz—the strain due to electric voltage along a perpendicular direction—in which the resulting elongation of the crystal per volt is proportional to the ratio between the crystal’s length and thickness.

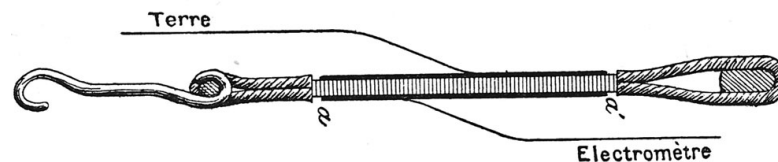


Fig. 1.1. The Curie's “quartz piézo-électrique”. Obtained from [2].

A year later, Lippmann deduced the reversibility of the piezoelectric effect from thermodynamic principles.

### 1.1.2 Echo Ranging with Ultrasound: Everything Starts with the Titanic

Shortly after the Titanic sank (1912), underwater detection systems and sonar, whose acronym holds for sound navigation and ranging, were developed for submarines navigation. The first patent for an underwater echo ranging sonar was filed by Richardson, an English meteorologist, one month after the sinking of the Titanic, and the first acoustical echo ranging system, the Fessenden oscillator, appeared in 1914.

By the end of the World War I, the French physicist P. Langevin, a student of Pierre Curie, and the Russian scientist C. Chilowsky, benefited from the recent discoveries of the diode and the triode, the vacuum tube amplifiers, to construct the first powerful active echo-ranging system which was later used to detect German U-boats. In 1917, they filed a patent, whose first page is displayed on Figure 1.2, which described their system in details. The transducer that Langevin used in the earlier days was a mosaic of thin quartz crystals glued between two steel plates (the composite having a resonant frequency of about 150 kHz), mounted in a housing suitable for submersion.

### 1.1.3 Ultrasound for Medical Imaging and Therapy

During their experiments, Langevin and Chilowski observed that the transmission of US waves lead to death of fishes that floated at the water surface. This was the first recognition of the

Oct. 23, 1923.

1,471,547

C. CHILOWSKY ET AL

PRODUCTION OF SUBMARINE SIGNALS AND THE LOCATION OF SUBMARINE OBJECTS

Filed May 19, 1917

2 Sheets-Sheet 1

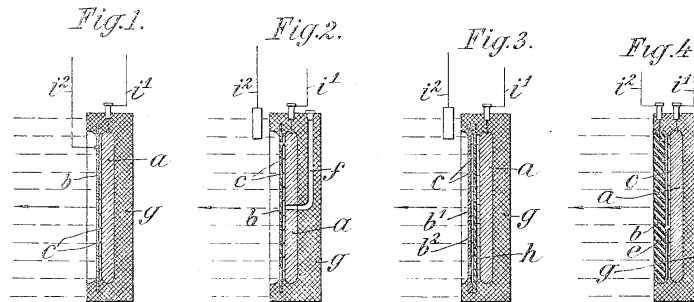


Fig. 1.2. Image of the sonar patent filed in 1917 by Constantin Chilowsky and Paul Langevin.

destructive ability of US. Between the 1930s and the 1950s, intense research on the safety of US and of its use as a therapeutic tool have been carried out. William Fry at the University of Illinois and Russell Meyers at the University of Iowa performed craniotomies and used US to destroy parts of the basal ganglia in patients with Parkinsonism.

Ultrasonic energy was also extensively used in physical and rehabilitation medicine. Jerome Gersten at the University of Colorado reported in 1953 the use of US in the treatment of patients with rheumatic arthritis. Other researchers such as Peter Wells and Douglas Gordon in England as well as Michele Arslan in Italy employed ultrasonic energy in the treatment of Meniere's disease.

In parallel, the possibility of utilizing US as a diagnosis tool has been investigated by many researchers, based on the A-mode scanner used for flaw detection in metals. The A-mode, which holds for amplitude mode, works as follows. A transducer sends a sequence of multiple ultrasonic pulses into a region of interest. Backscattered echoes induced by impedance variations are received and amplified by the system. An oscilloscope is used to display the amplitude of such echoes as a function of time [3].

Using existing systems, Ludwig, a graduate student from the University of Pennsylvania, performed experiments on an extensive amount of animal tissues, proposing different methodologies and frequencies. Its "June '49 report", published in 1949, is considered the first report on the diagnostic use of US in the United States. Later, he made an extensive number of TOF measurements and discovered that the average speed of sound in tissue is  $1540 \text{ m s}^{-1}$ , a value still used nowadays. In 1953, Edler and Hertz detected heart motion using an A-mode flaw-detection system and paved the way to "echocardiography", the application of US to the imaging of the heart [4].

A-mode was developed as a medical diagnosis tool based on echo-ranging systems. The first attempt to perform US imaging has been achieved by the Austrian neurologist Dussik who tried to locate brain tumors by measuring US wave attenuation through the skull. An example

image obtained with his system is given in Figure 1.3.

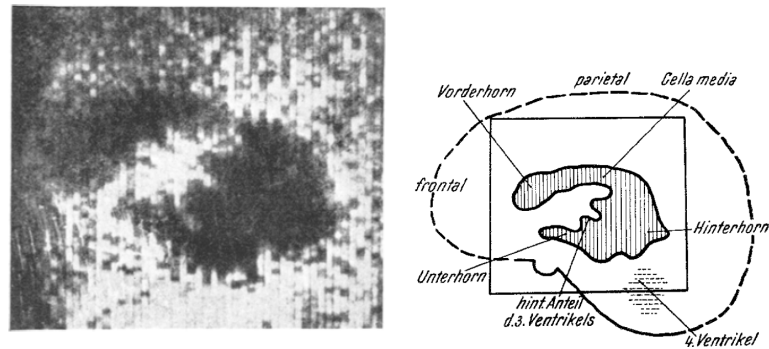


Fig. 1.3. Image of the brain ventricles with Dussik's system. Obtained from [5].

His paper [5], published in 1952, was precursor to many studies in the 1950s. Wild and Reid proposed the first pulse-echo imaging system based on a hand-held US probe. The main novelty compared to A-mode systems was the acquisition of multiple lines obtained from different positions of the transducer elements, controlled either in a freehand form or mechanically. For each position, a pulse is transmitted in the medium and backscattered echoes are displayed. Thus, multiple scan lines are displayed whose amplitudes depend on the depth. Because the brightness along each trace is proportional to the echo amplitude, this display presentation came to be known as “B-mode,” with “B” meaning “brightness”.

B-mode imaging then became the standard US imaging modality with various scanning methods such as translation, rotation or compounding (translation and rotation). First B-mode scanners were commercialized, with commercial success for some of them like the “Diasonograph”. This scanner was composed of an articulated arm onto which the transducer was mounted, whose motion was monitored with a spatial encoder and static images were displayed on a screen. Such a system weighted approximately one ton. With the revolution of the transistor and the integrated circuits, scanners became more and more sophisticated with increased dynamic range, gray scale imaging and memory capabilities. In the late 1970s, millions of clinical examinations were performed annually using US imaging [6].

All the systems presented so far were static B-mode scanners, which were used to perform a single image of the region of interest. However, the revolution of the electronics have also allowed the development of real-time imaging systems. In 1965, Siemens developed the Vidoson 635, the first real-time US B-mode imaging system, where a rectangle image was obtained by rotating three transducer elements in front of a parabolic reflector. An examination with the Vidoson 635 is shown on Figure 1.4(a).

The concept of multi-element electronic linear array has been firstly described by Buschmann in 1964 and the first real-time scanner employing such a linear array has been invented in 1971 by Bom in Rotterdam, in which the multiple transducer elements were sequentially driven by an electronic multiplexer, producing multiple scan lines. The system operated at a frequency of 3 MHz sweeping at a frame rate of 150 frames/sec. A year later, the earliest commercial linear-array scanner, displayed on Figure 1.4(b) and denoted as the “Multiscan”, was produced.

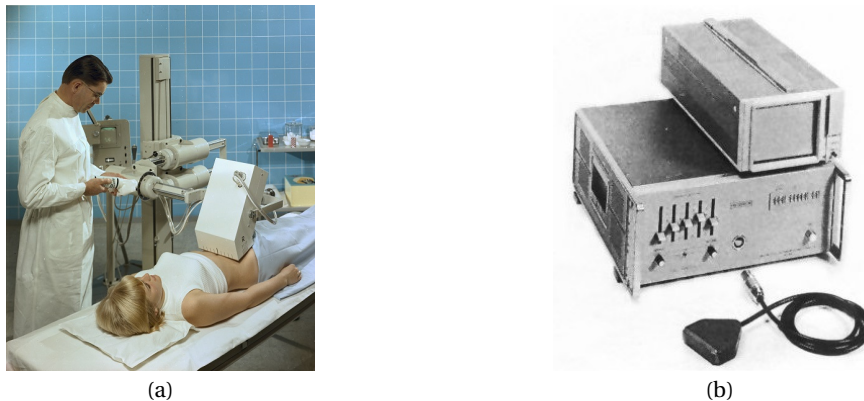


Fig. 1.4. Figure (a) shows a clinical examination with the Siemens Vidoson 635. Figure (b) displays the Multiscan assembly.

Simultaneously and independently to Bom's work, Leandre Pourcelot, a french engineer, pioneered the use of US Doppler in vascular research and developed the first European US Doppler velocimeter in 1963. In 1972, he developed, with his colleagues in Tours, one of the first real-time US imaging systems based on linear scanning of a multi-element linear array. In 1975, Von Ram and Thurstone, from Duke University, were able to produce real-time images of the heart with a 16-channel phased array scanner built in their laboratory [7]. During the 1980s, array-based systems became the dominant modality for imaging and more and more sophisticated systems with improved image quality were developed benefiting from the apparition of application-specific integrated circuits (ASICs), digital signal processing (DSP) chips, and the computer-aided design (CAD) of very large scale integration (VLSI) circuits.

### 1.1.4 Ultrasound Imaging in the 21st Century

Since the 1980s, US imaging has achieved a tremendous growth with the development of both the transducer technology and the electronics, e.g. microprocessors, low-cost analog to digital converters.

In the beginning of the 21st century, Philips commercialized the first real-time 3D US scanner based on a fully sampled 2900-element matrix array, where part of the image formation was performed in the probe head. Nowadays, US scanners are equipped with advanced imaging features such as

- Doppler, color-flow and vector imaging: Initially, Doppler shift US signals induced by blood flow were displayed (and even heard) since they lie in the audio range. Such information has important clinical impact on the diagnosis of malignant conditions where tissue vascularity is increased. Nowadays, US imaging systems exploit more advanced methods based on directional beamforming and speckle tracking. They display vector-flow images where the blood-flow velocity is calculated in parallel for all the pixels of the region of interest (See [8] for a detailed description).

- **Non-linear imaging:** Non-linear US imaging is performed in two ways. In contrast-enhanced imaging, microbubbles are injected intravenously as a contrast agent, and their non-linear responses are exploited to image blood vasculature alone, strongly decreasing tissue echoes. In tissue harmonic imaging, the non-linear propagation properties of tissues are exploited, providing superior resolution. It is used clinically for patients that are difficult to image, e.g. obese people.
- **Tissue characterization features:** Ultrasound tissue characterization can be defined as “The assessment by US of quantitative information about the histological characteristics, and pathological changes thereof, of biological tissues” [9]. The information extracted from US signals consists of acoustic characteristics of tissues, i.e. the attenuation and backscattering coefficients, both as function of frequency. Another application is elastography which allows for the identification of elastic and visco-elastic properties of tissues from the analysis of a sequence of US images [10]. The idea is to analyze variations in the US signals (propagation of shear and longitudinal waves) induced either by compression of the tissues (shear wave elasticity imaging) or by radiation force excitation (acoustic radiation force impulse imaging). Higher wave speeds and smaller displacements are associated with stiffer tissues, and slower wave speeds and larger displacements occur with more compliant tissues.

### 1.1.5 The Revolution of Ultrafast Ultrasound Imaging

The history of US imaging is closely linked to the developments of echo-ranging techniques and sonar, which were very active fields of research in the first half of the 20th century. First B-mode imaging systems were derived from A-mode devices commercially available at that time. In such systems, scan lines were sequentially constructed by mechanically sweeping a transducer element. In the second generation of B-mode imaging devices, scan lines were built by focusing multi-element arrays at various locations, leading to an increased signal-to-noise ratio (SNR) compared to systems based on a single transducer element.

In UFUS, imaging is seen from a completely different perspective. Indeed, instead of transmitting multiple focused waves to form scan lines, UFUS relies on the transmission of unfocused waves in the medium. Each of these unfocused waves insonifies the entire medium such that the backscattered echoes recorded by the transducer elements contain information of the whole medium. The process of imaging, denoted as beamforming, amounts to decoding these backscattered echoes in order to form a numerical image of the medium.

A neat way to understand UFUS imaging from a physical perspective, well explained by Tanter and Fink [11], is through the lens of holography [11, 12]. In optics, holographic imaging is performed into two steps described in the left part of Figure 1.5. In the first step, the interference pattern between the scattered field from the object and a plane incident field is recorded onto a holographic plate.

In a second step, the plate is illuminated with the complex conjugate of the incident field which generates a hologram of the original image, i.e. the complex conjugate of the scattered field, even though the object is not anymore present. The underlying idea of holographic imaging is to encode the phase of scattered field, which is not directly measurable, into an

intensity (of the interference pattern) on the plate. Then, the incident field can be seen as the key necessary to decode the phase information from the printed interference pattern.

In US imaging, the concept of holographic imaging can be applied in a slightly different way. Indeed, contrary to optical holography that relies on non-linear interferences to access the phase information, holographic US imaging exploits the reversible properties of transducer elements that are capable of recording both the amplitude and phase information of the scattered field. Hence the element raw-data can be directly used to generate a hologram of the object, without the need for the complex conjugate of the incident field, as described in the right part of Figure 1.5.

In a first step, an unfocused wave is transmitted in the medium whose backscattered echoes, i.e. the scattered field, are recorded by the transducer elements. By reversing the echoes (phase conjugation) and transmitting them in the medium, we construct a field that re-focuses optimally on the object of interest. Such a time-reversed propagation, introduced by Fink [13] for aberration correction and therapy, can also be used to synthesize a virtual image of the medium, in the so-called beamforming process.

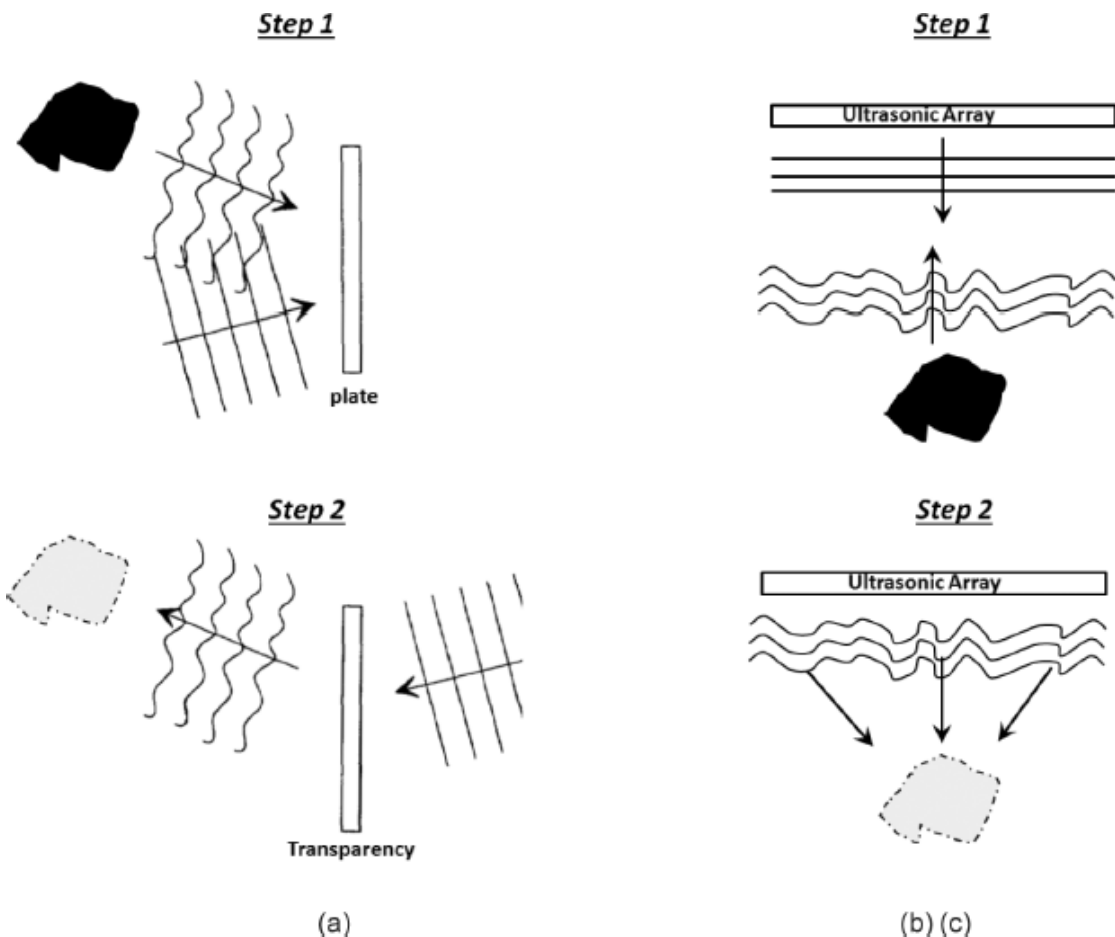


Fig. 1.5. Analogy between the two steps involved in (a)-optical holography, (b)-time reversal ultrasound imaging and (c)-ultrafast ultrasound imaging. Obtained from [11] with permission. © 2014 IEEE

---

## 1.2. Several Challenges in Ultrasound imaging

The term “ultrafast ultrasound” has been introduced in 1977 [14], in a seminal work by Bruneel *et al.* in which the authors managed to obtain B-mode images at 1 kHz, based on the interaction between light and sound waves. Two years later, the same group managed to reconstruct an entire virtual image with parallel analog beamforming, at a rate of 1 kHz [15]. Since then, UFUS has drawn strong interest from the US community. Two approaches have been developed in parallel (and concurrently), namely synthetic aperture (SA) imaging and PW (or DW) imaging. In SA imaging, every transducer element is used to transmit a spherical wave in a sequential manner, and a low-quality image is reconstructed by beamforming of the backscattered echoes. In a final step, the low quality images are recombined to form a high quality image [16–19]. Such approaches were not coined as “ultrafast” since they require as many insonifications as conventional beamforming to obtain images of sufficient quality. Another drawback of these approaches is the low penetration of single-element transmissions which lead to poor SNR when imaging deep tissues. In order to address the latter, methods based on DWs, where the virtual point source was located behind the probe, have been developed, allowing the use of subapertures instead of a single element [18]. In PW imaging, the transducer elements are excited in such a way that a planar wavefront is transmitted in the medium. The idea has been introduced by Lu *et al.* [20] under the appellation “non-diffractive” beam. In their work, they proposed a Fourier-based beamforming method where the image reconstruction is achieved through a remapping in the Fourier domain (non uniform Fourier transform) similar to migration techniques in seismic imaging [20–23]. In the beginning of the 2000s, Fink’s research group in Paris demonstrated that PW imaging associated with parallelized digital beamforming implemented on graphical processing units (GPUs) might lead to B-mode imaging at several kHz frame rate [24, 25]. Since then, UFUS has been extensively developed and it is now a quite mature technology. It has paved the way to several groundbreaking clinical applications of US imaging such as shear-wave elastography [24–26] and ultrafast Doppler imaging [27]. See [11] for an exhaustive review of the applications of UFUS in biomedical imaging. Since 2008, ultrafast PW imaging has been implemented in the Airexplorer™ system developed by Supersonic Imagine. It is also implemented in the Verasonics Vantage™ research system.

## 1.2 Several Challenges in Ultrasound imaging

### 1.2.1 Gaining More Physical Understanding of Ultrafast Ultrasound Imaging

The evolution of US imaging in the 20th century has been driven by technical breakthroughs, especially in the field of electronics. Most of the researchers, interested in studying the potential use of US in medical imaging and therapy, exploited existing echo-ranging devices to perform their research. Hence, the B-mode imaging pipeline, even in recent US imaging devices, is strongly influenced by the way A-line scans were originally acquired in echo-ranging systems.

System design in US imaging has been less driven by physical considerations than other medical imaging modalities such as computerized tomography (CT) and magnetic resonance imaging (MRI), which are based on strong mathematical foundations, maybe because of the need for real-time imaging.

Thanks to the work of Fink's group on time reversal [13] and other related topics, UFUS imaging has been introduced with some in-depth physical motivations. This is a first step towards the understanding of UFUS imaging. But, it should be possible to go further and define a forward model that would relate some quantity of interest to the set of measurements, in a similar way to photoacoustic tomography and CT. This would allow us to gain substantial understanding of the physics underlying the process of UFUS imaging and to revisit existing imaging algorithms.

### 1.2.2 High-quality Ultrafast Ultrasound Imaging with few Insonifications

UFUS imaging has paved the way to a whole range of clinical applications. But, it suffers from a degraded image quality compared to conventional imaging based on multi-focused beams. Such a degradation is problematic since it may negatively impact any medical diagnosis based on image features. The main reason of such a degradation is clear. Compared to the case of focused waves where the energy is concentrated in a specific region of interest, the energy of a PW or a DW is spread over the whole medium, resulting in lower SNR and poorer spatial resolution. One way to address this problem consists in recreating a synthetic focus by averaging multiple images obtained with different insonifications, in a process called coherent compounding [28, 29]. While the implementation of such a technique is straightforward, it requires multiple insonifications therefore reducing the frame rate. Coherent compounding also proportionally increases the power required to form an image, which may be problematic in challenging environments, e.g. systems operating on batteries. Hence, one active research topic in the US community aims to obtain high-quality images with as few insonifications as possible.

### 1.2.3 High-quality Ultrafast Ultrasound Imaging with a Reduced Number of Elements and Cables

While reducing the number of insonifications is key for UFUS imaging, we may also think about reducing the amount of data per insonification necessary to reconstruct a high-quality image. This may target two different applications, namely portable devices where the amount of data to be transferred will be limited by the transfer rate of the digital cable, and 3D imaging. Indeed, 3D imaging requires dense matrix arrays of several thousands of elements. Connecting such a number of elements to the back-end computer would require an extensive number of cables, which is either unfeasible or prohibitively expensive. Nowadays, only few cumbersome research systems are capable of directly connecting 1024-elements matrix arrays [30–32].

Hence, much research has focused on the reduction of the number of transducer elements or coaxial cables with application to 3D imaging. Most popular approaches are sparse-array techniques, where the number of elements in receive is reduced, micro-beamforming where part of the imaging process is achieved in the head of the probe, or time multiplexing. But these methods come with a drastic reduction of the image quality in terms of either resolution, contrast or frame rate. Hence, one active field of research focuses on the development of novel techniques for data-rate reduction in US imaging.

### **1.3 Roadmap of the Thesis**

This thesis is based on five chapters that address various inverse problems related to the challenges mentioned in Section 1.2.

#### **Chapter 2 - Basic Notions of Ultrasound**

In this chapter, we provide tools for the non-specialist to familiarize with US imaging. First, we review the main functional components of a US imaging system, with a brief description of each of them. We detail several essential steps of the imaging pipeline i.e. transmission and reception of US waves, image formation and envelope detection. We also describe the main features of US images and the quality metrics used to quantify some of these features. In a last section, we describe in more details the delay-and-sum (DAS) algorithm used for image formation in UFUS. We also describe the coherent compounding technique for enhanced UFUS imaging.

#### **Chapter 3 - Ultrasound Imaging as an Inverse Problem: A Time-domain Perspective**

In this chapter, we revisit pulse-echo US imaging and demonstrate that it can be expressed as a linear inverse problem. We first relate the element-raw data received by the transducer elements to local fluctuations of speed of sound and density through a linear measurement model defined via the well-known pulse-echo spatial impulse response model. This allows us to properly define the inverse problem associated with pulse-echo US imaging.

Secondly, we derive the measurement model in the continuous domain for various configurations, i.e. single emitter - single receiver, PW and DW imaging, for both 2D and 3D imaging. We show that it can be seen as quadratic Radon transform along specific quadric surfaces, whose shape depends on the configuration. This novel understanding allows us to revisit standard image formation techniques through the lens of the mathematics developed for the Radon transform. We specifically show that the DAS algorithm can be seen as a kind of backprojection technique, by analogy with image reconstruction in CT. We also introduce a novel formalism of the measurement model by appropriate parameterization of the quadrics. Then, we propose a discretization scheme of the parameterized model that allows us to provide efficient matrix-free evaluations of the measurement model and its adjoint, a key aspect towards the exploration of alternative approaches to solve the inverse problem.

#### **Chapter 4 - USSR: The UltraSound Sparse Regularization Framework**

In this chapter, we introduce USSR: The **UltraSound Sparse Regularization** framework which is based on two pillars: the measurement model introduced in Chapter 3 and the variational regularization methods, the algorithmic tools used to solve the inverse problems involved in this chapter.

We propose to address the following inverse problems:

- **Sparsely-regularized beamforming** where the standard image reconstruction process is posed as variational regularization problem with the aim of increased image quality.

## Chapter 1. Introductory Notes

---

We exploit a prior knowledge expressed as sparsity in a wavelet frame and solve the optimization problem using off-the-shelf proximal gradient methods;

- **Compressed beamforming** where the objective is to rely on compressed sensing (CS) principles in order to reduce the amount of data necessary to reconstruct a high-quality image. To do so, we propose different undersampling strategies, evaluate their performance in terms of CS-related quantities, and suggest a reconstruction algorithm based on a similar approach to sparsely-regularized beamforming;
- **Non-stationary blur modeling and image restoration** where we show that non-stationary blur in US imaging can be expressed as a composition of two operators, namely the measurement model and the DAS operator. Based on the formulations described in Chapter 3, we propose an efficient evaluation strategy of such non-stationary blur at the discrete level. We use the proposed model in a restoration method which solves a maximum-a-posteriori (MAP) estimation problem, based on a generalized Gaussian distribution (GGD) prior for the image under scrutiny.

## Chapter 5 - Compressive Multiplexing of Ultrasound Signals

We first describe a CS-based multiplexing method which aims to perform high-quality US imaging with a reduced number of coaxial cables connecting the probe to the back-end system, with an application to 3D imaging. The compression is based on an analog mixing of the element-raw data from several transducer elements, that could be ideally performed in the head of the probe. On the reconstruction side, we describe two methods based on different low dimensional models of US signals. The first one exploit joint sparsity in the Fourier domain with partially known support. The second one exploits sparsity in the pulse-stream model. To make the proposed approach more robust in realistic scenario, we provide an algorithm to estimate the pulse-echo waveform from compressed measurements. The technique solves a  $\ell_1/\ell_2$ -blind deconvolution problem where both the pulse-echo waveform and the signal representation are jointly estimated.

Finally, we propose a more theoretical contribution which deals with joint sparsity with partially known support, i.e. recovery of joint-sparse signals where part of their support is known *a priori*. We suggest recovery theorems which benefit from the knowledge of the partial support to ensure perfect recovery under weaker conditions than existing results. We also describe extensions of several rank-blind and rank-aware algorithms.

## Chapter 6 - Ultrasound Localization at the Rate of Innovation

In this chapter, we target another problem which is the localization of strong reflectors in US imaging, with application to flaws detection in non-destructive evaluation (NDE) or localization of microbubbles in contrast-enhanced US imaging.

We start with a study of the degrees of freedom associated with the localization of a finite number of point reflectors. We demonstrate that it is theoretically possible to retrieve the exact locations of  $K$  point reflectors with 3 transducer elements and  $2K + 1$  uniform measurements per element.

We detail a localization method that is able to operate at such a critical sampling rate. The technique is based on the following three steps:

1. **TOF-recovery:** For each transducer element, the TOFs of the pulses corresponding to the different point reflectors are recovered. This is achieved by modeling the element-raw data as a stream of pulse which can be sampled using the finite rate of innovation (FRI) framework;
2. **TOF-matching:** After recovering the TOFs along multiple transducer elements, we find ourselves with the unassigned distance geometry problem (uDGP). In this step, we determine the TOF correspondence across elements. More precisely, we assign a label to each TOF which corresponds to the point reflector from which the pulse originates. To do so, we rely on the concept of Euclidean distance matrix (EDM) which has been used for echo-sorting in acoustics [33];
3. **Localization:** We perform localization of each point reflector from the corresponding labeled TOFs using a method inspired from multilateration.



## 2 Basics of Ultrasound Imaging

Diane, I have studied all of the major imaging technologies over the last 25 years – CAT scanning, magnetic resonance imaging, angiography, and nuclear medicine. All of these technologies are very complicated in their own right. But among those, there is no question in my mind that ultrasound is the most difficult to learn.

---

*ABC Primetime Live*

Roy Filly

In this chapter, we introduce some basic concepts of US imaging, necessary for the understanding of this thesis. First, we briefly review the main functional components of a US imaging device and the standard imaging pipeline. We then describe the main features that characterize images obtained in US imaging and several metrics used to quantify the performance of a US imaging system. Finally, we detail state-of-the-art image formation approaches in UFUS imaging, i.e. DAS and coherent compounding.

### 2.1 An Ultrasound Imaging System in a Nutshell

#### 2.1.1 Diagram of an Ultrasound Imaging System

In this section, we introduce the main functional elements of a US imaging system. These notions are necessary for a non-expert to understand the process of image formation in a modern US imaging device. Obviously, a real US imaging system is composed of far more blocks than described here and we refer the interested reader to [34, 35] for more in-depth descriptions. Moreover, since our goal is to give a general understanding of a US imaging device, we point out that the arrangement of the components, as described in this section, may slightly differ in actual systems.

The essential elements are displayed in Figure 2.1 and described below:

- **Ultrasound Probe:** The probe is the most important component of a US acquisition system. Its function is to convert electrical signals to pressure waves and vice-versa by

means of piezoelectric elements, called transducer elements. A well-designed probe will be able to perform such conversions with as few artifacts as possible and with a maximum efficiency.

- **TX analog interface:** Interfaces the US probe during the transmission step (TX). It generates the excitation signal (electrical signal used to excite the transducer element) with an appropriate shape and voltage (transmit pulser) and sends it to the transducer elements with appropriate delays.
- **RX analog interface:** Interfaces the US probe during the reception step (RX). It performs the pre-amplification, where the dynamic range of the received radio-frequency (RF) signals is adjusted to the one of the system. It is also responsible for time-gain compensation (TGC) which compensates for the attenuation of the US wave induced by the propagation in the medium.
- **TX/RX controller:** Controls the parameters related to the transmit and receive schemes that are used by the TX and RX analog interfaces, e.g. the number of active elements, the delays, apodization, or parameters for the TGC.
- **Analog-to-digital converters (ADCs):** Perform the analog-to-digital conversion of the echo-signals at a sampling frequency  $f_s$ .
- **Beamformer:** Performs the reconstruction of the RF image from the echo-signals. The vast majority of systems employ the DAS beamforming algorithm to form the image. Modern US systems embed a digital beamformer but this operation was performed analogically in the old B-mode imaging systems.
- **Envelope detector:** Extracts the envelope signal from the RF image using Hilbert transform or in-phase quadrature demodulation.
- **Post-processing and display:** Stores the envelope image in display memory and performs log-compression and scan-conversion for gray-scale display on a monitor. In some cases, e.g. with convex probes, the scan-conversion may require a coordinate transformation and interpolation from the polar sector to the Cartesian coordinates of the display memory. The module may also embed some more advanced features such as noise removal or speckle reduction.

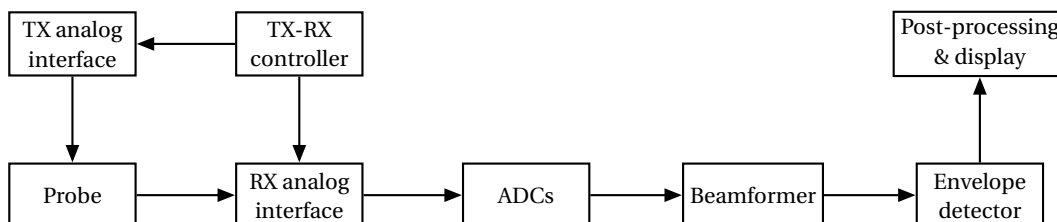


Fig. 2.1. Simplified diagram of an ultrasound system.

### 2.1.2 Transmission and Reception of Ultrasound Waves

The generation and reception of the US waves is achieved by the probe, which is an arrangement of transducer elements, i.e. tiny pieces of piezoelectric material grouped in different geometries, acoustically matched for propagation into soft tissues and connected electrically to front-end electronics.

**The Piezoelectric Elements:** The piezoelectric elements used in medical imaging are made of a synthetic ceramic, most often a lead-zirconate-titanate (PZT). A rectangular shaped transducer element is defined by a width ( $w$ ), height ( $L$ ) and thickness ( $d$ ), from which the fundamental resonance frequency is deduced as

$$f_0 = \frac{c}{2d}, \quad (2.1)$$

where  $c$  denotes the compressional speed of sound inside the crystal.

Thus, the desired fundamental resonance frequency is a key aspect in the fabrication of the transducer elements since it conditions its thickness. For instance, to design a PZT transducer element operating at 5 MHz, the thickness has to be set to 0.4 mm, given that the speed of sound in PZT is around  $4000 \text{ m s}^{-1}$ .

In order to characterize a transducer element, we rely on the concept of acousto-electrical impulse response  $h_{ae}(t)$ , which corresponds to the pressure wave generated by the element as a response of an electrical impulse  $\delta(t)$ . In addition, quantitative spectral features are provided in terms of center frequency  $f_c$  and fractional bandwidth  $B$  defined as

$$f_c = \frac{f_l + f_h}{2} \text{ and } B = \frac{f_h - f_l}{f_c}, \quad (2.2)$$

where  $f_h$  and  $f_l$  are the upper and lower frequency corresponding to a loss of  $-6 \text{ dB}$  compared to the spectral maximum. Usually, the bandwidth is expressed as a percentage of the center frequency.

Two representations in time and frequency of an example electro-acoustical impulse response are given in Figures 2.2(a) and 2.2(b), respectively. They correspond to the transducer elements of the Verasonics L11-5V probe. The center frequency is 7.8 MHz and the bandwidth is 60%. From Figure 2.2(a), we see that the transducer elements are able to transmit short acoustical pulses, of a fraction of a  $\mu\text{s}$ , in the medium. We will see in next sections that the duration of such pulses will impact the axial resolution of the resulting image as well as the penetration of the US wave.

**Fabrication of a US Probe:** A US probe is fabricated from a single piezoelectric crystal bonded with a matching layer and settled on a backing layer which is cut with a saw or by any other mean, as shown in Figure 2.3(a). On top of the crystal, the matching layer provides the interface between the piezoelectric crystal and the tissue. It is carefully designed such that it minimizes the acoustic impedance mismatch between the piezoelectric crystal and the human tissue.

## Chapter 2. Basics of Ultrasound Imaging

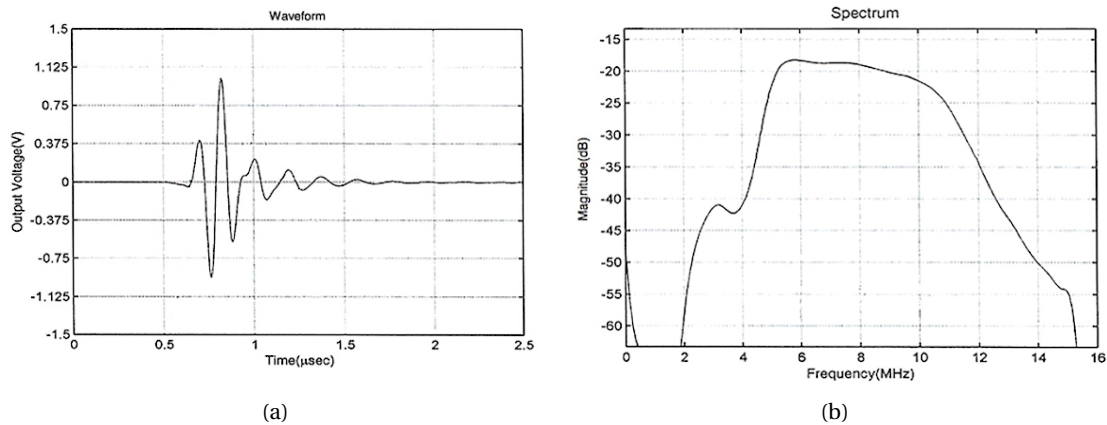


Fig. 2.2. Figure (a) presents the impulse response and Figure (b) displays the frequency spectrum of the Verasonics L11-5V probe.

In a final step, a connecting cable is added onto each element to ensure connection with the front-end electronics. In linear- and phased-arrays, an elevation acoustic lens is glued on top of the matching layer in order to focus the acoustical energy in the imaging area, resulting in higher signal to noise ratio and improved image quality, as can be seen on Figure 2.3(b).

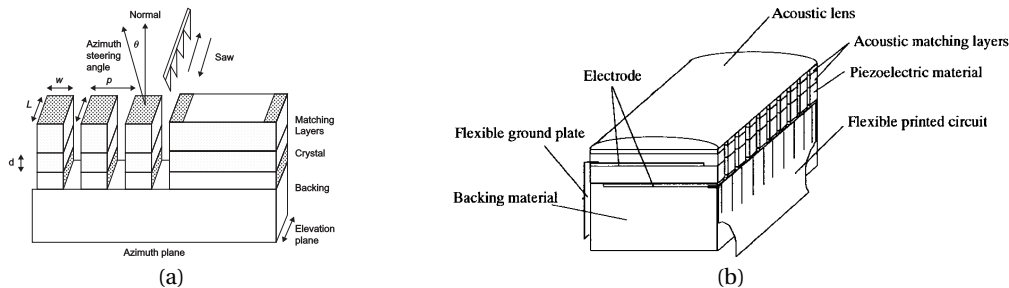


Fig. 2.3. Figure (a) presents the multilayer structure of a probe and Figure (b) describes a 1D array probe with an elevation lens. Obtained from [36] with permission.

**Characteristics of a US Probe:** A US probe is characterized by several quantities, namely, the *width* ( $w$  in Figure 2.3(a)) and *height* ( $L$  in Figure 2.3(a)) of the transducer elements, the *pitch* ( $p$  in Figure 2.3(a)) which is the distance between the centers of neighbouring transducer elements and the *kerf* which is the cut width between the elements.

We differentiate three main types of multi-element probes, namely linear probes, convex probes and phased-array probes, whose usage depends on the target application.

A linear probe (or linear-array probe), displayed on Figure 2.4(a), acquires data with a view to forming rectangular images of the region of interest and is designed as wide as possible in order to maximize the imaging area. It is characterized by a center frequency ranging between 2.5 MHz and 12 MHz and a pitch equal to one wavelength. The elements have a width of around one wavelength and their height is such that it allows to focus the acoustical energy in the region of interest in the elevation direction. Such a probe is typically used for imaging of

## 2.1. An Ultrasound Imaging System in a Nutshell

superficial structures (vascular examination) and in ultrasound-guided procedures where a high resolution may be required.

In order to image wider field of views, one uses a convex probe where the elements are arranged into a convex shape as shown on Figure 2.4(b). Such a probe is essentially a curved linear probe, characterized by a center frequency ranging between 2.5 MHz and 7.5 MHz and a pitch equal to one wavelength. It is used for abdominal examination and diagnosis of organs with a wide field of view.

A phased-array probe, displayed on Figure 2.4(c), has a smaller footprint than linear and convex probes with a pitch of a half wavelength. It usually works at lower center frequency than linear probes ranging typically between 2 MHz and 7.5 MHz. The elements are about half-wavelength wide. Such a probe is used to produce wide field-of-view images in regions where linear and convex probes cannot be used because they are too large, e.g. for inter-costal cardiac examinations.



Fig. 2.4. Examples of probes used in ultrasound imaging. Figure (a) presents a linear-array probe. Figure (b) shows a convex-array probe. Figure (c) displays a phased-array probe.

### 2.1.3 Forming Images from Echoes: Digital Ultrasound Beamforming

In conventional US systems, a RF image is built sequentially as a set of  $N_f$  scan lines, where each scan line is acquired by transmitting a focused beam in a subregion of the medium [28]. For a linear probe, each scan line represents a lateral section of the rectangular scan (Figure 2.5(a)) while for a convex or a phased-array probe, each scan line represents a sub-section of the sector scan, as displayed on Figures 2.5(b) and 2.5(c).

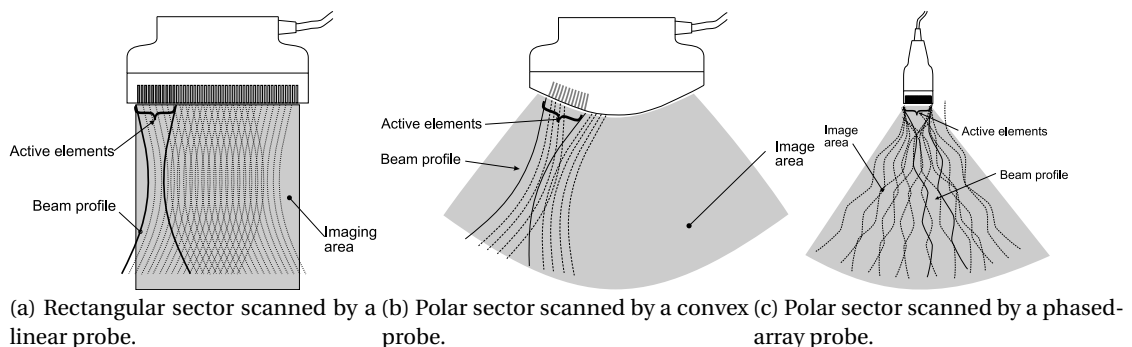


Fig. 2.5. Sectors scanned by the different types of probes. Obtained from [34] with permission.

With focused beams, the image quality is optimal around the focal point and decreases

## Chapter 2. Basics of Ultrasound Imaging

---

progressively away from the focal distance. If the region of interest is not moving too fast, multiple transmit focal points can be used for a single section in order to improve the image quality.

Focusing in transmission is achieved electronically by applying a delay profile to the transducer elements. Mathematically, consider a linear array made of  $N_x^t$  transducer elements located at  $\mathbf{p}_i = [x_i, 0]^\top$  which receive echo-signals  $m_i(t)$ ,  $i = 1, \dots, N_x^t$ .

On transmit, we focus the ultrasound beam at a desired focal point  $\mathbf{r}_f = [x_f, z_f]^\top$  by applying the following delay profile:

$$t_i = \frac{1}{c} \left( z_f - \sqrt{z_f^2 + (x_i - x_f)^2} \right), \quad i = 1, \dots, N_x^t, \quad (2.3)$$

where  $c$  denotes the speed of sound in the medium, supposed to be known and constant.

On receive, we rely on the DAS algorithm to estimate the brightness of reflectors at multiple depths from the element-raw data recorded by the transducer elements. For every field point, the DAS algorithm estimates the  $N_x^t$  round-trip TOF between the point considered and each transducer element and sums the signals evaluated at these specific delays.

Formally, for a field point  $\mathbf{r} = [x, z]^\top$ , the amplitude  $b(\mathbf{r})$  is evaluated as

$$b(\mathbf{r}) = \sum_{i=1}^{N_x^t} a_i(\mathbf{r}) m_i(\tau(\mathbf{r}, \mathbf{p}_i)), \quad (2.4)$$

$$\tau(\mathbf{r}, \mathbf{p}_i) = t_{Tx}(\mathbf{r}, \mathbf{p}_i) + t_{Rx}(\mathbf{r}, \mathbf{p}_i), \quad (2.5)$$

where  $t_{Tx}(\mathbf{r}, \mathbf{p}_i)$  and  $t_{Rx}(\mathbf{r}, \mathbf{p}_i)$  the delay in transmit and receive, and the coefficients  $a_i(\mathbf{r})$ ,  $i = 1, \dots, N_x^t$ , are apodization weights that can be used to reduce the side-lobe artefacts [37].

Continuing our example of the linear array, the round-trip TOF for a field point  $\mathbf{r} = [x_f, z]^\top$  that belongs to the scan line of interest is given by [28]:

$$\tau(\mathbf{r}, \mathbf{p}_i) = \frac{1}{c} \left( z + \sqrt{z^2 + (x_i - x_f)^2} \right). \quad (2.6)$$

Hence, the brightness along the scan-line can be expressed as a function of time as

$$b_f(t) = \sum_{i=1}^{N_x^t} a_i(t) m_i \left( \frac{1}{c} \left( \frac{ct}{2} + \sqrt{\left( \frac{ct}{2} \right)^2 + (x_i - x_f)^2} \right) \right), \quad (2.7)$$

where we use (2.4) with  $\mathbf{r} = [x_f, \frac{ct}{2}]$ .

Eventually, the resulting RF image is written as the concatenation of the  $N_f$  scan lines leading to

$$b(t) = [b_1(t), \dots, b_{N_f}(t)]. \quad (2.8)$$

### 2.1.4 Post-processing and Display

Due to spectral properties of the transducer elements, whose electro-acoustical impulse response has a frequency content concentrated around the center frequency, the element-raw data and the RF image are bandpass signals. Hence, each scan line can be expressed as a baseband signal modulated at the center frequency as

$$b_f(t) = \text{Re}\left(b_m(t) e^{i(2\pi f_c t + \varphi)}\right), \quad (2.9)$$

where  $f_c$  is the center frequency,  $\varphi \in [0, 2\pi]$  accounts for the phase shift, and  $b_m(t)$  is the envelope signal.

While the oscillations of the element raw-data are essential to the beamforming process, we are interested in extracting the envelope for display purpose because it is a smoother signal that is more pleasing for the human eye.

Hence, we perform an envelope detection either by Hilbert transform or by in Phase-Quadrature (IQ) demodulation. After the envelope extraction step, the envelope image is converted and log-compressed with a given dynamic range and eventually displayed a gray-scale display in real-time.

## 2.2 Important Features of an Ultrasound System

### 2.2.1 Radiated Field from an Ultrasound Array

A way to understand the behaviour of a US system consists in investigating the evolution of acoustical fields radiated by the probe in space and time.

Since a US array is a diffractive aperture, the diffraction theory developed for light by Huygens, Fresnel and later by Rayleigh and Sommerfeld [38], can be applied to the propagation of US waves, assuming a continuous sinusoidal displacement of the sources. The diffraction theory allows us to derive analytical formulations of the on-axis field variations, and of the far-field distribution, for apertures with simple shapes, e.g. circular or planar apertures [39]. For more complex shapes and other field positions, numerical integration of the contribution of each element is necessary. Although such a theory may not be directly applicable to US imaging due to the use of focused pulsed-wave excitations, it may help in understanding the general characteristics of radiated patterns.

A fundamental feature of those fields is that they can be divided into two zones, the Fresnel zone (or near field) where a complicated interference pattern is observed and most of the energy is confined within a transducer radius, and the Fraunhofer zone (far field) where the field is smoother and exhibits a spherical wave profile whose amplitude is modulated by the Fourier transform of the aperture. The boundary between the two zones, for an aperture of size  $a$  is usually given by  $\frac{a^2}{\lambda}$ . An illustration of a typical US radiated field from a circular aperture of radius  $a$  is given in Figure 2.6.

The on-axis variation of the field oscillates between maxima and minima, with a value of 0 infinitely far from the source. In the far-field, a large fraction of the energy is concentrated in the main lobe, whose width is defined by the first off-axis minimum. The remaining part of the energy lies in the sidelobes, which are often considered as noise.

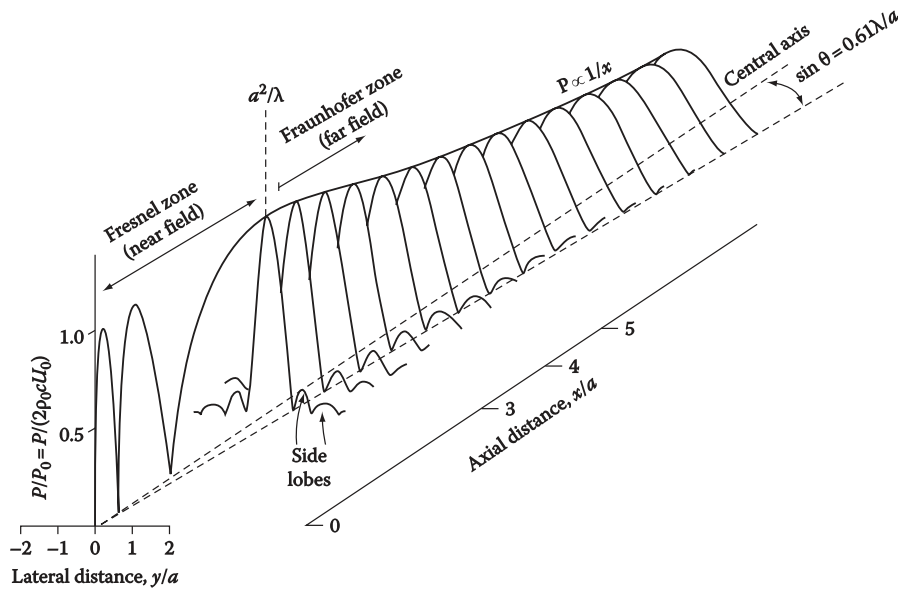


Fig. 2.6. On-axis radiated field of a planar circular source of radius  $a$ . Obtained from [34] with permission.

### 2.2.2 Spatial Resolution

The spatial resolution quantifies the ability of an imaging system to differentiate two close points, which is intrinsically linked to the point spread function (PSF), i.e. the impulse response of the imaging system. As an example, the spatial resolution of a diffraction system with a circular pupil is given by the Rayleigh criterion [38]. Indeed, the Rayleigh criterion defines an angle corresponding to the first zero of the order-one Bessel function of the first kind, which characterizes the PSF of a circular aperture.

In practice, a common criterion used to quantify the spatial resolution is the full width at half maximum (FWHM), defined as the distance between points at which the signal reaches half its maximum value.

In US imaging, the PSF is highly asymmetrical and we usually differentiate axial from lateral resolution. The axial resolution, also called longitudinal resolution, is defined for reflectors located parallel to the direction of propagation of the US beam. It is closely linked to the length of the US pulse transmitted in the medium and is commonly defined as follows [34]:

$$\text{Axial resolution} = \text{Half length of the pulse envelope at some defined level below the peak} \times \text{speed of sound.}$$

For a pulse with a Gaussian-shaped envelope and a speed of sound of  $1540 \text{ m s}^{-1}$ , the axial FWHM is given by [40, 41]

$$FWHM_{ax} [\text{mm}] = \frac{0.66}{B f_c}, \quad (2.10)$$

where  $B$  and  $f_c$  are the fractional bandwidth and center frequency [in MHz] of the transducer elements.

## 2.2. Important Features of an Ultrasound System

---

The lateral resolution is defined for reflectors located perpendicular to the direction of propagation of the US beam, within the scan plane. In the far field (Fraunhofer zone), it is related to the diffractive pattern generated by the aperture and is defined as follows [34]:

Lateral resolution = Full width of the beam at some defined level below the peak.

For a rectangular aperture of size  $L$ , the diffractive pattern at depth  $z$  is a sinc and the lateral FWHM is given by [37]

$$FWHM_{lat} = \frac{1.2\lambda z}{L}, \quad (2.11)$$

where  $\lambda$  designates the wavelength of the US wave.

Thus, we observe that the lateral resolution worsens with depth, which means that the quality of a US system may significantly change across the imaging range. This is quite annoying and one way to cope with that consists in adjusting the F-number of the aperture using transmit and receive apodizations [37].

### 2.2.3 Speckle

In the previous section, we have seen that a US imaging system does not have infinite resolution. Hence, we can define a resolution cell as the volume of space occupied by the PSF at a given depth. Such a resolution cell is very often composed of a continuum of point reflectors and, during the propagation of the US wave, the backscattered field from this cell would be composed of interferences of many spherical waves with random phases. The brightness of the resulting image will be random depending on the nature of those interferences. This results in a granular texture of the US image, denoted as speckle by analogy with the phenomenon observed in laser optics [42].

The appreciation of speckle is controversial in US imaging. Indeed, from a physicist point of view, speckle is noise (an “illusion” according to Szabo [43]) and is detrimental since it reduces image contrast and blurs the boundaries between tissue regions. However, a remarkable property of speckle is that it is deterministic in the sense that when the same experiment is reproduced twice, an identical speckle pattern must be observed. Thus, a modification of the speckle pattern often indicates motion and tracking the variations in speckle patterns is used for tissue-motion estimation, in vector flow imaging [8, 44] and in elastography [45].

Statistical properties of speckle have been widely studied in US, inspired by the work of Goodman who investigated the phenomenon in optics [46, 47]. Based on random walk models for the phase of the spherical waves, it can be shown that the probability density function (PDF) of the envelope image of speckle follows a K-distribution [48, 49], a generalization of the Rice distribution [50], whose shape depends on the number of scatterers within the resolution cell.

The most popular statistical model of speckle is the Rayleigh distribution [51, 52], which is a limited case of the K-distribution for high number of uncorrelated scatterers with uniformly distributed phase. The first order statistics of the Rayleigh PDF are used to define the SNR whose inverse is denoted as the speckle contrast. Interestingly, the value of the SNR corre-

sponding to a Rayleigh distribution can be found theoretically as 1.91 [51], which comforts the fact that speckle is noise. A common way to evaluate the ability of an imaging system to reconstruct speckle is achieved by performing statistical tests on the envelope image, such as the Kolmogorov-Smirnov test.

The notion of contrast, i.e. the ability to distinguish regions with different echogenicity, is closely linked to the amplitude of the speckle pattern. To measure the contrast, we rely on two very popular metrics which both quantify the ability to define a cyst-object from a speckle background. The first one is the contrast-to-noise ratio (CNR) in dB defined as [41]:

$$CNR = 20 \log \left( \frac{\mu_t - \mu_b}{\sqrt{(\sigma_t^2 + \sigma_b^2)/2}} \right), \quad (2.12)$$

where  $(\mu_t, \sigma_t^2)$  (resp.  $(\mu_b, \sigma_b^2)$ ) are the average pixel intensity and variance of the cyst region (resp. background) region. The second one is the contrast ratio (CR) defined as [43]:

$$CR = \frac{\mu_b - \mu_t}{\mu_b + \mu_t}. \quad (2.13)$$

The two metrics are slightly different since the CNR takes into account the speckle resolution in each region and would favor methods that remove the speckle pattern. In contrary, the CR is more agnostic to speckle.

### 2.2.4 Temporal Resolution

The temporal resolution, often called frame rate, and measured in *frame per second* [fps] or Hz, is the frequency at which two consecutive images are generated. It is inversely proportional to the time necessary to transmit a beam, receive and process the backscattered echoes, and repeat the process for every scan line of the final image. It characterizes how often the image can be updated on the screen and quantifies the ability of the US system to differentiate two consecutive events.

If one wants to build  $N_f$  scan lines at a maximum depth  $z_{max}$ , there exists an upper bound on the frame rate due to the propagation of the US wave given by

$$FR_{max} = \frac{c}{2N_f z_{max}}. \quad (2.14)$$

For instance, the frame rate associated with imaging a 10 cm depth composed of 128 scan lines is lower than 60 Hz.

### 2.2.5 Attenuation in Tissues

During the propagation in tissues, a US wave suffers from attenuation, i.e. absorption and dispersion, which significantly modifies the shape of the transmitted pulse. These effects are induced by friction, scattering and diffraction in the tissue.

To account for such effects, we introduce the material transfer function (MTF)  $M_t(f, z)$  [53]

## 2.2. Important Features of an Ultrasound System

---

which models the attenuation of the tissue in the frequency domain as a function of depth. A standard model of the MTF is by the following exponential

$$M_t(f, z) = e^{\gamma_T(f)z}, \quad (2.15)$$

where the absorption  $\gamma_T$  is defined as

$$\gamma_T(f) = -\alpha(f) - i\beta(f) = -\alpha(f) - i(k_0 + \beta_E(f)), \quad (2.16)$$

where  $k_0 = \omega/c_0$ ,  $\alpha(f)$  is the absorption term,  $\beta(f)$  is the dispersion terms, respectively and  $\beta_E(f)$  is the dispersion term induced specifically by the variations of the speed of sound.

We define the time-domain counter part of the MTF as the material impulse response function (MIRF):

$$m_t(t, z) = \mathcal{F}^{-1}\{M_t\}(t, z). \quad (2.17)$$

Thus, the US pulse at depth  $z$ ,  $p(z, t)$  is deduced from the transmitted pulse  $p(0, t) = p_0(t)$  as

$$p(z, t) = (p_0 \otimes_t m_t)(t, z) \Leftrightarrow P(z, f) = P_0(f) M_t(f, z). \quad (2.18)$$

In tissues, an accurate model of the absorption is the power-law defined as [54–56]

$$\alpha(f) = \alpha_0 |f|^y, \quad \alpha_0 \in \mathbb{R}_+, \quad (2.19)$$

where  $y \in [1, 1.7]$  [54–56].

Hence, the frequency dependent absorption has a low-pass effect, causing a down-shift of the center frequency with increasing depth. The coefficient  $\alpha_0$  is usually expressed in  $\text{dB MHz}^{-1} \text{cm}^{-1}$  or  $\text{dB MHz}^{-1} \text{cm}^{-1}$  at a certain frequency. Common values in medical US imaging are  $y = 1$  and  $\alpha_0 = 0.5 \text{ dB MHz}^{-1} \text{cm}^{-1}$ .

The term  $\beta_E(f)$  can be deduced from different models of the attenuation, e.g. the Kramers-Kronig model, the time causal model, and the classic relaxation model. Please refer to [57] for a review of those models. Using the time causal model [54, 57],  $\beta_E(f)$  is expressed as

$$\beta_E(f) = \begin{cases} \alpha_0 \tan\left(\frac{\pi y}{2}\right) f |f|^y & \text{if } y \in \mathbb{R} \setminus \mathbb{N} \text{ or } y \text{ even} \\ -\frac{2}{\pi} \alpha_0 f^y \ln|f| & \text{otherwise} \end{cases}, \quad (2.20)$$

and we can see that maximal dispersion is observed for  $y = 1$  or  $y$  odd, for a fixed absorption coefficient.

As an example, Figure 2.7 displays a pulse-echo waveform obtained as a convolution between a 2.5-cycle square excitation and a Gaussian-modulated sinusoidal pulse at 5 MHz, at 3 cm and 15 cm, for an attenuation coefficient  $\alpha_0 = 11 \times 10^{-6} \text{ Np m}^{-1} \text{ Hz}^{-1}$  and an attenuation factor of 1. The dispersion term is neglected.

On the leftmost figure, we report the frequency spectra of the pulses on which we observe the low-pass effect induced by the attenuation. The other three plots represent, from left to

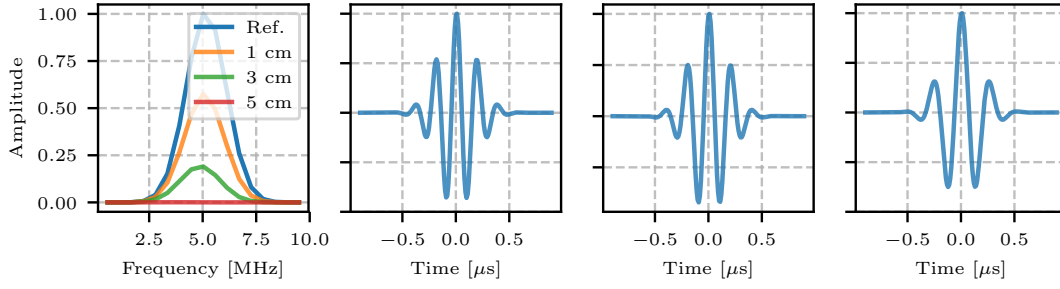


Fig. 2.7. The leftmost figure displays the frequency spectrum of the pulse-echo waveform at different depths. The three other figures show (from left to right) the reference pulse-echo waveform and the normalized pulse-echo waveform at 3 cm and 15 cm, respectively.

right, the reference pulse-echo waveform and the normalized pulse-echo waveform at 3.15 cm. We notice that the effect of the distortion of the shape of the pulse is significant at 15 cm. Empirically, we observe significant changes when working at more than 10 cm.

When designing a US system, there exists a critical trade-off between penetration and axial resolution which can be seen as the Heisenberg inequality of US imaging. Indeed, higher US frequencies are more attenuated in the tissues and therefore penetrate less but they result in an improved axial resolution.

This is the main reason why different frequencies are used for different applications. As an example, carotid imaging is usually performed at 7.8 MHz since we image superficial tissues, while liver imaging is achieved at a significantly lower frequency, around 3 MHz.

## 2.3 Image Formation in Ultrafast Ultrasound Imaging

In this section, we describe more formally PW and DW imaging which are two popular modalities of UFUS imaging. We present the DAS beamforming algorithm which is the state-of-the-art image formation method in UFUS imaging. We also describe coherent compounding which is the common way to increase the image quality in UFUS imaging.

In the remainder of this section, we consider a 2D medium  $\Omega \subset \mathbb{R}^2$  characterized by a density field  $\rho \in L_2(\Omega)$  and a speed of sound field  $c \in L_2(\Omega)$ . Associated with local fluctuations of those two fields, we introduce the tissue-reflectivity function (TRF)  $\gamma \in L_2(\Omega)$  which is the quantity of interest in conventional US imaging (See Chapter 3 for more details).

### 2.3.1 Delay-and-sum Beamforming in Ultrafast Ultrasound Imaging

Consider the configuration described in Figure 2.8 where the transducer elements, located at  $\mathbf{p}_i = [p_i, 0]^\top$ ,  $i = 1, \dots, N_x^t$ , generate a US wave during the transmit step and record echo-signals  $m_i(t) \in L_2([0, T])$ ,  $i = 1, \dots, N_x^r$ , during the receive step.

In UFUS, the RF image is no longer expressed as a set of scan-lines, as in conventional imaging, but as a matrix of pixel values. Puts formally, we consider a regular grid  $\Omega_{\hat{\gamma}}$  composed of  $N_g = N_x N_z$  points as follows

$$\Omega_{\hat{\gamma}} = \{\mathbf{r}_{kl} = [x_k, z_l]^\top \in \Omega, (k, l) = \{1, \dots, N_x\} \times \{1, \dots, N_z\}\}, \quad (2.21)$$

### 2.3. Image Formation in Ultrafast Ultrasound Imaging

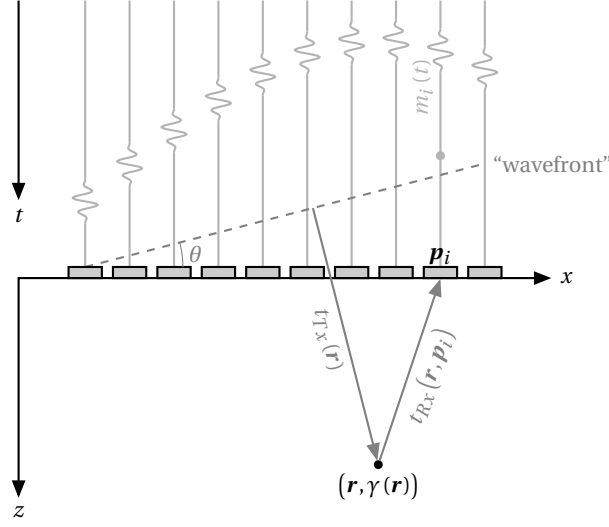


Fig. 2.8. Standard 2D ultrasound imaging configuration.

and we define the RF image as the matrix  $\hat{\mathbf{F}} \in \mathbb{R}^{N_x \times N_z}$  given element-wise by

$$\hat{\mathbf{F}}_{kl} = \sum_{i=1}^{N_x^t} a_i(\mathbf{r}_{kl}) m_i(\tau(\mathbf{r}_{kl}, \mathbf{p}_i)), \quad (2.22)$$

where  $a_i(\mathbf{r}_{kl})$  is the apodization coefficient and  $\tau(\mathbf{r}_{kl}, \mathbf{p}_i)$  is the round-trip TOF between the point  $\mathbf{r}_{kl}$  and the  $i$ -th transducer element.

In PW imaging, the round-trip TOF depends on the steering angle  $\theta$  [28] and is defined as:

$$\tau(\mathbf{r}_{kl}, \mathbf{p}_i) = \frac{z_l \cos \theta + x_k \sin \theta + \|\mathbf{r}_{kl} - \mathbf{p}_i\|_2}{c}, \quad i = 1, \dots, N_x^t, \quad (2.23)$$

where  $c$  is the speed of sound, assumed known and constant here.

In DW imaging, we set the delays such that the wavefront simulates a spherical wave emitted from a virtual point  $\mathbf{r}_n$  located behind the US probe. Hence, the round trip TOF depends on the location of this virtual source and can be expressed as [29]:

$$\tau(\mathbf{r}_{kl}, \mathbf{p}_i) = \frac{\|\mathbf{r}_{kl} - \mathbf{r}_n\|_2 + \|\mathbf{r}_{kl} - \mathbf{p}_i\|_2}{c}, \quad i = 1, \dots, N_x^t. \quad (2.24)$$

Hence, computing the RF image on the grid requires to perform  $N_x^t N_g$  TOF calculations which can be prohibitive even in 2D imaging, where  $N_x^t$  is typically few hundreds and  $N_g$  can be on the order of hundreds of thousands.

Nevertheless, we can see that the computations of the points  $\hat{\mathbf{F}}_{kl}$  using (2.22) are independent from each other, which make the proposed algorithm suitable for massively parallel implementations. This was a key aspect in the feasibility of such a modality [27] and current imaging systems which perform UFUS imaging are equipped with digital architectures capable of handling massively parallel computations, e.g. GPUs.

### 2.3.2 Coherent Compounding in Ultrafast Ultrasound Imaging

One of the main strengths of UFUS resides in its ability to perform imaging at few kHz frame rates, since the RF image  $\hat{\Gamma}$  can be reconstructed from a single PW or DW insonifications. However, such a RF image is of significantly lower quality, in terms of contrast and resolution, than images obtained with standard multiple focused scanlines [28, 29]. This is due to the fact that the acoustical energy of an unfocused wave is spread in the entire medium rather than focused in the specific region of interest.

To tackle this problem, coherent compounding proposes to average RF images obtained from different sequential transmissions [22, 28]. Formally, consider  $N_c$  RF images  $\hat{\Gamma}_c$ , reconstructed from  $N_c$  PW insonifications, with steering angles  $\theta_c$ ,  $c = 1, \dots, N_c$ . The RF image obtained by coherent plane wave compounding (CPWC) is expressed as

$$\hat{\Gamma}_{cpwc} = \frac{1}{N_c} \sum_{c=1}^{N_c} \hat{\Gamma}_c. \quad (2.25)$$

The increase of image quality induced by CPWC can be explained by the fact that using multiple PWs resynthesizes a focus at each point of the medium [28] which increases the SNR accordingly. In [28], the authors discuss this aspect and show that CPWC with only few tens of PWs with appropriate angles is similar to “optimal multifocus”, which corresponds to a situation similar to focusing on each point of the medium. The choice of the optimal sequence of angles is discussed in [58].

The main drawback of CPWC is the decrease of the temporal resolution, directly proportional to the number of insonifications. Hence, depending of the application, the optimal trade-off between image quality and frame rate has to be discussed.

Figure 2.9 illustrates the difference between conventional B-mode imaging using focused wave (left most image) and CPWC for an increasing number of PWs.

We observe that with few tens of PWs, the image quality is similar to that of conventional focused waves, leading to a significant increase of the frame rate. We also notice the trade-off between image quality and temporal resolution.

The same principle, denoted as coherent diverging wave compounding (CDWC), has been introduced for DW imaging, where the averaging is achieved over RF images reconstructed from DW insonifications with different virtual sources. The optimal positions of the sources are discussed in [29]. As for CPWC, the increase of quality induced by CDWC can be explained by the fact that it resynthesizes a focus at each point of the medium [28].

### 2.3. Image Formation in Ultrafast Ultrasound Imaging

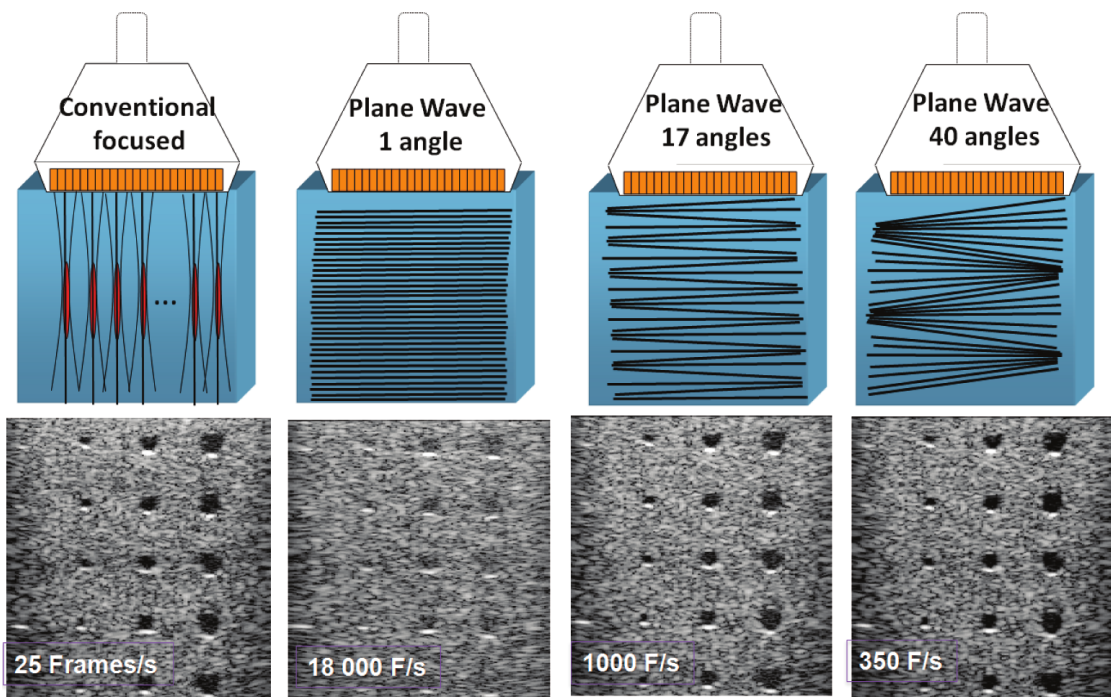


Fig. 2.9. Conventional focused and ultrafast ultrasound imaging for a region of interest of 4 cm. In the leftmost image, 128 focused beams are used with 4 focal depths. Obtained from [11] with permission. © 2014 IEEE.



## 3 Pulse-echo Ultrasound Imaging Seen as an Inverse Problem

J'ai donc montré de quelle façon l'on peut concevoir que la lumière s'étend successivement par des ondes sphériques, et comment il est possible que cette extension se fasse avec une aussi grande vitesse, que les expériences et les observations célestes la demandent.

---

*Traité de la Lumière*  
Christiaan Huygens

In this chapter, we revisit pulse-echo US imaging and demonstrate that it can be formulated as an inverse problem which relates the echo signals recorded at each transducer element to variations of acoustic impedance in the medium. Such a view allows us to bring a novel understanding of UFUS imaging in terms of projections onto quadric surfaces, very similar to CT. It also permits to revisit several common procedures in UFUS imaging introduced in Chapter 2, such as the DAS algorithm and the coherent compounding.

In the first half of the chapter, which covers the first three sections, we settle the theoretical bases that permit to express US imaging as an inverse problem. After an introductory section which details the existing approaches, Section 3.2 describes the pulse-echo spatial impulse response model, which is key for the formulation of the proposed inverse problem. In Section 3.3, we exploit the model previously introduced to define the inverse problem associated with pulse-echo US imaging, both at the continuous and the discrete levels.

The second half of the chapter is dedicated to the reformulation of the measurement model for several configurations, i.e. single emitter-single receiver, the building block of SA imaging, PW imaging and DW imaging, in 2D and 3D. First, we show that the action of the measurement model can be expressed in terms of projections onto quadric surfaces (or conics in 2D) whose shapes depend on the configuration. Hence, echo signals recorded by the transducer elements gather many projections in a similar way to the linear Radon transform in CT imaging. Then, we provide an alternative formulation of such projections which rely on appropriate parameterizations of the quadric surfaces involved in the measurement model. We use this

alternative formulation to bring efficient matrix-free formulations of the measurement model and its adjoint in the discrete domain, which is a key aspect towards the feasibility of iterative methods in US imaging.

#### 3.1 Existing Approaches and Motivations

US imaging has a long-time history with inverse problems. Indeed, while B-mode imaging is the most used US imaging modality, propagation of US waves is a far richer phenomenon that may permit to perform quantitative imaging. Such problems, which aim to recover quantities characterizing an object from scattered radiations are a special kind of inverse problems called inverse scattering problems.

US tomography aims to recover maps of speed of sound and attenuation from pressure fields measured at various locations. Transmission mode tomography, where two transducer elements are placed face to each other with the medium of interest in between, has been an active research topic since the beginning of the 1970s. Early attempts exploited straight ray propagation and related TOF differences to variations of density with the linear Radon transform [59], as in CT imaging, and more advanced models which account for variations of refractive index along the ray have been described few years later [60]. Acoustic diffraction tomography, introduced by Mueller *et al.* [61, 62] based on the seminal work of Wolf for optical imaging [63], was a major advance in US tomography. Indeed, Wolf devised a method to reconstruct maps of quantitative parameters from scattered data under the simplifying first-order Born approximation. Since then, many improvements on the initial technique have been proposed, e.g. filtered backprojection for accelerated inversion [64], multi-frequency diffraction tomography [65, 66] and full wave inversion methods [67, 68].

Reflection mode US tomography, which is based on data recorded in a pulse-echo mode has been significantly less studied in the literature, probably because the mathematical machinery to solve such problems is far less established than in transmission-mode tomography. Norton and colleagues proposed a backprojection method to reconstruct reflectivity maps from data collected along a circle in 2D [69], and a sphere, a cylinder and an infinite plane in 3D [70], assuming a straight line propagation path. Jensen [71] suggested a formalism to model pulse-echo imaging exploiting the spatial impulse response model introduced by Tupholme [72] and Stepanishen [73].

The models derived for US tomography form the mathematical basis for the measurement models described in the context of inverse problems for UFUS imaging. In PW imaging, Schiffner and Schmitz [74–76] and Zhang *et al.* [77] express a measurement model based on the Lippmann-Schwinger equation, well-known in diffraction tomography, linearized thanks to the first-order Born approximation. Alternatively, David *et al.* [78, 79], Ozkan *et al.* [80] and Wang *et al.* [81], propose a time-domain formulation of the measurement model, inspired by the work of Jensen [71]. The main issue related to these models is their computational complexity, usually translated into storage requirements of the corresponding matrix representations. The models proposed by David *et al.* [78] and Schiffner and Schmitz [74] require the storage of several hundreds of GB for matrix coefficients in 2D. Zhang *et al.* [77] have divided the image into stripes in order to make the problem tractable. This issue severely limits the

### 3.2. Hail to the Pulse-echo Spatial Impulse Response Model

appeal of iterative image reconstruction methods that can be leveraged in the context of pulse-echo US imaging. In addition, none of the above models are scalable to 3D imaging and, to the best of our knowledge, no extension of the proposed models to 3D imaging has been proposed.

### 3.2 Hail to the Pulse-echo Spatial Impulse Response Model

In this section, we construct the pulse-echo spatial impulse response model, which is a key tool in the formulation of the proposed inverse problem. Indeed, this model allows us to compute the pressure at the surface of a receiving piston, in the case where another piston transmits a pressure wave in a scattering medium.

To build the model, we start by describing the spatial impulse response, which allows us to compute the pressure field generated by a baffle piston whose surface is moving. In a second section, we describe the formalism used to model the scattering of the medium which permits to compute the scattered pressure at the surface of the second piston. Finally, we put the different pieces together to describe the pulse-echo spatial impulse response model.

#### 3.2.1 Acoustical Understanding of the Spatial Impulse Response

We provide a theoretical derivation of the spatial impulse response, which permits to compute the pressure field generated by a movable baffle piston at any point of an homogeneous medium. The derivation described below is based on the work of Tupholme [72] and Stepanishen [73].

We consider the configuration described in Figure 3.1 where a movable baffle piston of surface  $S$  is mounted in an infinite planar baffle. We are interested in a specific field point  $\mathbf{r}$  embedded

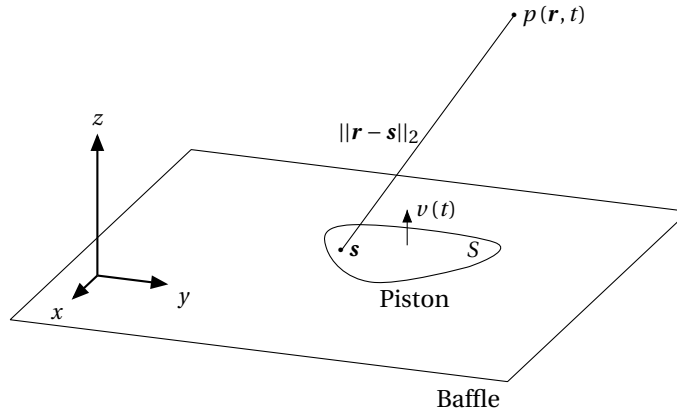


Fig. 3.1. Geometry for a baffled piston.

in a homogeneous medium of constant speed of sound  $c$ . At  $t = 0$ , the piston and baffle are coplanar and the medium is at rest with uniform density  $\rho_0$  and pressure  $p_0$ . At  $t > 0$ , the piston starts to move with a velocity  $v(\mathbf{r}, t)$ , resulting in a perturbation of the medium.

We are interested in the half-space  $\Omega = \{\mathbf{r} = [x, y, z]^T \mid z \geq 0\}$  on which we define the pressure and velocity fields as  $p(\mathbf{r}, t)$  and  $v(\mathbf{r}, t)$ , respectively. We introduce the velocity potential

### Chapter 3. Pulse-echo Ultrasound Imaging Seen as an Inverse Problem

---

$\Phi(\mathbf{r}, t) = \Phi(x, y, z, t)$  defined by the following equations:

$$\begin{cases} p(\mathbf{r}, t) &= \rho_0 \frac{\partial \Phi(\mathbf{r}, t)}{\partial t} \\ v(\mathbf{r}, t) &= -\nabla \Phi(\mathbf{r}, t) \end{cases} \quad (3.1)$$

We assume that the piston velocity  $v(t)$  is uniform over the surface of the piston (rigid piston) and we define the following velocity field

$$v^0(\mathbf{r}, t) = \begin{cases} v(t) & \text{if } \mathbf{r} \in S, t > 0 \\ 0 & \text{otherwise} \end{cases} \quad (3.2)$$

The velocity potential satisfies the following initial-boundary value problem [73]:

$$\begin{cases} \frac{1}{c^2} \frac{\partial^2 \Phi(\mathbf{r}, t)}{\partial t^2} - \nabla^2 \Phi(\mathbf{r}, t) = 0, \mathbf{r} \in \Omega, t > 0 \\ \Phi(\mathbf{r}, t) = \frac{\partial \Phi(\mathbf{r}, t)}{\partial t} = 0, \mathbf{r} \in \Omega, t = 0 \\ \frac{\partial \Phi(\mathbf{r}, t)}{\partial z} = v^0(\mathbf{r}, t) \end{cases} \quad (3.3)$$

where the equation in the first row states that  $\Phi(\mathbf{r}, t)$  has to follow the homogeneous wave equation in  $\Omega$  and the two other equations account for the initial and boundary conditions, respectively.

The solution of the above defined initial-value boundary problem is well-known and can be expressed as follows [73]:

$$\Phi(\mathbf{r}, t) = \int_0^t \int_{\mathbf{s} \in S} v(\mathbf{s}, u) g(\mathbf{r}, t; \mathbf{s}, u) d\mathbf{s} du \quad (3.4)$$

where  $g(\mathbf{r}, t; \mathbf{s}, u)$  is the time-dependent Green's function [82] defined as

$$g(\mathbf{r}, t; \mathbf{s}, u) = \frac{\delta\left(t - u - \frac{\|\mathbf{r} - \mathbf{s}\|_2}{c}\right)}{2\pi \|\mathbf{r} - \mathbf{s}\|_2} \quad (3.5)$$

Now, using the fact that the velocity is uniform on the surface of the piston, Equation (3.4) simplifies to:

$$\Phi(\mathbf{r}, t) = \int_0^t v(u) \int_{\mathbf{s} \in S} \frac{\delta\left(t - u - \frac{\|\mathbf{r} - \mathbf{s}\|_2}{c}\right)}{2\pi \|\mathbf{r} - \mathbf{s}\|_2} d\mathbf{s} du = (v \otimes_t h(\mathbf{r}, \cdot))(t), \quad (3.6)$$

where  $h(\mathbf{r}, t)$  defines the spatial impulse response of the piston as

$$h(\mathbf{r}, t) = \int_{\mathbf{s} \in S} \frac{\delta\left(t - \frac{\|\mathbf{r} - \mathbf{s}\|_2}{c}\right)}{2\pi \|\mathbf{r} - \mathbf{s}\|_2} d\mathbf{s}. \quad (3.7)$$

Equation (3.7) is the well-known Rayleigh integral [35, 83]. It can be interpreted in terms of the Huygens-Fresnel principle which states that "every point that receives a luminous disturbance generates a spherical wave of similar frequency, amplitude and phase". In the case of our baffle piston, the velocity potential corresponding to  $v(t) = \delta(t)$  is indeed the sum of the spherical

### 3.2. Hail to the Pulse-echo Spatial Impulse Response Model

waves generated by the infinitely many points at the surface of the piston which would reach  $\mathbf{r}$  at time  $t$ .

We can deduce the pressure field in any point of the medium using (3.1) as

$$p(\mathbf{r}, t) = \left( \rho_0 \frac{\partial v}{\partial t} \otimes_t h(\mathbf{r}, \cdot) \right) (t). \quad (3.8)$$

Equation (3.8) defines the desired convolution model in the sense that we can define the pressure field in any point of the medium as the convolution between the acceleration of the piston and the spatial impulse response.

From (3.7), we observe that the key aspect of the spatial impulse response model resides in the ability to calculate  $h(\mathbf{r}, t)$  for a given geometry of the piston. Analytical solutions have been derived for various piston geometries, e.g. flat circular [72], flat rectangle [84, 85], flat triangle [86] and spherical [87, 88].

Jensen and Svendsen [89] have also proposed a numerical procedure to compute the spatial impulse response for a plane piston with arbitrary shape, based on an approximation of the piston surface with small rectangles from which the analytical spatial impulse response is known. Such a method is used in the well-known Field II simulation software<sup>1</sup>.

#### 3.2.2 The Pulse-echo Spatial Impulse Response Model

We consider the configuration described in Figure 3.2, in which two pistons of surface  $S_1$  and  $S_2$  are placed in a infinite rigid baffle. We also consider a scattering medium  $\Omega$ . More precisely,  $\Omega$  is characterized by a propagation velocity  $c$  and a density  $\rho$  which slightly fluctuate around their mean values  $\rho_0$  and  $c_0$  as

$$\rho(\mathbf{r}) = \rho_0 + \Delta\rho(\mathbf{r}) \text{ and } c(\mathbf{r}) = c_0 + \Delta c(\mathbf{r}).$$

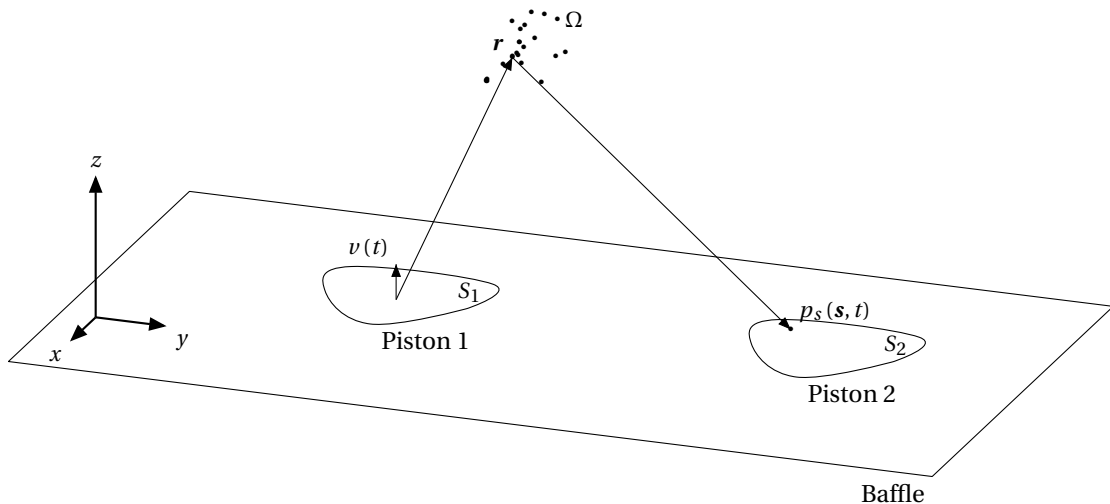


Fig. 3.2. Geometry for a pulse-echo experiment with two pistons.

<sup>1</sup><http://field-ii.dk/>

### Chapter 3. Pulse-echo Ultrasound Imaging Seen as an Inverse Problem

---

We define  $h_1(\mathbf{r}, t)$  and  $h_2(\mathbf{r}, t)$  as the impulse responses associated with pistons 1 and 2 given by (3.7). We assume that piston 1 transmits the acoustical wave in the medium and piston 2 records backscattered echoes from the medium. From Section 3.2.1, we know that the pressure field generated by piston 1 at any point of the medium is described by (3.8):

$$p_1(\mathbf{r}, t) = \left( \rho_0 \frac{\partial v}{\partial t} \otimes_t h_1(\mathbf{r}, \cdot) \right) (t). \quad (3.9)$$

Assuming that  $\Delta\rho \ll \rho_0$  and  $\Delta c \ll c_0$ , we can derive the corresponding wave equation as [71]:

$$\nabla^2 p - \frac{1}{c_0^2} \frac{\partial^2 p}{\partial t^2} = -\frac{2\Delta c}{c_0^3} \frac{\partial^2 p}{\partial t^2} + \frac{1}{\rho_0} \nabla(\Delta\rho) \cdot \nabla p, \quad (3.10)$$

where the two terms on the right hand side of the equation are the scattering terms induced by the inhomogeneities in density and propagation velocity, which vanish for an homogeneous medium.

The pressure in any point of the scattering medium  $\Omega$  can therefore be obtained from (3.10) using the time-dependent Green function (3.5) as follows

$$\begin{aligned} p_{sc}(\mathbf{s}, t) &= \int_{\mathbf{r} \in \Omega} \int_0^T \left( \frac{1}{\rho_0} \nabla(\Delta\rho(\mathbf{r})) \cdot \nabla p(\mathbf{r}, u) - \frac{2\Delta c(\mathbf{r})}{c_0^3} \frac{\partial^2 p(\mathbf{r}, u)}{\partial t^2} \right) g(\mathbf{r}, u; \mathbf{s}, t) d\mathbf{r} du \\ &= \int_{\mathbf{r} \in \Omega} \int_0^T (Lp)(\mathbf{r}, u) g(\mathbf{r}, u; \mathbf{s}, t) d\mathbf{r} du, \end{aligned} \quad (3.11)$$

where  $T \in \mathbb{R}_+$  is the integration time and  $L$  is the linear scattering operator defined as

$$\begin{aligned} L: L_2(\Omega) &\rightarrow L_2(\Omega) \\ p &\rightarrow \frac{2\Delta c}{c_0^3} \frac{\partial^2 p}{\partial t^2} + \frac{1}{\rho_0} \nabla(\Delta\rho) \cdot \nabla p \end{aligned} \quad (3.12)$$

The total pressure field in the scattering medium can be decomposed as

$$p(\mathbf{s}, t) = p_1(\mathbf{s}, t) + p_{sc}(\mathbf{s}, t), \quad (3.13)$$

where  $p_1$  is the incoming pressure field, generated by piston 1.

We notice that the pressure field appears on both side of (3.11). Hence, Equation (3.11) cannot be solved directly. In order to simplify the problem, we apply the first-order Born approximation which assumes that  $p_{sc} \ll p_1$  such that we can approximate the total field  $p$  by the incoming field  $p_1$  on the right hand side of (3.11).

Hence, we have that

$$p_{sc}(\mathbf{s}, t) = \int_{\mathbf{r} \in \Omega} \int_0^T (Lp_1)(\mathbf{r}, u) g(\mathbf{r}, u; \mathbf{s}, t) d\mathbf{r} du. \quad (3.14)$$

Now, the pressure at the surface of piston 2 can be expressed as the integral of the scattered

### 3.2. Hail to the Pulse-echo Spatial Impulse Response Model

field  $p_{sc}(\mathbf{s}, t)$  along the surface  $S_2$

$$\begin{aligned}
 p_2(t) &= \int_{\mathbf{s} \in S_2} \int_{\mathbf{r} \in \Omega} \int_0^T (Lp_1)(\mathbf{r}, u) g(\mathbf{r}, u; \mathbf{s}, t) du d\mathbf{r} dS \\
 &= \int_{\mathbf{r} \in \Omega} \left[ L \left( \rho_0 \frac{\partial v}{\partial t} \otimes_t h_1 \right) \otimes_t h_2 \right] (\mathbf{r}, t) d\mathbf{r} \\
 &= \int_{\mathbf{r} \in \Omega} L \left( \rho_0 \frac{\partial v}{\partial t} \otimes_t h_1 \otimes_t h_2 \right) (\mathbf{r}, t) d\mathbf{r} \\
 &= \int_{\mathbf{r} \in \Omega} L \left( \rho_0 \frac{\partial v}{\partial t} \otimes_t h_{12} \right) (\mathbf{r}, t) d\mathbf{r}, \tag{3.15}
 \end{aligned}$$

where  $h_{12}(\mathbf{r}, t) = (h_1(\mathbf{r}, \cdot) \otimes_t h_2(\mathbf{r}, \cdot))(t)$  is the pulse-echo spatial impulse response.

Finally, we can show [71] that (3.15) can be rewritten as

$$p_2(t) = \int_{\mathbf{r} \in \Omega} \gamma(\mathbf{r}) \left( \rho_0 \frac{\partial^3 v}{\partial^3 t} \otimes_t h_{12}(\mathbf{r}, \cdot) \right) (t) d\mathbf{r}, \tag{3.16}$$

where  $\gamma(\mathbf{r})$  is called the TRF [90] defined by

$$\gamma(\mathbf{r}) = \frac{\Delta \rho(\mathbf{r})}{\rho_0} - \frac{2 \Delta c(\mathbf{r})}{c_0}. \tag{3.17}$$

The TRF is a fundamental quantity in US imaging since it quantifies the scattering of the medium which therefore depends on the local fluctuations in speed of sound and density.

In addition, Equation (3.16) defines the pulse-echo spatial impulse response model which characterizes the backscattered echoes received by piston 2 when piston 1 vibrates. Such a model depends on the pulse-echo spatial impulse response  $h_{12}(\mathbf{r}, t)$ .

#### 3.2.3 The Pulse-echo Waveform: From Pressure Fields to Echo Signals

As described in Section 2.1.2, transducer elements are capable of converting a pressure field into an electrical signal through the reversible piezoelectric effect. To model this aspect, we rely on the acousto-electrical impulse response of the transducer element, denoted as  $h_{ae}(t)$  as well as the electro-acoustical impulse response  $h_{ea}(t)$  such that

$$m_2(t) = (h_{ae} \otimes_t p_2)(t), \tag{3.18}$$

corresponds to the echo-signals recorded by piston 2 during the time  $T$  when piston 1 is vibrating.

Additionally, an excitation signal  $e(t)$  is usually inputted to a transducer element in order to generate an acoustic pulse in the medium through the electro-acoustical impulse response.

Finally, we come up with the following pulse-echo spatial impulse response model

$$m_2(t) = \left( v_{pe} \otimes_t \int_{\mathbf{r} \in \Omega} \gamma(\mathbf{r}) h_{12}(\mathbf{r}, \cdot) d\mathbf{r} \right) (t), \tag{3.19}$$

where  $v_{pe}$  is called the pulse-echo waveform, with a slight abuse of notation due to the

derivative, and is computed as

$$v_{pe}(t) = (h_{ae} \otimes_t h_{ea} \otimes_t e)(t). \quad (3.20)$$

Thus, we can define the following linear measurement model,  $H_{12} : L_2(\Omega) \rightarrow L_2([0, T])$ , associated with the proposed pulse-echo imaging configuration as

$$\begin{aligned} H_{12} : L_2(\Omega) &\rightarrow L_2([0, T]) \\ \gamma &\mapsto v_{pe} \otimes_t \int_{\mathbf{r} \in \Omega} \gamma(\mathbf{r}) h_{12}(\mathbf{r}, \cdot) d\mathbf{r} \end{aligned} \quad (3.21)$$

such that

$$m_2(t) = (H_{12}\gamma)(t).$$

### 3.3 Ultrasound Imaging Seen as an Inverse Problem

In this section, we use the pulse-echo spatial impulse response model, described in Section 3.2, to define the inverse problem involved in pulse-echo US imaging at the continuous level. Along with the definition of the inverse problem, we also introduce several notions that will be of major importance in the remainder of this work. In a second section, we focus on the discretization of the inverse problem, which will be of interest in this thesis.

#### 3.3.1 Inverse Problem at the Continuous Level

In Section 3.2, the pulse-echo spatial impulse response model has been introduced for a simple configuration which consists of two transducer elements.

To generalize to a standard pulse-echo imaging configuration, we define

- $N_t$  transducer elements on transmit with corresponding surfaces  $S_i^t$ , impulse responses  $h_{S_i^t}(\mathbf{r}, t)$  and transmit delays  $t_i$ ,  $i = 1, \dots, N_t$ ;
- $N_r$  transducer elements on receive with corresponding surfaces  $S_j^r$  and impulse responses  $h_{S_j^r}(\mathbf{r}, t)$ ,  $j = 1, \dots, N_r$ .

We assume that the same excitation signal  $e(t)$  is inputted to every transducer element on transmit and that the electro-acoustical and acousto-electrical impulse responses are the same for every transducer element, which allow us to define a single pulse-echo waveform  $v_{pe}(t)$ .

We are interested in the extension of (3.21) to the configuration defined above. Since US propagation is assumed to be linear, we can deduce the received signal by the  $j$ -th transducer element using the superposition principle as follows:

$$m_j = \sum_{i=1}^{N_t} H_{ij}\gamma,$$

### 3.3. Ultrasound Imaging Seen as an Inverse Problem

where  $H_{ij} : L_2(\Omega) \rightarrow L_2([0, T])$  is the measurement model (3.21) in the case where the  $i$ -th transducer element is used on transmit and the  $j$ -th transducer element is used on receive. We observe that the element raw-data are related to the TRF, which contains information about the scattering of the medium. Hence, by leveraging appropriate inversion methods, one may be able to recover the TRF from the measurements.

We now introduce several fundamental definitions that will be used in the remainder of the chapter. We first define a pulse-echo US imaging configuration.

**Definition 1** (Pulse-echo US Imaging Configuration). *A pulse-echo US imaging configuration is defined by*

- A set of  $N_t$  planar transducer elements on transmit, with corresponding surfaces  $S_i^t \subset \mathbb{R}^2$ , spatial impulse responses  $h_{S_i^t}(\mathbf{r}, t)$  and transmit delays  $t_i$ ,  $i = 1, \dots, N_t$ . These transducer elements are used to generate a US wave in the medium;
- A set of  $N_r$  planar transducer elements used on receive with corresponding surfaces  $S_j^r \subset \mathbb{R}^2$ , impulse responses  $h_{S_j^r}(\mathbf{r}, t)$ ,  $j = 1, \dots, N_r$ . These transducer elements record the backscattered pressure from the medium during in the time interval  $[0, T]$ ;
- A pulse-echo waveform  $v_{pe}(t) = (h_{ae} \circledast_t e \circledast_t h_{ea})(t)$ , where  $e(t)$  denotes the excitation signal, and  $h_{ae}(t)$  and  $h_{ea}(t)$  are the acousto-electrical impulse responses of the transducer elements.

Hence, we define the measurements corresponding to the above pulse-echo US imaging configuration as follows

$$m = [m_1, \dots, m_{N_r}]^T \in L_2([0, T])^{N_r}, \quad (3.22)$$

where  $m_j \in L_2([0, T])$  represents the echo-signal recorded by the  $j$ -th transducer element.

In order to formalize the inverse problem, we introduce the measurement model associated with the pulse-echo configuration, which relates the element-raw data to the TRF.

**Definition 2** (Measurement Model in Pulse-echo US Imaging). *The measurement model associated with a pulse-echo US imaging configuration is the linear operator  $H : L_2(\Omega) \rightarrow L_2([0, T])^{N_r}$  defined element-wise by*

$$(H\gamma)_j = \sum_{i=1}^{N_t} H_{ij}\gamma, \quad j = 1, \dots, N_r, \quad (3.23)$$

where  $H_{ij} : L_2(\Omega) \rightarrow L_2([0, T])$  is defined in (3.21).

We now have all the ingredients to define the continuous inverse problem associated with pulse-echo US imaging.

**Definition 3** (Continuous Inverse Problem in Pulse-echo US Imaging). *Consider a pulse-echo US imaging configuration with measurements  $m \in L_2([0, T])^{N_r}$  and the measurement*

### Chapter 3. Pulse-echo Ultrasound Imaging Seen as an Inverse Problem

model  $H : L_2(\Omega) \rightarrow L_2([0, T])^{N_r}$ . The continuous inverse problem associated with the proposed configuration can be formulated as

Find  $\gamma \in L_2(\Omega)$  such that  $m = H\gamma$ .

#### 3.3.2 From Continuous to Discrete Inverse Problem

In Section 3.3.1, we have derived a formulation of the inverse problem at the continuous level. Even though we could have studied continuous inversion methods, quite popular nowadays, the focus of this work is on discrete inversion methods. Hence, while the discretization of the element-raw data is intrinsic to the US imaging system, we also discretize the TRF, which will have a significant impact on the performance of the methods.

**Discretization of the Element-raw Data:** Sampling of the element-raw data is achieved by taking uniform samples at a rate  $T_s = 1/f_s$ , where  $f_s$  is the sampling frequency. Such a rate should satisfy as much as possible Nyquist rate requirements. Hence we have the following correspondence

$$\begin{array}{ccc} \text{Continuous measurements} & & \text{Discrete measurements} \\ m = [m_1, \dots, m_{N_r}] \in L_2([0, T])^{N_r} & \rightarrow & \mathbf{M} = [\mathbf{M}_1, \dots, \mathbf{M}_{N_r}]^\top \in \mathbb{R}^{N_r \times N}, \end{array}$$

where  $N$  is equal to  $\lfloor f_s T \rfloor$  and the  $k$ -th sample of the  $i$ -th transducer element is given by  $\mathbf{M}_{ik} = m_i(kT_s)$ . Thus, if the transducer elements are arranged into a matrix probe characterized by  $N_x^t$  elements in the lateral dimension and  $N_y^t$  elements in the elevation dimension, where  $N_x^t N_y^t = N_r$ , the measurements can equivalently be represented as a 3D-tensor  $\mathbf{M} \in \mathbb{R}^{N_x^t \times N_y^t \times N}$ , a matrix  $\mathbf{M} = [\mathbf{M}_1, \dots, \mathbf{M}_{N_r}] \in \mathbb{R}^{N_r \times N}$  or a vector  $\mathbf{m} = [\mathbf{M}_1^\top, \dots, \mathbf{M}_{N_r}^\top]^\top \in \mathbb{R}^{NN_r}$ .

**Discretization of the TRF:** We restrict ourselves to a discrete problem over a regular grid, i.e. we are interested in retrieving values of  $\gamma(\mathbf{r})$  at specific points of the 3D lattice described hereafter. We consider a discrete medium  $\Omega_d$  as a 3D-box with spacings  $(\Delta_x, \Delta_y, \Delta_z)$  and boundaries  $(x_{min}, x_{max})$ ,  $(y_{min}, y_{max})$  and  $(z_{min}, z_{max})$ , in the lateral, elevation and axial dimension, respectively. Puts formally, the discrete coordinates are expressed as

$$\begin{cases} x_l &= x_{min} + (l-1)\Delta_x \\ y_m &= y_{min} + (m-1)\Delta_y \\ z_n &= z_{min} + (n-1)\Delta_z \end{cases}, \quad (l, m, n) \in \{1, \dots, N_x\} \times \{1, \dots, N_y\} \times \{1, \dots, N_z\},$$

where  $N_x$ ,  $N_y$  and  $N_z$  are defined as

$$N_x = \left\lfloor \frac{x_{max} - x_{min}}{\Delta_x} \right\rfloor, \quad N_y = \left\lfloor \frac{y_{max} - y_{min}}{\Delta_y} \right\rfloor, \quad N_z = \left\lfloor \frac{z_{max} - z_{min}}{\Delta_z} \right\rfloor.$$

We are interested in recovering the 3D-tensor  $\mathbf{\Gamma} \in \mathbb{R}^{N_x \times N_y \times N_z}$  defined element-wise by

$$\mathbf{\Gamma}_{lmn} = \gamma(x_{min} + (l-1)\Delta_x, y_{min} + (m-1)\Delta_y, z_{min} + (n-1)\Delta_z). \quad (3.24)$$

### 3.4. Measurement Model for a Single Emitter - Single Receiver Configuration

Equivalently, we can write  $\Gamma$  as a 2D-matrix  $\Gamma \in \mathbb{R}^{N_x N_y \times N_z}$  or as a vector  $\boldsymbol{\gamma} \in \mathbb{R}^{N_x N_y N_z}$ . The discrete inverse problem is finally expressed as

$$\text{Find } \Gamma \in \mathbb{R}^{N_x \times N_y \times N_z} \text{ subject to } \mathbf{M} = \mathbf{H}\Gamma, \quad (3.25)$$

where  $\mathbf{H} : \mathbb{R}^{N_x \times N_y \times N_z} \rightarrow \mathbb{R}^{N_x^t \times N_y^t \times N}$  is the discrete measurement model, obtained by discretization of the continuous operator  $H$  defined in Section 3.3.1.

### 3.4 Measurement Model for a Single Emitter - Single Receiver Configuration

In this section, we propose to understand the effect of the measurement model and consequently the relationship between the measurements and the TRF in the most simple configuration, i.e. when a single emitter and a single receiver are used. Such a configuration is a building block of synthetic aperture focusing techniques (SAFT), widely used at the early times of US imaging [91, 92], as well as in synthetic aperture radar (SAR) imaging [93–96].

#### 3.4.1 Spatial Impulse Response of a Transducer Element

We describe the simplifying assumptions that we perform to model the spatial impulse response of a transducer element. Such assumptions will be used in the remaining sections of this chapter.

We propose to approximate the transducer element as a planar rectangular surface of width  $l$ , height  $h$ , center  $\mathbf{p}$  and surface  $S = lh$ , as described on Figure 3.3.

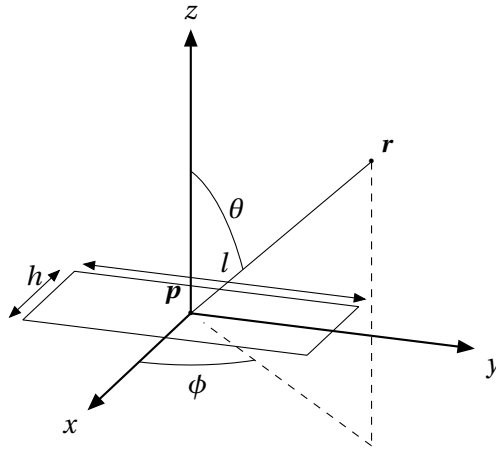


Fig. 3.3. Planar rectangular transducer element.

Such a transducer element is characterized by a center frequency  $f_c$  and we suppose that the speed of sound  $c$  is constant and known in the medium, so that we can define the wavelength  $\lambda = \frac{c}{f_c}$ . The corresponding spatial impulse response at any point in the field is therefore given by (3.7).

In addition, we rely on the Fraunhofer assumption [38], which states that in the far field ( $z \gg \pi \max(l, h)^2 / \lambda$ ), the observed pressure field can be directly obtained from the Fourier trans-

form of the transducer aperture.

In this case, the expression of the spatial impulse response can be drastically simplified as:

$$h(\mathbf{r}, t) = o(\mathbf{r}, \mathbf{p}) \frac{\delta\left(t - \frac{\|\mathbf{r} - \mathbf{p}\|_2}{c}\right)}{2\pi \|\mathbf{r} - \mathbf{p}\|_2} S, \quad (3.26)$$

where  $o(\mathbf{r}, \mathbf{p})$  is the element directivity defined as

$$o(\mathbf{r}, \mathbf{p}) = \text{sinc}\left(\frac{l \sin\theta \cos\phi}{\lambda}\right) \text{sinc}\left(\frac{h \sin\theta \sin\phi}{\lambda}\right). \quad (3.27)$$

Turnbull and Foster [97] have extended (3.27) for a soft-baffle condition, more common in US imaging, as

$$o(\mathbf{r}, \mathbf{p}) = \text{sinc}\left(\frac{l \sin\theta \cos\phi}{\lambda}\right) \text{sinc}\left(\frac{h \sin\theta \sin\phi}{\lambda}\right) \cos\theta. \quad (3.28)$$

In other words, Equation (3.26) states that under the far-field assumption, the transducer element can be approximated as a point source, propagating a spherical wave whose amplitude is modulated by the element directivity (Fourier transform of the aperture).

As an example, Figure 3.4 displays the directivity (in elevation direction in the axis of the transducer element) of a square transducer element of 275  $\mu\text{m}$  width with a center frequency of 3.3 MHz typically used in 3D imaging, assuming a soft-baffle condition. We observe the

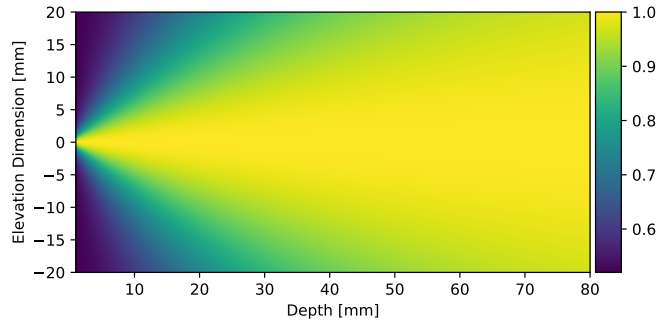


Fig. 3.4. Element directivity of a planar transducer element assuming a soft-baffle condition.

expected behaviour of a diffracting aperture. The transducer element is less and less selective for an increasing depth.

### 3.4.2 Continuous Measurement Model in 3D

Now, let us consider the configuration described in Figure 3.2, in which the two pistons are replaced by two transducer elements of the same surface  $S$ , centered at  $\mathbf{p} = [\mathbf{p}_x, \mathbf{p}_y, \mathbf{p}_z]^\top$  and  $\mathbf{q} = [\mathbf{q}_x, \mathbf{q}_y, \mathbf{q}_z]^\top$ , respectively, and whose spatial impulse responses are approximated by (3.26).

We define

1. the delay on transmit  $t_{Tx}(\mathbf{r}, \mathbf{p})$  as the time necessary for the US wave transmitted by

### 3.4. Measurement Model for a Single Emitter - Single Receiver Configuration

the transducer element located at  $\mathbf{p}$  to reach the field point  $\mathbf{r} \in \Omega$ ;

2. the delay on receive  $t_{Rx}(\mathbf{r}, \mathbf{q})$  as the time necessary for the US wave that reaches the field point  $\mathbf{r} \in \Omega$  to attain the transducer element located at  $\mathbf{q}$ .

In this case, the element-raw data recorded by the transducer element are expressed using (3.21) as

$$m_2 = H_{12}\gamma = v_{pe} \otimes_t (G\gamma), \quad (3.29)$$

where the linear integral operator  $G: L_2(\Omega) \rightarrow L_2([0, T])$  is defined by

$$G\gamma = \int_{\mathbf{r} \in \Omega} o_{pe}(\mathbf{r}, \mathbf{p}, \mathbf{q}) \gamma(\mathbf{r}) \delta(\cdot - t_{Tx}(\mathbf{r}, \mathbf{p}) - t_{Rx}(\mathbf{r}, \mathbf{q})) d\mathbf{r}, \quad (3.30)$$

where

$$t_{Tx}(\mathbf{r}, \mathbf{p}) = \frac{\|\mathbf{r} - \mathbf{p}\|_2}{c} \text{ and } t_{Rx}(\mathbf{r}, \mathbf{q}) = \frac{\|\mathbf{r} - \mathbf{q}\|_2}{c}, \quad (3.31)$$

and  $o_{pe}(\mathbf{r}, \mathbf{p}, \mathbf{q})$  accounts for the directivity of the transducer elements, the surfaces of the transducer elements and the decay of the spherical wavefront as

$$o_{pe}(\mathbf{r}, \mathbf{p}, \mathbf{q}) = \frac{S^2 o(\mathbf{r}, \mathbf{p}) o(\mathbf{r}, \mathbf{q})}{4\pi^2 \|\mathbf{r} - \mathbf{p}\|_2 \|\mathbf{r} - \mathbf{q}\|_2}. \quad (3.32)$$

In order to express the measurement model  $H$  more explicitly, we introduce the implicit function  $\phi(\mathbf{r}, \mathbf{p}, \mathbf{q}, t)$  defined by

$$\begin{cases} \phi(\mathbf{r}, \mathbf{p}, \mathbf{q}, t) &= t - \frac{\|\mathbf{r} - \mathbf{p}\|_2 + \|\mathbf{r} - \mathbf{q}\|_2}{c} \\ \nabla_{\mathbf{r}} \phi(\mathbf{r}, \mathbf{p}, \mathbf{q}, t) &= \frac{1}{c} \left( \frac{\mathbf{p} - \mathbf{r}}{\|\mathbf{r} - \mathbf{p}\|_2} + \frac{\mathbf{q} - \mathbf{r}}{\|\mathbf{r} - \mathbf{q}\|_2} \right). \end{cases} \quad (3.33)$$

We can observe that  $\phi$  is a smooth function of  $\mathbf{r}$  and that  $|\nabla_{\mathbf{r}} \phi| \neq 0$  for  $\mathbf{r} \in \Omega$ . We define  $\partial S(\mathbf{p}, \mathbf{q}, t)$ , the 0-level set of  $\phi(\cdot, \mathbf{p}, \mathbf{q}, t)$ , as

$$\partial S(\mathbf{p}, \mathbf{q}, t) = \{\mathbf{r} \in \Omega \mid \phi(\mathbf{r}, \mathbf{p}, \mathbf{q}, t) = 0\}. \quad (3.34)$$

In light of the above introduced implicit function, Equation (3.30) can be rewritten as

$$\begin{aligned} G\gamma &= \int_{\mathbf{r} \in \Omega} o_{pe}(\mathbf{r}, \mathbf{p}, \mathbf{q}) \gamma(\mathbf{r}) \delta(\phi(\mathbf{r}, \mathbf{p}, \mathbf{q}, \cdot)) d\mathbf{r} \\ &= \int_{\mathbf{r} \in \Omega} \gamma(\mathbf{r}) w(\mathbf{p}, \mathbf{q}, \mathbf{r}, \cdot) \delta(\phi(\mathbf{r}, \mathbf{p}, \mathbf{q}, \cdot)) |\nabla_{\mathbf{r}} \phi(\mathbf{r}, \mathbf{p}, \mathbf{q}, \cdot)| d\mathbf{r}, \end{aligned} \quad (3.35)$$

where

$$w(\mathbf{p}, \mathbf{q}, \mathbf{r}, t) = \frac{o_{pe}(\mathbf{r}, \mathbf{p}, \mathbf{q})}{|\nabla_{\mathbf{r}} \phi(\mathbf{r}, \mathbf{p}, \mathbf{q}, t)|}. \quad (3.36)$$

### Chapter 3. Pulse-echo Ultrasound Imaging Seen as an Inverse Problem

---

Equation (3.52) is very interesting since it corresponds to a surface integral over the interface defined by  $\partial S(\mathbf{p}, \mathbf{q}, t)$  [98], from which we can derive the explicit representation as follows:

$$G\gamma = \int_{\mathbf{r} \in \partial S(\mathbf{p}, \mathbf{q}, \cdot)} w(\mathbf{p}, \mathbf{q}, \mathbf{r}, \cdot) \gamma(\mathbf{r}) d\sigma(\mathbf{r}), \quad (3.37)$$

where  $d\sigma(\mathbf{r})$  is the measure along the interface.

We observe that the action of  $G$  consists of an integration over a surface given by the 0-level set of  $\phi$ , which depends on the relative locations of the transducer elements. Thus, we can make a clear analogy with CT as well as transmission-mode US tomography. The measurements  $m(t)$  recorded by the transducer element located at  $\mathbf{q}$  correspond to projections of the TRF onto hypersurfaces of  $\Omega$ . Then, the results of such projections are blurred by the pulse-echo waveform in order to obtain the recorded electrical signal.

Hence, while the problem of retrieving the values of a function from its means along hypersurfaces is a challenging task (possible for hypersurfaces of specific shapes), we face an even more difficult problem since such projections are blurred when acquired by the transducer element.

Now, consider that we have access to a parametric formulation of the interface  $\partial S(\mathbf{p}, \mathbf{q}, t)$  such that

$$\mathbf{r} \in \partial S(\mathbf{p}, \mathbf{q}, t) \Leftrightarrow \exists (\alpha, \beta) \in [\alpha_l, \alpha_u] \times [\beta_l, \beta_u] \mid \mathbf{r} = \mathbf{r}(\alpha, \beta, \mathbf{p}, \mathbf{q}, t),$$

where  $\alpha_l \in \mathbb{R}$ ,  $\beta_l \in \mathbb{R}$ ,  $\alpha_u \in \mathbb{R}$ ,  $\beta_u \in \mathbb{R}$  are such that  $\alpha_l \leq \alpha_u$  and  $\beta_l \leq \beta_u$ .

Using well-known properties of integrals on parameterized surfaces, we can reformulate (3.37) as

$$G\gamma = \iint_{[\alpha_l, \alpha_u] \times [\beta_l, \beta_u]} w(\mathbf{p}, \mathbf{q}, \alpha, \beta, \cdot) \gamma(\mathbf{r}(\alpha, \beta, \mathbf{p}, \mathbf{q}, \cdot)) \left\| \frac{\partial \mathbf{r}}{\partial \alpha} \wedge \frac{\partial \mathbf{r}}{\partial \beta} \right\|_2 d\alpha d\beta. \quad (3.38)$$

Equation (3.38) provides a nice formalism since the surface integral is reduced to a more standard two dimensional integral on bounded intervals. This step will significantly facilitate the discretization of  $G\gamma$  necessary to the definition of the inverse problem in the discrete domain.

In the remainder of the section, we derive the parametric equations for the proposed configuration, first in a specific case where the same transducer is used on transmit and receive and then in the general case.

**Particular Case - Same Transducer on Transmit and Receive:** When the same transducer is used on transmit and receive (i.e.  $\mathbf{p} = \mathbf{q}$ ), the implicit function simplifies to

$$\begin{cases} \phi(\mathbf{r}, \mathbf{p}, t) &= t - \frac{2\|\mathbf{r}-\mathbf{p}\|_2}{c} \\ \nabla_{\mathbf{r}}\phi(\mathbf{r}, \mathbf{p}, t) &= \frac{2}{c} \frac{\mathbf{p}-\mathbf{r}}{\|\mathbf{r}-\mathbf{p}\|_2} \end{cases}, \quad (3.39)$$

### 3.4. Measurement Model for a Single Emitter - Single Receiver Configuration

and the surface integral (3.37) reduces to

$$G\gamma = \frac{c}{2} \int_{\mathbf{r} \in \partial S(\mathbf{r}, \mathbf{p}, t)} o_{pe}(\mathbf{r}, \mathbf{p}) \gamma(\mathbf{r}) d\sigma(\mathbf{r}). \quad (3.40)$$

In addition, the interface  $\partial S(\mathbf{r}, \mathbf{p}, t)$  defined by

$$\partial S(\mathbf{r}, \mathbf{p}, t) = \left\{ \mathbf{r} \in H \mid \|\mathbf{r} - \mathbf{p}\|_2 = \frac{ct}{2} \right\}, \quad (3.41)$$

is a sphere whose Cartesian equation is given by

$$(x - p_x)^2 + (y - p_y)^2 + z^2 = \frac{(ct)^2}{4}, \quad \mathbf{r} = [x, y, z]^\top \in \Omega, \quad (3.42)$$

defined when  $\frac{ct}{2} > \sqrt{(x - p_x)^2 + (y - p_y)^2}$ .

We can observe that (3.42) is a sphere of radius  $\frac{ct}{2}$  and center  $\mathbf{p}$ , as displayed on the leftmost figure of Figure 3.5.

When  $\mathbf{p}$  is moving on an hyperplane surrounding the medium of interest, the set of all the spherical projections  $G\gamma$ , denoted as the complete set of projections, corresponds to the spherical Radon transform, a generalization of the classical linear Radon transform. Such a mathematical object has been relatively well studied in the context of multimonostatic US imaging [99] and solutions have been derived for various shapes of the hyperplane such as spheres [70], planar surfaces [70, 100], and cylindrical surfaces [70].

We can straightforwardly derive a set of parametric equations of the sphere as

$$\begin{cases} x(\alpha, \beta, \mathbf{p}, t) &= p_x + \frac{ct}{2} \cos(\alpha) \sin(\beta) \\ y(\alpha, \beta, \mathbf{p}, t) &= p_y + \frac{ct}{2} \sin(\alpha) \sin(\beta) \\ z(\alpha, \beta, \mathbf{p}, t) &= \frac{ct}{2} \cos(\beta) \end{cases}, \quad (3.43)$$

where  $(\alpha, \beta) \in [0, 2\pi] \times [0, \frac{\pi}{2}]$ .

**General Case:** In the general case where  $\mathbf{p} \neq \mathbf{q}$ , the interface  $\partial S(\mathbf{p}, \mathbf{q}, t)$  is defined by

$$\partial S(\mathbf{p}, \mathbf{q}, t) = \{ \mathbf{r} \in \Omega \mid \|\mathbf{r} - \mathbf{p}\|_2 + \|\mathbf{r} - \mathbf{q}\|_2 = ct \}. \quad (3.44)$$

In order to facilitate the characterization of the surface, we introduce the rotation matrix  $\mathbf{R}_\theta$  which rotates the coordinate system around the  $z$ -axis by an angle  $\theta$  such that

$$\sin(\theta) = \frac{p_y - q_y}{\|\mathbf{p} - \mathbf{q}\|_2} \quad \text{and} \quad \cos(\theta) = \frac{q_x - p_x}{\|\mathbf{p} - \mathbf{q}\|_2}. \quad (3.45)$$

In the rotated system, the coordinates of the transducer elements are  $\mathbf{p}' = [p'_x, 0, 0]^\top$  and  $\mathbf{q}' = [q'_x, 0, 0]^\top$ , where  $p'_x = \cos(\theta) p_x - \sin(\theta) p_y$  and  $q'_x = \cos(\theta) q_x - \sin(\theta) q_y$ .

In the rotated coordinate system, Equation (3.44) defines a prolate spheroid, displayed on the rightmost figure of Figure 3.5, whose Cartesian equation is detailed in Proposition 1.



Fig. 3.5. The leftmost figure represents an example spheroid in the particular case when  $\mathbf{p} = \mathbf{q}$ . The rightmost figure displays an example prolate spheroid in the general case when  $\mathbf{p} \neq \mathbf{q}$ . The light gray accounts for the part of the surface that is outside the positive half volume.

**Proposition 1** (Cartesian equation of the prolate spheroid). *When  $ct > \|\mathbf{p} - \mathbf{q}\|_2$ ,  $\partial S$  given by (3.44) is defined by  $\partial S = \{z > 0\} \cap S_p$  where  $S_p$  is a prolate spheroid whose Cartesian equation is expressed as*

$$\frac{4 \left( x - \frac{p'_x + q'_x}{2} \right)^2}{(ct)^2} + \frac{4y^2 + 4z^2}{(ct)^2 - (q'_x - p'_x)^2} = 1, \mathbf{r} = [x, y, z]^\top \in \Omega.$$

*Proof.* Since a rotation is an isometry, we can express the equality involved in the definition of  $\partial S(\mathbf{p}, \mathbf{q}, t)$  in (3.44) in the rotated coordinate system as

$$\|\mathbf{r}' - \mathbf{p}'\|_2 + \|\mathbf{r}' - \mathbf{q}'\|_2 = ct. \quad (3.46)$$

We introduce  $\mathbf{r}'_c = \frac{\mathbf{p}' + \mathbf{q}'}{2}$  which is the rotated barycenter of the transducer elements. We can express (3.46) using  $\mathbf{r}'_c$  as

$$\begin{aligned} & \|\mathbf{r}' - \mathbf{p}'\|_2 + \|\mathbf{r}' - \mathbf{q}'\|_2 = ct \\ \Leftrightarrow & \left\| \mathbf{r}' - \mathbf{r}'_c + \frac{\mathbf{q}' - \mathbf{p}'}{2} \right\|_2 + \left\| \mathbf{r}' - \mathbf{r}'_c + \frac{\mathbf{p}' - \mathbf{q}'}{2} \right\|_2 = ct \\ \Leftrightarrow & \|\mathbf{r}_s - \mathbf{r}_f\|_2 + \|\mathbf{r}_s + \mathbf{r}_f\|_2 = ct, \end{aligned} \quad (3.47)$$

where  $\mathbf{r}_f = \frac{\mathbf{q}' - \mathbf{p}'}{2}$  and  $\mathbf{r}_s = \mathbf{r}' - \mathbf{r}'_c$  corresponds to the translated coordinates in the rotated system.

### 3.4. Measurement Model for a Single Emitter - Single Receiver Configuration

We now work on (3.47), which is easier to manipulate than (3.46):

$$\begin{aligned}
& \|\mathbf{r}_s - \mathbf{r}_f\|_2 + \|\mathbf{r}_s + \mathbf{r}_f\|_2 = ct \\
& \Rightarrow \|\mathbf{r}_s - \mathbf{r}_f\|_2^2 = (ct)^2 - 2(ct) \|\mathbf{r} + \mathbf{r}_f\|_2 + \|\mathbf{r} + \mathbf{r}_f\|_2^2 \\
& \Leftrightarrow 2(ct) \|\mathbf{r} + \mathbf{r}_f\|_2 = (ct)^2 + 4\langle \mathbf{r}, \mathbf{r}_f \rangle \\
& \Rightarrow 4(ct)^2 \|\mathbf{r} + \mathbf{r}_f\|_2^2 = [(ct)^2 + 4\langle \mathbf{r}, \mathbf{r}_f \rangle]^2 \\
& \Leftrightarrow 4(ct)^2 (\|\mathbf{r}\|_2^2 + \|\mathbf{r}_f\|_2^2) = (ct)^4 + 16\langle \mathbf{r}, \mathbf{r}_f \rangle^2.
\end{aligned}$$

Now, we develop the expression in terms of the cartesian coordinates of the different points, knowing that  $\mathbf{r}_f = [x_f, 0, 0]^\top$ , where  $x_f = \frac{q'_x - p'_x}{2}$ , and  $\mathbf{r}_s = [x_s, y, z]^\top$ , where  $x_s = x - x_s = x - \frac{p'_x + q'_x}{2}$ . This leads to:

$$\begin{aligned}
4(ct)^2 (x_s^2 + y^2 + z^2 + x_f^2) &= (ct)^4 + 16x_s^2 x_f^2 \\
\Leftrightarrow x_s^2 [(ct)^2 - 4x_f^2] + (y^2 + z^2) (ct)^2 &= (ct)^2 \left( \frac{(ct)^2}{4} - x_f^2 \right) \\
\Leftrightarrow \frac{4x_s^2}{(ct)^2} + \frac{4y^2 + 4z^2}{(ct)^2 - 4x_f^2} &= 1, \tag{3.48}
\end{aligned}$$

where the last equivalence holds if and only if  $ct > q'_x - p'_x = \|\mathbf{p} - \mathbf{q}\|_2$ .

Since  $(ct)^2 > (ct)^2 - 4x_f^2$ , Equation (3.48) defines a prolate spheroid [101], centered at  $\mathbf{r}_c$  with the x-axis as the symmetry axis (in the rotated coordinate domain).  $\square$

The above described prolate spheroid is centered at the barycenter of the two transducer elements and its direction is aligned with the axis formed by the two transducer elements. Its foci are the two transducer elements.

The length of the semi-major axis is  $\frac{ct}{2}$  which makes sense since it corresponds to the maximal round-trip distance the US wave can travel in the time interval  $[0, t]$ , when  $y = z = 0$ .

The length of the semi-minor axis is given by  $\sqrt{\frac{(ct)^2}{4} - \left(\frac{p'_x - q'_x}{2}\right)^2}$ . Such a value also makes sense physically since it corresponds to the maximum depth that can be reached in the time interval  $[0, t]$ , given the distance between the transducer elements. It can be easily demonstrated that

this is attained at the point  $x_s = \frac{p'_x + q'_x}{2}$  for which  $z = \sqrt{\frac{(ct)^2}{4} - \left(\frac{p'_x - q'_x}{2}\right)^2}$ .

Regarding the inequality  $ct > \|\mathbf{p} - \mathbf{q}\|_2$ , it states that the single emitter - single receiver configuration imposes to wait for an incompressible amount of time, proportional to the distance between the transducer elements, before the receiver starts to record a signal sent by the emitter. Indeed, it is physically impossible that an ultrasound wave emitted from the emitter located at  $\mathbf{p}$  to the receiver located at  $\mathbf{q}$  at time  $t < \|\mathbf{p} - \mathbf{q}\|_2 / c$ .

As a final remark, we also notice that the Cartesian equation is consistent with the case where  $\mathbf{p} = \mathbf{q}$ . Indeed, when  $p'_x = q'_x$ , the Cartesian equation of the prolate spheroid reduces to

$$(x - p_x)^2 + y^2 + z^2 = \frac{(ct)^2}{4},$$

### Chapter 3. Pulse-echo Ultrasound Imaging Seen as an Inverse Problem

which corresponds to a sphere centered at the location of the transducer element with radius  $\frac{ct}{2}$ .

Hence we observe that  $G\gamma$  is an elliptical projection of the TRF on a prolate spheroid with foci located at the two transducer elements. By appropriately moving the transducer elements, it would be possible to acquire a set of elliptical projections which may form an elliptical Radon transform, as discussed in Appendix A.2.3. These methods have been discussed in few papers [102–104] and inversion techniques are proposed for two specific distribution of the TRF [102].

We can derive a set of parametric equations of the prolate spheroid as

$$\begin{cases} x(\alpha, \beta, \mathbf{p}, \mathbf{q}, t) &= \frac{1}{2}(p'_x + q'_x + ct \cos(\alpha) \sin(\beta)) \\ y(\alpha, \beta, \mathbf{p}, \mathbf{q}, t) &= \frac{1}{2}\sqrt{(ct)^2 - (p'_x - q'_x)^2} \sin(\alpha) \sin(\beta) \\ z(\alpha, \beta, \mathbf{p}, \mathbf{q}, t) &= \frac{1}{2}\sqrt{(ct)^2 - (p'_x - q'_x)^2} \cos(\beta) \end{cases}, \quad (3.49)$$

where  $(\alpha, \beta) \in [0, 2\pi] \times [0, \frac{\pi}{2}]$ .

#### 3.4.3 Discretization of the Measurement Model in 3D

The discretization of the measurement model is schematically described below

$$\begin{array}{ccc} \text{Continuous formulation} & & \text{Discrete Formulation} \\ m = v_{pe} \otimes_t (G\gamma) \in L_2([0, T]) & \rightarrow & \mathbf{M} = \mathbf{v}_{pe} * (\mathbf{G}\Gamma) \in \mathbb{R}^N \end{array}$$

where  $\mathbf{v}_{pe} \in \mathbb{R}^F$ , is the sampled pulse-echo waveform,  $F$  being its support, and  $\mathbf{G}: \mathbb{R}^{N_x \times N_y \times N_z} \rightarrow \mathbb{R}^N$  is the discretized projection operator.

Let us now focus on the discretization of the projection operator, defined in a general case by

$$G\gamma = \iint_{[\alpha_l, \alpha_u] \times [\beta_l, \beta_u]} w'(\mathbf{p}, \mathbf{q}, \alpha, \beta, \cdot) \gamma(\mathbf{r}(\alpha, \beta, \mathbf{p}, \mathbf{q}, \cdot)) d\alpha d\beta,$$

where  $w'(\mathbf{p}, \mathbf{q}, \alpha, \beta, t) = w(\mathbf{p}, \mathbf{q}, \alpha, \beta, t) \times \left\| \frac{\partial \mathbf{r}}{\partial \alpha} \wedge \frac{\partial \mathbf{r}}{\partial \beta} \right\|_2$ .

Based on the parametric formulation (3.38), the discretization is straightforward using standard numerical approximations methods [105].

To do so, we introduce the following set of uniformly spaced quadrature nodes

$$\begin{cases} \alpha_s &= \alpha_l + (s-1) \Delta_\alpha \\ \beta_j &= \beta_l + (j-1) \Delta_\beta \end{cases}, (s, j) \in \{1, \dots, N_\alpha\} \times \{1, \dots, N_\beta\},$$

where  $\Delta_\alpha = \frac{|\alpha_u - \alpha_l|}{N_\alpha}$  and  $\Delta_\beta = \frac{|\beta_u - \beta_l|}{N_\beta}$ .

### 3.4. Measurement Model for a Single Emitter - Single Receiver Configuration

We consider the time instants  $t_k = kT_s$ ,  $k = 0, \dots, N-1$ , from which we can write that

$$\begin{aligned} (G\gamma)(t_k) &= \sum_{s=1}^{N_\alpha} \sum_{j=1}^{N_\beta} \int_{\alpha_s - \frac{\Delta\alpha}{2}}^{\alpha_s + \frac{\Delta\alpha}{2}} \int_{\beta_j - \frac{\Delta\beta}{2}}^{\beta_j + \frac{\Delta\beta}{2}} w'(\mathbf{p}, \mathbf{q}, \alpha, \beta, t_k) \gamma(\mathbf{r}(\alpha, \beta, \mathbf{p}, \mathbf{q}, t_k)) d\alpha d\beta \\ &\approx \Delta_\alpha \Delta_\beta \sum_{s=1}^{N_\alpha} \sum_{j=1}^{N_\beta} w'(\mathbf{p}, \mathbf{q}, \alpha_s, \beta_j, t_k) \gamma(\mathbf{r}(\alpha_s, \beta_j, \mathbf{p}, \mathbf{q}, t_k)), \end{aligned} \quad (3.50)$$

where (3.50) is obtained by midpoint quadrature in each subinterval.

We observe that (3.50) requires the evaluation of  $w'$  and  $\gamma$  at many points of the continuous domain. As described in Section 3.3.2, we only have access to  $\Gamma$ , i.e. the TRF  $\gamma$  evaluated on the regular 3D lattice. We therefore introduce interpolation operators  $\mathbf{I}_{\alpha_s, \beta_j} : \mathbb{R}^{N_x \times N_y \times N_z} \rightarrow \mathbb{R}^N$  such that

$$\mathbf{I}_{\alpha_s, \beta_j} \Gamma \approx [\gamma(\mathbf{r}(\alpha_s, \beta_j, \mathbf{p}, \mathbf{q}, 0)), \dots, \gamma(\mathbf{r}(\alpha_s, \beta_j, \mathbf{p}, \mathbf{q}, T))]^\top.$$

We can see that  $(\mathbf{I}_{\alpha_s, \beta_j} \Gamma)_k \approx \gamma(\mathbf{r}(\alpha_s, \beta_j, \mathbf{p}, \mathbf{q}, t_k))$  which can be realized with any interpolation method, e.g. nearest neighbor interpolation or trilinear interpolation.

Using such operators, we can express the discretized projection operator  $\mathbf{G}$  using (3.50) as

$$\mathbf{G}\Gamma = \Delta_\alpha \Delta_\beta \sum_{s=1}^{N_\alpha} \sum_{j=1}^{N_\beta} \mathbf{w}'_{\alpha_s, \beta_j} \circ (\mathbf{I}_{\alpha_s, \beta_j} \Gamma), \quad (3.51)$$

where  $\mathbf{w}'_{\alpha_s, \beta_j} \in \mathbb{R}^N$  is defined element-wise by evaluating  $w'$  at time instants  $t_k$ ,  $k = 1, \dots, N$ .

#### 3.4.4 Continuous Measurement Model in 2D

Most of the configurations described further in this work consider a 2D scenario where imaging is performed in the plane  $\Omega = \{z > 0\} \cap \{y = 0\}$ . In such a case, the linear integral operator  $G$  is a curvilinear integral on  $\partial S(\mathbf{p}, \mathbf{q}, t)$  defined in a similar way to the 3D case by

$$G\gamma = \int_{\mathbf{r} \in \partial S(\mathbf{p}, \mathbf{q}, \cdot)} w(\mathbf{p}, \mathbf{q}, \mathbf{r}, \cdot) \gamma(\mathbf{r}) dl(\mathbf{r}), \quad (3.52)$$

where  $dl(\mathbf{r})$  designates the measure along the curve and  $\partial S(\mathbf{p}, \mathbf{q}, t)$  is defined by

$$\partial S(\mathbf{p}, \mathbf{q}, t) = \{\mathbf{r} \in \Omega \mid \phi(\mathbf{r}, \mathbf{p}, \mathbf{q}, t) = 0\}. \quad (3.53)$$

As expected from the study in 3D,  $\partial S(\mathbf{p}, \mathbf{q}, t)$  is an ellipse whose Cartesian equation is given by

$$\frac{4(x - \frac{p_x + q_x}{2})^2}{(ct)^2} + \frac{4z^2}{(ct)^2 - (p_x - q_x)^2} = 1, \quad \mathbf{r} = [x, z]^\top \in \Omega, \quad (3.54)$$

defined for  $\mathbf{p} = [p_x, 0]^\top$ ,  $\mathbf{q} = [q_x, 0]^\top$  and  $ct > \|\mathbf{p} - \mathbf{q}\|_2$ .

The two foci of the ellipse are the two transducer elements and the semi-major and semi-minor

axes,  $a$  and  $b$ , are given by

$$\begin{cases} a = \frac{ct}{2} \\ b = \frac{\sqrt{(ct)^2 - (p_x - q_x)^2}}{2} \end{cases} \quad (3.55)$$

In addition, it is straightforward to derive a set of parametric equations defined as

$$\begin{cases} x(\alpha, \mathbf{p}, \mathbf{q}) = \alpha + \frac{p_x + q_x}{2} \\ z(\alpha, \mathbf{p}, \mathbf{q}) = K \sqrt{\frac{(ct)^2}{4} - \alpha^2} \end{cases} \quad (3.56)$$

where  $K = \sqrt{1 - \left(\frac{p_x - q_x}{ct}\right)^2}$  and  $\alpha \in \left[0, \frac{ct}{2}\right]$ .

The parametric equations give another insight on the ellipse, namely that the time instant  $t$  defines bounds on  $x$  such that  $x \in \left[\frac{p_x + q_x}{2}, \frac{ct + p_x + q_x}{2}\right]$  and on  $z$  such that  $z \in \left[0, \frac{\sqrt{(ct)^2 - (p_x - q_x)^2}}{2}\right]$ .

Intuitively, for a given time instant, when the distance between the transducer elements increases, the ellipse tends to be flatter and flatter since most of the allocated time is dedicated to the travel time between the two transducer elements. In the extreme case where  $\mathbf{p} = \mathbf{q}$ , we see that the upper bound on the depth is given by  $\frac{ct}{2}$  which is the maximal depth, among all the possible configurations, the US wave can reach during the time  $t$ .

### 3.4.5 Discretization of the Measurement Model in 2D

The discretization of the measurement model is very similar to the 3D case. The measurements  $\mathbf{M} \in \mathbb{R}^N$  are expressed as

$$\mathbf{M} = \mathbf{v}_{pe} * (\mathbf{G}\mathbf{\Gamma}). \quad (3.57)$$

The projection is now mapping from a function defined on a 2D lattice to  $\mathbb{R}^N$ ,  $\mathbf{G} : \mathbb{R}^{N_x \times N_z} \rightarrow \mathbb{R}^N$ , expressed using the midpoint rule as

$$\mathbf{G} = \Delta_\alpha \sum_{s=1}^{N_\alpha} \mathbf{w}'_{\alpha_s} \circ (\mathbf{I}_{\alpha_s} \mathbf{\Gamma}_s), \quad (3.58)$$

where  $N_\alpha$  is a positive integer,  $\{\alpha_s\}_{s=1}^{N_\alpha}$  and  $\Delta_\alpha$  are the quadrature nodes and weight, respectively, and the interpolation operators  $\mathbf{I}_{\alpha_s} : \mathbb{R}^{N_x} \rightarrow \mathbb{R}^N$  are defined by

$$\mathbf{I}_{\alpha_s} \mathbf{\Gamma}_s \approx [\gamma(\mathbf{r}(\alpha_s, \mathbf{p}, \mathbf{q}, 0)), \dots, \gamma(\mathbf{r}(\alpha_s, \mathbf{p}, \mathbf{q}, T))]^\top.$$

Regarding the choice of the quadrature nodes, we can write that

$$x = \alpha + \frac{p_x + q_x}{2} \Leftrightarrow \alpha = x - \frac{p_x + q_x}{2}, \quad (3.59)$$

from which we can deduce  $N_\alpha \leq N_x$  uniform quadrature nodes from the  $N_x$  points in the lateral dimension of the lattice (the sign  $\leq$  comes from the condition  $\alpha < \frac{ct}{2}$ ). Consequently,

$\Delta_\alpha = \Delta_x$  and  $\mathbf{G}$  can be expressed as

$$\mathbf{G} = \Delta_x \sum_{s=1}^{N_x} \mathbf{w}'_{\alpha_s} \circ (\mathbf{I}_{\alpha_s} \Gamma_s), \quad (3.60)$$

where  $\mathbf{I}_{\alpha_s} : \mathbb{R}^{N_x} \rightarrow \mathbb{R}^N$  are 1D-interpolation operators.

### 3.5 Measurement Model in Diverging Wave Imaging

We consider the pulse-echo imaging configuration described in Definition 1 where we assume that the same set of transducer elements is used on transmit and receive.

In addition, we suppose that the transducer elements are arranged into a matrix probe located in the plane  $z = 0$ , with spacing  $\Delta_x^t$  and  $\Delta_y^t$  in the lateral and elevation dimension, respectively. We therefore consider the following uniform grid of transducer elements:

$$\mathbf{p}_{ij} = \left[ i\Delta_x^t, j\Delta_y^t, 0 \right]^\top, \quad (i, j) \in \{1, \dots, N_x^t\} \times \{1, \dots, N_y^t\},$$

where  $N_x^t$  and  $N_y^t$  are the number of transducer elements in lateral and elevation dimension, respectively, such that  $N_t = N_x^t N_y^t$ .

The measurements are represented as a tensor  $\mathbf{M} \in \mathbb{R}^{N_x^t \times N_y^t \times N}$  or equivalently as a matrix  $\mathbf{M} \in \mathbb{R}^{N_x^t N_y^t \times N}$  or a vector  $\mathbf{m} \in \mathbb{R}^{N_x^t N_y^t N}$ .

#### 3.5.1 Continuous Measurement Model in 3D

In DW imaging, the transducer elements are excited in such a way that a diverging wavefront, issued from a virtual point source located at  $\mathbf{r}_n$  behind the US probe, is transmitted in the medium [29].

In order to generate the diverging wavefront that would come from the virtual point  $\mathbf{r}_n = [x_n, y_n, z_n]^\top$ , the transducer elements are excited with the following delay profile

$$\begin{cases} t_{ij} &= \frac{\|\mathbf{p}_{ij} - \mathbf{r}_n\|_2}{c} - t_0 \\ t_0 &= \min_{i,j} \frac{\|\mathbf{p}_{ij} - \mathbf{r}_n\|_2}{c} \end{cases},$$

where the offset delay  $t_0$  is used to set the minimum values of  $t_{ij}$  to 0.

Under the wavefront assumption, the time delay on transmit does not depend on the transducer element and is given by

$$t_{Tx}(\mathbf{r}) = \frac{\|\mathbf{r} - \mathbf{r}_n\|_2}{c} - t_0. \quad (3.61)$$

Thus, the measurement model associated with the DW imaging configuration,  $H : L_2(\Omega) \rightarrow L_2([0, T])^{N_x^t \times N_y^t}$ , can be expressed element-wise by

$$(H\gamma)_{ij} = v_{pe} \otimes_t (G_{ij}\gamma), \quad (3.62)$$

where  $G_{ij} : L_2(\Omega) \rightarrow L_2([0, T])$  is defined by

$$G_{ij}\gamma = \int_{\mathbf{r} \in \Omega} o_{pe}(\mathbf{r}, \mathbf{p}_{ij}) \gamma(\mathbf{r}) \delta(\phi(\mathbf{r}, \mathbf{p}_{ij}, \mathbf{r}_n, \cdot)) d\mathbf{r}, \quad (3.63)$$

in which the implicit function is given by

$$\phi(\mathbf{r}, \mathbf{p}_{ij}, \mathbf{r}_n, t) = t + t_0 - \frac{\|\mathbf{r} - \mathbf{p}_{ij}\|_2 + \|\mathbf{r} - \mathbf{r}_n\|_2}{c},$$

and the element directivity is slightly changed compared to (3.32) due to the wavefront assumption such that

$$o_{pe}(\mathbf{r}, \mathbf{p}_{ij}) = S \frac{o(\mathbf{r}, \mathbf{p}_{ij})}{2\pi \|\mathbf{r} - \mathbf{p}_{ij}\|_2}. \quad (3.64)$$

The implicit function is remarkably close to the one expressed for the single emitter-single receiver in Section 3.4.2 by considering the virtual source as the emitter and the transducer elements as the receivers. We define the 0-level set of the implicit function as the following interface

$$\partial S(\mathbf{p}_{ij}, \mathbf{r}_n, t) = \{\mathbf{r} \in \Omega \mid \|\mathbf{r} - \mathbf{p}_{ij}\|_2 + \|\mathbf{r} - \mathbf{r}_n\|_2 = c(t + t_0)\},$$

from which we can rewrite (3.63) as the following surface integral

$$G_{ij}\gamma = \int_{\mathbf{r} \in \partial S(\mathbf{p}_{ij}, \mathbf{r}_n, \cdot)} w(\mathbf{p}_{ij}, \mathbf{r}_n, \mathbf{r}, \cdot) \gamma(\mathbf{r}) d\sigma(\mathbf{r}), \quad (3.65)$$

where  $d\sigma(\mathbf{r})$  is the measure along the surface and  $w$  is given by

$$w(\mathbf{p}_{ij}, \mathbf{r}_n, \mathbf{r}, t) = \frac{o_{pe}(\mathbf{r}, \mathbf{p}_{ij})}{|\nabla_{\mathbf{r}} \phi(\mathbf{r}, \mathbf{p}_{ij}, \mathbf{r}_n, t)|}.$$

Each operator  $G_{ij}$  is an elliptical projection over a prolate spheroid whose foci are the virtual source and the transducer element, respectively. The measurement model gathers many of these projections for various locations of the transducer elements  $\mathbf{p}_{ij}$ . The set of projections can be analyzed in terms of the elliptical Radon transform, in the special case where one focus is fixed (the virtual source) and the other varies on an hyperplane (the transducer elements).

Regarding the Cartesian equation of the prolate spheroid, we slightly change the formulation compared to Section 3.4.2 since we consider a fixed coordinate system, with  $x$ -axis and  $y$ -axis parallel to the probe. This allows us to derive a more generic formulation than the one provided in Section 3.4.2.

Hence, we introduce the rotation matrices  $\mathbf{R}_\theta$  and  $\mathbf{R}_\xi$  which perform the rotations of angles  $\theta$

and  $\xi$  described in Figure 3.6 and defined as

$$\theta = \arctan\left(\frac{i\Delta_x^t - x_n}{y_n - j\Delta_y^t}\right) \text{ and } \xi = \arctan\left(\frac{z_n}{\sqrt{(x_n - i\Delta_x^t)^2 + (y_n - j\Delta_y^t)^2}}\right). \quad (3.66)$$

Thus, by sequential application of  $\mathbf{R}_\theta$  and  $\mathbf{R}_\xi$ , the coordinate system is rotated such that its

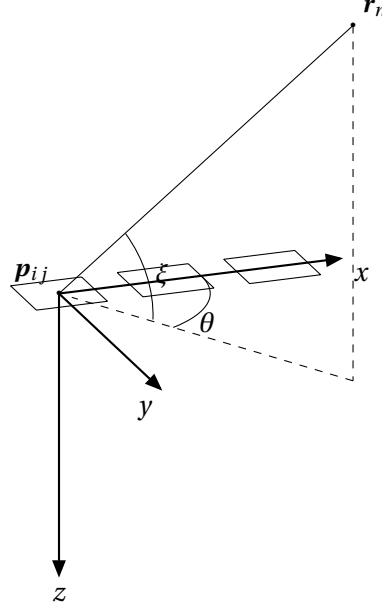


Fig. 3.6. Coordinate system and angle convention for diverging wave imaging.

$x$ -axis is parallel to the direction  $\mathbf{r}_n - \mathbf{p}_{ij}$ .

We define the new coordinates in the rotated domain as  $\mathbf{r}' = \mathbf{R}_\theta \mathbf{R}_\xi \mathbf{r}$ ,  $\mathbf{r}'_n = \mathbf{R}_\theta \mathbf{R}_\xi \mathbf{r}_n$  and  $\mathbf{p}'_{ij} = \mathbf{R}_\theta \mathbf{R}_\xi \mathbf{p}_{ij}$  and we express the Cartesian equation of the prolate spheroid as in Section 3.4.2 as

$$\frac{4\left(x' - \frac{p'_{ijx} + x'_n}{2}\right)^2}{(ct)^2} + \frac{4y'^2 + 4z'^2}{(ct)^2 - (p'_{ijx} - x'_n)^2} = 1. \quad (3.67)$$

**Parametric Equations - The Elegant Approach:** Using the above introduced Cartesian equation, we can easily deduce the set of parametric equations as

$$\begin{cases} x'(\alpha, \beta, \mathbf{p}_{ij}, \mathbf{r}_n, t) = \frac{1}{2}\left(p'_{ijx} + x'_n + c(t + t_0) \cos(\alpha) \sin(\beta)\right) \\ y'(\alpha, \beta, \mathbf{p}_{ij}, \mathbf{r}_n, t) = \frac{1}{2}\sqrt{(c(t + t_0))^2 - 4x_f'^2} \sin(\alpha) \sin(\beta) \\ z'(\alpha, \beta, \mathbf{p}_{ij}, \mathbf{r}_n, t) = \frac{1}{2}\sqrt{(c(t + t_0))^2 - 4x_f'^2} \cos(\beta) \end{cases}, (\alpha, \beta) \in [0, 2\pi] \times \left[0, \frac{\pi}{2}\right], \quad (3.68)$$

### Chapter 3. Pulse-echo Ultrasound Imaging Seen as an Inverse Problem

from which we obtain the set of parametric equations in the original coordinate system as:

$$\mathbf{r}(\alpha, \beta, \mathbf{p}_{ij}, \mathbf{r}_n, t) = \mathbf{R}_{-\xi} \mathbf{R}_{-\theta} [x'(\alpha, \beta, \mathbf{p}_{ij}, \mathbf{r}_n, t), y'(\alpha, \beta, \mathbf{p}_{ij}, \mathbf{r}_n, t), z'(\alpha, \beta, \mathbf{p}_{ij}, \mathbf{r}_n, t)]^\top.$$

Based on the set of parametric equations introduced above, we can perform a change of variables in (3.65) which defines the following parameterized integral:

$$G_{ij}\gamma = \iint_{[0, 2\pi] \times [0, \frac{\pi}{2}]} w'(\mathbf{p}_{ij}, \mathbf{r}_n, \mathbf{r}(\alpha, \beta, \mathbf{p}_{ij}, \mathbf{r}_n, \cdot), \cdot) \gamma(\mathbf{r}(\alpha, \beta, \mathbf{p}_{ij}, \mathbf{r}_n, \cdot)) d\alpha d\beta,$$

where  $w' = w \times \left\| \frac{\partial \mathbf{r}}{\partial \alpha} \wedge \frac{\partial \mathbf{r}}{\partial \beta} \right\|_2$ .

**Parametric Equations - The Brute-force Approach:** Alternatively, we can directly express the parametric equations associated with the 0-level set of the implicit function  $\phi(\mathbf{r}, \mathbf{p}_{ij}, \mathbf{r}_n, t)$  in the form  $z = f(x, y)$ . This would greatly help for the discretization since it would be possible to rely on the points of the 3D lattice.

To obtain this parametric formulation, many calculations are required and we rely on a formal calculus software (using Wolfram Mathematica for instance). Using such a tool, we can demonstrate that a set of parametric equations can be defined as follows:

$$\begin{cases} x(\alpha, \beta, \mathbf{p}_{ij}, \mathbf{r}_n, t) = \alpha \\ y(\alpha, \beta, \mathbf{p}_{ij}, \mathbf{r}_n, t) = \beta \\ z(\alpha, \beta, \mathbf{p}_{ij}, \mathbf{r}_n, t) = g(\alpha, \beta, \mathbf{p}_{ij}, \mathbf{r}_n, t) \end{cases}, \quad (3.69)$$

where  $g$  is a lengthy function whose complete expression is detailed in Section B.1.1 of Appendix B.

#### 3.5.2 Discretization of the Measurement Model in 3D

The discretization process in the case of DW imaging does not significantly vary from the one derived in the single emitter-single receiver configuration. We define the discrete measurement model as follows:

$$\mathbf{M} = \mathbf{H}\mathbf{\Gamma} = \mathbf{v}_{pe} * (\mathbf{G}\mathbf{\Gamma}) \in \mathbb{R}^{N_x' \times N_y' \times N} \rightarrow \mathbf{M}_{ij} = (\mathbf{H}\mathbf{\Gamma})_{ij} = \mathbf{v}_{pe} * (\mathbf{G}_{ij}\mathbf{\Gamma}) \in \mathbb{R}^N, \quad (3.70)$$

where  $\mathbf{G}_{ij} : \mathbb{R}^{N_x \times N_y \times N_z} \rightarrow \mathbb{R}^N$  is the discretized projection operator associated with the transducer element located at  $\mathbf{p}_{ij}$ .

In order to perform the discretization, we rely on the set of parametric equations introduced in the brute-force approach. We introduce the following set of uniformly spaced quadrature nodes:

$$\begin{cases} \alpha_s = x_{min} + (s-1)\Delta_x \\ \beta_m = y_{min} + (m-1)\Delta_y \end{cases}, \quad (s, m) \in \{1, \dots, N_x\} \times \{1, \dots, N_y\},$$

where  $N_x, \Delta_x, N_y, \Delta_y$  are defined by the discretization of the medium, discussed in Section 3.3.2.

### 3.5. Measurement Model in Diverging Wave Imaging

Hence, we can express the discretized projection operator  $\mathbf{G}_{ij}$  as:

$$\mathbf{G}_{ij}\mathbf{\Gamma} = \Delta_x\Delta_y \sum_{s=1}^{N_x} \sum_{m=1}^{N_y} \mathbf{w}'_{\alpha_s, \beta_m} \circ \mathbf{I}_{\alpha_s, \beta_m}^{ij} \mathbf{\Gamma}_{sm}, \quad (3.71)$$

where  $\mathbf{w}'_{\alpha_s, \beta_m} \in \mathbb{R}^N$  is defined element-wise by evaluating  $w'$  at time instants  $t_k$ ,  $k = 1, \dots, N$ , and  $\mathbf{I}_{\alpha_s, \beta_m}^{ij} : \mathbb{R}^{N_z} \rightarrow \mathbb{R}^N$  are 1D-interpolation operators over the axial dimension defined as

$$\mathbf{I}_{\alpha_s, \beta_m}^{ij} \mathbf{\Gamma}_{sm} \approx [\gamma(\mathbf{r}(\alpha_s, \beta_m, \mathbf{p}_{ij}, \mathbf{r}_n, 0)), \dots, \gamma(\mathbf{r}(\alpha_s, \beta_m, \mathbf{p}_{ij}, \mathbf{r}_n, T))]^\top.$$

**Matrix-free Evaluation of the Measurement Model:** Thus, we have derived a way to compute the forward operation  $\mathbf{G}\mathbf{\Gamma}$ , and consequently  $\mathbf{H}\mathbf{\Gamma}$  in a matrix-free fashion in the context of DW imaging. The algorithm is detailed in Algorithm 1 below.

---

**Algorithm 1** Matrix-free Computation of  $\mathbf{H}\mathbf{\Gamma}$  for UFUS Imaging in 3D

---

**Require:**  $\mathbf{r}_n, \mathbf{t}, \{\mathbf{p}_{ij}\}_{i,j=1}^{N_x^t, N_y^t}, \{\alpha_s\}_{s=1}^{N_x}, \{\beta_m\}_{m=1}^{N_y}, \mathbf{\Gamma}, \mathbf{v}_{pe}$

**initialization:**  $\mathbf{M} = \mathbf{0}$

**for**  $(i, j) \in \{1, \dots, N_x^t\} \times \{1, \dots, N_y^t\}$  **do**

$$\hat{\mathbf{M}}_{ij} = \Delta_x\Delta_y \sum_{s=1}^{N_x} \sum_{m=1}^{N_y} \mathbf{w}'_{\alpha_s, \beta_m} \circ (\mathbf{I}_{\alpha_s, \beta_m}^{ij} \mathbf{\Gamma}_{sm})$$

$$\mathbf{M}_{ij} = \mathbf{v}_{pe} * \hat{\mathbf{M}}_{ij}$$

**end for**

**return**  $\mathbf{M}$

---

The main advantage of Algorithm 1 is the reduced memory footprint compared to existing approaches, which makes it scalable to 3D imaging. Regarding the complexity of the proposed approach, the computation of  $\mathbf{H}\mathbf{\Gamma}$  requires to perform the following operations:

1.  $N_x^t N_y^t N_x N_y$  interpolations where each interpolation has a computational complexity of  $O(LN)$  with  $L$  the support of the interpolation kernel ( $L \ll N_z$ );
2.  $N_x^t N_y^t N_x N_y$  point-wise multiplications with  $\mathbf{w}'_{\alpha_s}$ , each of which having a cost of  $O(N)$ ;
3.  $N_x^t N_y^t$  convolutions with  $\mathbf{v}_{pe}$  each of which with a complexity of  $O(N \log N)$ .

The overall computation complexity of  $\mathbf{H}\mathbf{\Gamma}$  is therefore:

$$\text{Cost}(\mathbf{H}\mathbf{\Gamma}) = O\left(LN_x^t N_y^t N_x N_y N + N_x^t N_y^t N_x N_y N + N_x^t N_y^t N \log N\right) = O\left(N_x^t N_y^t N_x N_y N\right). \quad (3.72)$$

#### 3.5.3 Continuous Measurement Model in 2D

Since most of the UFUS imaging configurations considered in this thesis are in 2D, we also present the measurement model in the context of 2D imaging, although it may be derived directly from the measurement model in 3D. Hence, this section is dedicated to the reader that

### Chapter 3. Pulse-echo Ultrasound Imaging Seen as an Inverse Problem

wants to perform 2D imaging and does not want to go through the unnecessary complexity of the 3D formalism.

In 2D imaging, we consider the configuration described in Figure 3.7, where the transducer elements are located at  $\mathbf{p}_i = [i\Delta_x^t, 0]^\top$ ,  $i = 1, \dots, N_x^t$ . The virtual point is positioned at  $\mathbf{r}_n = [x_n, z_n]^\top$  behind the probe.

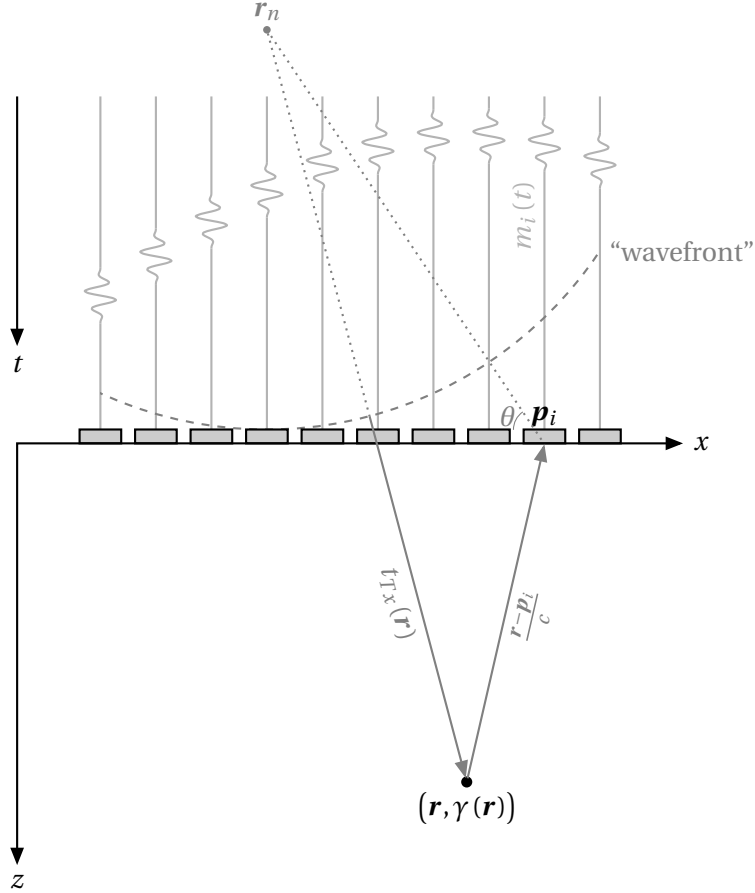


Fig. 3.7. Standard 2D diverging-wave imaging configuration.

Thus, the measurements are considered as  $M \in L_2([0, T])^{N_x^t}$  and the measurement model,  $H: L_2(\Omega) \rightarrow L_2([0, T])^{N_x^t}$ , can be expressed element-wise as

$$(H\gamma)_i = v_{pe} \otimes_t (G_i\gamma), \quad (3.73)$$

where  $G_i: L_2(\Omega) \rightarrow L_2([0, T])$  is the linear integral operator defined by

$$G_i\gamma = \int_{\mathbf{r} \in \Omega} o_{pe}(\mathbf{r}, \mathbf{p}_i) \gamma(\mathbf{r}) \delta(\phi(\mathbf{r}, \mathbf{p}_i, \mathbf{r}_n, \cdot)) d\mathbf{r}, \quad (3.74)$$

$$\phi(\mathbf{r}, \mathbf{p}_i, \mathbf{r}_n, t) = t + t_0 - \frac{\|\mathbf{r} - \mathbf{p}_i\|_2 + \|\mathbf{r} - \mathbf{r}_n\|_2}{c}.$$

We define the 0-level set of the implicit function  $\phi$ , which is now a 1D curve, as the following

interface

$$\partial S(\mathbf{p}_i, \mathbf{r}_n, t) = \{\mathbf{r} \in \Omega \mid \|\mathbf{r} - \mathbf{p}_i\|_2 + \|\mathbf{r} - \mathbf{r}_n\|_2 = c(t + t_0)\}, \quad (3.75)$$

from which we can rewrite (3.74) as the following line integral

$$G_i \gamma = \int_{\mathbf{r} \in \partial S(\mathbf{p}_i, \mathbf{r}_n, \cdot)} w(\mathbf{p}_i, \mathbf{r}_n, \mathbf{r}, \cdot) \gamma(\mathbf{r}) dl(\mathbf{r}), \quad (3.76)$$

where  $dl(\mathbf{r})$  is the measure along the curve and  $w$  is given by

$$w(\mathbf{p}_i, \mathbf{r}_n, \mathbf{r}, t) = \frac{o_{pe}(\mathbf{r}, \mathbf{p}_i)}{|\nabla_{\mathbf{r}} \phi(\mathbf{r}, \mathbf{p}_i, \mathbf{r}_n, t)|}.$$

When  $c(t + t_0) > \|\mathbf{r}_n - \mathbf{p}_i\|_2$ , Equation (3.75) defines the intersection between the half-plane  $z > 0$  and an ellipse with foci located at  $\mathbf{r}_n$  and  $\mathbf{p}_i$  and with semi-major and semi-minor axes,  $a$  and  $b$ , given by

$$a = \frac{c(t + t_0)}{2} \text{ and } b = \frac{1}{2} \sqrt{(c(t + t_0))^2 - \|\mathbf{r}_n - \mathbf{p}_i\|_2^2}.$$

**Parametric Equations - The Elegant Approach:** In order to derive the set of parametric equations associated with (3.75), we introduce the rotation  $\mathbf{R}_\theta$  of angle  $\theta = \arctan\left(\frac{|x_n - i\Delta_x^t|}{z_n}\right)$ , such that

$$\begin{cases} x &= x' \cos(\theta) + z' \sin(\theta) \\ z &= z' \cos(\theta) - x' \sin(\theta) \end{cases},$$

where  $[x', z']^\top$  are expressed in the rotated coordinate system.

In the rotated coordinate system, the ellipse can be defined using the following set of parametric equations

$$\begin{cases} x'(\alpha) &= \frac{p_{ix} + x_n}{2} \cos(\theta) - \frac{z_n}{2} \sin(\theta) + a \cos(\alpha) \\ z'(\alpha) &= \frac{p_{ix} + x_n}{2} \sin(\theta) + \frac{z_n}{2} \cos(\theta) + b \sin(\alpha) \end{cases}, \alpha \in [\alpha_l, \alpha_u],$$

where  $\alpha_l \leq \alpha_u \in \mathbb{R}$ . This leads to the following parametric equations in the main coordinate system:

$$\begin{cases} x(\alpha) &= \frac{p_{ix} + x_n}{2} + a \cos(\theta) \cos(\alpha) + b \sin(\theta) \sin(\alpha) \\ z(\alpha) &= \frac{z_n}{2} + b \cos(\theta) \sin(\alpha) - a \sin(\theta) \cos(\alpha) \end{cases} \Leftrightarrow \mathbf{r} = \frac{\mathbf{p}_i + \mathbf{r}_n}{2} + \mathbf{R}_{-\theta} [a \cos(\alpha), b \sin(\alpha)]^\top,$$

where  $\alpha \in [\alpha_l, \alpha_u]$ .

The identification of  $\alpha_l$  and  $\alpha_u$  are not technically difficult but requires some calculations that are detailed below. We are interested in the following inequality

$$\frac{z_n}{2} + b \cos(\theta) \sin(\alpha) - a \sin(\theta) \cos(\alpha) > 0. \quad (3.77)$$

### Chapter 3. Pulse-echo Ultrasound Imaging Seen as an Inverse Problem

---

We introduce  $A = a \sin(\theta)$  and  $B = b \cos(\theta)$ , such that the inequality becomes

$$\frac{z_n}{2} + B \sin(\alpha) - A \cos(\alpha) > 0. \quad (3.78)$$

To solve such a trigonometric inequality, we use the Weierstrass substitution, which is detailed below:

$$t = \tan\left(\frac{\alpha}{2}\right) \Leftrightarrow \sin(\alpha) = \frac{2t}{1+t^2} \text{ and } \cos(\alpha) = \frac{1-t^2}{1+t^2}.$$

Inequality (3.78) now becomes a polynomial inequality on  $t$

$$\left(\frac{z_n}{2} + A\right)t^2 + 2Bt + \frac{z_n}{2} - A > 0. \quad (3.79)$$

Let us study the sign of the coefficient  $\left(\frac{z_n}{2} + A\right)$  which is closely linked to the sign of the polynomial. We have the following

$$\frac{z_n}{2} + A = \frac{z_n + c(t+t_0)\sin(\theta)}{2} = \frac{z_n \left(1 + \frac{c(t+t_0)}{\|r_n - p_i\|_2}\right)}{2} < 0,$$

since  $z_n < 0$ . Thus, (3.79) is valid between the roots of the polynomial, which are given by

$$t = \frac{(\cos(\theta) \pm 1)b}{a \sin(\theta)}. \quad (3.80)$$

Since  $\sin(\theta) < 0$ , we deduce the following values for  $\alpha_l$  and  $\alpha_u$

$$\begin{cases} \alpha_l &= 2 \arctan\left(\frac{(\cos(\theta)+1)b}{a \sin(\theta)}\right) \\ \alpha_u &= 2 \arctan\left(\frac{(\cos(\theta)-1)b}{a \sin(\theta)}\right) \end{cases}.$$

Using the set of parametric equations, we write the line integral (3.76) as

$$G_i \gamma = \int_{\alpha_l}^{\alpha_u} w'(\mathbf{p}_i, \mathbf{r}_n, \mathbf{r}(\alpha, \mathbf{p}_i, \mathbf{r}_n, t)) \gamma(\mathbf{r}(\alpha, \mathbf{p}_i, \mathbf{r}_n, t)) d\alpha, \quad (3.81)$$

where  $w' = w \times \sqrt{\left(\frac{\partial x}{\partial \alpha}\right)^2 + \left(\frac{\partial z}{\partial \alpha}\right)^2}$ .

**Parametric Equations - The Brute-force Approach:** As for the 3D case, it may be convenient to express the parametric equations of the ellipse as  $z = g(x)$ .

To obtain this parametric formulation, many calculations are required and we rely on a formal calculus software (using Wolfram Mathematica for instance). Using such a tool, we can demonstrate that a set of parametric equations can be defined as follows:

$$\begin{cases} x(\alpha, \mathbf{r}_n, t) &= \alpha \\ z(\alpha, \mathbf{p}_i, \mathbf{r}_n, t) &= g(\alpha, \mathbf{p}_i, \mathbf{r}_n, t) \end{cases}, \quad (3.82)$$

where  $g$  is a lengthy function detailed in Section B.1.2 of Appendix B.

### 3.5.4 Discretization of the Measurement Model in 2D

As for the 3D case, we define the discrete measurement model as follows

$$\mathbf{M} = \mathbf{H}\mathbf{\Gamma} = \mathbf{v}_{pe} * (\mathbf{G}\mathbf{\Gamma}) \in \mathbb{R}^{N_x^t \times N} \rightarrow \mathbf{M}_i = (\mathbf{H}\mathbf{\Gamma})_i = \mathbf{v}_{pe} * (\mathbf{G}_i\mathbf{\Gamma}) \in \mathbb{R}^N, \quad (3.83)$$

where  $\mathbf{G}_i : \mathbb{R}^{N_x \times N_z} \rightarrow \mathbb{R}^N$  is the discretized projection operator associated with the  $i$ -th transducer element, obtained by discretization of the integral (3.81).

We introduce the following set of uniformly spaced quadrature nodes:

$$\alpha_s = x_{min} + (s-1)\Delta_x, \quad s \in \{1, \dots, N_x\},$$

where  $N_x$  and  $\Delta_x$  are defined by the discretization of the medium, discussed in Section 3.3.2. Thus, we can express the discretized projection operator  $\mathbf{G}_i$  as:

$$\mathbf{G}_i\mathbf{\Gamma} = \Delta_x \sum_{s=1}^{N_x} \mathbf{w}'_{\alpha_s} \circ \mathbf{I}_{\alpha_s}^i \mathbf{\Gamma}_s, \quad (3.84)$$

where  $\mathbf{w}'_{\alpha_s} \in \mathbb{R}^N$  is defined element-wise by evaluating  $w'$  at time instants  $t_k$ ,  $k = 1, \dots, N$ , and  $\mathbf{I}_{\alpha_s}^i : \mathbb{R}^{N_z} \rightarrow \mathbb{R}^N$  are 1D-interpolation operators over the axial dimension.

**Matrix-free Evaluation of the Measurement Model:** In a similar way to the 3D case, we can derive a matrix-free evaluation strategy of  $\mathbf{H}\mathbf{\Gamma}$ . The algorithm is detailed in Algorithm 2 below.

---

#### Algorithm 2 Matrix-free Computation of $\mathbf{H}\mathbf{\Gamma}$ for UFUS Imaging in 2D

---

**Require:**  $r_n, \mathbf{t}, \{\mathbf{p}_i\}_{i=1}^{N_x^t}, \{\alpha_s\}_{s=1}^{N_x}, \mathbf{\Gamma}, \mathbf{v}_{pe}$   
**initialization:**  $\mathbf{M} = 0$   
**for**  $i \in \{1, \dots, N_x^t\}$  **do**  
      $\hat{\mathbf{M}}_i = \Delta_x \sum_{s=1}^{N_x} \mathbf{w}'_{\alpha_s} \circ (\mathbf{I}_{\alpha_s}^i \mathbf{\Gamma}_s)$   
      $\mathbf{M}_i = \mathbf{v}_{pe} * \hat{\mathbf{M}}_i$   
**end for**  
**return**  $\mathbf{M}$

---

The computation of  $\mathbf{H}\mathbf{\Gamma}$  requires to perform the following operations:

1.  $N_x^t N_x$  interpolations where each interpolation kernel has a computational complexity of  $O(LN)$  with  $L$  the support of the interpolation kernel ( $L \ll N_z$ );
2.  $N_x^t N_x$  point-wise multiplications with  $\mathbf{w}'_{\alpha_s}$ , each of which having a cost of  $O(N)$ ;
3.  $N_x^t$  convolutions with  $\mathbf{v}_{pe}$  each of which with a complexity of  $O(N \log N)$ .

The overall computation complexity of  $\mathbf{H}\mathbf{\Gamma}$  is therefore:

$$\text{Cost}(\mathbf{H}\mathbf{\Gamma}) = O(LN_x N_x^t N + N_x N_x^t N + N_x^t N \log N) = O(N_x N_x^t N), \quad (3.85)$$

since  $\log N \ll N_x^t$  in US imaging.

### 3.6 Measurement Model in Plane-wave Imaging

We consider transducer elements arranged on the following regular grid:

$$\mathbf{p}_{ij} = \left[ i\Delta_x^t, j\Delta_y^t, 0 \right]^\top, \quad (i, j) \in \{1, \dots, N_x^t\} \times \{1, \dots, N_y^t\},$$

where  $N_x^t$  and  $N_y^t$  are the number of transducer elements in lateral and elevation dimension, respectively, such that  $N_t = N_x^t N_y^t$ .

The measurements are represented as a tensor  $\mathbf{M} \in \mathbb{R}^{N_x^t \times N_y^t \times N}$  or equivalently as a matrix  $\mathbf{M} \in \mathbb{R}^{N_x^t N_y^t \times N}$  or a vector  $\mathbf{m} \in \mathbb{R}^{N_x^t N_y^t N}$ .

#### 3.6.1 Continuous Measurement Model in 3D

In PW imaging, the transducer elements are excited in such a way that a planar wavefront is transmitted in the medium [28]. Depending on the delay profile, we can steer the wavefront in both lateral and elevation dimensions with angles  $\theta_x$  and  $\theta_y$ , respectively. Usually, PWs are steered in only one direction, i.e.  $\theta_x = 0$  or  $\theta_y = 0$ .

In the remainder, we consider steering in the lateral dimension, such that  $\theta_y = 0$  and  $\theta_x \neq 0$ . The results can be easily adapted to the case of steering in the elevation dimension.

In order to generate the planar wavefront, with steering angle  $\theta_x$ , the transducer elements are excited with the following delay profile along the lateral dimension

$$t_{ij} = \begin{cases} \frac{|\mathbf{p}_{ij,x} - \mathbf{p}_{1j,x}|}{c} \cotan(\theta_x), & \text{if } \theta_x \geq 0 \\ \frac{|\mathbf{p}_{ij,x} - \mathbf{p}_{N_x^t j,x}|}{c} \cotan(\theta_x), & \text{otherwise} \end{cases}.$$

Under the wavefront assumption, the delay on transmit is given by

$$\begin{cases} t_{Tx}(\mathbf{r}) &= \frac{\langle \mathbf{r}, \mathbf{e}_\theta \rangle}{c}, \\ \mathbf{e}_\theta &= [\sin(\theta_x), 0, \cos(\theta_x)]^\top. \end{cases}$$

The measurement model,  $H: L_2(\Omega) \rightarrow L_2([0, T])^{N_x^t \times N_y^t}$ , can be expressed element-wise by

$$(H\gamma)_{ij} = v_{pe} \otimes_t (G_{ij}\gamma),$$

where  $G_{ij}: L_2(\Omega) \rightarrow L_2([0, T])$  is defined by

$$G_{ij}\gamma = \int_{\mathbf{r} \in \Omega} o_{pe}(\mathbf{r}, \mathbf{p}_{ij}) \gamma(\mathbf{r}) \delta(\phi(\mathbf{r}, \mathbf{p}_{ij}, \boldsymbol{\theta}, t)) d\mathbf{r}, \quad (3.86)$$

in which the implicit function is defined as

$$\begin{cases} \phi(\mathbf{r}, \mathbf{p}_{ij}, \boldsymbol{\theta}, t) &= t - \frac{\|\mathbf{r} - \mathbf{p}_{ij}\|_2 + \langle \mathbf{r}, \mathbf{e}_\theta \rangle}{c} \\ \nabla_{\mathbf{r}} \phi(\mathbf{r}, \mathbf{p}_{ij}, \boldsymbol{\theta}, t) &= \frac{1}{c} \left( \frac{\mathbf{p}_{ij} - \mathbf{r}}{\|\mathbf{r} - \mathbf{p}_{ij}\|_2} - \mathbf{e}_\theta \right), \end{cases}$$

and the element directivity  $o_{pe}$  is the same as for DW imaging and is given by (3.64). When  $\theta_x = 0$ , we have that

$$\nabla_{\mathbf{r}}\phi(\mathbf{r}, \mathbf{p}_{ij}, \boldsymbol{\theta}, t) = \frac{1}{c} \left( \frac{\mathbf{p}_{ij} - \mathbf{r}}{\|\mathbf{r} - \mathbf{p}_{ij}\|_2} - [0, 0, 1]^\top \right), \quad (3.87)$$

which is 0 when  $x = p_{ij_x}$  and  $y = p_{ij_y}$ .

However, when  $\theta_x \neq 0$  we observe that the gradient may vanish for some values of  $\mathbf{r}$  that are on the 1D curve defined by

$$\nabla\phi(\mathbf{r}, \mathbf{p}_{ij}, \boldsymbol{\theta}, t) = \mathbf{0} \Leftrightarrow \begin{cases} y = p_{ij_y} \\ z = |(x - p_{ij_x}) \cotan(\theta)| \end{cases}.$$

Theoretically, this is problematic since the the surface integral cannot be defined when the gradient of the implicit function vanishes at some points. However, in practice, even though the equality does not hold in the continuous domain, the parametric equations may still be used in the discrete domain where it is highly unlikely that the gradient vanishes.

Based on the implicit function  $\phi$ , we can rewrite (3.86) as the following surface integral

$$G_{ij}\gamma = \int_{\mathbf{r} \in \partial S(\mathbf{p}_{ij}, \boldsymbol{\theta}, t)} w(\mathbf{p}_{ij}, \boldsymbol{\theta}, \mathbf{r}, \cdot) \gamma(\mathbf{r}) d\sigma(\mathbf{r}), \quad (3.88)$$

where  $d\sigma(\mathbf{r})$  is the measure along the surface,  $\partial S(\mathbf{p}_{ij}, \boldsymbol{\theta}, t)$  is the following interface

$$\partial S(\mathbf{p}_{ij}, \boldsymbol{\theta}, t) = \{\mathbf{r} \in \Omega \mid ct - \|\mathbf{r} - \mathbf{p}_{ij}\|_2 + \langle \mathbf{r}, \mathbf{e}_\theta \rangle = 0\}, \quad (3.89)$$

and  $w$  is given by

$$w(\mathbf{p}_{ij}, \boldsymbol{\theta}, \mathbf{r}, t) = \frac{o_{pe}(\mathbf{r}, \mathbf{p}_{ij})}{|\nabla_{\mathbf{r}}\phi(\mathbf{r}, \mathbf{p}_{ij}, \boldsymbol{\theta}, t)|},$$

We now proceed to the derivation of the Cartesian equations and parametric equations of the interface. We introduce the rotation of angle  $-\theta_x$  along the  $y$ -axis,  $\mathbf{R}_{-\theta_x}$  such that the transducer elements are defined as follows in the rotated coordinate system

$$\mathbf{p}'_{ij} = \begin{bmatrix} p'_{ij_x} \\ p'_{ij_y} \\ p'_{ij_z} \end{bmatrix}^\top = \begin{bmatrix} p_{ij_x} \cos(\theta_x) \\ p_{ij_y} \\ p_{ij_x} \sin(\theta_x) \end{bmatrix}^\top.$$

In addition, we also consider the following translation  $\mathbf{T}_{\mathbf{p}'_{ij}}$  such that

$$\mathbf{T}_{\mathbf{p}'_{ij}} \mathbf{r} = \begin{bmatrix} x - p'_{ij_x} \\ y - p'_{ij_y} \\ z - p'_{ij_z} \end{bmatrix}^\top, \quad \mathbf{r} = \begin{bmatrix} x \\ y \\ z \end{bmatrix}^\top.$$

Using the above introduced transformations, we demonstrate that the interface is a circular paraboloid whose Cartesian equation is detailed in Proposition 2.

**Proposition 2** (Cartesian equation of the circular paraboloid). *The interface  $\partial S(\mathbf{p}_{ij}, \boldsymbol{\theta}, t)$  given by (3.89), is defined, when  $ct \neq p_{ij'_z}$ , by  $\partial S = \{z > 0\} \cap P$  where  $P$  is a circular paraboloid whose*

Cartesian equation is defined by

$$\frac{x_s^2 + y_s^2}{2(p'_{ijz} - ct)} - z_s = \frac{p'_{ijz} - ct}{2}, \mathbf{r}_s = [x_s, y_s, z_s]^\top = \mathbf{T}_{\mathbf{p}'_{ij}} \mathbf{R}_{-\theta_x} \mathbf{r}, \mathbf{r} \in \Omega. \quad (3.90)$$

*Proof.* Assume that  $\theta_y = 0$  such that  $\mathbf{e}_\theta = [e_x, e_y, e_z]^\top = [\sin(\theta_x), 0, \cos(\theta_x)]^\top$ . The rotation of angle  $-\theta_x$  around the y-axis associates to each vector  $\mathbf{r} = [x, y, z]^\top$  a vector  $\mathbf{r}' = [x', y', z']^\top$  such that

$$\mathbf{r}' = [x \cos(\theta_x) - z \sin(\theta_x), y, z \cos(\theta_x) + x \sin(\theta_x)]^\top = [x e_z - z e_x, y, z e_z + x e_x]^\top.$$

The result is obtained by working on the equation involved in  $\partial S(\mathbf{p}_{ij}, \boldsymbol{\theta}, t)$  as detailed below.

$$\begin{aligned} ct &= \|\mathbf{r} - \mathbf{p}_{ij}\|_2 + \langle \mathbf{r}, \mathbf{e}_\theta \rangle \\ \Rightarrow (ct - \langle \mathbf{r}, \mathbf{e}_\theta \rangle)^2 &= \|\mathbf{r} - \mathbf{p}_{ij}\|_2^2 \\ \Leftrightarrow (ct)^2 - 2ct(xe_x + ze_z) + (xe_x + ze_z)^2 &= (x - p_{ijx})^2 + (y - p_{ijy})^2 + z^2 \\ \Leftrightarrow (ct)^2 - 2ctz' + z'^2 &= (x' - p'_{ijx})^2 + (y' - p'_{ijy})^2 + (z' - p'_{ijz})^2 \\ \Leftrightarrow (ct)^2 - p'_{ijz}{}^2 &= (x' - p'_{ijx})^2 + (y' - p'_{ijy})^2 - z'(2p'_{ijz} - 2ct) \\ \Leftrightarrow \frac{ct \neq p'_{ijz} (x' - p'_{ijx})^2 + (y' - p'_{ijy})^2}{2(p'_{ijz} - ct)} - \left( z' - \frac{ct + p'_{ijz}}{2} \right) &= 0 \\ \Leftrightarrow \frac{x_s^2 + y_s^2}{2(p'_{ijz} - ct)} - z_s &= \frac{p'_{ijz} - ct}{2}, \end{aligned}$$

where  $\mathbf{r}_s = [x_s, y_s, z_s]^\top = \mathbf{T}_{\mathbf{p}'_{ij}} \mathbf{r}'$ . □

Hence,  $G_{ij}$  performs a quadratic projection of the TRF onto a paraboloid characterized by the above Cartesian equation. The measurement model gathers many of these projections (onto different paraboloids) for various locations of the transducer elements  $\mathbf{p}_{ij}$  and can be analyzed in terms of the parabolic Radon transform described in Section A.2.4 of Appendix A. Unfortunately, an analytical inversion formula of such a transform does not exist in 3D except for very specific configurations.

**Parametric Equations - The Elegant Approach:** Associated with the Cartesian equation defined in (3.90), we can define a set of parametric equations in the new coordinate system as

$$\begin{cases} x_s(\alpha, \beta, \mathbf{p}_{ij}, \boldsymbol{\theta}, t) &= \alpha \\ y_s(\alpha, \beta, \mathbf{p}_{ij}, \boldsymbol{\theta}, t) &= \beta \\ z_s(\alpha, \beta, \mathbf{p}_{ij}, \boldsymbol{\theta}, t) &= \frac{\alpha^2 + \beta^2 - (p'_{ijz} - ct)^2}{2(p'_{ijz} - ct)} \end{cases}, \quad (3.91)$$

where the following condition holds for  $\alpha$  and  $\beta$ :

$$(\alpha, \beta) \in \mathbb{R}^2 \text{ such that } \operatorname{sgn}(p'_{ijz} - ct) \left( \alpha^2 + \beta^2 - (p'_{ijz} - ct)^2 \right) > 0.$$

The corresponding set of parametric equations in the original coordinate system is obtained by composition of the inverse rotation and translation operations, such that

$$\mathbf{r}(\alpha, \beta, \mathbf{p}_{ij}, \boldsymbol{\theta}, t) = \mathbf{T}_{-\mathbf{p}'_i} \mathbf{R}_{\theta_x} [x_s(\alpha, \beta, \mathbf{p}_{ij}, \boldsymbol{\theta}, t), y_s(\alpha, \beta, \mathbf{p}_{ij}, \boldsymbol{\theta}, t), z_s(\alpha, \beta, \mathbf{p}_{ij}, \boldsymbol{\theta}, t)]^\top,$$

from which we define the parameterized integral as follows:

$$G_{ij}\gamma = \iint_{[x_l, x_u] \times [y_l, y_u]} w'(\mathbf{p}_{ij}, \boldsymbol{\theta}, \mathbf{r}(\alpha, \beta, \mathbf{p}_{ij}, \boldsymbol{\theta}, \cdot), \cdot) \gamma(\mathbf{r}(\alpha, \beta, \mathbf{p}_{ij}, \boldsymbol{\theta}, \cdot)) d\alpha d\beta,$$

where  $x_l, x_u, y_l, y_u$  are lower and upper bounds for  $\alpha$  and  $\beta$ , respectively (obtained from the parametric equations), and  $w' = w \times \left\| \frac{\partial \mathbf{r}}{\partial \alpha} \wedge \frac{\partial \mathbf{r}}{\partial \beta} \right\|_2$ .

**Parametric Equations - The Brute Force Approach:** As for DW imaging, we can derive an alternative set of parametric equations, more convenient for discretization purpose, as follows

$$\begin{cases} x(\alpha, \beta, \mathbf{p}_{ij}, \boldsymbol{\theta}, t) = \alpha \\ y(\alpha, \beta, \mathbf{p}_{ij}, \boldsymbol{\theta}, t) = \beta \\ z(\alpha, \beta, \mathbf{p}_{ij}, \boldsymbol{\theta}, t) = g(\alpha, \beta, \mathbf{p}_{ij}, \boldsymbol{\theta}, t) \end{cases}, \quad (3.92)$$

where  $g$  is a lengthy function whose complete expression is detailed in Section B.2.1 of Appendix B.

### 3.6.2 Discretization of the Measurement Model in 3D

The discretization process is similar to the one described for DW imaging. We define the discrete measurement model as follows:

$$\mathbf{M} = \mathbf{H}\boldsymbol{\Gamma} = \mathbf{v}_{pe} * (\mathbf{G}\boldsymbol{\Gamma}) \in \mathbb{R}^{N_x^t \times N_y^t \times N_z^t \times N} \rightarrow \mathbf{M}_{ij} = (\mathbf{H}\boldsymbol{\Gamma})_{ij} = \mathbf{v}_{pe} * (\mathbf{G}_{ij}\boldsymbol{\Gamma}) \in \mathbb{R}^N, \quad (3.93)$$

where  $\mathbf{G}_{ij} : \mathbb{R}^{N_x \times N_y \times N_z} \rightarrow \mathbb{R}^N$  is the discretized projection operator associated with the transducer element located at  $\mathbf{p}_{ij}$ .

To perform the numerical approximation of the integral, we rely on the set of parametric equations introduced in the brute-force approach. We introduce the following quadrature nodes:

$$\begin{cases} \alpha_s = x_{min} + (s-1)\Delta_x \\ \beta_m = y_{min} + (m-1)\Delta_y \end{cases}, \quad (s, m) \in \{1, \dots, N_x\} \times \{1, \dots, N_y\},$$

where  $N_x, \Delta_x, N_y, \Delta_y$  are defined by the discretization of the medium, discussed in Section 3.3.2.

We express the discretized projection operator  $\mathbf{G}_{ij}$  as:

$$\mathbf{G}_{ij}\boldsymbol{\Gamma} = \Delta_x \Delta_y \sum_{s=1}^{N_x} \sum_{m=1}^{N_y} \mathbf{w}'_{\alpha_s, \beta_m} \circ \left( \mathbf{I}_{\alpha_s, \beta_m}^{ij} \boldsymbol{\Gamma}_{sm} \right), \quad (3.94)$$

where  $\mathbf{w}'_{\alpha_s, \beta_m} \in \mathbb{R}^N$  is defined element-wise by evaluating  $w'$  at time instants  $t_k$ ,  $k = 1, \dots, N$ , and  $\mathbf{I}_{\alpha_s, \beta_m}^{ij} : \mathbb{R}^{N_z} \rightarrow \mathbb{R}^N$  are 1D-interpolation operators over the axial dimension defined as

$$\mathbf{I}_{\alpha_s, \beta_m}^{ij} \boldsymbol{\Gamma}_{sm} \approx [\gamma(\mathbf{r}(\alpha_s, \beta_m, \mathbf{p}_{ij}, \boldsymbol{\theta}, 0)), \dots, \gamma(\mathbf{r}(\alpha_s, \beta_m, \mathbf{p}_{ij}, \boldsymbol{\theta}, T))]^\top.$$

**Matrix-free Evaluation of the Measurement Model:** Using the discretization introduced above, we can derive a matrix-free evaluation strategy of  $\mathbf{H}\boldsymbol{\Gamma}$  in exactly the same way as for DW imaging, described in Algorithm 1.

The overall computation complexity of  $\mathbf{H}\boldsymbol{\Gamma}$  is  $O(N_x^t N_y^t N_x N_y N)$  (See Section 3.5.2 for more details).

### 3.6.3 Continuous Measurement Model in 2D

In 2D imaging, we consider the configuration described in Figure 3.8, where the transducer elements are located at  $\mathbf{p}_i = [i\Delta_x^t, 0]^\top$ ,  $i = 1, \dots, N_x^t$ .

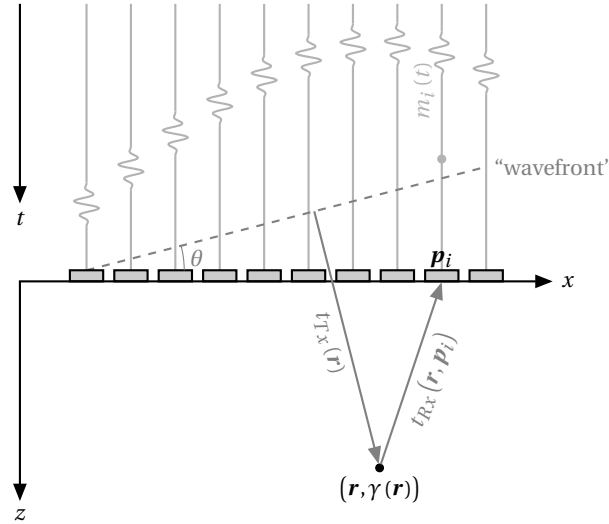


Fig. 3.8. Standard 2D plane-wave imaging configuration.

The measurements are defined as  $M \in L_2([0, T])^{N_x^t}$  and the measurement model,  $H : L_2(\Omega) \rightarrow L_2([0, T])^{N_x^t}$ , can be expressed element-wise as

$$(H\boldsymbol{\gamma})_i = v_{pe} \otimes_t (G_i \boldsymbol{\gamma}), \quad (3.95)$$

where  $G_i : L_2(\Omega) \rightarrow L_2([0, T])$  is defined by

$$G_i \gamma = \int_{\mathbf{r} \in \Omega} o_{pe}(\mathbf{r}, \mathbf{p}_i) \gamma(\mathbf{r}) \delta(\phi(\mathbf{r}, \mathbf{p}_i, \theta, \cdot)) d\mathbf{r}, \quad (3.96)$$

with the implicit function given by

$$\phi(\mathbf{r}, \mathbf{p}_i, \theta, t) = t - \frac{\|\mathbf{r} - \mathbf{p}_i\|_2 - x \sin(\theta) - z \cos(\theta)}{c}.$$

We define the one dimensional curve given by the 0-level set of the implicit function  $\phi$ , as the following interface

$$\partial S(\mathbf{p}_i, \theta, t) = \{\mathbf{r} \in \Omega \mid \|\mathbf{r} - \mathbf{p}_i\|_2 - x \sin(\theta) - z \cos(\theta) = ct\},$$

which can be used to rewrite (3.96) as

$$G_i \gamma = \int_{\mathbf{r} \in \partial S(\mathbf{p}_i, \theta, \cdot)} w(\mathbf{p}_i, \theta, \mathbf{r}, \cdot) \gamma(\mathbf{r}) dl(\mathbf{r}), \quad (3.97)$$

where  $dl(\mathbf{r})$  is the measure along the curve and  $w$  is given by

$$w(\mathbf{p}_i, \theta, \mathbf{r}, t) = \frac{o_{pe}(\mathbf{r}, \mathbf{p}_i)}{|\nabla_{\mathbf{r}} \phi(\mathbf{r}, \mathbf{p}_i, \theta, t)|}.$$

In order to derive the Cartesian equations associated with the interface, we introduce the rotation matrix of angle  $\theta$ ,  $\mathbf{R}_\theta$  such that  $\mathbf{r}' = \mathbf{R}_\theta \mathbf{r}$  and  $\mathbf{p}'_i = \mathbf{R}_\theta \mathbf{p}_i$ . In the rotated domain, the equation defining the interface can be expressed as follows

$$\begin{aligned} & \|\mathbf{r} - \mathbf{p}_i\|_2 - x \sin(\theta) - z \cos(\theta) = ct \\ \Leftrightarrow & \|\mathbf{r}' - \mathbf{p}'_i\|_2 - z' = ct \\ \Rightarrow & z' = \frac{1}{2ct} \left( (ct)^2 - (x' - \mathbf{p}_{i_x} \cos(\theta))^2 \right). \end{aligned} \quad (3.98)$$

Hence, (3.98) defines a parabola in the rotated coordinate domain with vertex  $[\mathbf{p}_{i_x} \cos(\theta), ct/2]^\top$ , focal point  $[\mathbf{p}_{i_x} \cos(\theta), 0]^\top$ , and directrix given by the equation  $z = -ct$ .

**Parametric Equations - The Elegant Approach:** We derive a set of parametric equations in the rotated domain based on the Cartesian Equation (3.98) as

$$\begin{cases} x'(\alpha, \mathbf{p}_i, \theta, t) = \alpha \\ z'(\alpha, \mathbf{p}_i, \theta, t) = \frac{1}{2ct} \left( (ct)^2 - (\alpha - \mathbf{p}_{i_x} \cos(\theta))^2 \right) \end{cases}, \quad (3.99)$$

defined for  $\alpha \in [\mathbf{p}_{i_x} \cos(\theta) - ct, \mathbf{p}_{i_x} \cos(\theta) + ct]$ . The set of parametric equations in the original domain is therefore defined by rotation of angle  $\theta$  of the above defined coordinates as

$$\begin{cases} x(\alpha, \mathbf{p}_i, \theta, t) = \alpha \cos(\theta) + z'(\alpha, \mathbf{p}_i, \theta, t) \sin(\theta) \\ z(\alpha, \mathbf{p}_i, \theta, t) = -\alpha \sin(\theta) + z'(\alpha, \mathbf{p}_i, \theta, t) \cos(\theta) \end{cases} \quad (3.100)$$

This allows us to perform the change of variable in (3.97) which can be written as

$$G_i \gamma = \int_{[\alpha_l, \alpha_u]} w'(\mathbf{p}_i, \theta, \mathbf{r}(\alpha, \mathbf{p}_i, \theta, \cdot), \cdot) \gamma(\mathbf{r}(\alpha, \mathbf{p}_i, \theta, \cdot)) d\alpha,$$

where  $\alpha_u = \mathbf{p}_{i_x} \cos(\theta) + ct$ ,  $\alpha_l = \mathbf{p}_{i_x} \cos(\theta) - ct$  and  $w' = w \times \sqrt{\left(\frac{\partial x}{\partial \alpha}\right)^2 + \left(\frac{\partial z}{\partial \alpha}\right)^2}$ .

**Parametric Equations - The Brute-force Approach:** To obtain the parametric formulation in the brute-force approach, many calculations are required and we rely on a formal calculus software (using Wolfram Mathematica for instance). We obtain a set of parametric equations of the following form:

$$\begin{cases} x(\alpha, \mathbf{p}_i, \theta, t) = \alpha \\ z(\alpha, \mathbf{p}_i, \theta, t) = g(\alpha, \mathbf{p}_i, \theta, t) \end{cases} \quad (3.101)$$

where  $\alpha \in [x_{min}, x_{max}]$  and  $g$  is detailed in Section B.2.2 of Appendix B.

### 3.6.4 Discretization of the Measurement Model in 2D

The discretization process is the same as for DW imaging and is briefly reminded below:

$$\mathbf{M} = \mathbf{H}\mathbf{\Gamma} = \mathbf{v}_{pe} * (\mathbf{G}\mathbf{\Gamma}) \in \mathbb{R}^{N_x^i \times N} \rightarrow \mathbf{M}_i = (\mathbf{H}\mathbf{\Gamma})_i = \mathbf{v}_{pe} * (\mathbf{G}_i \mathbf{\Gamma}) \in \mathbb{R}^N, \quad (3.102)$$

where  $\mathbf{G}_i : \mathbb{R}^{N_x \times N_z} \rightarrow \mathbb{R}^N$  is the discretized projection operator associated with the  $i$ -th transducer element, obtained by discretization of the continuous operator  $G_i$ .

We rely on the set of parametric equations introduced in the brute-force approach. We introduce the following set of uniformly spaced quadrature nodes:

$$\alpha_s = x_{min} + (s-1) \Delta_x, \quad s \in \{1, \dots, N_x\},$$

where  $N_x$  and  $\Delta_x$  are defined by the discretization of the medium, discussed in Section 3.3.2. Thus, we can express the discretized projection operator  $\mathbf{G}_i$  as:

$$\mathbf{G}_i \mathbf{\Gamma} = \Delta_x \sum_{s=1}^{N_x} \mathbf{w}'_{\alpha_s} \circ \left( \mathbf{I}_{\alpha_s}^i \mathbf{\Gamma}_s \right), \quad (3.103)$$

where  $\mathbf{w}'_{\alpha_s} \in \mathbb{R}^N$  is defined element-wise by evaluating  $w'$  at time instants  $t_k$ ,  $k = 1, \dots, N$ , and  $\mathbf{I}_{\alpha_s}^i : \mathbb{R}^{N_z} \rightarrow \mathbb{R}^N$  are 1D-interpolation operators over the axial dimension.

**Matrix-free Evaluation of the Measurement Model** Using the discretization introduced above, we can derive a matrix-free evaluation strategy of  $\mathbf{H}\mathbf{\Gamma}$  in exactly the same way as

### 3.7. Adjoint of the Measurement Model: Revisiting the Delay-and-sum Algorithm from a Functional Perspective

---

for DW imaging, described in Algorithm 2. The overall computation complexity of  $H\Gamma$  is  $O(N_x N_x^t N)$  (See Section 3.5.4 for more details).

### 3.7 Adjoint of the Measurement Model: Revisiting the Delay-and-sum Algorithm from a Functional Perspective

In this section, we derive the adjoint operator of the measurement model  $H$  corresponding to the different configurations described in previous sections. We also show that the formulation of the adjoint allows us to provide a novel understanding of the DAS algorithm.

The motivations for the derivation of the adjoint operator are twofold:

1. In most restoration methods, the computation of the adjoint operator  $H^*$  is required at some point. For instance, restoration approaches that require to solve a convex optimization problem need to compute the gradient of a data fidelity term, usually expressed using the squared  $\ell_2$ -norm. Such a gradient is therefore defined as  $H^* (H\Gamma - M)$ .
2. In tomographic image reconstruction methods involving the linear Radon transform (LRT), the adjoint operator is usually called backprojector since it takes projections along the different lines and “smears” them to recreate an image. The backprojector is used in the well-known backprojection algorithm, which is a very popular inversion method of the LRT, as described in Appendix B.

#### 3.7.1 Derivation of the Adjoint of the Measurement Model

In this section, the derivations are limited to the 3D case. But the formulations for the 2D case can be easily deduced using a similar reasoning.

**Adjoint Operator at the Continuous Level:** Since the measurement model  $H$  is linear, the adjoint operator  $H^* : L_2([0, T])^{N_x^t \times N_y^t} \rightarrow L_2(\Omega)$  is defined by

$$\langle H\gamma, m \rangle_{L_2([0, T])^{N_x^t \times N_y^t}} = \langle \gamma, H^* m \rangle_{L_2(\Omega)}, \quad (3.104)$$

### Chapter 3. Pulse-echo Ultrasound Imaging Seen as an Inverse Problem

where  $u(t) = v_{pe}(-t)$  is the matched filter of the pulse-echo waveform. Thus, it can be derived from the definition of the measurement model as follows

$$\begin{aligned}
\langle H\gamma, m \rangle &= \sum_{i=1}^{N_x^t} \sum_{j=1}^{N_y^t} \int_0^T (H\gamma)_{ij}(t) m_{ij}(t) dt \\
&= \sum_{i=1}^{N_x^t} \sum_{j=1}^{N_y^t} \int_0^T \int_{\mathbf{r} \in \Omega} o_{pe}(\mathbf{r}, \mathbf{p}_{ij}) \gamma(\mathbf{r}) v_{pe}(t - t_{Tx}(\mathbf{r}) - t_{Rx}(\mathbf{r}, \mathbf{p}_{ij})) m_{ij}(t) dt d\mathbf{r} \\
&= \int_{\mathbf{r} \in \Omega} \sum_{i=1}^{N_x^t} \sum_{j=1}^{N_y^t} o_{pe}(\mathbf{r}, \mathbf{p}_{ij}) \gamma(\mathbf{r}) \int_0^T v_{pe}(t - t_{Tx}(\mathbf{r}) - t_{Rx}(\mathbf{r}, \mathbf{p}_{ij})) m_{ij}(t) dt d\mathbf{r} \\
&\stackrel{u(t)=v_{pe}(-t)}{=} \int_{\mathbf{r} \in \Omega} \gamma(\mathbf{r}) \sum_{i=1}^{N_x^t} \sum_{j=1}^{N_y^t} o_{pe}(\mathbf{r}, \mathbf{p}_{ij}) (u \otimes_t m_{ij})(t_{Tx}(\mathbf{r}) + t_{Rx}(\mathbf{r}, \mathbf{p}_{ij})) d\mathbf{r} \\
&= \langle \gamma, H^* m \rangle_{L_2(\Omega)}.
\end{aligned}$$

Hence, the adjoint operator is expressed at the continuous level as

$$H^* m = \sum_{i=1}^{N_x^t} \sum_{j=1}^{N_y^t} o_{pe}(\cdot, \mathbf{p}_{ij}) (u \otimes_t m_{ij})(t_{Tx}(\cdot) + t_{Rx}(\cdot, \mathbf{p}_{ij})). \quad (3.105)$$

The structure of the adjoint operator (3.105) is very similar to the one of the backprojector described for the LRT. In a first step, the element-raw data are convolved with the matched filter of the pulse echo-waveform, i.e. the element-raw data are correlated with the pulse-echo waveform. Such a technique is a well established method used to increase the SNR in radar and sonar. In US imaging, it is used for pulse compression [106].

In a second step, the samples of the filtered element-raw data corresponding to the round-trip TOFs for the field point  $\mathbf{r} \in \Omega$  are summed up. This smears the information contained in the various elliptical or parabolic projections in order to recreate an image, in a similar way to the backprojector in LRT.

**Adjoint Operator at the Discrete Level:** The discrete adjoint operator  $H^* : \mathbb{R}^{N_x^t \times N_y^t \times N} \rightarrow \mathbb{R}^{N_x \times N_y \times N_z}$  can be directly expressed from (3.105) as

$$H^* M = \sum_{i=1}^{N_x^t} \sum_{j=1}^{N_y^t} \mathbf{O}_{ij} \circ (\mathbf{I}_{ij} \tilde{M}_{ij}), \quad (3.106)$$

where  $\mathbf{O}_{ij} \in \mathbb{R}^{N_x \times N_y \times N_z}$  is defined by the value of the pulse-echo element directivity for any point of the medium,  $\tilde{M} \in \mathbb{R}^{N_x^t \times N_y^t \times N}$  is defined by

$$\tilde{M}_{ij} = (\mathbf{u} * M_{ij}),$$

### 3.7. Adjoint of the Measurement Model: Revisiting the Delay-and-sum Algorithm from a Functional Perspective

and  $\mathbf{I}_{ij} : \mathbb{R}^N \rightarrow \mathbb{R}^{N_x \times N_y \times N_z}$  performs many 1D interpolations of the element-raw data along the time-dimension defined by

$$(\mathbf{I}_{ij} \tilde{\mathbf{M}}_{ij})_{lmn} \approx (u \otimes m_{ij}) (t_{Tx}([x_l, y_m, z_n]^\top) + t_{Rx}([x_l, y_m, z_n]^\top, \mathbf{p}_{ij})).$$

**Matrix-free Evaluation of the Adjoint of the Measurement Model:** Using the formulation in the discrete domain, we derive a matrix-free evaluation of  $\mathbf{H}^*$ , detailed in Algorithm 3 below, very similar to the DAS algorithm.

---

#### Algorithm 3 Matrix-free Computation of $\mathbf{H}^* \mathbf{M}$ for UFUS Imaging in 3D

---

**Require:**  $\{\mathbf{p}_{ij}\}_{i,j=1}^{N_x, N_y}$ ,  $\{\alpha_s\}_{s=1}^{N_x}$ ,  $\{\beta_m\}_{m=1}^{N_y}$ ,  $\{z_n\}_{n=1}^{N_z}$ ,  $\mathbf{M}$ ,  $\mathbf{u}$   
**initialization:**  $\Gamma = 0$   
**for**  $(i, j) \in \{1, \dots, N_x\} \times \{1, \dots, N_y\}$  **do**  
     $\tilde{\mathbf{M}}_{ij} = \mathbf{u} * \mathbf{M}_{ij}$   
**end for**  
 $\Gamma = \sum_{i=1}^{N_x} \sum_{j=1}^{N_y} \mathbf{O}_{ij} \circ (\mathbf{I}_{ij} \tilde{\mathbf{M}}_{ij})$   
**return**  $\Gamma$

---

#### 3.7.2 A Functional Interpretation of the Delay-and-sum Algorithm

In the same spirit as the measurement model, we can express the DAS algorithm at the continuous level in terms of a linear operator  $D : L_2([0, T])^{N_t} \rightarrow L_2(\Omega)$ , defined by

$$Dm = \sum_{i=1}^{N_x} \sum_{j=1}^{N_y} a(\mathbf{r}, \mathbf{p}_{ij}) m_{ij} (t_{Tx}(\cdot) + t_{Rx}(\cdot, \mathbf{p}_{ij})), \quad (3.107)$$

where  $a(\mathbf{r}, \mathbf{p}_{ij})$  are the apodization coefficients.

Hence, we immediately notice, by comparison with (3.105), that the DAS operator is an approximate adjoint operator under the following assumptions:

- The pulse-echo waveform is a Dirac:  $v_{pe}(t) = \delta(t)$ ;
- the term  $o_{pe}$  is replaced by the apodization coefficients.

The main reason for such assumptions is that they lead to better image quality. Indeed, in standard imaging configurations, convolving with the matched filter results in blurred images (due to the fact that very short pulses are transmitted), and the element-directivity contains a  $1/\|\mathbf{r} - \mathbf{p}_i\|_2$  factor that over-attenuates deepest regions.

Additionally, such a view legitimates the use of the DAS algorithm for image reconstruction since exploiting adjoint operators as an approximate inverse is common in image reconstruction. It can be seen as a least-squares solution of the inverse problem when the Gram operator associated with the linear operator is the identity.

### Chapter 3. Pulse-echo Ultrasound Imaging Seen as an Inverse Problem

---

Another benefit of defining the DAS as a linear operator is that we can easily derive its adjoint,  $D^* : L_2(\Omega) \rightarrow L_2([0, T])^{N_x \times N_y}$ , defined element-wise by

$$(D^* \gamma)_{ij} = \int_{\mathbf{r} \in \Omega} a(\mathbf{r}, \mathbf{p}_{ij}) \gamma(\mathbf{r}) \delta(\cdot - t_{Tx}(\mathbf{r}) - t_{Rx}(\mathbf{r}, \mathbf{p}_{ij})) d\mathbf{r}, \quad (3.108)$$

which is very similar to the measurement model  $H$ .

## 4 USSR: The UltraSound Sparse Regularization Framework

Nothing in the world takes place without optimization, and there is no doubt that all aspects of the world that have a rational basis can be explained by optimization methods.

---

*De Curvis Elasticis*  
Leonhard Euler

In this chapter, we introduce USSR: The **UltraSound Sparse Regularization** framework which exploits the measurement model introduced in Chapter 3 inside a variational regularization framework with different applications: enhanced image reconstruction, compressed beamforming and image restoration. The idea is to exploit the matrix-free formulations of the proposed model to explore alternative reconstruction methods based on iterative approaches. After a brief reminder on variational methods and convex algorithms for inverse problem in imaging, we present a sparsely-regularized beamforming approach where sparsity in a wavelet frame is used as a prior in our inverse problem. We show that the technique leads to a significantly higher image quality than the standard DAS algorithm and performs high-quality imaging with very few insonifications. Motivated by these results, we extend the proposed approach to compressed beamforming, where the idea is to complicate the image reconstruction problem by reducing the amount of data per insonification. Hence, we compose the measurement model with an undersampling operator and discuss different undersampling strategies based on CS principles. On the reconstruction side, we rely on the same sparsity prior and the same algorithm as for sparsely-regularized beamforming. In a fourth section, we propose a model of non-stationary blur in US imaging, based on the composition of the measurement model and the DAS operator. We show that such a composition coupled with the formulations described in Chapter 3 permit to significantly decrease the computational complexity associated with the evaluation of the non-stationary blur, from quadratic to linear with respect to the size of the grid. We use the proposed model in a MAP estimation algorithm where a GGD prior is used for the TRF and demonstrate that it outperforms existing image restoration methods in US imaging.

## 4.1 A Brief Overview of Variational Regularization in Imaging

### 4.1.1 Variational Regularization for Imaging Problems

Many imaging problems aim to recover an image or a set of parameters from partial or indirect measurements, e.g. Radon or Fourier measurements. Such problems are popular in various areas of science and engineering e.g. medical imaging, astronomical imaging and geology. Mathematically, an inverse problem can be formulated as reconstructing a signal  $x \in X$  from measurements  $y \in Y$ , where

$$y = H(x) + e. \quad (4.1)$$

In the above equation,  $X$  and  $Y$  are topological vector spaces, e.g. Banach or Hilbert spaces,  $H: X \rightarrow Y$  is the forward operator, sometimes called “measurement model”, and  $e \in Y$  accounts for additive measurement noise. Given (4.1), the imaging problem can be expressed as follows

$$\text{Estimate } x \text{ from } y \text{ measured by (4.1).} \quad (4.2)$$

A popular way to solve (4.2) is by minimizing a data-fidelity term,  $J: X \times Y \rightarrow \mathbb{R}_+$ , that measures the discrepancy between the reconstruction and the measured data. Mathematically, we define the following minimization problem

$$\min_{x \in X} J(H(x), y), \quad (4.3)$$

which can be interpreted as a maximum likelihood estimation problem, where  $J$  represents either the negative likelihood or log-likelihood of a probability distribution.

A common pitfall of this approach is over-fitting in the sense that a small change of the data may result in a significant change in the solution of (4.3). This occurs in the case where the operator  $H$  is ill-posed or ill-conditioned.

A popular technique for preventing the reconstruction against over-fitting is variational regularization [107, 108] where an additional regularization term  $R: X \rightarrow \mathbb{R}_+$ , which encodes some prior knowledge on the solution, is introduced in the minimization problem. Formally, the variational regularization problem is defined as

$$\min_{x \in X} J(H(x), y) + \lambda R(x), \quad (4.4)$$

where  $\lambda \in \mathbb{R}_+$  is the regularization parameter which controls the trade-off between the data-discrepancy term and the regularization term. Typical examples of regularization terms are the  $\ell_2$ -norm with the so-called Tikhonov regularization (ridge regression in statistics) [108], the  $\ell_1$ -norm with the famous least-absolute shrinkage and selection operator (LASSO) [109], and total variation (TV) [110].

Depending on the properties of the functions  $R$ ,  $J$  and  $H$ , different optimization frameworks can be leveraged to solve (4.4). In this chapter, we restrict our attention to a very limited subset of such techniques. More precisely, we consider  $H$  to be a linear operator acting between two

## 4.1. A Brief Overview of Variational Regularization in Imaging

---

Hilbert spaces of real (or complex) vectors or matrices such that we express (4.1) as

$$\mathbf{y} = \mathbf{H}\mathbf{x} + \mathbf{e}, \quad (4.5)$$

where  $\mathbf{y} \in \mathbb{K}^m$ ,  $\mathbf{x} \in \mathbb{K}^n$ ,  $\mathbf{H} : \mathbb{K}^n \rightarrow \mathbb{K}^m$  and  $\mathbf{e} \in \mathbb{K}^m$ . We consider the squared  $\ell_2$ -norm for the data-fidelity term and focus on convex regularization terms.

Hence, we are interested in the following optimization problem

$$\min_{\mathbf{x} \in \mathbb{K}^n} \frac{1}{2} \|\mathbf{H}\mathbf{x} - \mathbf{y}\|_2^2 + \lambda R(\mathbf{x}). \quad (4.6)$$

### 4.1.2 Proximal Gradient Methods for Convex Regularization

Convex problems have been extensively studied in the literature and many techniques have been developed to solve them [111]. In this work, we focus on a particular type of techniques, known as proximal gradient methods, that has recently gained substantial interest in the signal processing community [112, 113].

Proximal gradient methods exploit the concept of proximity operator, introduced by Moreau [114] and reminded in Definition 4, which extends the notion of projection onto closed convex sets to convex functions.

**Definition 4** (Proximity operator, Definition 2.1 of [113]). *Let  $f$  be a lower-semicontinuous function of  $\mathbb{R}^n$ . For every  $\mathbf{x} \in \mathbb{R}^n$ , the minimization problem*

$$\min_{\mathbf{z} \in \mathbb{R}^n} f(\mathbf{z}) + \frac{1}{2} \|\mathbf{x} - \mathbf{z}\|_2^2, \quad (4.7)$$

*admits a unique solution, which is denoted by  $\text{prox}_f(\mathbf{x})$ . The operator  $\text{prox}_f : \mathbb{R}^n \rightarrow \mathbb{R}^n$  therefore defined is the proximity operator of  $f$ .*

Proximity operators enjoy many interesting properties that are described in Table 2 of [113]. From a Bayesian perspective, they can be interpreted as a particular form of denoising under additive Gaussian noise with a prior whose density is given by  $\exp(-f)$  [115].

Proximal gradient algorithms exploit the fact that (4.6) admits at least a unique solution expressed as the following fixed point iteration [116]

$$\mathbf{x} = \text{prox}_{\lambda\tau R}(\mathbf{x} - \tau \mathbf{H}^*(\mathbf{H}\mathbf{x} - \mathbf{y})), \quad (4.8)$$

where  $\tau \in \mathbb{R}_+$  is a step size.

Hence, proximal gradient algorithms suggest to perform the following iteration

$$\mathbf{x}^{(i+1)} = \text{prox}_{\lambda\tau^{(i)} R}(\mathbf{x}^{(i)} - \tau^{(i)} \mathbf{H}^*(\mathbf{H}\mathbf{x}^{(i)} - \mathbf{y})), \quad (4.9)$$

where the step sizes  $(\tau^{(i)})_{i \in \mathbb{N}}$ , are chosen in a specific bounded interval.

As the proximity operator is the extension of the concept of projection, one may see proximal gradient algorithms as an extension of the well-known projected gradient method, where the projection step is replaced by a proximal step [117].

A very popular proximal gradient method is the fast iterative shrinkage thresholding algorithm (FISTA), introduced by Beck and Teboulle [118], which is an accelerated version of (4.9) offering a quadratic rate of convergence of the objective function. The method is detailed in Algorithm (4).

---

**Algorithm 4** Fast iterative shrinkage thresholding algorithm [118].

---

**Require:**  $H, \mathbf{x}^{(0)}, R, t^{(0)} = 1, L \geq \lambda_{\max}(\mathbf{H}^* \mathbf{H})$

**initialization:**  $i = 1, \mathbf{z}^{(0)} = \mathbf{x}^{(0)}$

**repeat**

$$\mathbf{x}^{(i+1)} = \text{prox}_{\frac{1}{L}R} \left( \mathbf{z}^{(i)} - \frac{1}{L} \mathbf{H}^* (\mathbf{H} \mathbf{z}^{(i)} - \mathbf{y}) \right)$$

$$t^{(i+1)} = \frac{1 + \sqrt{4t^{(i)2} + 1}}{2}$$

$$\mu^{(i)} = 1 + \frac{t^{(i)} - 1}{t^{(i+1)}}$$

$$\mathbf{z}^{(i+1)} = \mathbf{x}^{(i)} + \mu^{(i)} (\mathbf{x}^{(i+1)} - \mathbf{x}^{(i)})$$

$$n \leftarrow n + 1$$

**until** a stopping criterion is met

---

In the remainder of the chapter, we use FISTA everytime we need to use a convex optimization algorithm. We also summarize several proximity operators associated with the different regularization terms used along the chapter in Appendix C.

## 4.2 Sparsely Regularized Beamforming for Enhanced Ultrafast Ultrasound Imaging

### 4.2.1 Motivations and Existing Approaches

Standard image reconstruction in UFUS imaging is performed via the DAS algorithm which can be seen as a backprojection of the measurement model described in Chapter 3 under several simplifying assumptions (See Section 3.7.2 for more details.).

Images reconstructed with the DAS algorithm suffer from a degraded image quality, i.e. reduced contrast due to side lobes and grating lobes and low resolution due to limited aperture of the probe and finite duration of the acoustical pulse. To obtain a more decent image quality, coherent compounding is required which decreases the temporal resolution.

Alternative approaches to DAS based on regularization, where imaging is performed by solving problems of the form of (4.6), have been explored in the literature. Popular techniques exploit sparse regularization, where the regularization term  $R$  is a sparsity promoting term in a transform domain, expressed as

$$R(\mathbf{x}) = \|\Psi^* \mathbf{x}\|_1, \tag{4.10}$$

where  $\Psi : \mathbb{K}^d \rightarrow \mathbb{K}^n$ ,  $d \geq n$ , is a general transform, e.g. a basis, a frame or an overcomplete dictionary.

The objective of such methods is to reduce the number of insonifications necessary to obtain high-quality images. Schiffner and Schmitz [74] have suggested to exploit sparsity in the image domain itself and proposed a regularization approach suitable for media composed of few

## 4.2. Sparsely Regularized Beamforming for Enhanced Ultrafast Ultrasound Imaging

strong reflectors. Such a regularization has also been used by David *et al.* [78] and Szasz *et al.* [119]. However, promoting sparsity in the image domain does not preserve speckle, which is of crucial importance for some applications in US imaging. To address this issue, Szasz *et al.* have explored Tikhonov [119] and elastic-net regularization [120]. Alternatively, David *et al.* [79] and Zhang *et al.* [77] have proposed to exploit sparsity through the wavelet transform, well-known to preserve textural information in natural images. Recently, Ozkan *et al.* [80] have proposed a more sophisticated regularization term promoting smoothness both in the frequency and image domains.

All the above mentioned approaches lead to significantly improved image quality with impressive reduction of the side-lobe level. However, they suffer from major drawbacks that severely limit their appeal for potential use in realistic scenario. The main issue is their computational complexity, usually translated into storage requirements of the matrix representation of the forward operators, which leads to reconstruction methods that are not scalable to 3D imaging and not compatible with real-time imaging.

In addition, sparse regularization approaches require a very fine tuning of the regularization parameter.

### 4.2.2 Sparse Regularization for Enhanced Ultrasound Image Reconstruction

We propose a novel sparsely regularized US beamforming approach with two main innovations:

- We rely on the matrix-free formulations of the forward and adjoint operators introduced in Chapter 3 to propose an approach with drastically reduced memory footprint and computation times compared to existing methods.
- We exploit sparsity in an overcomplete transform composed of concatenation of wavelet bases which allows us to better preserve textural information than existing techniques.

Regarding the measurement model, we consider the 2D imaging setting described in Sections 3.5 and 3.6, where  $N_x^t$  transducer elements arranged in a linear- or phased-array probe, characterized by a pulse-echo waveform  $v_{pe}$ , with inter-element spacing  $p$ . We assume that we record backscattered echoes in the time interval  $[0, T]$ , with sampling frequency  $f_s$ , leading to measurements  $\mathbf{M} \in \mathbb{R}^{N_x^t \times N}$ , where  $N = \lfloor T f_s \rfloor$ . We also consider the discrete TRF  $\mathbf{\Gamma} \in \mathbb{R}^{N_x \times N_z}$  such that we define the following inverse problem

$$\mathbf{M} = \mathbf{H}\mathbf{\Gamma} = \mathbf{v}_{pe} * (\mathbf{G}\mathbf{\Gamma}), \quad (4.11)$$

where the different quantities are defined in Sections 3.5 and 3.6 for PW and DW imaging, respectively.

Since it is more suitable to work with vectors rather than matrices in variational regularization, we reformulate (4.11) by considering flattened measurements  $\mathbf{m} \in \mathbb{R}^{N N_x^t}$ , obtained by concatenating the echo signals to form a single vector, as well as flattened TRF  $\boldsymbol{\gamma} \in \mathbb{R}^{N_x N_z}$  such that

$$\mathbf{m} = \mathbf{H}\boldsymbol{\gamma}, \quad (4.12)$$

where, with a slight abuse of notation,  $\mathbf{H} : \mathbb{R}^{N_x N_z} \rightarrow \mathbb{R}^{N N_x^t}$  designates the flattened measurement model.

In the remainder, we perform the following assumptions on the measurement model:

- We compute the element directivity based on the paper of Selfridge *et al.* [121];
- we rely on spline interpolation for all the interpolations involved in the evaluation of the forward and adjoint operators;
- we consider that  $v_{pe}(t) = \delta(t)$  in the measurement model since we are interested in enhanced beamforming.

Inspired by previous works achieved at LTS 5 on sparsity averaging with applications to compressive imaging [122] and radio-interferometric imaging [123], the proposed sparsifying transform, denoted as sparsity averaging (SARA), is composed of a concatenation of 8 Daubechies wavelet transforms with different mother wavelets. Mathematically, the operator is written as:

$$\Psi = \frac{1}{\sqrt{q}} [\Psi_1, \dots, \Psi_q], \quad (4.13)$$

where  $q$  is equal to 8 and  $\Psi_i$  denotes the  $i$ -th Daubechies wavelet transform. The choice of such a model is rather empirical and mainly justified by its superiority against simpler wavelet models in computational imaging [122].

Hence, the problem of interest is expressed as

$$\min_{\gamma \in \mathbb{R}^{N_x N_z}} \frac{1}{2} \|\mathbf{H}\gamma - \mathbf{m}\|_2^2 + \lambda \|\Psi^* \gamma\|_1, \quad (4.14)$$

and is solved using FISTA in which the proximal operator associated with the  $\ell_1$ -norm in the SARA model is detailed in Appendix C.

### 4.2.3 Experiments and Results

In order to evaluate the proposed approach, we perform the following experiments:

1. **Plane-wave imaging:** The different experiments are performed with the ATL-L12-5 50mm probe whose settings are given in Table 4.1. For each experiment, a sequence of 15 PWs (5 MHz, 1-cycle, tri-state waveforms) is transmitted with steering angles uniformly distributed between  $-7.5^\circ$  and  $7.5^\circ$ . No apodization is used on transmit.
  - **Numerical simulations:** The system described above is simulated using the Field II software [89]. Two phantoms are considered:
    - *Point-reflector phantom:* It consists of bright reflectors laterally positioned at 5 mm and spaced in depth by 10 mm. At depths of 10 mm and 30 mm, bright reflectors are distributed laterally with a step of 5 mm.
    - *Anechoic-inclusion phantom:* It consists of an anechoic inclusion of 8 mm diameter, centered at a depth of 40 mm, embedded in a medium with a high

## 4.2. Sparsely Regularized Beamforming for Enhanced Ultrafast Ultrasound Imaging

density of scatterers with random positions and amplitudes (20 scatterers per resolution cell).

- **Plane-wave imaging challenge in medical ultrasound (PICMUS) dataset:** The methods are also evaluated on the standardized PICMUS dataset [124]. More precisely, the simulated dataset as well as the *in vivo* carotids are used. The settings corresponding to these experiments are available on the PICMUS website<sup>1</sup>.
- ***In vivo* experiments:** Two *in vivo* carotid images were acquired using a Verasonics Vantage™ scanner (Redmond, WA, USA) with the ATL L12-5 50 mm probe whose settings are given in Table 4.1.

2. **Diverging-wave imaging:** The different experiments are performed with a simulated ATL P4-2V probe whose settings are given in Table 4.1. For each experiment, a sequence of 15 DWs (2.5 MHz, 1-cycle, tri-state waveforms) is transmitted with virtual point sources located  $-2.9$  mm behind the probe and uniformly distributed between  $-5.9$  mm and  $5.9$  mm in the lateral dimension. No apodization is used on transmit.

- **Numerical simulations:** We exploit the numerical simulation of the following phantoms:
  - *Point-reflector phantom:* It consists of bright reflectors centered in the field and spaced in depth every 20 mm. At 50 mm depth, bright reflectors are laterally distributed with a step of 20 mm.
  - *Anechoic-inclusion phantom:* The anechoic-inclusion phantom is the same as for the PW experiment.

TABLE 4.1  
CHARACTERISTICS OF THE ATL L12-5 50 MM AND P4-2V PROBES

	L12-5 50mm	P4-2v
Number of elements	128	64
Center frequency	7.8 MHz	2.5 MHz
Wavelength	0.198 mm	0.62 mm
Sampling frequency	31.2 MHz	15.6 MHz
Pitch	0.195 mm	0.32 mm
Kerf	0.05 mm	0.05 mm

The proposed image reconstruction method is evaluated against the DAS algorithm as well as the best state-of-the-art image reconstruction algorithms on the PICMUS dataset. Once the RF image is reconstructed using any of the above mentioned methods, we extract the envelope with the Hilbert transform and perform normalization and log-compression over a range of 40 dB to get the B-mode image.

The DAS algorithm used in this study is the one described by Montaldo *et al.* [28] for PW imaging and by Papadacci *et al.* [29] for DW imaging. It is used with a linear interpolation for delay calculations and with an apodization that accounts for the element directivity according

<sup>1</sup>[https://www.creatis.insa-lyon.fr/Challenge/IEEE\\_IUS\\_2016/home](https://www.creatis.insa-lyon.fr/Challenge/IEEE_IUS_2016/home)

to Selfridge *et al.* [121]. For the iterative approaches, the hyper-parameters are empirically tuned depending on the image. The stopping criterion is set to be the maximum number of iterations.

**Contrast Study on the Anechoic-inclusion Phantom:** First, we evaluate the benefits of the proposed method on the image contrast, which is related to the side-lobe level in the final image. To quantify the contrast, we rely on the CNR defined in Section 2.2.3 and computed on the anechoic inclusion phantom.

Figure 4.1 displays the CNR values for PW and DW imaging, respectively, with 1 insonification for the proposed approach and 1 to 15 insonifications for the DAS algorithm.

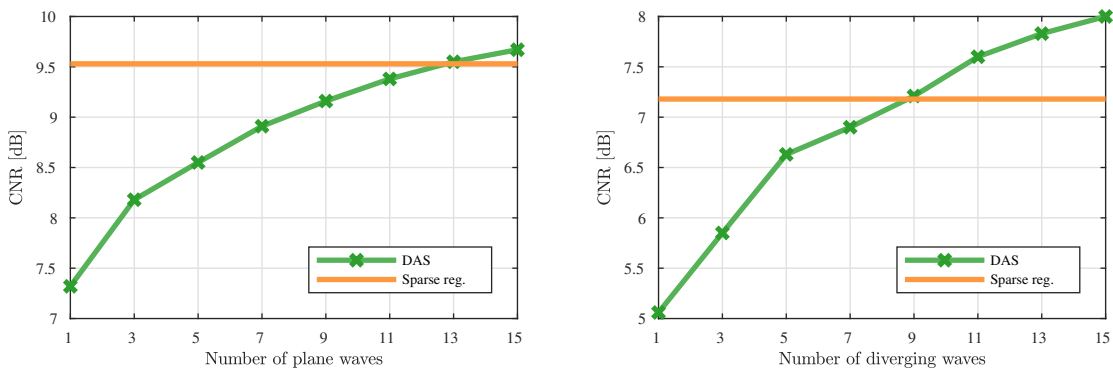


Fig. 4.1. Contrast-to-noise ratio [dB] calculated on the simulated anechoic-inclusion phantom as a function of the number of insonifications for (left)-plane wave imaging and (right)-diverging wave imaging. The orange line corresponds to the contrast-to-noise ratio of the sparsely regularized beamforming with 1 insonification and the green line is the contrast-to-noise ratio obtained with the delay-and-sum algorithm for 1 to 15 insonifications.

It can be noticed that, with only 1 insonification, the proposed method leads to a contrast similar to the DAS algorithm with more than 9 insonifications, and performs significantly better than the DAS algorithm for 1 to 9 insonifications.

Figure 4.2 displays the log-compressed B-mode images of the anechoic-inclusion phantom reconstructed with the DAS algorithm and using the proposed approach, for a single insonification and for PW and DW imaging, respectively.

We observe that the noise present inside the anechoic area, due to the side lobes of the PSF, has been suppressed by the regularization. We also notice that the speckle is relatively well reconstructed with the proposed approach even though its density is slightly decreased, resulting in a darkening of the deepest part of the image. This effect is due to the fact that part of the speckle is not well preserved by the SARA model, therefore considered as noise and suppressed during the image reconstruction process [125].

**Reconstruction of the Point-reflector Phantom:** The point-reflector phantom is used to assess the quality of the proposed approach in the particular case where only few strong reflectors are present. A typical application is harmonic imaging of microbubbles in low-concentrations where the individual responses of the sparse microbubbles are visible. The

## 4.2. Sparsely Regularized Beamforming for Enhanced Ultrafast Ultrasound Imaging

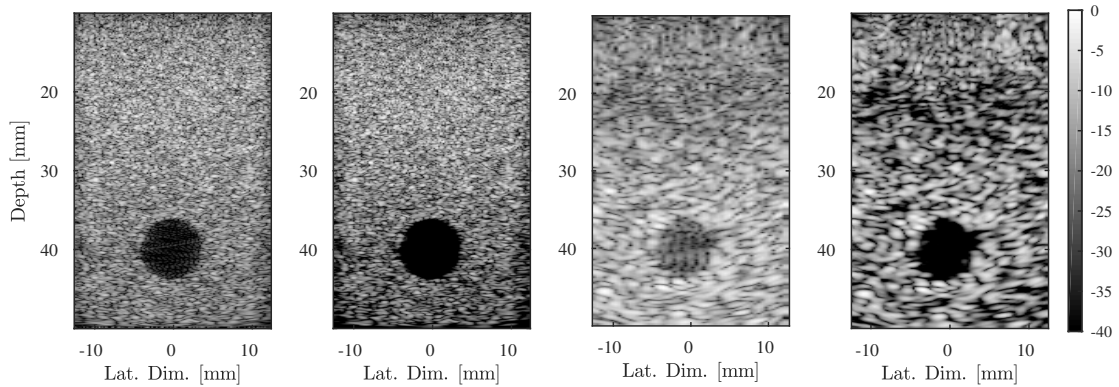


Fig. 4.2. From left to right. Log-compressed B-mode images of the anechoic-inclusion phantom reconstructed with the delay-and-sum algorithm for 1 plane-wave insonification, the sparsely regularized beamforming for 1 plane-wave insonification, the delay-and-sum algorithm for 1 diverging-wave insonification, the sparsely regularized beamforming for 1 diverging-wave insonification.

quality is evaluated on the resolution, calculated as the FWHM of the PSF, defined in Section 2.2.2.

For PW imaging, the proposed approach leads to lateral and axial resolutions of 0.10 mm for every point with 1 PW insonification, while the DAS algorithm gives lateral and axial resolutions of 0.20 mm for both points, constant for compounding experiments with 1 to 11 PWs insonifications. The increase is more pronounced in DW imaging where the proposed approach leads to lateral resolutions of 0.50 mm and 0.90 mm and axial resolutions of 0.50 mm for the points located at 30 mm and 50 mm, while the DAS algorithm with 11 DW insonifications exhibits lateral resolutions of 1.40 mm and 2.80 mm and axial resolutions of 0.50 mm.

The increase in resolution can be visually assessed on Figure 4.3, which displays the log-compressed B-mode images of the point-reflector phantom reconstructed with the DAS algorithm and with the proposed approach, for both PW and DW imaging.

**Reconstruction of the *In vivo* Carotids:** The proposed method is evaluated on the *in vivo* carotid images. Due to the lack of a ground truth image, the evaluation of the image quality is limited to visual assessment. Figure 4.4 displays B-mode images for two different carotid acquisitions, reconstructed with the proposed method and using the DAS algorithm with 1 PW insonification.

We notice that the proposed method leads to a significant reduction of the sidelobe artefacts close to regions with high echogenicity, while preserving important structures of the images, e.g. the anechoic artery and the tissue area. This illustrates the great potential of sparse regularization for reducing the number of insonifications required to perform high-quality imaging.

**Reconstruction of the PICMUS Dataset:** So far, the proposed approach has been compared to the DAS algorithm. It is now well established that the DAS algorithm is not the highest quality beamforming and it could be interesting to compare the technique against the best

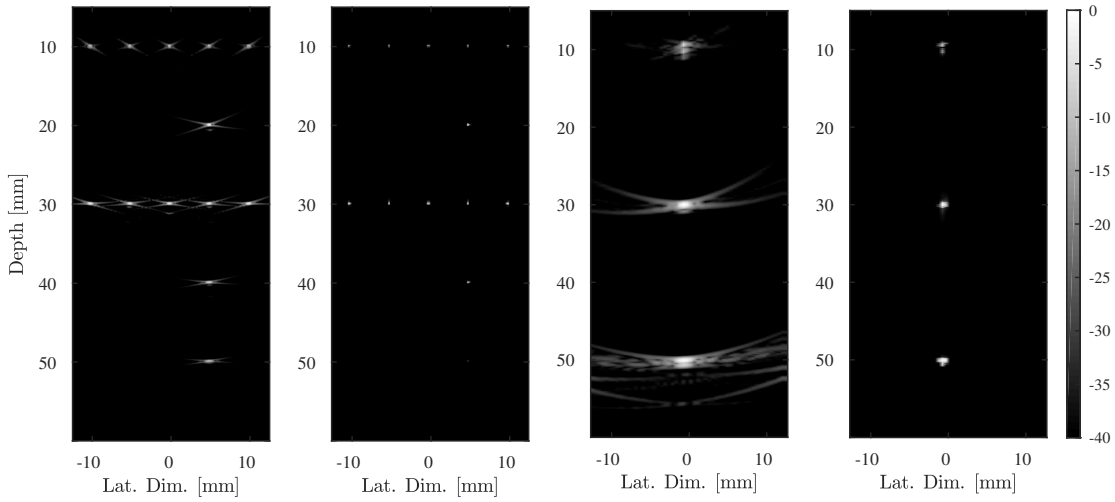


Fig. 4.3. From left to right. Log-compressed B-mode images of the point-reflector phantom reconstructed with the delay-and-sum algorithm for 1 plane-wave insonification, the sparsely regularized beamforming for 1 plane-wave insonification, the delay-and-sum algorithm for 1 diverging-wave insonification, the sparsely regularized beamforming for 1 diverging-wave insonification.

image reconstruction algorithms.

We use the proposed method to reconstruct simulated images from the standardized PICMUS dataset [124]. We compare the results against the ones obtained with two minimum-variance beamforming approaches [126, 127] and two sparse-based approaches [120, 128]. The comparison is performed on the contrast and the axial and lateral resolutions, implemented in the context of the challenge. The results, displayed in Table 4.2, show that the proposed method is competitive against the best state-of-the-art approaches in terms of contrast and outperforms the other techniques on the resolution.

TABLE 4.2  
COMPARISON OF THE PROPOSED SPARSELY REGULARIZED BEAMFORMING AGAINST STATE-OF-THE-ART METHODS ON THE SIMULATED PICMUS DATASET

Method	Contrast phantom	Resolution phantom	
	CNR [dB]	Lat. res. [mm]	Ax. res. [mm]
DAS	9.96	0.57	0.40
Besson <i>et al.</i> [128]	15.81	0.15	0.17
Deylami <i>et al.</i> [127]	<b>17.19</b>	<b>0.08</b>	0.24
Szasz <i>et al.</i> [120]	15.52	0.14	<b>0.11</b>
Varray <i>et al.</i> [126]	12.65	0.38	0.14
Proposed method	15.71	<b>0.08</b>	<b>0.11</b>

The proposed method is lastly used to reconstruct *in vivo* carotid images of the PICMUS dataset. The log-compressed B-mode images, displayed on Figure 4.5 show a significant improvement compared to the DAS algorithm.

A visual comparison against images obtained with best state-of-the-art methods, that one can

## 4.2. Sparsely Regularized Beamforming for Enhanced Ultrafast Ultrasound Imaging

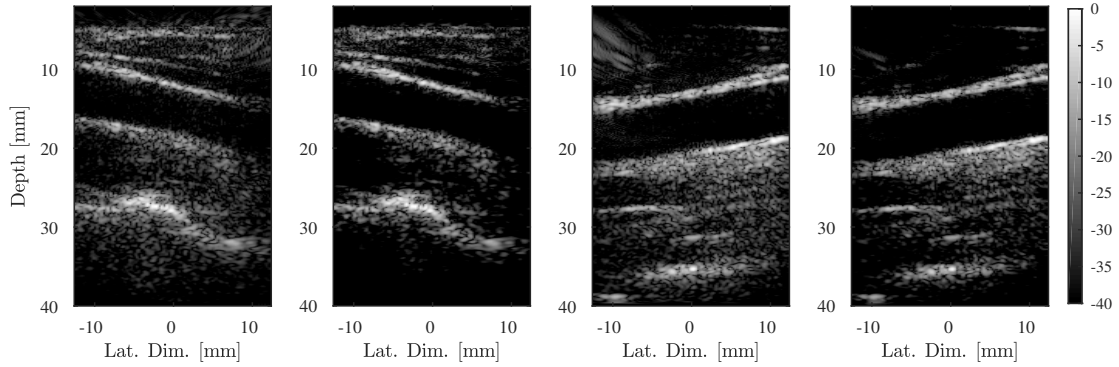


Fig. 4.4. From left to right. Log-compressed B-mode images of a first *in vivo* carotid reconstructed with the delay-and-sum algorithm and with the sparsely regularized beamforming for 1 plane-wave insonification. Log-compressed B-mode images of a second *in vivo* carotid reconstructed with the delay-and-sum algorithm and with the sparsely regularized beamforming for 1 plane-wave insonification.

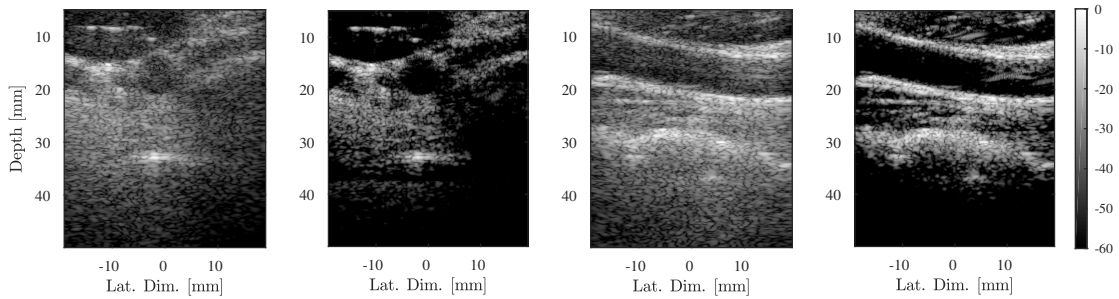


Fig. 4.5. From left to right. Log-compressed B-mode images of a cross-section view of an *in vivo* carotid reconstructed with the delay-and-sum algorithm and with the sparsely regularized beamforming for 1 plane-wave insonification. Log-compressed B-mode images of a longitudinal view of an *in vivo* carotid reconstructed with the delay-and-sum algorithm and with the sparsely regularized beamforming for 1 plane-wave insonification.

find on the PICMUS website<sup>2</sup>, shows that the proposed method outperforms most of them in terms of visual quality (in both contrast and resolution).

**Computation Times of the Proposed Method:** The computation times for 50 iterations of the optimization algorithm are 119 ms, 164 ms and 163 ms for the two *in vivo* carotids. Regarding DW imaging, the method takes 319 ms on the point-reflector phantom.

These timings are two to three orders of magnitude faster than state-of-the-art methods. Indeed, in their latest work, David *et al.* [78] reported computation times between 3 and 5 min. Szasz *et al.* [119] reported reconstruction times between 10 s and 1 min.

The relative timings of the main operations involved in the image reconstruction process are reported in Table 4.3.

We first observe that the timings are relatively well balanced between the different operations. We also notice that the computation times of the operations  $H\mathbf{x}$  and  $H^*\mathbf{y}$  highly depend on the relative size of the element-raw-data and image grids. Indeed, the computation time of the operation  $H\mathbf{x}$  is longer than the one of  $H^*\mathbf{y}$  in the DW case since the image grid is larger than

<sup>2</sup>[https://www.creatis.insa-lyon.fr/Challenge/IEEE\\_IUS\\_2016/home](https://www.creatis.insa-lyon.fr/Challenge/IEEE_IUS_2016/home)

TABLE 4.3

RELATIVE TIMINGS OF THE MAIN OPERATIONS INVOLVED IN SPARSELY REGULARIZED BEAMFORMING FOR THE CYST PHANTOM IN PLANE-WAVE IMAGING AND THE POINT-REFLECTOR PHANTOM IN DIVERGING-WAVE IMAGING

Operation	Plane wave (cyst.)	Diverging wave (point ref.)
$Hx$	22.1 %	32.9 %
$H^*y$	22.5 %	11.7 %
$\Psi\alpha$	24.9 %	25.5 %
$\Psi^*x$	24.0 %	24.1 %
Others	6.5 %	5.8 %

the element-raw-data grid. It is not the case in the PW case where the two grids are the same.

### 4.3 Compressed Ultrasound Beamforming

#### 4.3.1 Motivation and Existing Approaches

Sparsely regularized beamforming, described in Section 4.2, aims to reduce the number of insonifications necessary to obtain high-quality images in UFUS. Compressed beamforming goes one step further and explores the ability of the proposed method to produce high quality images while reducing the amount of data collected per insonification.

From a system point-of-view, the main motivation is to investigate the ability to reduce the number of transducer elements used on receive or at least the number of coaxial cables necessary to carry the echo signals from the probe to the back-end system (See Chapter 5 for an in-depth discussion on the motivations).

The goal is also to study the feasibility of an ultrasonic “single-pixel camera” [129], i.e. to investigate the ability to leverage CS principles to perform US imaging with few sensors (See Section 5.1 for a more detailed introduction on CS.).

With the considerable attention that CS has raised since its introduction by Candes and colleagues in 2006 [130], compressed beamforming techniques have recently been investigated in US imaging.

A first group of methods, mainly explored by Eldar’s group in Technion, relies on FRI sampling of US signals [131]. The technique is based on approximating the element-raw data as a sum of  $L$  pulses,  $L$  being the number of scatterers in the medium, which can be reconstructed with at least  $2L + 1$  samples acquired with a specific sampling kernel. Apart from the application of FRI to US signals, their main contribution is the derivation of a specific sampling kernel for stream of pulses, denoted as sum-of-sinc kernels. In later studies, they applied a similar strategy to RF images, which can also be approximated as stream of pulses [132] and whose Fourier coefficients can be related to the ones of the element-raw data [133, 134]. They have demonstrated high-quality imaging with a data-rate reduction of  $10\times$  compared to existing imaging techniques. But their approach becomes less interesting when the number of pulses is high and fails to reconstruct the textural information in images.

Other approaches, more aligned with the CS framework than the one described above have also been investigated. Liebgott *et al.* [135] have studied various CS strategies on the element-raw data, i.e. different compression schemes and different sparsity transforms. Many studies

have focused on RF images, with the objective of reducing the data rate. Quinsac *et al.* [136] have investigated various masking techniques coupled with sparsity in the Fourier domain. Based on this work, Basarab *et al.* have exploited joint sparsity in the Fourier domain and improved the compression capability of the Fourier-based approach [137]. Lorintiu *et al.* [138] have studied data-driven strategies coupled with similar masks to the ones used by Quinsac *et al.* Alternatively, Quinsac *et al.* [139] and Dobigeon *et al.* [140] have investigated Bayesian CS techniques where sparsity is expressed in terms of a prior probability distribution of the unknown image. In a similar fashion, Achim *et al.* have proposed to exploit  $\alpha$ -stable distributions as models for RF data both in the image domain [141] and in the Fourier domain [142].

Only few groups have considered including the image reconstruction model in the CS problem. David *et al.* [78] have investigated several undersampling strategies, based on a reduction of the number of transducer elements, coupled with a time-domain model for the US propagation. While being the first paper dealing with the concepts of coherence associated with the image reconstruction model, the results are limited to sparse sources, which is of limited interest in US imaging.

Recently, Kruizinga *et al.* [143] have proposed a single transducer-element probe for 3D US imaging with the underlying motivations of mimicking the single pixel camera. Their idea, inspired by the concept of acoustic holograms [144], consists in using a large piezoelectric element which transmits and receives through a rotating plastic coding mask. Due to higher speed of sound inside the mask, the coherence of the US propagation, usually required for beamforming, is partially broken. Hence, the propagation matrix is significantly closer to a random matrix, which is desirable for CS reconstruction.

#### 4.3.2 Proposed Compressed Beamforming Approach

During the thesis, we have investigated different compressed beamforming strategies with various degrees of complexity. We have started with very simple schemes, denoted as “the naive strategy”, which have helped us in designing more complex strategies, i.e. “channel mixing” and “channel and time mixing”.

Formally, we consider the same configuration as described in Section 4.2. We introduce an additional undersampling operator  $\mathbf{S} : \mathbb{R}^{NN_x^t} \rightarrow \mathbb{R}^{LM}$ , where  $M \leq N_x^t$  and  $L \leq N$ , such that

$$\mathbf{y} = \mathbf{S}\mathbf{m} = \mathbf{S}\mathbf{H}\boldsymbol{\gamma} = \mathbf{H}_d\boldsymbol{\gamma}, \quad (4.15)$$

where  $\mathbf{H}_d = \mathbf{S}\mathbf{H} \in \mathbb{R}^{NM}$ .

Associated with such a model, we define the compression ratio as

$$C = \frac{LM}{NN_x^t}, \quad (4.16)$$

where  $C \in [0, 1]$  ideally as small as possible.

On the reconstruction side, we are interested the following minimization problem

$$\min_{\boldsymbol{\gamma} \in \mathbb{R}^{N_x N_z}} \frac{1}{2} \|\mathbf{S}\mathbf{H}\boldsymbol{\gamma} - \mathbf{y}\|_2^2 + \lambda \|\boldsymbol{\Psi}^* \boldsymbol{\gamma}\|_1, \quad (4.17)$$

where  $\Psi$  is a sparsifying transform as considered in Section 4.2.

**The Naive Strategy:** In a first attempt to perform compressed beamforming, we adopt a naive approach quite similar to the one proposed by David *et al.* [78]. The objective is to reduce the number of transducer elements used on receive. We investigate the following undersampling schemes:

- *Scheme 1 - Uniformly spaced transducers:* The transducers are uniformly selected across the aperture.
- *Scheme 2 - Randomly chosen transducers:* The transducers are selected randomly in the aperture.

Mathematically, the undersampling operator associated with such a strategy is defined as  $\mathbf{S} : \mathbb{R}^{NN_x^t} \rightarrow \mathbb{R}^{NM}$ , with  $M < N_x^t$  the number of transducer elements selected according to the strategy. From the perspective of the measurement model introduced in Chapter 3, this amounts to significantly reducing the number of projections available for the reconstruction. This naturally leads to more artifacts when the reconstruction is performed with the DAS algorithm. More specifically, the first scheme will generate aliasing artifacts in the form of grating lobes. Regarding the second scheme, it will not induce any grating lobe due to the randomness in the choice of the transducer-element locations but the side lobes will be significantly increased.

**Mixing Schemes:** Intuitively, removing projections may have a significant impact on the image reconstruction. Hence, we can think about designing a strategy such that the loss of information is minimized. The underlying idea is to spread the information as much as possible between the element raw-data and the desired-image, thus lowering the coherence, similarly to sparse MRI acquisition [145].

Since the echo signals represent projections along conics, e.g. parabola and ellipses related to the TOF, we can deduce that only few samples of the TRF contribute to each sample of an echo signal and that close echo signals are highly correlated. This contributes to a highly coherent measurement model which is not desirable for CS. Nevertheless, it is interesting to note that each point of the element raw-data space generates a different conic in the medium, up to the discretization. Since two non-identical conics may intersect in at most four points, the information contained in samples of the echo signals, sufficiently spaced from each other, are complementary. Taking into account such an observation, our idea consists in mixing the information contained in various samples of the echo signals in order to reduce the loss of information induced by the undersampling.

Mathematically, we define the undersampling operator  $\mathbf{S} = \mathbf{P}\mathbf{W}$ , where  $\mathbf{P} \in \mathbb{R}^{MN \times NN_x^t}$ ,  $M < N_x^t$ , which selects transducer elements as in the naive strategy, and  $\mathbf{W} \in \mathbb{R}^{NN_x^t \times NN_x^t}$  (or equivalently  $\mathbf{W} : \mathbb{R}^{N \times N_x^t} \rightarrow \mathbb{R}^{N \times N_x^t}$ ) is a mixing operator which spreads the information across every element. The matrix  $\mathbf{W}$  is designed as a random matrix with independent identically distributed (i.i.d.) entries drawn from a probability distribution. Recall that  $\mathbf{M}_{li}$  denotes the element raw-data

received at time  $t_l$  by the  $i$ -th transducer element, we denote by  $\mathbf{M}_{uj}^W$  the mixed element raw-data at time  $t_u$  on the  $j$ -th synthetic mixed channel, defined by the following

$$\mathbf{M}_{uj}^W = \sum_{i=1}^N \sum_{l=1}^{N_x^t} w_{ujil} \mathbf{M}_{li}, \forall j \in \{1, \dots, N_x^t\}, \quad (4.18)$$

where  $w_{jlk_u}$  are drawn from any probability distribution.

The main drawback of this strategy resides in the design of the linear operator  $\mathbf{W}$ . As an example, if we consider that the element raw-data are acquired over 1000 depth samples, with 128 transducer elements, and that the grid of the desired image is the same as the grid of the element raw-data, then  $\mathbf{W}$  requires 131 GB of memory to store the matrix coefficients, in double precision. In order to address this issue, we suggest two strategies, denoted as channel mixing (CMIX) and channel and time mixing (CTMIX). CMIX consists of a random summation of the signals coming from the different transducers elements at a given time instant such that (4.18) becomes

$$\mathbf{M}_{uj}^W = \sum_{l=1}^{N_x^t} w_{ujul} \mathbf{M}_{ul}, \forall j \in \{1, \dots, N_x^t\}. \quad (4.19)$$

The operator  $\mathbf{W}$  is significantly less complex since it only performs a mixing across transducer elements, not across the time dimension. In addition, such a mixing could be achievable in hardware, providing a probe which integrates a system able to perform CMIX in a pre-beamforming step. However, it is clear that the mixing effect of CMIX is limited compared to a fully random mixing.

CTMIX extends the principle of CMIX by considering mixing across both transducer elements and  $D < N$  time samples to limit the increase of complexity. Mathematically, it can be defined as

$$\mathbf{M}_{uj}^W = \sum_{i=1}^D \sum_{l=1}^{N_x^t} w_{ujil} \mathbf{M}_{li}, \forall j \in \{1, \dots, N_x^t\}, \quad (4.20)$$

in which the time samples are chosen randomly in the entire range of time. When  $D = N$ , CTMIX is equivalent to the case where a random matrix is used. When  $D = 1$ , CTMIX may be equivalent to CMIX.

#### 4.3.3 Experiments and Results

To evaluate the proposed method, we rely on the same set of experiments as in Section 4.2.3.

**On the Coherence of the Proposed Strategies:** In order to investigate the relevance of the proposed strategy in the context of CS, we propose to compute the mutual coherence of the matrix  $\mathbf{H}_d \Psi$  for different mixing schemes and sparsifying bases  $\Psi$ .

The mutual coherence of a matrix  $\mathbf{A} = [\mathbf{A}_1, \dots, \mathbf{A}_L] \in \mathbb{C}^{M \times L}$  is measured as the maximal normal-

ized inner product of its columns:

$$\mu(\mathbf{A}) = \max_{k,j,k \neq j} \frac{|\langle \mathbf{A}_k, \mathbf{A}_j \rangle|}{\|\mathbf{A}_k\|_2 \cdot \|\mathbf{A}_j\|_2}. \quad (4.21)$$

It plays a crucial role in CS since it directly impacts the performance of the CS reconstruction (See Section 5.1 for more details). Ideally, we would like  $\mu(\mathbf{A})$  to be as small as possible, knowing that  $\mu(\mathbf{A})$  lies between the Welch bound [146] and 1.

For computational purposes, we fix  $N_x^t = 32$  and  $N = 256$  which corresponds to a depth ranging between 5 mm and 11 mm. The measurement model considered in the study is based on a PW imaging configuration (single PW with normal incidence).

Two different bases  $\Psi$  are evaluated, namely the Dirac basis ( $\Psi$  is the identity) and the Haar wavelet (Daubechies 1 wavelet) basis, since we are interested in wavelet-based models. Our choice of wavelet basis is limited to Haar wavelet since it is the only one that has a corresponding matrix expression which facilitates the computation of the mutual coherence.

Four different sampling strategies are compared: uniform selection of transducer elements, random selection of transducer elements, CMIX and CTMIX. Regarding CMIX and CTMIX, the coefficients of  $\mathbf{W}$  are generated with coefficients distributed according to i.i.d. normal and Rademacher distributions. For CTMIX, the coherence is evaluated for  $D = 1, 3, 10, 20, 30, 40$ .

Figures 4.6(a) and 4.6(b) display the mutual coherence  $\mu(\mathbf{H}_d \Psi)$  for a number of measurements ranging between 5 % and 100 %, where  $\mathbf{H}_d$  is square in the case of 100 %, with  $\Psi$  being Dirac and Haar bases, respectively. It can be seen that the main benefit of the CMIX and CTMIX strategies resides in their ability to limit the increase of the coherence  $\mu(\mathbf{H}_d \Psi)$  induced by the undersampling of the raw data. In addition, it can be noticed that this effect is more pronounced for the Haar basis than for the Dirac basis.

A comparison between CMIX and CTMIX shows that CTMIX has lower coherence than CMIX. This was expected, since CTMIX provides a better mixing than CMIX. Regarding the impact of the probability distribution of the random coefficients on  $\mu(\mathbf{H}_d \Psi)$ , Figure 4.6(c) shows that there is no significant difference in coherence between Gaussian and Rademacher random coefficients. Regarding CTMIX, Figure 4.6(d) displays the values of  $\mu(\mathbf{H}_d \Psi)$  for the different values of  $D$ . It can be seen that the mutual coherence decreases when  $D$  increases. Such a result is consistent with the analysis carried out in Section 4.3.2. For  $D \geq 10$ , we observe similar values of the coherence in the considered range of compression ratios.

**Reconstruction of the Point-reflector Phantom:** In a first experiment, we focus on the point-reflector phantom which is highly sparse therefore favorable for a CS reconstruction. We propose to apply the compressed beamforming framework for a number of measurements ranging between 5 % and 50 %. The B-mode images, displayed on Figures 4.7 and 4.8 for PW and DW imaging, respectively, show that the proposed reconstruction strategy, coupled with CMIX, leads to high-quality reconstruction of point reflectors even for low numbers of measurements (less than 5 %) for both PW and DW imaging.

Figure 4.9 reports the peak-signal-to-noise ratio (PSNR) values, calculated on the normalized envelope image (normalized means divided by its maximum value), of the different methods

### 4.3. Compressed Ultrasound Beamforming

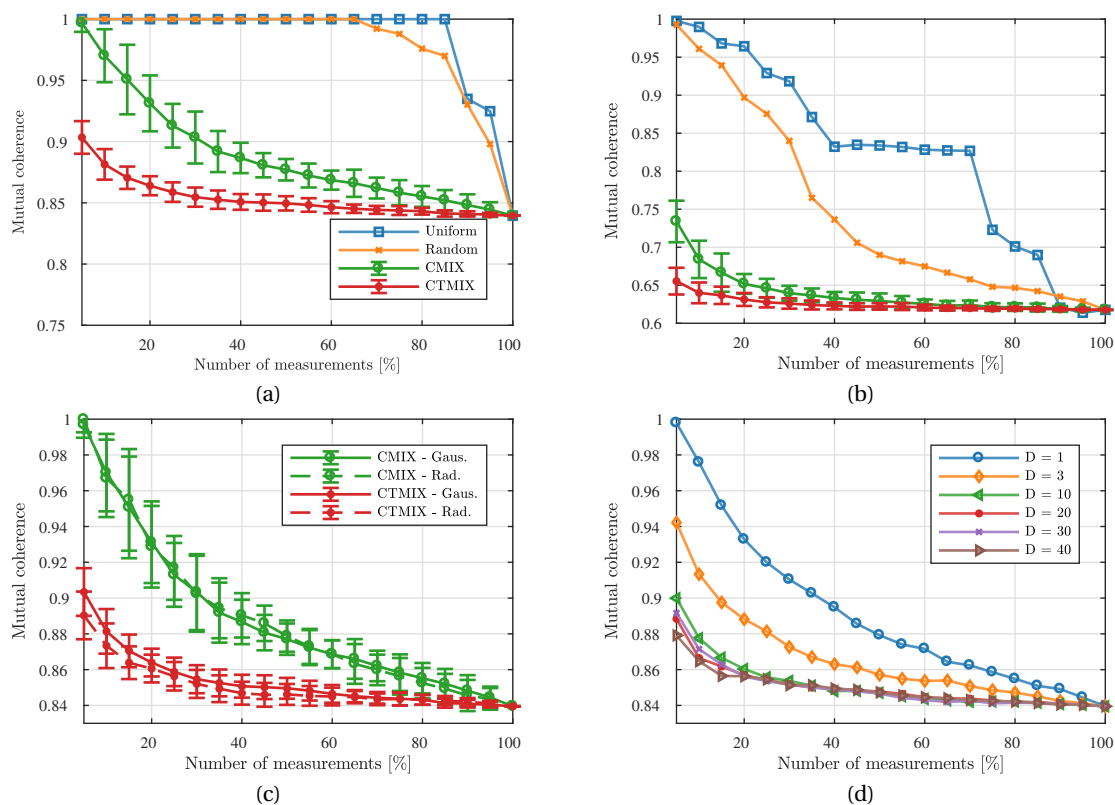


Fig. 4.6. Figures (a) and (b) display the mutual coherence against the number of measurements for the Dirac basis and the Haar basis for the uniform selection of transducer elements, the random selection of transducer elements, CMIX and CTMIX ( $D = 10$ ). Figure (c) displays the coherence for CMIX and CTMIX with mixing coefficients drawn using normal and Rademacher distributions. Figure (d) reports the coherence of CTMIX for different values of  $D$ .

against the reference image, chosen to be the one reconstructed with DAS without data compression. It can be concluded that CMIX and CTMIX achieve high quality reconstructions for all the considered number of measurements. It can also be observed that, in the case of CMIX, the PSNR drops for numbers of measurements lower than 5 % while it remains constant for CTMIX. Such results corroborate the study on mutual coherence performed in the previous paragraph.

Regarding the naive strategy, it can be seen that the PSNR remains high until 10 % measurements and dramatically decreases for lower numbers of measurements. Indeed, because the proposed undersampling strategy is highly coherent, the number of measurements required for high-quality reconstruction is higher than for mixing strategies.

**Contrast Study on the Anechoic-inclusion Phantom:** In this experiment, we reconstruct the anechoic-inclusion phantom for different numbers of measurements, namely 20 %, 25 % and 50 %. We compare the naive strategy (uniform selection of transducer elements), with CMIX and CTMIX. For CTMIX, we set  $D = 5$  and the random coefficients are drawn from a normal distribution.

The values of the CNR, reported in Table 4.4 show that CTMIX and CMIX outperform the naive

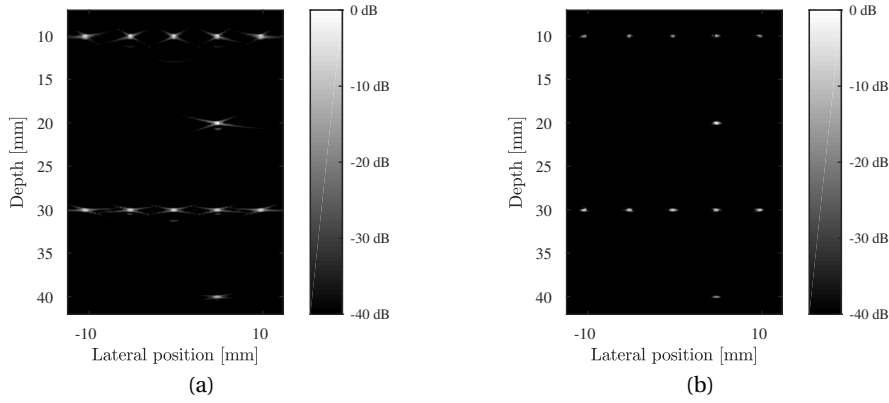


Fig. 4.7. Log-compressed B-mode images of the point-reflector phantom for 1 plane-wave insonification. Figure (a) displays the log-compressed B-mode image reconstructed with the delay-and-sum algorithm. Figure (b) shows the log-compressed B-mode image reconstructed with compressed beamforming coupled with CMIX strategy with 4 % measurements.

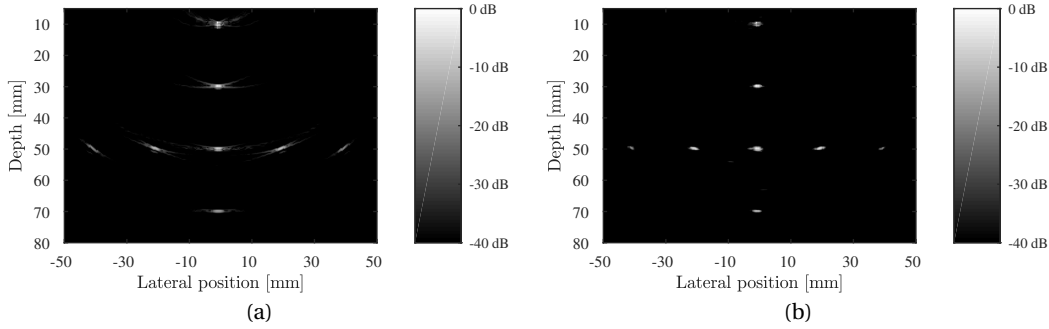


Fig. 4.8. Log-compressed B-mode images of the point-reflector phantom for 1 diverging-wave insonification. Figure (a) shows the log-compressed B-mode image reconstructed with the delay-and-sum algorithm. Figure (b) displays the log-compressed B-mode image reconstructed with compressed beamforming coupled with CMIX strategy with 4 % measurements.

strategy.

We also notice that CTMIX leads to similar results to CMIX except for a number of measurements of 20 % where CTMIX significantly outperforms CMIX.

For the naive strategy, we observe a dramatic decrease of the CNR for 20 % measurements. The same coherence argument as for the point-reflector phantom may be used to explain such a fact. Compared to the point-reflector phantom, the decrease appears at a significantly higher number of measurements because the anechoic-inclusion phantom is less compressible than the point-reflector phantom.

**Reconstruction of the *In vivo* Carotids:** Figures 4.10(b) and 4.10(d) display the B-mode images of the *in vivo* carotids reconstructed with the proposed approach (CMIX and CTMIX) for a compression ratio of 20 %. Figures 4.10(a) and 4.10(c) display reference images, reconstructed with the DAS algorithm from uncompressed data.

We notice that textural areas such as carotid plaques and muscle fibers, as well as anechoic

### 4.3. Compressed Ultrasound Beamforming

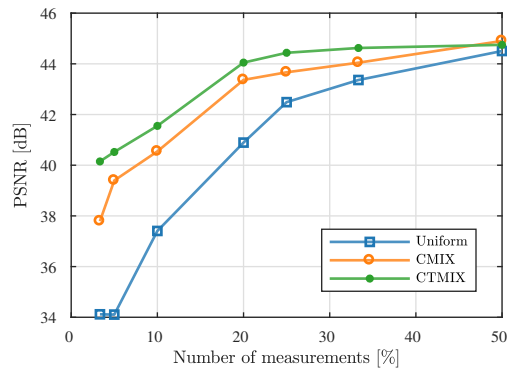


Fig. 4.9. Peak-signal-to-noise ratio against the number of measurements calculated on the point-reflector phantom for 1 plane-wave insonification and CTMIX, CMIX and the uniform selection of transducer elements.

TABLE 4.4

CONTRAST-TO-NOISE RATIO [dB] FOR THE THREE CONSIDERED COMPRESSED BEAMFORMING STRATEGIES AND FOR VARIOUS NUMBERS OF MEASUREMENTS

Method	Number of measurements		
	50 %	25 %	20 %
Uniform	8.81	6.03	0.57
CMIX	9.15	8.06	6.92
CTMIX	<b>9.16</b>	<b>8.10</b>	<b>7.30</b>

areas, are well reconstructed with the proposed method. However, speckle areas, especially in the far field, are not well recovered by the proposed approach, resulting in a darkening of the deepest part of Figures 4.10(b) and 4.10(d). This can be due to a slight decay of the intensity across the imaging range because of a non-optimal setting of the TGC. This may also be explained by the fact that the wavelet-based models do not manage to preserve the entire speckle information, which is therefore suppressed during the image reconstruction process.

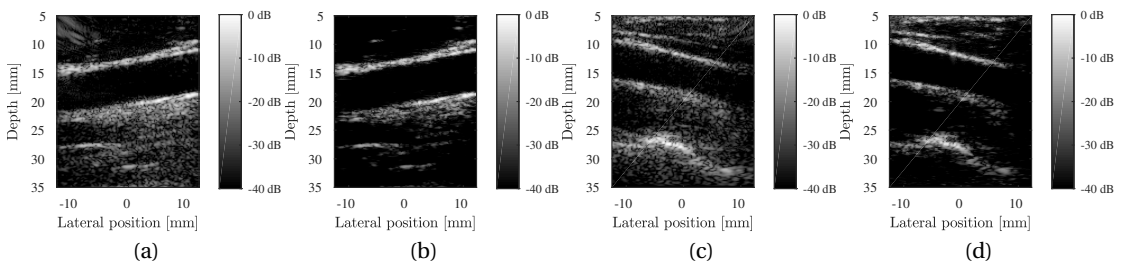


Fig. 4.10. Log-compressed B-mode images of the *in vivo* carotids for 1 plane-wave insonification. Figures (a) and (c) display the log-compressed B-mode images reconstructed with the delay-and-sum algorithm. Figures (b) and (d) show the log-compressed B-mode images reconstructed with compressed beamforming coupled with the CMIX strategy and 20% measurements.

## 4.4 Non-stationary Blur Modeling and Image Restoration

### 4.4.1 Motivations and Existing Approaches

Sections 4.2 and 4.3 focus on sparse regularization approaches for enhanced US imaging, where we would like to recover a high-quality RF image. In this section, we emphasize on US image restoration, a slightly different problem that has been extensively investigated in the community.

US imaging process exploits the transducer elements for both transmitting acoustic pulses and recording the response of the medium to these pulses as echo signals (the element-raw data). The set of these signals is related to the spatial distribution of variations in acoustic impedance, i.e. in medium density and sound velocity, denoted as the TRF, by the US propagation operator described in Chapter 3. Due to finite aperture of the probe and bandpass properties of the impulse response of each transducer element, retrieving the TRF from the echo signals is an ill-posed problem. In standard US imaging, the DAS operator is used as an approximate inverse of the propagation operator, which makes sense since it can be seen as an adjoint propagation under several simplifying assumptions. Such an approximation leads to the RF image, a blurred estimate of the TRF. The PSF is introduced to relate these quantities. Because of the wave propagation and diffraction effects in the medium, the blur is highly spatially variant, as can be seen in Figure 4.11.

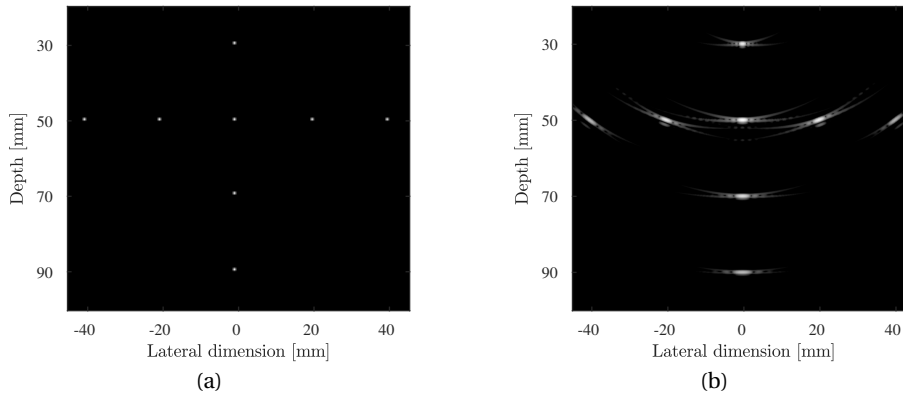


Fig. 4.11. Figure (a) displays the tissue-reflectivity function of the point-reflector phantom. Figure (b) presents the corresponding log-compressed B-mode image reconstructed with the delay-and-sum algorithm. We clearly notice the spatially varying blur induced by the delay-and-sum beamforming.

While the principles of the propagation of US waves in a homogeneous and lossless medium are known for more than a century, only few recent studies have focused on understanding the PSF from a physical point of view [147–149]. In the vast majority of works, the PSF is estimated in a preliminary step either through *in vitro* measurements or by simulation [150–156]. Other approaches estimate directly the PSF on the RF image in a first stage and then use the estimated PSF to perform the deconvolution. The PSF estimation is performed using homomorphic filtering of the cepstrum [157–159], generalized homomorphic filtering [90, 160, 161], inverse filtering [162–166] and power spectrum equalization [167]. Alternatively, blind deconvolution approaches, where the PSF and the TRF are jointly recovered have been very popular recently, with the development of regularization approaches, e.g. MAP estimation.

Such methods involve either parametric [168–171] or non-parametric [153, 172] formulations of the PSF.

In addition, evaluating existing models non-stationary blur [147, 148] requires to perform matrix-vector products with large matrices (around  $10^{10}$  coefficients for 2D US images), practically challenging with standard numerical tools.

Such a problem is standard in shift-variant image deblurring and many simplification strategies have been developed in the literature. Most of them are based on the assumption that the non-stationary blur can be approximated by a relatively low number of basis filters. The evaluation of the blur is then performed as a weighted sum of convolutions with the basis filters [173] (See [174] for an exhaustive description of such methods). In this group of techniques, sectional methods are probably the most popular ones [175–179]. In such approaches, the image is divided into sub-regions where the blur is considered stationary. Then, by appropriately masking the image, shift-invariant convolutions are applied in each sub-region independently forming different sub-images that are interpolated to form the blurred image. In this case, the basis filters correspond to blur kernels. Other techniques rely on global or local [174] low-rank approximations [173, 174, 180–182] of non-stationary blur where the basis filters are the corresponding eigenvectors.

Alternatively, several recent works propose to approximate the blur with an operator that has desirable properties, e.g. diagonalizability [183], regularity [184] or sparsity [185, 186] in given frames.

In the context of US imaging, most advanced techniques achieve shift-variant restoration using sectional methods [90, 179] which assume lateral stationarity of the blur, suited to the case of US imaging with focused waves. These approaches are evidently not valid in PW and DW imaging where the diffraction effect is pronounced, as displayed in Figure 4.11.

In this section, we describe a novel model of non-stationary blur in US imaging with PW and DW insonifications. Contrary to many existing approaches, the model is motivated from physical aspects related to the propagation of US waves and from the US imaging process. We also propose an approximation of the non-stationary blur for image restoration which exploits the above introduced decomposition coupled with an appropriate discretization of the element-raw data. We demonstrate that its evaluation, based on efficient formulations of discrete operators described in Chapter 3, scales linearly, rather than quadratically, with the size of the grid, better than shift-invariant blur evaluation methods. We show an example application of US image restoration. More precisely, we use the proposed model in a MAP estimation algorithm, with a GGD prior for the TRF [153, 161]. We test the method on an extensive number of experiments, namely a numerical phantom of point reflectors, a numerical calibration phantom and two *in vivo* carotids, for both PW and DW imaging.

### 4.4.2 Mathematical Modelling of Non-stationary Blur

We consider a US imaging configuration similar to the one detailed in Sections 3.5 and 3.6 for DW and PW imaging, respectively. Mathematically, we consider a 2D imaging configuration composed of  $N_x^t$  transducer elements arranged in a linear- or phased-array probe, characterized by a pulse-echo waveform  $\nu_{pe}$ , with inter-element spacing  $p$ . Such transducer elements

## Chapter 4. USSR: The UltraSound Sparse Regularization Framework

---

are used to transmit an acoustic wave in the medium  $\Omega \subset \mathbb{R}^2$  which contains inhomogeneities as local fluctuations in acoustic impedance, defining the TRF  $\gamma \in L_2(\Omega)$ . The transducer elements also record the backscattered echoes during a time  $T$ , defining the element-raw data  $m(t) \in L_2([0, T])^{N_x^t}$ .

Associated with such a configuration, we define the measurement model, sometimes denoted as the US propagation operator in this section,  $H: \gamma \mapsto m$  as well as the DAS operator  $D: m \mapsto \hat{\gamma}$ , where  $\hat{\gamma} \in L_2(\Omega)$  denotes the RF image.

We define our model of non-stationary blur as the composition of these two operators as follows

$$\begin{aligned} K: L_2(\Omega) &\rightarrow L_2(\Omega) \\ \gamma &\mapsto \hat{\gamma} = DH\gamma. \end{aligned} \quad (4.22)$$

From a physical perspective, such a model makes sense since it models the whole process of US imaging, from the transmission to the RF image. We also notice that the operator is akin to blur since it relates the true TRF  $\gamma$  to its blurred estimate  $\hat{\gamma}$ .

In order to better highlight the fact that  $K$ , defined in (4.22), is indeed a model of non-stationary blur, we derive the corresponding bivariate PSF kernel. Recall from Chapter 3 that the US propagation operator can be expressed element-wise as

$$(H\gamma)_i(t) = \int_{\mathbf{r} \in \Omega} o_{pe}(\mathbf{r}, \mathbf{p}_i) v_{pe}(t - \tau(\mathbf{r}, \mathbf{p}_i)) \gamma(\mathbf{r}) d\mathbf{r}, \quad (4.23)$$

and that the DAS operator can be written as

$$(Dm)(\mathbf{r}) = \sum_{i=1}^{N_x^t} a(\mathbf{r}, \mathbf{p}_i) m_i(\tau(\mathbf{r}, \mathbf{p}_i)) \quad (4.24)$$

where  $o_{pe}(\mathbf{r}, \mathbf{p}_i)$  accounts for the element directivity and decay of the reflected wave,  $a(\mathbf{r}, \mathbf{p}_i)$  are the apodization coefficients and  $\tau(\mathbf{r}, \mathbf{p}_i) = t_{Tx}(\mathbf{r}) + t_{Rx}(\mathbf{r}, \mathbf{p}_i)$  denotes the round-trip TOF.

We can express  $K$  in a more explicit fashion using (4.23) and (4.24):

$$\begin{aligned} \hat{\gamma}(\mathbf{r}) &= (K\gamma)(\mathbf{r}) \\ &\stackrel{(4.24)}{=} \sum_{i=1}^{N_x^t} a(\mathbf{r}, \mathbf{p}_i) m_i(\tau(\mathbf{r}, \mathbf{p}_i)) \\ &\stackrel{(4.23)}{=} \int_{\mathbf{s} \in \Omega} \sum_{i=1}^{N_x^t} a(\mathbf{r}, \mathbf{p}_i) o_{pe}(\mathbf{s}, \mathbf{p}_i) v_{pe}(\tau(\mathbf{r}, \mathbf{p}_i) - \tau(\mathbf{s}, \mathbf{p}_i)) \gamma(\mathbf{s}) d\mathbf{s}. \end{aligned} \quad (4.25)$$

Hence, the non-stationary blur model  $K$ , defined in (4.22) as the composition of the DAS and US propagation operators, can also be expressed as the following Fredholm integral of the first

kind, standard in shift-variant blur modeling [174],

$$\begin{aligned}
 K : L_2(\Omega) &\rightarrow L_2(\Omega) \\
 \gamma &\mapsto \int_{\mathbf{s} \in \Omega} \gamma(\mathbf{s}) k(\cdot, \mathbf{s}) d\mathbf{s},
 \end{aligned} \tag{4.26}$$

where  $k : \Omega \times \Omega \rightarrow \Omega$ , the bivariate kernel of  $K$ , defines the PSF and can be expressed as follows

$$k(\mathbf{r}, \mathbf{s}) = \sum_{i=1}^{N_x^t} a(\mathbf{r}, \mathbf{p}_i) o_{pe}(\mathbf{s}, \mathbf{p}_i) v_{pe}(\tau(\mathbf{r}, \mathbf{p}_i) - \tau(\mathbf{s}, \mathbf{p}_i)). \tag{4.27}$$

From (4.27), we observe that if we assume that  $\gamma(\mathbf{r}) = \delta(\mathbf{r} - \mathbf{r}_0)$ , with  $\mathbf{r}_0 \in \Omega$ , then

$$\hat{\gamma}(\mathbf{r}) = k(\mathbf{r}, \mathbf{r}_0),$$

leading to a more natural interpretation of  $k$  as the PSF, i.e. the response of the US system to a TRF composed of a single point reflector located at  $\mathbf{r}_0$ . Moreover, in a spatially invariant case, the bivariate kernel  $k(\mathbf{r}, \mathbf{s})$  is simplified to a univariate one leading to  $k(\mathbf{r}, \mathbf{s}) = k(\mathbf{r} - \mathbf{s})$ . Under this approximation, Equation (4.26) becomes the standard bi-dimensional analytical convolution.

At the continuous level, the adjoint of the operator  $K$  described in (4.22) can straightforwardly be decomposed as the composition of the adjoint DAS and adjoint propagation operators, both described in Chapter 3,

$$K^* = H^* D^*, \quad K^* : L_2(\Omega) \rightarrow L_2(\Omega), \tag{4.28}$$

with

$$H^* : L_2([0, T])^{N_x^t} \rightarrow L_2(\Omega), \quad D^* : L_2(\Omega) \rightarrow L_2([0, T])^{N_x^t}.$$

Interestingly, using the same reasoning as for  $K$ , we can show that  $K^*$  can also be expressed using the PSF kernel defined in (4.27), by flipping the two arguments, i.e. using a symmetrised kernel  $\tilde{k}(\mathbf{r}, \mathbf{s}) = k(\mathbf{s}, \mathbf{r})$ , such that

$$\begin{aligned}
 K^* : L_2(\Omega) &\rightarrow L_2(\Omega) \\
 \gamma &\mapsto \int_{\mathbf{s} \in \Omega} \gamma(\mathbf{s}) k(\mathbf{s}, \cdot) d\mathbf{s}.
 \end{aligned} \tag{4.29}$$

#### 4.4.3 Evaluation Strategy of the Proposed Model of Non-stationary Blur

In this section, we express the non-stationary blur model over a regular grid, as defined in Section 3.3.2. More precisely, the TRF  $\Gamma \in \mathbb{R}^{N_x \times N_z}$  is defined on a regular grid

$$\Omega_\gamma = \{\mathbf{s}_{uv} = (x_u, z_v) \in \Omega, u = 1, \dots, N_x, v = 1, \dots, N_z\},$$

and the RF image  $\hat{\Gamma} \in \mathbb{R}^{\hat{N}_x \times \hat{N}_z}$  is defined on a second regular grid

$$\Omega_{\hat{\gamma}} = \{\mathbf{r}_{kl} = (x_k, z_l) \in \Omega, k = 1, \dots, \hat{N}_x, l = 1, \dots, \hat{N}_z\}$$

A common approximation of (4.26) is achieved by numerical approximation of the continuous integral, leading to

$$\hat{\Gamma} = \mathbf{K}\Gamma, \quad (4.30)$$

where  $\mathbf{K} : \mathbb{R}^{N_x \times N_z} \rightarrow \mathbb{R}^{\hat{N}_x \times \hat{N}_z}$ , is defined element-wise by

$$\mathbf{K}_{kluv} = k(\mathbf{r}_{kl}, \mathbf{s}_{uv}) \Delta_{uv},$$

where  $\Delta_{uv}$  is the elementary volume for the normalization of  $\mathbf{K}$ . The evaluation of (4.30) requires  $O(N_x N_z \hat{N}_x \hat{N}_z N_x^t)$  operations, which is not computable for realistic 2D US imaging configurations where  $N_x N_z$  and  $\hat{N}_x \hat{N}_z$  are of the order of  $10^4$  to  $10^6$ .

**Proposed Evaluation Strategy:** Many fast approximation strategies of non-stationary blur of the form (4.26) have been described in the literature and briefly reviewed in Section 4.4.1 (See [174] for an exhaustive review of such methods). In this section, we present an alternative approach based on the specific property of the non-stationary blur in US imaging, i.e. its decomposition in terms of the propagation and DAS operators.

As for the continuous model of the blur  $K$ , the discrete operator  $\mathbf{K} : \mathbb{R}^{N_x \times N_z} \rightarrow \mathbb{R}^{\hat{N}_x \times \hat{N}_z}$  defined in (4.30) can be decomposed as follows

$$\mathbf{K} = \mathbf{D}_d \mathbf{H}_d, \quad (4.31)$$

where  $\mathbf{H}_d : \mathbb{R}^{N_x \times N_z} \rightarrow L_2([0, T])^{N_x^t}$  and  $\mathbf{D}_d : L_2([0, T])^{N_x^t} \rightarrow \mathbb{R}^{\hat{N}_x \times \hat{N}_z}$  are the partly discretized propagation and DAS operators. More precisely,  $\mathbf{D}_d$  is computed by evaluating  $D$  on the regular grid  $\Omega_{\hat{\gamma}}$  and  $\mathbf{H}_d$  is computed element-wise by numerical approximation of the continuous integral involved in the measurement model on the regular grid  $\Omega_{\hat{\gamma}}$ .

In such forms, the operators  $\mathbf{D}_d$  and  $\mathbf{H}_d$  are qualified as “partly” discretized since they involve as domain and codomain, respectively, the space  $L_2([0, T])^{N_x^t}$ . Such a space, while suitable for mathematical characterization of the operators is not practical in terms of computations since we cannot evaluate  $\mathbf{D}_d$  and  $\mathbf{H}_d$ . Hence the sequential split assumption is not useful for evaluation purpose and one would still rely on (4.30) to compute  $\mathbf{K}\Gamma$ .

In order to benefit from the sequential split assumption, we propose to discretize the time dimension of the element-raw data such that the continuous space  $[0, T]$  is approximated by  $N$  uniformly spaced time instants, with corresponding sampling frequency  $f_s$ . Such an assumption is particularly suited to US imaging due to the bandpass signal properties of the element-raw data, which can be accurately reconstructed from uniform samples acquired at the Nyquist rate (or using bandpass sampling). Hence, an appropriate discretization of the element-raw data space may result in an accurate approximation of the non-stationary blur. In addition, performing the discretization of the element-raw data is aligned with most

recent US imaging systems, such as the Verasonics Vantage™, which operate on digitized element-raw data.

Exploiting this discrete formulation, we express our approximation of the blur-model as follows

$$\mathbf{K} = \mathbf{D}\mathbf{H}, \quad (4.32)$$

where  $\mathbf{D} : \mathbb{R}^{N_x \times N_x^t} \rightarrow \mathbb{R}^{\hat{N}_x \times \hat{N}_z}$  is the discretized DAS operator and  $\mathbf{H} : \mathbb{R}^{N_x \times N_z} \rightarrow \mathbb{R}^{N_x \times N_x^t}$  is the discretized propagation operator. The adjoint operator can be straightforwardly deduced from  $\mathbf{K}$  as

$$\mathbf{K}^* = \mathbf{H}^* \mathbf{D}^*. \quad (4.33)$$

Hence, using the sequential split assumption, the evaluation of  $\mathbf{K}$  results in the consecutive evaluation of  $\mathbf{H}$  and  $\mathbf{D}$ . Additionally, with this simple additional discretization of the “latent” element-raw data space, we benefit from very efficient matrix-free implementations of the discretized US propagation operator  $\mathbf{H}$  and DAS operator  $\mathbf{D}$  that have been described in Chapter 3.

**Computational Complexity of the Proposed Strategy** As already mentioned, the evaluation of  $\mathbf{K} : \mathbb{R}^{N_x \times N_z} \rightarrow \mathbb{R}^{N_x \times N_x^t}$  defined in (4.30) requires *a priori*  $O((N_x N_z)^2 N_x^t)$  operations using (4.27). Such a computational complexity prevents from its use in realistic imaging cases, where  $N_x N_z$  ranges between  $10^4$  and  $10^6$  and  $N_x^t$  is few hundreds.

To solve the above limitation, the proposed evaluation strategy decomposes the computation of  $\mathbf{K}\mathbf{T}$  as follows:

$$\mathbf{K}\mathbf{T} = \mathbf{D}(\mathbf{H}\mathbf{T}), \quad (4.34)$$

where  $\mathbf{H}\mathbf{T}$  is first performed, generating a pseudo raw data  $\mathbf{M}$ , followed by the application of the DAS operator  $\mathbf{D}\mathbf{M}$ .

The overall computational complexity of the operation  $\mathbf{K}\mathbf{T}$  can be easily deduced from the computational complexity of the measurement model and its adjoint, detailed in Chapter 3, such that:

$$\text{Cost}(\mathbf{K}\mathbf{T}) = O(N_x^t N_x N_z) \ll O((N_x N_z)^2 N_x^t), \quad (4.35)$$

since  $N \approx N_z$  in standard US imaging configurations.

An equivalent reasoning for the computation of the adjoint operation  $\mathbf{K}^* \hat{\mathbf{T}}$  leads to the same computational complexity as the forward operation. Indeed, the only difference between the two computations resides in the convolution which is negligible in the computational cost. Thus, the proposed decomposition results in a significant decrease of the computational complexity from quadratic to linear with respect to the number of grid points  $N_x N_z$ . Compared to the common approximation strategies of non-stationary blur, we can draw the following conclusions. If we assume that shift-variant blurs have been stored as matrices of

size  $N_x^b \times N_z^b$ , where  $N_z^b < N_z$  and  $N_x^b < N_x$  (as it is often the case), their evaluations would require  $O(N_x N_z \log N_x N_z)$  computations using a Fourier-domain approach or  $O(N_x^b N_z^b N_x N_z)$  otherwise.

Using the Fourier-domain approach, the computational complexity is usually slightly lower than the proposed approach, since  $\log N_x N_z < N_x^t$ , but the method does not scale as well as the proposed approach with respect to the grid size. Otherwise, the complexity highly depends on the size of the blur matrix while the complexity remains linear with respect to the grid size.

#### 4.4.4 Proposed Image Restoration Technique

Since I had the chance to collaborate with Dr. Zhouye Chen who was a post-doctoral student in Prof. Wiaux's laboratory in 2017, I decided to benefit from her experience in restoration methods applied to US imaging [153]. I have therefore implemented one of the restoration approaches she had worked on during her PhD thesis.

More precisely, we use a  $\ell_p$ -norm minimization ( $p \in [1, 2]$ ) algorithm, one of the most recent methods introduced in US image restoration [148, 153, 155, 161, 168, 172]. Since the discretized blur operator  $\mathbf{K}$  has been described as a tensor in Section 4.4.3, we have to introduce the reshaping operator  $\mathbf{P} : \mathbb{R}^{N_x \times N_z} \rightarrow \mathbb{R}^{N_x N_z}$ , such that  $\boldsymbol{\gamma} = \mathbf{P}\boldsymbol{\Gamma} \in \mathbb{R}^{N_x N_z}$ . We are therefore interested in solving the following optimization problem,

$$\min_{\tilde{\boldsymbol{\gamma}} \in \mathbb{R}^{N_x N_z}} \lambda \|\tilde{\boldsymbol{\gamma}}\|_p^p + \frac{1}{2} \|\hat{\boldsymbol{\gamma}} - \tilde{\mathbf{K}}\tilde{\boldsymbol{\gamma}}\|_2^2, \quad (4.36)$$

where  $\tilde{\mathbf{K}} = \mathbf{P}\mathbf{K}\mathbf{P}^* \in \mathbb{R}^{N_x N_z \times N_x N_z}$  accounts for the discretized PSF operator and  $\hat{\boldsymbol{\gamma}} = \mathbf{P}\hat{\boldsymbol{\Gamma}} \in \mathbb{R}^{N_x N_z}$ , in which  $\hat{\boldsymbol{\Gamma}}$  is the RF image acquired by the US imaging system.

The values of  $p$  are set to 1, 4/3 or 3/2, depending on the experiment, similar to the values used in [153] since their corresponding proximity operator are analytically defined (See Appendix C). We use FISTA, described in Section 4.1.2, to solve the above minimization problem.

#### 4.4.5 Experiments and Results

In order to evaluate the proposed approach, we perform the following experiments:

1. **Diverging-wave imaging:** A simulated experiment is performed with a standard phased-array probe (P4-2v) whose characteristics are given in Table 4.5. A single DW (2.5 MHz, 1-cycle sinusoidal wave) is transmitted with a corresponding virtual point source located  $-2.9$  mm behind the probe and laterally centered. No apodization is used on transmit.

The data are acquired on a numerical point-reflector phantom with eight reflectors with unit amplitude and located at positions described on Figure 4.12(a). As for previous sections, we use the Field II software to simulate the data.

2. **Plane-wave imaging:** Two standard linear-array probes are used, namely the L11-4v and the L12-5 50mm, whose characteristics are given in Table 4.5.

The L11-4v is used in two simulated configurations (using Field II) for which a single PW (5.208 MHz, 2.5-cycle square excitation) with normal incidence is transmitted without apodization:

#### 4.4. Non-stationary Blur Modeling and Image Restoration

- A point-reflector phantom described in Figure 4.12(b);
- the PICMUS numerical phantom<sup>3</sup>.

The L12-5 50mm is used to acquire *in vivo* measurements of two carotids on a Verasonics Vantage™ system (Redmond, WA, USA). A single PW (5 MHz, 1-cycle square excitation) with normal incidence is transmitted without apodization.

TABLE 4.5  
CHARACTERISTICS OF THE P4-2V, L11-4V AND L12-5 50MM PROBES

	Diverging wave P4-2v	Plane wave L11-4v	Plane wave L12-5 50mm
Element number	64	128	128
Center frequency	2.7 MHz	5.133 MHz	7.8 MHz
Sampling frequency	10.8 MHz	20.832 MHz	31.2 MHz
Element width	255 $\mu\text{m}$	270 $\mu\text{m}$	Unknown
Pitch	280 $\mu\text{m}$	300 $\mu\text{m}$	195 $\mu\text{m}$
Elevation focus	60 mm	20 mm	Unknown

Regarding the reconstruction methods, we compare three different PSF estimation techniques:

- the proposed non-stationary PSF;
- a stationary PSF estimated from the data using the method described in [90], denoted as stationary PSF 1;
- a stationary PSF previously simulated on Field II using a phantom made of a single scatterer located at 25 mm for PW imaging and 45 mm for DW imaging, denoted as stationary PSF 2.

The restoration is performed on RF images, obtained by applying the DAS operator on the element-raw data. The image grid spacing is set to one third of the wavelength in the lateral direction and one eighth of the wavelength in the axial direction.

**Point-reflector Experiment:** For these experiments, the  $\ell_p$ -based restoration is tested with a value of  $p$  equal to 1 since we are dealing with sparse images. The comparison is based on the axial and lateral resolution, calculated as the FWHM computed on the log-compressed B-mode image. The regularization parameter is empirically set to its highest value so that all the point reflectors are visible, if possible.

Table 4.6 reports the lateral and axial resolution values for the DW configuration described in Figure 4.12(a). We can see that the proposed method outperforms the models based on a stationary PSF on the lateral resolution especially. This makes sense since the diffraction effect is important in DW imaging configurations resulting in significant variability in the lateral dimension. Regarding the axial resolution, it is relatively stationary along the imaging plane and the proposed method does not significantly outperform the stationary models. Figure 4.13

<sup>3</sup><https://www.creatis.insa-lyon.fr/EvaluationPlatform/picmus/index.html>

shows the B-mode images of the point reflectors for standard DAS beamforming (top row), restoration with the proposed method (middle row) and restoration with the stationary PSF 1 (bottom row). It illustrates the benefit of the proposed method compared to stationary models for image restoration in case of imaging configurations with high lateral variability.

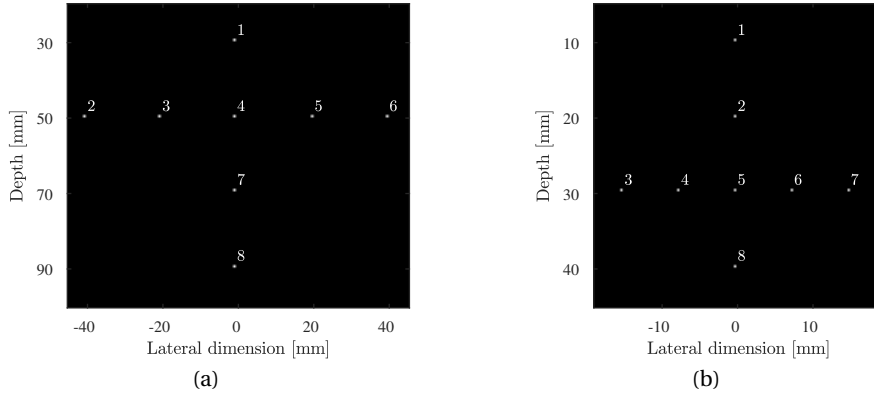


Fig. 4.12. Numerical point-reflector phantom. Figure (a) displays the phantom used in diverging-wave imaging. Figure (b) presents the phantom used in plane-wave imaging.

TABLE 4.6  
COMPARISON OF THE RESTORATION METHODS ON THE POINT-REFLECTOR PHANTOM IN THE DIVERGING WAVE EXPERIMENT

Method		1	2	3	4	5	6	7	8
Lat. Res [mm]	Prop. PSF	<b>0.32</b>	<b>0.19</b>	0.21	<b>0.50</b>	0.21	<b>0.21</b>	<b>0.60</b>	<b>0.60</b>
	Stat. PSF 1	0.90	0.21	<b>0.19</b>	1.4	<b>0.19</b>	<b>0.21</b>	2.2	2.7
	Stat. PSF 2	6.9	9.5	9.5	2.9	9.5	9.5	1.6	3.2
Ax. Res [mm]	Prop. PSF	0.43	0.21	0.42	0.24	<b>0.07</b>	<b>0.07</b>	0.21	0.21
	Stat. PSF 1	<b>0.28</b>	<b>0.07</b>	<b>0.08</b>	<b>0.08</b>	0.41	0.08	<b>0.08</b>	<b>0.08</b>
	Stat. PSF 2	0.46	3.6	3.6	0.55	3.6	3.6	0.37	0.39

When using the method with the stationary PSF 2, it can be noted that the values for both the axial and the lateral resolution are not satisfactory, except for point reflectors 4, 7 and 8. This is due to the fact that the PSF used in the restoration experiment has been simulated with a point reflector centered at 45 mm, close to point reflector 4, and that point reflectors 7 and 8 are centered as well. The high values of the resolution that one may observe in Table 4.6 are due to the fact that several points are not reconstructed. Regarding the method with the stationary PSF 1, the results are better. This can be explained by the fact that the PSF estimation method returns a sort of “averaged PSF” over the entire image, resulting in a rather uniform value of the resolution. We can nevertheless observe a non-uniformity of the resolution with respect to depth (point reflectors 7 and 8), which emphasizes the inability of the method to capture non-stationary blur.

In the PW experiment, it can be noticed on Table 4.7 that the proposed approach is either close to or better than the best of the methods based on a stationary PSF, which means that

#### 4.4. Non-stationary Blur Modeling and Image Restoration

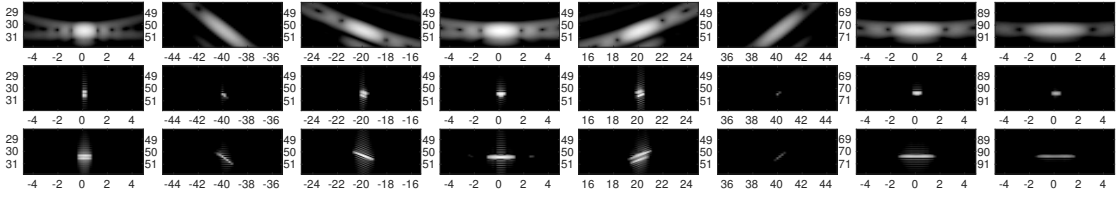


Fig. 4.13. From left to right. Close-up of the log-compressed B-mode images of point reflector 1 to point reflector 8 for the diverging-wave configuration (Fig. 4.12(a)) obtained with standard delay-and-sum beamforming (top row), restored with the proposed model of non-stationary blur (middle row) and restored with the stationary point-spread-function 1 (bottom row).

it represents a best compromise between lateral and axial resolution. However, the results on the lateral resolution are less striking than for the DW experiment which is justified by the reduced non-stationarity of the blur compared to the DW experiment. Regarding the

TABLE 4.7  
COMPARISON OF THE RESTORATION METHODS ON THE POINT-REFLECTOR PHANTOM IN THE PLANE-WAVE EXPERIMENT

	Method	1	2	3	4	5	6	7	8
Lat. Res [mm]	Prop. PSF	<b>0.11</b>	<b>0.11</b>	0.11	<b>0.11</b>	<b>0.11</b>	<b>0.11</b>	<b>0.10</b>	<b>0.11</b>
	Stat. PSF 1	<b>0.11</b>	0.12	0.11	<b>0.11</b>	0.12	0.15	0.13	0.12
	Stat. PSF 2	<b>0.11</b>	0.11	<b>0.10</b>	<b>0.11</b>	<b>0.11</b>	<b>0.11</b>	0.11	<b>0.11</b>
Ax. Res [mm]	Prop. PSF	<b>0.04</b>	0.11	<b>0.04</b>	<b>0.04</b>	<b>0.04</b>	<b>0.04</b>	<b>0.04</b>	<b>0.04</b>
	Stat. PSF 1	0.21	<b>0.04</b>						
	Stat. PSF 2	<b>0.04</b>	0.22	<b>0.04</b>	0.22	0.22	0.22	<b>0.04</b>	<b>0.04</b>

stationary PSF 2, while the lateral resolution is relatively constant along the image, the values of the axial resolution is varying significantly. This is due to our choice of regularization parameter. Indeed, it is set so that all the point reflectors are visible. When the regularization parameter is too high, the first point reflectors that vanish are point reflectors 3 and 7 since they are the ones with the highest mismatch with the centered PSF pattern used in the restoration. With a close look on Tables 4.6 and 4.7, one may highlight some non-uniformity in the values of the resolution obtained with the proposed method. This can be explained by several approximations made in the physical model of the blur:

- no three-dimensional propagation: The proposed model neglects the effects related to the three-dimensional propagation in the Field II simulation, especially the element height and the elevation focus;
- planar/spherical wavefront assumption: We assume that a planar or spherical wavefront, for PW and DW respectively, of constant amplitude propagates in the medium;
- grid mismatch induced by the discretization of the continuous propagation operator and the continuous medium.

**PICMUS Phantom Experiment:** In this experiment, we compare the methods based on the CNR and the lateral and axial resolution, computed on the PICMUS phantom. We use the metrics implemented in the framework of the challenge.

The results are reported in Table 5.1 for the  $\ell_p$ -based restoration, with  $p = 1.3$  and 1.5, and with the proposed non-stationary PSF as well as the two stationary ones.

On Table 4.8, we can observe that the proposed PSF outperforms the other methods on the lateral resolution but not particularly on the axial resolution. Indeed, the variability of the PSF in the axial dimension is mainly due to variations of the pulse-echo waveform induced either by frequency-dependent attenuation or by near-field effects (due to the finite element height). In the proposed simulation, we are in far-field and the frequency-dependent attenuation is not taken into account. Thus, a shift-invariant model is relatively accurate.

In order to illustrate the above remarks, Figure 4.15 displays the x-axis and z-axis sections corresponding to the points 1 and 2 on Figure 4.14, located at  $z = 14$  mm and  $x = 0$  mm and 15 mm, respectively. While the effect of the proposed method is not evident on the axial dimension (bottom row), it is significant in the lateral dimension (top row).

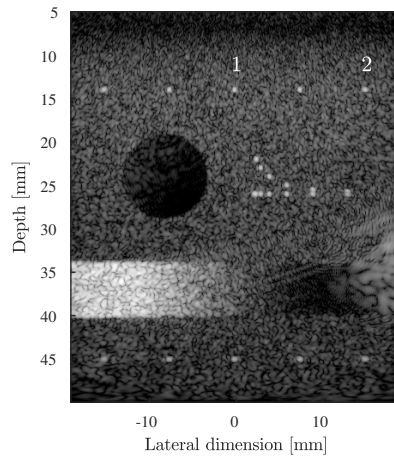


Fig. 4.14. Log-compressed B-mode image of the numerical PICMUS phantom.

Regarding the results of the restoration procedure, we observe that  $p = 1.3$  leads to better resolution (as can be seen on Figure 4.15) but lower contrast than  $p = 1.5$ . This can be explained by a close look at the definition of the CNR. Indeed, it may be deduced from the equation of the CNR that it favors piecewise-continuous regions where  $\sigma_b$  and  $\sigma_t$  tend to 0. On the contrary, high-resolution images exhibit more “spiky” behaviour in speckle region than low-resolution images which usually result in lower mean and higher variance, therefore in a lower CNR. In  $\ell_p$ -based restoration, the value of  $p$  impacts the shape of the GGD prior, resulting in variation of the resolution of the recovered TRF. The lower  $p$ , the tighter the shape of the prior, the better the resolution and the lower the CNR.

**In vivo Carotids Experiment:** Low resolution demodulated RF images of the two carotids, obtained by DAS beamforming without restoration, are displayed on Figs. 4.16(a) and 4.16(e). The B-mode images of the  $\ell_p$ -based restoration technique for the first carotid, and for  $p = 1.5$ ,

#### 4.4. Non-stationary Blur Modeling and Image Restoration

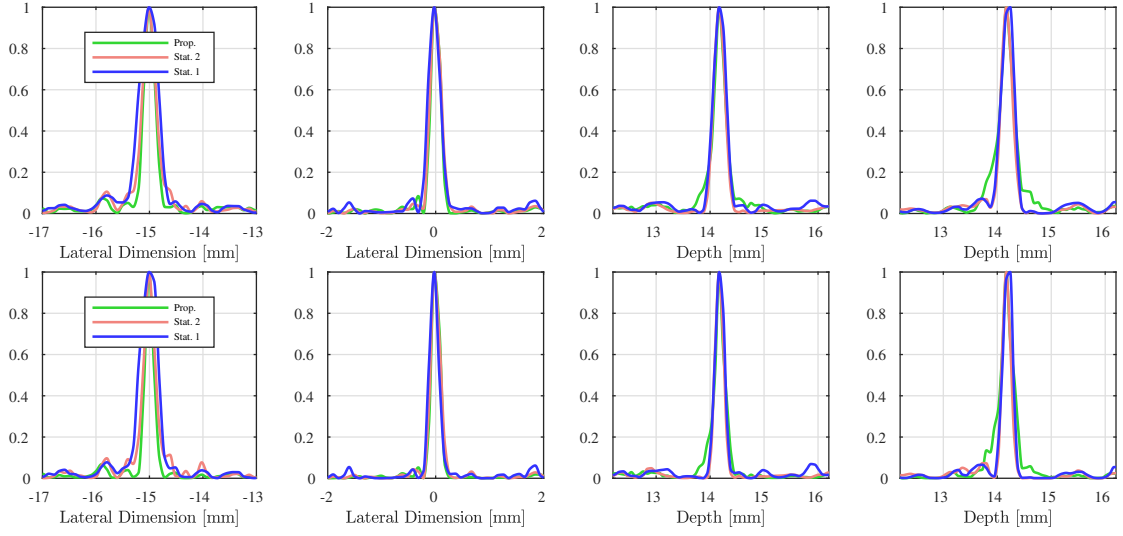


Fig. 4.15. x-axis (top row) and z-axis (bottom row) sections corresponding to the points 1 and 2 of Figure 4.14, located at  $z = 14$  mm and  $x = 0$  mm and 15 mm respectively, for  $p = 1.5$  (2 left plots) and  $p = 1.3$  (2 right plots) and for the different blur models.

TABLE 4.8  
COMPARISON OF THE RESTORATION METHODS ON THE NUMERICAL PICMUS PHANTOM

Value of $p$	CNR [dB]	Method	Lateral Resolution [mm]		Axial Resolution [mm]	
			14 mm	45 mm	14 mm	45 mm
$p = 1.5$	7.00	Prop. PSF	<b>0.21</b>	<b>0.35</b>	0.24	0.28
		Stat. PSF 1	0.25	0.46	<b>0.23</b>	0.30
		Stat. PSF 2	0.30	0.41	0.27	<b>0.26</b>
$p = 1.3$	6.00	Prop. PSF	<b>0.17</b>	<b>0.25</b>	0.20	0.24
		Stat. PSF 1	0.21	0.45	<b>0.17</b>	0.22
		Stat. PSF 2	0.27	0.36	0.20	<b>0.18</b>

are displayed on Figs. 4.16(b), 4.16(c) and 4.16(d). The B-mode images of the  $\ell_p$ -based restoration technique for the second carotid, and for  $p = 1.3$ , are displayed on Fig. 4.16(f), 4.16(g) and 4.16(h).

In order to quantify the benefits of the proposed model of the blur, we rely on the tissue-to-clutter ratio (TCR) [41] and the SNR [41] metrics. The TCR is a widely used measure of the contrast defined as the ratio between the average pixel intensity in a tissue region and in a background region at the same depth (to avoid bias due to time-gain compensation). Formally, it is given by

$$\text{TCR} = 20 \log_{10} \left( \frac{\mu_t}{\mu_b} \right), \quad (4.37)$$

where  $\mu_t$  and  $\mu_b$  designate mean pixel intensities inside the tissue and the background regions, respectively, calculated on the normalized envelope.

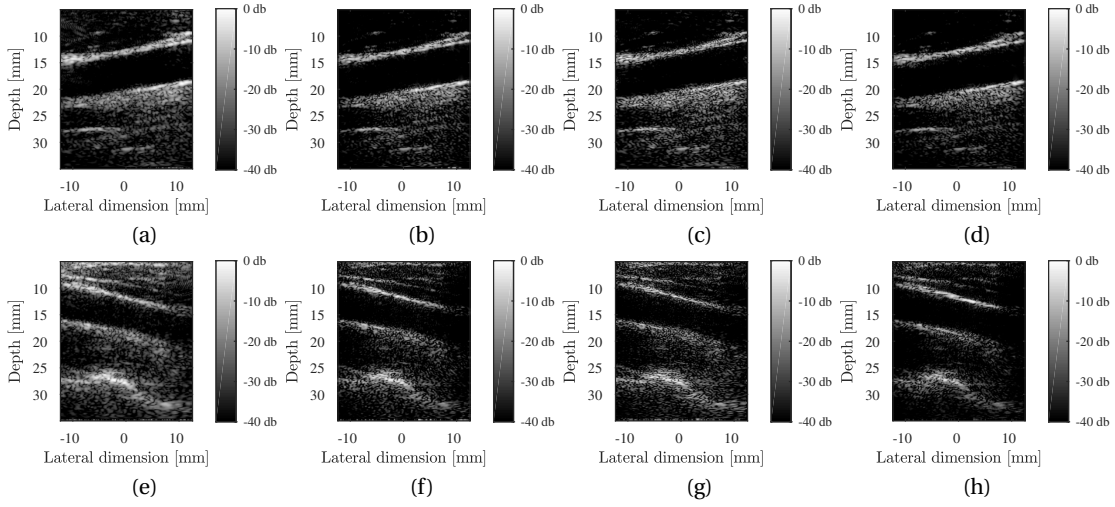


Fig. 4.16. Figures (a-d) present the log-compressed B-mode images of the *in vivo* carotid 1. Figure (a) displays the low-resolution (LR) image reconstructed with the delay-and-sum algorithm. Figure (b) shows the high-resolution (HR) image obtained with the restoration algorithm ( $p = 1.5$ ) with the proposed model of non-stationary blur. Figures (c-d) show the HR image reconstructed with the restoration algorithm ( $p = 1.5$ ) with the stationary point-spread-functions 1 and 2. Figures (e-h) present the log-compressed B-mode images of the *in vivo* carotid 2. Figure (e) displays the LR image reconstructed with the delay-and-sum algorithm. Figure (f) shows the HR image obtained with the restoration algorithm ( $p = 1.3$ ) with the proposed model of non-stationary blur. Figures (g-h) show the HR image reconstructed with the restoration algorithm ( $p = 1.3$ ) with the stationary point-spread-functions 1 and 2.

The SNR is calculated as

$$\text{SNR} = \frac{|\mu_t - \mu_b|}{\sqrt{\sigma_b^2 + \sigma_t^2}}, \quad (4.38)$$

where  $(\mu_t, \mu_b)$  and  $(\sigma_t, \sigma_b)$  are the mean and standard deviation of the pixel intensities of a tissue and a blood regions, respectively, calculated on a linearized image obtained from the log-compressed B-mode image. We choose a background region located inside the carotid artery and a tissue region located at the same depth, as described on Figure 4.17.

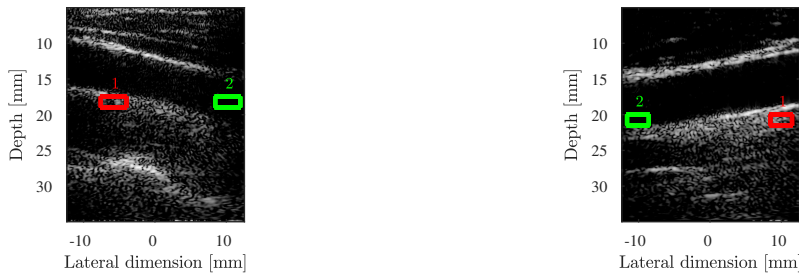


Fig. 4.17. Tissue (1) and blood (2) regions of the *in vivo* carotids used for the computation of the tissue-to-clutter ratio and signal-to-noise ratio.

TCR and SNR values, reported on Table 4.9, demonstrate that the proposed non-stationary model outperforms stationary models for nearly all the experiments. Regarding the impact of

#### 4.4. Non-stationary Blur Modeling and Image Restoration

the value of  $p$ , the same trend as for the PICMUS experiment is observed, i.e. a lower value of  $p$  leads to a lower SNR induced by higher variance of the speckle pattern. In addition, visual assessment of the B-mode images shows that the restoration methods all lead to significantly higher resolution than the unprocessed B-mode image. The deblurring effect is more pronounced for the proposed method and the stationary PSF 1 than for the stationary PSF 2, as can be seen on the artery wall. In addition, the proposed method allows a better reconstruction of the textured area, such as the speckle region under the lower artery wall, than both methods based on a stationary PSF.

TABLE 4.9  
COMPARISON OF THE RESTORATION METHODS ON THE IN VIVO CAROTIDS

Value of $p$	Carotid number	Method	SNR [-]	TCR [dB]
$p = 1.5$	1	Prop. PSF	<b>49.1</b>	<b>29.5</b>
		Stat. PSF 1	27.9	26.2
		Stat. PSF 2	38.6	28.1
$p = 1.3$	2	Prop. PSF	21.5	<b>30.5</b>
		Stat. PSF 1	21.1	24.4
		Stat. PSF 2	<b>36.1</b>	28.4

**On Computation Times of the Proposed Approach:** The objective of this experiment is to empirically validate and discuss the practical implications of the complexity study, performed in Section 4.4.3 in terms of computational times necessary to evaluate the forward blur operator.

More precisely, we consider a PW experiment with the L11-4v probe described in Table 4.5. We compare various grid sizes characterized by the corresponding values of  $N_x$  and  $N_z$ . For each tuple  $(N_x, N_z)$ , we estimate the average evaluation time of the forward blur operator over 10 runs on an Intel Core i7-4930K CPU @ 3.40 GHz equipped with MATLAB R 2017A. We compare the proposed evaluation strategy, the one described by Roquette *et al.* [148] and the evaluation of a stationary blur model using Fourier domain approach.

Table 4.10 reports the computation times of the three methods for the different grid sizes.

We can see that the proposed strategy is two orders of magnitude faster than the one developed by Roquette *et al.* even in the configuration with the smallest grid size. In addition, we observe significant differences in scaling between the two methods resulting from the difference in computational complexity.

We notice that the proposed strategy is several orders of magnitude slower than the stationary method. This is due to the fact that the Fourier-domain approach relies on fast Fourier transforms which have been highly optimized in MATLAB (built-in function) while the proposed approach entirely relies on a non-optimized MATLAB code. First implementations of the propagation and DAS operators on graphical processing units highlight the high potential for parallelizability of the proposed method [187, 188].

In addition, Figure 4.18 displays ratios of evaluation times between the proposed method

TABLE 4.10  
COMPUTATION TIMES OF DIFFERENT BLUR EVALUATION STRATEGIES

$(N_x, N_z)$	Evaluation times		
	Roquette <i>et al.</i>	Proposed	Stationary
(64, 100)	$3.5 \times 10^1$ s	$8.8 \times 10^{-2}$ s	$3.7 \times 10^{-4}$ s
(128, 200)	$3.4 \times 10^2$ s	$1.1 \times 10^{-1}$ s	$6.5 \times 10^{-4}$ s
(256, 200)	$1.6 \times 10^3$ s	$1.9 \times 10^{-1}$ s	$1.2 \times 10^{-3}$ s

and the stationary model for realistic values of the grid sizes. Indeed, we fix  $N_x = 512$  which corresponds to one fourth wavelength spacing and we vary  $N_z$  between 1000 and 8000. We empirically observe that the proposed methods scales better with the grid than the Fourier domain approach which corroborates the theoretical study of the complexity performed in Section 4.4.3.

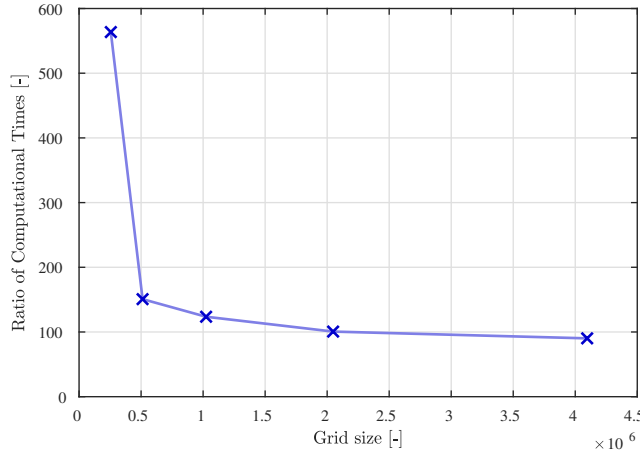


Fig. 4.18. Ratio of computation times between the proposed non-stationary blur evaluation strategy and the Fourier-based evaluation of stationary blur for varying grid sizes.

## 4.5 Discussion and Perspectives

In previous sections of this chapter, we have described three different methods which exploit convex optimization mostly with sparsity prior to tackle various inverse problems related to US imaging. In this section, we propose to discuss some general limitations of these approaches and the solutions that can be developed to tackle these issues.

### 4.5.1 Limitations of Convex Optimization Methods in Ultrasound Imaging

**Relevance of the Prior Terms:** The different techniques explored in this chapter rely on a regularization term, expressed either by sparsity in a SARA model or by the  $\ell_p$ -norm. A natural question that people often ask when I present the methods at scientific conference concerns the relevance of such prior terms in the context of US imaging. This is indeed a very good question that should be discussed.

Regarding the sparsity in the SARA model, it is clear that it outperforms the other existing models and is therefore relatively suited to US imaging. A strength of the model is its ability to reconstruct areas where specular reflection is present, e.g. muscle fibers and artery walls, as it can be seen on the various B-mode images of the carotids. However, we are still not convinced that it is the best model for US imaging. The main reason is that fully-developed speckle patterns are not compressible in the model and are therefore not always accurately reconstructed with the proposed methods. This may be an issue for several applications of UFUS such as vector flow imaging, which are based on speckle tracking. Related to this aspect, vector flow imaging not only requires the speckle to be preserved, but also the coherence of the speckle patterns across various frames such that speckle correlation can be applied. With the proposed approach, we cannot guarantee that such a coherence would be maintained.

A way to better preserve the speckle pattern may consist in using data-driven priors i.e. dictionaries learned on a training set by means of dictionary learning algorithms. This has been recently applied to US image reconstruction [138]. At first sight, such a technique appears to be particularly well suited to US imaging. Indeed, US probes are usually dedicated to a specific application and work at a given frequency. This permits to restrict the size of the training set and facilitates the learning procedure. However, such types of priors suffer from two major drawbacks. The first one is the risk of over-fitting. Indeed, it is a difficult task to build a training set of US images whose quality depends on an infinite variety of parameters such as the positioning of the probe, the patient anatomy, etc. In addition, having a sparsity prior expressed in a dictionary prevents us from using fast transforms, which makes its use more difficult in a real-time environment.

Another interesting approach, recently introduced in US imaging, consists in using different sparsity priors to account for the various components of the RF image. The RF image is typically decomposed in a foreground image, mainly composed of bright reflectors, and a background image composed of fully-developed speckle. Yankelevsky *et al.* [189] suggest to represent the foreground image using the short-time Fourier transform while the background is modeled using dictionary learning. We have also explored an approach based on morphological component analysis [190], where we propose to rely on sparsity in the Dirac basis for the foreground image and on sparsity in the SARA model for the background image [128]. The main drawback of such approaches is the ability to separate the foreground from the background.

**The Reconstruction Algorithm:** The proposed methods perform image reconstruction using a convex optimization algorithm. Such an algorithm necessitates at least few hundreds of iterations to converge. Given the amount of computations performed per iteration, it is very challenging to perform real-time reconstructions even in 2D. With high-end GPU, we have managed to perform 200 iterations of FISTA in few seconds [187].

More importantly a major drawback of proposed reconstruction algorithms is that they depend on the regularization parameter  $\lambda$ , which accounts for the trade-off between the two terms involved in the minimization problem. In practice, we have observed that the methods are highly sensitive to this parameter. Due to the lack of a ground truth image, it may be very difficult to tune such a parameter. In many studies, it is manually tuned such that it gives the

best quality on the image of interest and the process has to be performed for each image. This is a completely non-intuitive use of such a method from a statistical perspective, where the regularizer is used to avoid over-fitting.

A solution to this problem consists in using deep neural networks (DNNs) in order to tune the hyper-parameters, as it has been introduced by Gregor and Lecun with the learned iterative shrinkage thresholding algorithm [191]. Doing so, the efficiency of each iteration of FISTA is maximized and the number of iterations required for convergence is significantly reduced. We have investigated such an approach recently (See Section 4.5.3 for more details.).

### 4.5.2 Towards Compressed Sensing for Ultrasound Imaging

At the time of publication of the corresponding articles, CTMIX and CMIX went one step further towards CS in US image reconstruction. Indeed, they outperformed existing compression strategies, mainly based on simplistic selection strategies. In addition, we provide a comprehensive explanation of the proposed schemes in terms of the limited increase of the mutual coherence induced by the undersampling.

However, we face one major obstacle which is the high coherence of the measurement model. Indeed, CMIX and CTMIX strategies manage to maintain the coherence constant when the number of measurements is decreased, but the coherence remains high relative to the corresponding Welch bound. Such a high mutual coherence may be explained by the fact two consecutive measurements correspond to projections of the medium onto surfaces induced by the round-trip TOFs. Hence, consecutive measurements are highly correlated. In addition, the information contained in each measurement is, by construction, highly localized, which is not favorable for CS where one would like the information to be spread as much as possible. At this point, we naturally wonder whether it would be possible to change the nature of the projections in order to decrease the coherence. In fact, this is a relatively difficult task since projections are the consequence of the propagation of US waves in a homogeneous medium. Thus, if we want to do CS in US imaging, we should entirely rethink the measurement process to satisfy the coherence requirements. In terms of US propagation, a random measurement model implies that each sample of the element raw-data receives contributions from the whole medium. In other words, it means that the duality between time and depth, which is at the heart of US imaging, is not valid anymore since echoes from points at different positions reach the transducer elements at the same time.

Thus, a random measurement model  $H$  is unfeasible via pulse-echo imaging in a homogeneous medium, due to the fact that US waves satisfy the Helmholtz equation. The only way to address this issue consists in placing a heterogeneous medium in front of the US probe as suggested by Kruizinga *et al.* [143]. However, such a new design raises many questions regarding the choice and the modeling of the heterogeneous medium. It can be easily understood that such a medium may not generate a purely random matrix but will be somewhere in-between a purely random case and the highly coherent case of the homogeneous medium. With the recent article of Kruizinga *et al.* [143] and the development of optical computing [192] on the one hand, and the research on acoustic metamaterials on the other hand, we believe that we are at the beginning of CS for US imaging and that there is still plenty of research to

perform on this topic.

### 4.5.3 USSR 2.0: Deep Neural Networks for Ultrasound Image Reconstruction

With the astonishing success of deep learning in various image processing tasks, a boom in using DNN to solve inverse problems in imaging has been observed recently [193–197] with applications to several medical imaging modalities, e.g. CT [198, 199], MRI [200] and US imaging [201–203].

In the framework of model-based US image reconstruction, we see two possible ways of applying DNNs. The first one consists in using the DNN to enhance the RF image obtained with the DAS algorithm as presented in [204]. In such a technique, we train a convolutional neural network (CNN) to perform a regression between the space of RF images reconstructed from few insonifications and the space of RF images reconstructed from significantly more insonifications.

Mathematically, we denote our DNN as a non-linear mapping  $f_\theta : \mathbb{R}^{N_x \times N_z} \rightarrow \mathbb{R}^{N_x \times N_z}$ , where  $\theta$  are the trainable parameters. Given the measurements  $\mathbf{M} \in \mathbb{R}^{N \times N_x^t}$  typically obtained from few PW insonifications, we perform the following computation

$$\tilde{\Gamma} = f_\theta(\mathbf{D}\mathbf{M}), \quad (4.39)$$

where  $\mathbf{D}$  is the DAS operator.

The advantages of such an approach are evident compared to convex optimization. First, it is a non-iterative procedure which requires significantly less computations than a convex optimization algorithm. The inference time of a CNN is of the order to 10 ms on an high-end desktop GPU, which makes (4.39) compatible with real-time imaging. In addition, the proposed reconstruction method does not depend on any hyper-parameter.

We have recently applied such an approach to enhance RF images obtained from a single PW insonification [203]. From left to right, Figure 4.19 shows B-mode images of the numerical PICMUS phantom obtained from 1 PW insonification, reconstructed by a first CNN architecture (U-Net16 in [203]), reconstructed by a second CNN architecture (U-Net64 in [203]) and reconstructed from 75 PW insonifications. We notice the astonishing increase of the image

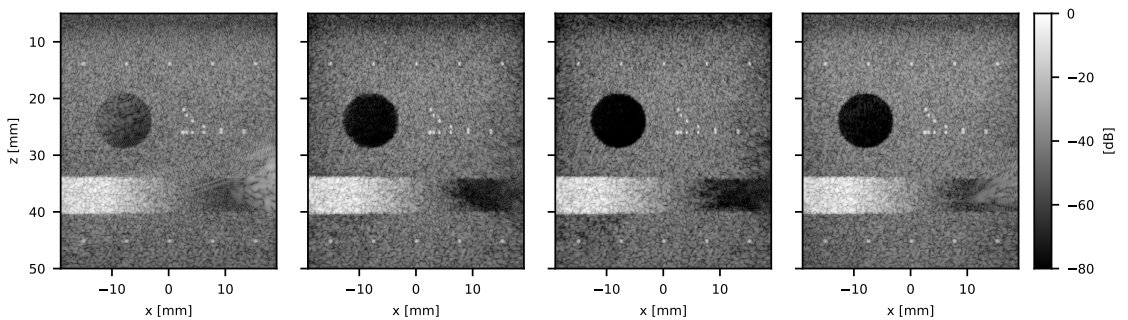


Fig. 4.19. Log-compressed B-mode images of the numerical PICMUS phantom reconstructed (from left to right) with the delay-and-sum algorithm for 1 plane-wave insonification, the delay-and-sum algorithm followed by U-Net16 for 1 plane-wave insonification, the delay-and-sum algorithm followed by U-Net64 for 1 plane-wave insonification, and the delay-and-sum algorithm for 75 plane-wave insonifications. From [203].

quality induced by the CNN.

The second way of exploiting DNNs in the US imaging process consists in replacing the proximal step of FISTA, akin to denoising, by an inference from a DNN, which leads to the following step for FISTA

$$\mathbf{x}^{(n+1)} = f_{\theta} \left( \mathbf{z}^{(n)} - \frac{1}{L} \mathbf{H}^* (\mathbf{H} \mathbf{z}^{(n)} - \mathbf{y}) \right). \quad (4.40)$$

One may interpret the resulting algorithm as a projected gradient descent [198] or as plug-and-play FISTA [205].

Interestingly, (4.39) can be seen as one iteration (up to a scaling factor) of (4.40), when the initial solution is set to  $\mathbf{\Gamma} = \mathbf{0}$ . Such a method is currently under study in the laboratory.

# 5 Compressive Multiplexing of Ultrasound Signals

Essentially, all models are wrong, but some are useful

---

*Statistics for Experimenters*  
Georges P. Box

Three-dimensional US imaging requires dense matrix arrays of thousands of transducer elements. Connecting such a number of elements to the back-end computer would necessitate an extensive number cables, which is either unfeasible or prohibitively expensive.

Nowadays, only few cumbersome research systems are capable of directly connecting 1024-element-matrix arrays [30–32]. Hence, much research has focused on the reduction of the number transducer elements or coaxial cables with application to 3D imaging.

Sparse arrays techniques have been extensively studied to perform 3D imaging with a reduced number of elements [206]. Many different strategies have been designed such as random sparse arrays [207, 208], Vernier arrays [209] and row-column addressed arrays [210–212]. While proposing a notable reduction on the number of transducer elements, such methods have a significant impact on the image quality due to a higher level of side lobes and possibly the apparition of grating lobes [206].

Alternatives to sparse array techniques have also been widely studied, including mechanical scanning with free-hand [213] or motorized [214] 1D arrays, time multiplexing [215–217] and micro-beamforming, where part of the imaging process is performed analogically in the probe head [218]. Like sparse array techniques, these methods impact the image quality as well as the temporal resolution (for time multiplexing and mechanical scanning).

In this chapter, we propose a novel method to reduce the number of coaxial cables while maintaining a significantly higher quality than existing approaches. The technique exploits the well-known CS framework to compress the signals in the analog domain and benefits from recent advances in US signal modeling on the reconstruction side. The remainder of the chapter is organized as follows. Section 5.1 introduces the CS framework from the sensing to the reconstruction. Section 5.2 introduces the concept of joint-sparsity with partially known support, which will be useful for the proposed method. Section 5.3 details two low-dimensional models of echo-signals, which are essential ingredients for the proposed compression technique, described in Section 5.4.

## 5.1 A Short Tour on Compressed Sensing

### 5.1.1 Sensing Sparse Signals: A Novel Paradigm

Sampling, i.e. the process of converting a continuous signal into a discrete sequence, has been revolutionized by the seminal work of Shannon and Nyquist (independently by Whittaker and Kotelnikov). They introduced the well-known Whittaker-Kotelnikov-Shannon (WKS) sampling theorem for continuous-time bandlimited signals [219, 220]. The theorem states that if a signal contains no frequency higher than  $\omega_{max}$ , it can be completely determined by a set of uniformly spaced samples, taken at a frequency higher than  $\omega_{max}$ , the well-known *Nyquist rate*.

This work has marked the beginning of information theory since it has permitted to move from an entirely analog world to a digital one, in which signals are encoded with bits and stored in computer memory.

Since the 1990s, modeling signals through sparsity has raised a considerable interest in various fields of applied mathematics, e.g. in signal compression [221] and denoising [222] and in statistics, where the LASSO is a well-known shrinkage method to avoid over-fitting [109].

Recently, the use of sparsity has been extended to signal sensing in the so-called CS framework, introduced independently by Candes [130] and Donoho [223]. The main idea of CS relies on the fact that the degrees of freedom of a discrete signal can be much smaller than its length. For continuous-time signals, this notion has been quantified by the “rate of innovation”, which characterizes the sparsity of a signal per unit of time [224, 225]. For some parametric signals with FRI, e.g. streams of Diracs, or streams of pulses [224], the rate of innovation can be significantly lower than the Nyquist rate.

CS differs from other sampling paradigms such as WKS or FRI, in the sense that it works on finite dimensional vectors in  $\mathbb{R}^n$ . Hence, it leverages results from concentration of measure and probability theory rather than harmonic analysis.

### 5.1.2 Sensing and Recovery Guarantees for Sparse Signals

We say that a vector  $\mathbf{x} \in \mathbb{R}^n$  is  $k$ -sparse, with  $k < n$ , if it has at most  $k$  non-zero components. A common measure of sparsity is the  $\ell_0$ -norm defined as

$$\|\mathbf{x}\|_0 = \lim_{p \rightarrow 0} \|\mathbf{x}\|_p^p = |\text{supp}(\mathbf{x})|. \quad (5.1)$$

We also define the set of  $k$ -sparse vectors of  $\mathbb{R}^n$  as

$$\Sigma_k = \{\mathbf{x} \in \mathbb{R}^n \mid \|\mathbf{x}\|_0 \leq k\}. \quad (5.2)$$

The set  $\Sigma_k$  is non-linear since the sum of two  $k$ -sparse vectors is  $2k$ -sparse in general, which makes it difficult to manipulate. Geometrically speaking,  $\Sigma_k$  can be seen as a finite union of  $\binom{n}{k}$   $k$ -dimensional canonical subspaces of  $\mathbb{R}^n$  [226]. This interpretation gives a flavor of how difficult the recovery of  $k$ -sparse signals can be. It would require to identify a canonical subspace among  $\binom{n}{k}$  candidates, which is a NP-hard problem.

In many scenarios, signals are not sparse themselves but admit a sparse representation in a

basis or a frame,  $\Psi: \mathbb{R}^n \rightarrow \mathbb{R}^d$ ,  $d \geq n$ , i.e. the coefficients  $\mathbf{c} = \Psi^* \mathbf{x}$  are sparse.

We define a sensing procedure as a linear mapping  $\mathbf{A}: \mathbb{R}^n \rightarrow \mathbb{R}^m$  (equivalently a matrix  $\mathbf{A} \in \mathbb{R}^{m \times n}$ ), where  $m < n$ , such that  $\mathbf{y} = \mathbf{A}\mathbf{x} \in \mathbb{R}^m$ . In CS, we acquire linear non-adaptive measurements, in the sense that the matrix  $\mathbf{A}$  is fixed in advance.

Signal recovery is formulated as the following minimization problem

$$\min_{\mathbf{x} \in \mathbb{R}^n} \|\mathbf{x}\|_0 \text{ subject to } \mathbf{y} = \mathbf{A}\mathbf{x}, \quad (5.3)$$

which is a NP-hard problem [227].

A way to make Problem (5.3) more tractable consists in replacing the  $\ell_0$ -norm by the  $\ell_1$ -norm which leads to the well-known basis pursuit problem [228]

$$\min_{\mathbf{x} \in \mathbb{R}^n} \|\mathbf{x}\|_1 \text{ subject to } \mathbf{y} = \mathbf{A}\mathbf{x}. \quad (5.4)$$

Problems (5.3) and (5.4) can be extended to noisy scenarios by considering an inequality constraint of the form  $\|\mathbf{y} - \mathbf{A}\mathbf{x}\|_2 \leq \epsilon$  which leads to the well-known basis pursuit denoising problem defined as

$$\min_{\mathbf{x} \in \mathbb{R}^n} \|\mathbf{x}\|_1 \text{ subject to } \|\mathbf{y} - \mathbf{A}\mathbf{x}\|_2 \leq \epsilon. \quad (5.5)$$

CS provides a set of requirements on  $\mathbf{A}$  and  $k$  to provide guarantees of uniqueness for the solutions of Problems (5.3) and (5.4).

In the following, we review the most important theorems necessary to gain some basic understanding of CS. We refer the interested reader to [229] for an in-depth overview of CS.

The first theorem, detailed below, is rather simple and sets a necessary and sufficient condition on  $\mathbf{A}$  so that there is a unique  $k$ -sparse vector, solution of (5.3).

**Theorem 1** (Corollary 1 of [230]). *The  $k$ -sparse vector  $\mathbf{x} \in \Sigma_k$ , such that  $\mathbf{y} = \mathbf{A}\mathbf{x}$ , is the unique solution to Problem (5.3) if and only if*

$$\text{spark}(\mathbf{A}) > 2k. \quad (5.6)$$

This theorem states that the solution of (5.3) is unique if and only if the null-space of  $\mathbf{A}$  does not contain any  $2k$ -sparse vector. Intuitively, this makes sense. Indeed, if two non-identical  $k$ -sparse vectors are solutions of (5.3), then their difference is a  $2k$ -sparse vector and lies in the null-space of  $\mathbf{A}$ . This is not possible if  $\text{spark}(\mathbf{A}) > 2k$ .

Moreover, since  $\text{spark}(\mathbf{A}) \in [2, m + 1]$ , Theorem 1 sets a lower bound on the number of measurements as  $m \geq 2k$ . Such a lower bound makes sense since a  $k$ -sparse signal has exactly  $2k$  degrees of freedom.

In the CS literature, the well-known tool used to ensure stability and recovery guarantee is the restricted isometry property (RIP), introduced by Candès [231] and reminded in the definition hereafter.

**Definition 5** (RIP [231]). *A matrix  $\mathbf{A} \in \mathbb{R}^{m \times n}$  satisfies the RIP or order  $k$  if there exists  $\delta_k \in [0, 1]$*

such that

$$(1 - \delta_k) \|\mathbf{x}\|_2^2 \leq \|\mathbf{Ax}\|_2^2 \leq (1 + \delta_k) \|\mathbf{x}\|_2^2, \forall \mathbf{x} \in \Sigma_k.$$

The RIP property states that the matrix  $\mathbf{A}$  acts as a quasi-isometry on the set of  $k$ -sparse vectors. In addition, the eigenvalues of the Gram matrix  $\mathbf{A}_J^\top \mathbf{A}_J$ , for any subset  $J \subset \{1, \dots, n\}$  of cardinality  $k$ , are in the following interval  $[1 - \delta_k, 1 + \delta_k]$ , which makes the Gram matrix invertible.

An interesting case corresponds to the  $2k$ -RIP which can be written as follows

$$(1 - \delta_{2k}) \|\mathbf{x} - \mathbf{x}'\|_2^2 \leq \|\mathbf{Ax} - \mathbf{Ax}'\|_2^2 \leq (1 + \delta_{2k}) \|\mathbf{x} - \mathbf{x}'\|_2^2, \forall (\mathbf{x}, \mathbf{x}') \in \Sigma_k^2.$$

This is very close to the Johnson-Lindenstrauss lemma [232] applied to the set of  $k$ -sparse vectors, if  $\delta_{2k} \leq 1/2$ , and the measurements can be seen as stable embeddings of the  $k$ -sparse vectors.

Additionally, we have the following proposition that relates the RIP property to the spark.

**Proposition 3** (RIP and spark). *If a matrix  $\mathbf{A} \in \mathbb{R}^{m \times n}$  satisfies the RIP property of order  $2k$ , with  $\delta_{2k} < 1$ , then  $\text{spark}(\mathbf{A}) > 2k$ .*

*Proof.* If  $\mathbf{A} \in \mathbb{R}^{m \times n}$  satisfies the RIP property of order  $2k$ , with  $\delta_{2k} < 1$ , then we have that  $\|\mathbf{Ax}\|_2^2 \geq (1 - \delta_{2k}) \|\mathbf{x}\|_2^2 > 0, \forall \mathbf{x} \in \Sigma_{2k} \setminus \{\mathbf{0}\}$ . Thus,  $\mathcal{N}(\mathbf{A}) \cap \Sigma_{2k} = \{\mathbf{0}\} \Leftrightarrow \text{spark}(\mathbf{A}) > 2k$ .  $\square$

Thus, Theorem 1 holds for a matrix  $\mathbf{A}$  that satisfies the RIP property of order  $2k$ .

So far, we have established recovery guarantees for Problem (5.3) in terms of spark and RIP of the measurement matrix. However, Problem (5.3) is NP-hard. In order for CS to be more practical, recovery guarantees for the convex basis pursuit problem should be established.

To provide an exact recovery guarantee of  $k$ -sparse vectors with basis pursuit, we need a slightly stronger condition on the matrix  $\mathbf{A}$  which is detailed in the theorem hereafter.

**Theorem 2** (Noiseless recovery. Theorem 1.2 of [233]). *The  $k$ -sparse vector  $\mathbf{x} \in \Sigma_k$  such that  $\mathbf{y} = \mathbf{Ax}$  is the unique solution of (5.4) if  $\mathbf{A}$  satisfies the RIP property of order  $2k$ , with  $\delta_{2k} < \sqrt{2} - 1$ .*

This is a remarkable result that proves exact recovery of  $k$ -sparse vectors by solving a simple convex optimization problem.

In addition, Theorem 2 can be extended to the case of bounded additive noise as follows.

**Theorem 3** (Recovery under bounded noise. Theorem 1.3 of [233]). *Consider that  $\mathbf{x} \in \Sigma_k$  is measured by  $\mathbf{y} = \mathbf{Ax} + \mathbf{e}$ ,  $\|\mathbf{e}\|_2 \leq \epsilon$ , such that  $\mathbf{A}$  satisfies the RIP property of order  $2k$ , with  $\delta_{2k} < \sqrt{2} - 1$ . The solution  $\mathbf{x}^*$  of (5.5) obeys*

$$\|\mathbf{x} - \mathbf{x}^*\|_2 \leq C_1 \epsilon,$$

$$\text{where } C_1 = \frac{4\sqrt{1+\delta_{2k}}}{1-(1+\sqrt{2})\delta_{2k}}.$$

There is still a major issue related to the recovery conditions stated in the above theorems. Indeed, the calculation of the RIP constant of order  $k$  is a NP-hard problem, similar to Problem 5.3, since it requires a combinatorial search over  $\binom{n}{k}$   $k$  sub-matrices.

To address this problem, we introduce the notion of coherence, defined as follows for  $\mathbf{A} \in \mathbb{R}^{m \times n}$

$$\mu(\mathbf{A}) = \max_{\substack{i, j \in \{1, \dots, n\} \\ i \neq j}} \frac{|\mathbf{A}_i^\top \mathbf{A}_j|}{\|\mathbf{A}_i\|_2 \|\mathbf{A}_j\|_2}. \quad (5.7)$$

The coherence is the maximal inner product between two columns of  $\mathbf{A}$  which quantifies whether  $\mathbf{A}$  is closed to a basis or not. Using the Gershgorin circle theorem, it can be related to the spark via the following inequality

$$\text{spark}(\mathbf{A}) > 1 + \frac{1}{\mu(\mathbf{A})}. \quad (5.8)$$

Thus, the condition in Theorem 1 can be straightforwardly transformed into a condition on the coherence, far simpler to check.

Additionally, Theorem 4 provides conditions on the coherence for stable recovery in the presence of bounded additive noise.

**Theorem 4** (Recovery under bounded noise. Theorem 3.1 of [234]). *Consider that  $\mathbf{x} \in \Sigma_k$  is measured by  $\mathbf{y} = \mathbf{A}\mathbf{x} + \mathbf{e}$ ,  $\|\mathbf{e}\|_2 \leq \epsilon$ , such that  $\mathbf{A}$  has coherence  $\mu$  and  $k < (1 + 1/\mu)/4$ . The solution  $\mathbf{x}^*$  of (5.5) obeys*

$$\|\mathbf{x} - \mathbf{x}^*\|_2 \leq \frac{\|\mathbf{e}\|_2 + \epsilon}{\sqrt{1 - \mu(4k - 1)}}. \quad (5.9)$$

### 5.1.3 Sensing Matrices in Compressed Sensing

So far, we have established performance guarantees under RIP conditions on the sensing matrix. We now provide sensing matrices that satisfy such RIP conditions (or coherence conditions).

First, we can set a lower bound on the number of measurements for a sensing matrix to satisfy the RIP property of order  $2k$ . More precisely, Davenport [229] has shown that if  $\mathbf{A} \in \mathbb{R}^{m \times n}$  satisfies the RIP property of order  $2k$ , with  $\delta_{2k} \leq 1/2$ , then

$$m \geq Ck \log\left(\frac{n}{k}\right),$$

with  $C = \frac{1}{2} \log(\sqrt{24} + 1)$ .

This statement gives some hope since the lower bound is logarithmic with respect to  $n$  and linear with respect to  $k$ , which means that it may be possible to drastically reduce the number of measurements.

Random matrices are very appealing candidates for such a task. Intuitively, this makes sense given the analogy between CS and random projections (and the Johnson-Lindenstrauss lemma) that we previously drew.

More precisely, consider two numbers  $(\epsilon, \delta) \in [0, 1]^2$ . It can be shown (Theorem 2.12 in [235]) that Gaussian random matrices (where the entries are drawn from a normal distribution with variance  $1/m$ ) and Bernoulli random matrices (where the entries take the values  $\pm 1/\sqrt{m}$  with equal probability) satisfy the RIP property of order  $k$ , with  $\delta_k \leq \delta$ , with probability of at least  $1 - \epsilon$  if

$$m \geq C\delta^{-2} \left( k \log\left(\frac{n}{k}\right) + \log(\epsilon^{-1}) \right), \quad (5.10)$$

for a universal constant  $C > 0$ . Thus, using random matrices, we can achieve a lower bound on the number measurements close to the one derived by Davenport. Hence, random matrices are optimal sensing matrices in this context.

In addition, random matrices are universal in the sense that given a basis  $\Psi$  and a random matrix  $A$  that satisfies the RIP property with high probability, then  $A\Psi$  also satisfies the RIP property with high probability. Intuitively, it is clear that if  $A$  is a Gaussian matrix, then  $A\Psi$  is also Gaussian.

In practice, Gaussian matrices are not feasible and several architectures have proposed sub-optimal approaches such as the random convolution [236], the compressive multiplexer [237], the random modulator pseudo-integrator [238], the spread spectrum technique [239], the random demodulator [240], the modulated wideband converter [241]. Recently, CS matrices have also been approximated by multiply scattering media in optics [192, 242] and by a delay mask in US imaging [143].

## 5.2 Joint Sparsity with Partially Known Support

### 5.2.1 Joint Sparsity: Compressed Sensing Applied to Multiple Measurement Vectors

The CS problem described in Section 5.1 is usually denoted as a single measurement vector (SMV) problem since we are interested in estimating a single vector  $\mathbf{x} \in \mathbb{R}^n$  from compressed linear measurements  $\mathbf{y} = A\mathbf{x} \in \mathbb{R}^m$ .

The multiple measurement vectors (MMV) problem addresses the recovery of multiple sparse vectors that share a common non-zero support. Formally, we consider  $N$   $k$ -sparse vectors of  $\mathbb{R}^n$  stacked in a matrix  $\mathbf{X} \in \mathbb{R}^{n \times N}$ , such that  $\|\mathbf{X}_i\|_0 \leq k$ , for  $i = 1, \dots, N$ . We measure these vectors with a sensing matrix  $A \in \mathbb{R}^{m \times n}$  such that  $\mathbf{Y} = A\mathbf{X} \in \mathbb{R}^{m \times N}$ .

We define  $\|\mathbf{X}\|_{0,\text{row}}$ , the extension of the  $\ell_0$ -norm to the MMV setting, as

$$\|\mathbf{X}\|_{0,\text{row}} = \sum_{i=1}^n \mathbf{1}_{\|\mathbf{X}_{(i)}\|_0 > 0},$$

where  $\|\cdot\|$  is an arbitrary norm. Thus,  $\|\mathbf{X}\|_{0,\text{row}}$  counts the number of non-zero rows of  $\mathbf{X}$ .

We also define the set of  $k$ -row sparse matrices of  $\mathbb{R}^{n \times N}$  as follows

$$\Sigma_k^{(n,N)} = \{\mathbf{X} \in \mathbb{R}^{n \times N} \mid \|\mathbf{X}\|_{0,\text{row}} \leq k\}. \quad (5.11)$$

The structural assumption that the columns  $\mathbf{X}_i$  share the same support induces that  $\mathbf{X} \in \Sigma_k^{(n,N)}$ .

Using the zero-row norm, the MMV problem is recast as the following minimization problem

$$\min_{\mathbf{X} \in \mathbb{R}^{n \times N}} \|\mathbf{X}\|_{0,\text{row}} \text{ subject to } \mathbf{Y} = \mathbf{A}\mathbf{X}. \quad (5.12)$$

Evidently, the MMV problem can be solved by considering  $N$  independent SMV problems but we would completely lose the additive structure induced by the shared non-zero support. In such a case, the recovery guarantees are the same as in the SMV problem.

Chen and Huo [243] and later Davies and Eldar [244] have quantified the benefits of the additional structure in terms of an upper bound on the sparsity as described in Theorem 5.

**Theorem 5** (Uniqueness condition for the MMV problem. Theorem 2 of [244]). *The matrix  $\mathbf{X} \in \Sigma_k^{(n,N)}$  is the unique solution of (5.12) if and only if  $\mathbf{Y} = \mathbf{A}\mathbf{X}$  and*

$$k < \frac{\text{spark}(\mathbf{A}) - 1 + \text{rank}(\mathbf{Y})}{2}. \quad (5.13)$$

Additionally, Davies and Eldar have demonstrated (Lemma 1 in [244]) that (5.13) is equivalent to

$$k < \frac{\text{spark}(\mathbf{A}) - 1 + \text{rank}(\mathbf{X})}{2}. \quad (5.14)$$

By comparing (5.14) with (5.6), we immediately see the benefits of the shared support which provides an additional term, related to the rank of the measurements, to the upper bound on the sparsity. This is interesting since it shows that in order to devise a method to solve (5.12), we should account for the information contained in the rank of  $\mathbf{Y}$ .

### 5.2.2 Recovery Methods in Joint Sparsity

In this thesis, we focus on two groups of methods, namely multiple signal classification (MUSIC)-based techniques and greedy approaches. Many other techniques have been developed such as mixed-norm algorithms which exploit extensions of  $\ell_1$ -minimization algorithms [245–247]. See [248] for a review of these methods.

**MUSIC-based Recovery:** Feng and Bresler [249] have demonstrated that  $\mathbf{X}$  can be retrieved by singular value decomposition (SVD) of  $\mathbf{Y}$ , when  $\text{rank}(\mathbf{Y}) = k$ , in a similar fashion to MUSIC in estimation of direction of arrival.

Indeed, we have, by definition, that the column space of  $\mathbf{Y}$ ,  $\mathcal{R}(\mathbf{Y})$ , is a subset of the column space of  $\mathbf{A}$ ,  $\mathcal{R}(\mathbf{A})$ . In addition, assume that the non-zero rows of  $\mathbf{X}$  are indexed by  $J \subset \{1, \dots, n\}$ , such that

$$\mathbf{Y} = \mathbf{A}\mathbf{X} = \mathbf{A}_J \mathbf{X}_{(J)}. \quad (5.15)$$

In the full-rank case, and when  $N > n$ , we have that  $\text{rank}(\mathbf{Y}) = \text{rank}(\mathbf{A}_J) = k$  and  $\mathcal{R}(\mathbf{Y}) = \mathcal{R}(\mathbf{A}_J)$ . By SVD of  $\mathbf{Y}$ , we compute an orthonormal basis  $\mathbf{Q} \in \mathbb{R}^{n \times k}$  of  $\mathcal{R}(\mathbf{Y})$ . Since  $\mathcal{R}(\mathbf{Y}) =$

$\mathcal{R}(A_J)$ , we identify the index set  $J$  as

$$\forall i \in \{1, \dots, n\}, \|(I - \mathbf{Q}\mathbf{Q}^\top) \mathbf{A}_i\|_2 = \mathbf{0} \Leftrightarrow i \in J, \quad (5.16)$$

where  $I - \mathbf{Q}\mathbf{Q}^\top = \mathbf{P}_{\mathcal{R}(Y)^\perp}$ , is the projection on the orthogonal complement of  $\mathcal{R}(Y)$ .

$\mathbf{X}_{(J)}$  is finally obtained using the pseudo-inverse of  $\mathbf{A}_J$  as  $\mathbf{X}_{(J)} = \mathbf{A}_J^\dagger \mathbf{Y}$ .

The two main drawbacks of this approach is the full-rank condition, which is not achievable in every application, and the robustness in a noisy scenario. Indeed, in the presence of noise, the signal subspace can only be approximated (using well known threshold methods [250]) and recovery is no longer guaranteed.

**Greedy Algorithms:** Several greedy algorithms, designed for the SMV problem, have been extended to the MMV problem leading to the simultaneous orthogonal matching pursuit [251, 252], the simultaneous normalized hard thresholding pursuit [253], the simultaneous compressive sampling matching pursuit [253] and the simultaneous normalized iterative hard thresholding (SNIHT) [253]. The recovery guarantees are the same as for the SMV problem and the main benefit of such algorithms is the ability to recover simultaneously the set of  $k$ -sparse vectors.

We now focus on the extension of the iterative hard thresholding (IHT) algorithm, coined as theSNIHT algorithm, where the main iteration of IHT is replaced by the following one

$$\mathbf{X}^{(i)} = \mathcal{H}_k \left( \mathbf{X}^{(i-1)} + \mu \mathbf{A}^\top (\mathbf{Y} - \mathbf{A}\mathbf{X}^{(i-1)}) \right), \quad (5.17)$$

where  $\mu \in \mathbb{R}_+$  is a step-size and  $\mathcal{H}_k(\mathbf{X})$  is a non-linear operator that sets all but the  $k$  rows of  $\mathbf{X}$  with largest  $\ell_2$ -norm to 0.

SNIHT proposes an extension to normalized IHT based on a specific update of the step size, described in Algorithm 5.

---

**Algorithm 5** SNIHT. Algorithm 1 of [253]

---

**Require:**  $A, Y, k$

**initialization:**  $i = 1, \mathbf{R}^0 = \mathbf{Y}, \mathbf{X}^0 = \mathbf{0}$

**repeat**

$$\omega^{(i)} = \left\| (\mathbf{A}^* \mathbf{R}^{(i-1)})_{(J^{(i-1)})} \right\|_F^2 / \left\| \mathbf{A}_{J^{(i-1)}} (\mathbf{A}^* \mathbf{R}^{(i-1)})_{(J^{(i-1)})} \right\|_F^2$$

$$\mathbf{X}^{(i)} = \mathcal{H}_k \left( \mathbf{X}^{(i-1)} + \omega^{(i)} (\mathbf{A}^* \mathbf{R}^{(i-1)}) \right)$$

$$J^{(i)} = \text{supp}(\mathbf{X}^{(i)})$$

$$i \leftarrow i + 1$$

**until** a stopping criterion is met

**return**  $\mathbf{X}^{(i)}$

---

**Subspace Pursuit Methods:** Subspace pursuit methods identify the subspace  $\mathcal{R}(A_J)$  iteratively. Two very similar approaches, namely rank aware orthogonal recursive matching pursuit (RA-ORMP) and orthogonal subspace matching pursuit (OSMP), have been suggested independently by Davies and Eldar [244] and Lee *et al.* [250], respectively.

OSMP, detailed in Algorithm 6, works as follows. First, it estimates the signal subspace  $\hat{S}$  and therefore an initial index set  $J$  from the measurements  $\mathbf{Y}$  by SVD in a similar way to MUSIC-based methods. Then, given the estimated index set  $J$  from previous iteration and the signal subspace  $\hat{S}$ , we add to  $J$  the index  $i \in \{1, \dots, n\} \setminus J$  such that

$$i = \operatorname{argmax}_{k \in \{1, \dots, n\} \setminus J} \frac{\left\| \mathbf{P}_{\mathcal{R}(\mathbf{P}_{\mathcal{R}(A_J)}^\perp \mathbf{P}_{\hat{S}})} \mathbf{A}_k \right\|_2}{\left\| \mathbf{P}_{\mathcal{R}(\mathbf{P}_{\mathcal{R}(A_J)}^\perp)} \mathbf{A}_k \right\|_2}. \quad (5.18)$$

RA-ORMP slightly differs from OSMP in the sense that there is no estimation of the signal subspace and the index  $i$  is chosen as

$$i = \operatorname{argmax}_{k \in \{1, \dots, n\} \setminus J} \frac{\left\| \mathbf{P}_{\mathcal{R}(\mathbf{P}_{\mathcal{R}(A_J)}^\perp \mathbf{Y})} \mathbf{A}_k \right\|_2}{\left\| \mathbf{P}_{\mathcal{R}(\mathbf{P}_{\mathcal{R}(A_J)}^\perp)} \mathbf{A}_k \right\|_2}. \quad (5.19)$$

In fact, the two iterations are the same in the noiseless case since  $\hat{S} = \mathcal{R}(\mathbf{Y})$ . In the noisy scenario, the noise induces that  $\operatorname{rank}(\mathbf{Y}) = \min(m, N)$  and the signal subspace differs from  $\mathcal{R}(\mathbf{Y})$ .

Hence, we notice that subspace pursuit methods look for the most correlated subspace to  $\mathcal{R}(\mathbf{P}_{\mathcal{R}(A_J)}^\perp \mathbf{P}_{\hat{S}})$  (resp.  $\mathcal{R}(\mathbf{P}_{\mathcal{R}(A_J)}^\perp \mathbf{Y})$  for RA-ORMP), among the one dimensional subspaces  $\mathcal{R}(\mathbf{P}_{\mathcal{R}(A_J)}^\perp \mathbf{A}_k)$ , where the correlation can be expressed in terms of the angle between two subspaces [250]. This justifies the term ‘‘subspace pursuit’’ with analogy to the matching pursuit technique developed for sparse approximation.

---

**Algorithm 6** OSMP. Algorithm 4 of [250]

---

**Require:**  $A, \mathbf{Y}, k$

**initialization:**  $i = 1, J = \emptyset$

$\mathbf{P}_{\hat{S}} \in \mathbb{R}^{m \times m} \leftarrow$  Estimation of the signal subspace

**repeat**

$$i \leftarrow \operatorname{argmax}_{k \in \{1, \dots, n\} \setminus J} \left\| \mathbf{P}_{\mathcal{R}(\mathbf{P}_{\mathcal{R}(A_J)}^\perp \mathbf{P}_{\hat{S}})} \mathbf{A}_k \right\|_2 / \left\| \mathbf{P}_{\mathcal{R}(\mathbf{P}_{\mathcal{R}(A_J)}^\perp)} \mathbf{A}_k \right\|_2$$

$$J \leftarrow J \cup \{i\}$$

**until**  $|J| = k$

**return**  $J$

---

Regarding the recovery guarantees of both algorithms, they have been proved to exactly recover  $k$ -row sparse vectors in the full-rank case.

**Subspace Augmented MUSIC Methods:** Subspace augmented MUSIC methods target rank-defective cases when  $\text{rank}(\mathbf{Y}) = r < k$ . They provide a two-stage framework which combines the MUSIC based approach to estimate the signal subspace with a subspace pursuit method (or more recently a semi-supervised classification [254]) to estimate the remaining  $k - r$  indices. Two almost equivalent frameworks have been proposed in the literature, namely subspace augmented MUSIC (SA-MUSIC) [250] and compressive MUSIC (CS-MUSIC) [248].

In SA-MUSIC, the signal subspace  $\hat{S}$  is firstly estimated from  $\mathbf{Y}$ . Then,  $k - r$  indices are estimated using the previously described OSMP algorithm. Finally,  $J$  is retrieved via MUSIC-based recovery on the augmented space  $\tilde{S} = \hat{S} + \mathcal{R}(\mathbf{A}_{J_1})$ , where  $J_1$  is the set of  $k - r$  indices identified by OSMP.

In CS-MUSIC,  $k - r$  indices are estimated using any MMV algorithm. However, the remaining  $r$  components are not estimated using MUSIC as in SA-MUSIC, but using a generalized MUSIC criterion [248].

### 5.2.3 Joint Sparsity with Partially Known Support

In some applications of CS, part of the signal support is known *a priori*. For instance, this is the case when one wants to recover a time sequence of sparse signals with the support slowly changing across time. In such cases, the idea consists in solving a CS problem on the unknown part of the support only, resulting in fewer unknown coefficients and hopefully weaker recovery conditions than conventional CS. The concept has been introduced independently by von Borries *et al.* [255], Khajehnejad *et al.* [256] and Vaswani and Lu [257].

Puts formally, consider a  $k$ -sparse signal  $\mathbf{x} \in \Sigma_k$  whose non-zero support is  $J \subset \{1, \dots, n\}$  such that  $J = J_0 \cup J_1$  and  $J_0$  is known. Vaswani and Lu have proposed to solve the following  $\ell_0$ -minimization problem

$$\min_{\mathbf{x} \in \mathbb{R}^n} \|\mathbf{x}_{J_0}\|_0 \text{ subject to } \mathbf{y} = \mathbf{A}\mathbf{x}. \quad (5.20)$$

They have also provided the corresponding  $\ell_1$ -minimization problem. Regarding this problem, Khajehnejad *et al.* and later Friedlander *et al.* [258] have proposed a more general formulation based on a weighted  $\ell_1$ -norm.

Recovery guarantees for (5.20) have been established in [257]. More particularly, it has been demonstrated that the solution of (5.20) is unique if  $\mathbf{A}$  satisfies the RIP property of order  $2k - |J_0|$ , with  $\delta_{2k - |J_0|} < 1$ , which is weaker than the requirement  $\delta_{2k} < 1$  of Theorem 1.

Carrillo *et al.* [259, 260] have suggested various extensions of greedy algorithms to solve (5.20), i.e. IHT, compressive sampling matching pursuit (CoSaMP) and orthogonal matching pursuit (OMP). Moreover, they have derived weaker conditions for perfect recovery for IHT [260].

**Uniqueness Conditions:** To the best of our knowledge, the problem of joint sparsity with partially known support has never been discussed in the literature. Motivated by the potential applicability of such a framework in US imaging (cf. Section 5.3.1), we investigate the extension of Theorem 5 to partial known support.

In the remainder, we consider a matrix  $\mathbf{X} \in \Sigma_k^{(n,N)}$  such that  $\text{supp}(\mathbf{X}) = J = J_0 \cup J_1$ , with

## 5.2. Joint Sparsity with Partially Known Support

$J_0 \subset \{1, \dots, n\}$  and  $J_1 \subset \bar{J}_0$ , and we measure  $\mathbf{Y} = \mathbf{A}\mathbf{X}$ , with  $\mathbf{A} \in \mathbb{R}^{m \times n}$ .

First, we reformulate the MMV problem with partially known support as:

$$\min_{\mathbf{X} \in \mathbb{K}^{n \times N}} \|\mathbf{X}_{(\bar{J}_0)}\|_{0, \text{row}} \quad \text{subject to } \mathbf{Y} = \mathbf{A}\mathbf{X}. \quad (5.21)$$

The following theorem provides a guarantee for uniqueness of the solution of (5.21) expressed in terms of an upper bound on the row sparsity  $k$ .

**Theorem 6.** *The matrix  $\mathbf{X} \in \Sigma_k^{(n, N)}$ , with  $\text{supp}(\mathbf{X}) = J_0 \cup J_1$ ,  $J_0$  known, is the unique solution of (5.21), if  $\mathbf{Y} = \mathbf{A}\mathbf{X}$  and*

$$k < \frac{\text{spark}(\mathbf{A}) + |J_0|}{2}. \quad (5.22)$$

*Proof.* The proof follows by contradiction. Define  $\mathbf{X}^1 \in \mathbb{K}^{n \times N}$  and  $\mathbf{X}^2 \in \mathbb{K}^{n \times N}$  such that  $\mathbf{X}^1 \neq \mathbf{X}^2$  and both are solutions of (5.21). Consider that the rows of  $\mathbf{X}^1$  (resp.  $\mathbf{X}^2$ ) are supported on  $J_0 \cup \Delta_1$  (resp.  $J_0 \cup \Delta_2$ ) such that  $|\Delta_1| = |\Delta_2| = u \leq k - |J_0|$ . Thus, the rows of  $\mathbf{X}^1 - \mathbf{X}^2$  are supported on  $J_0 \cup \Delta_1 \cup \Delta_2$  and

$$\mathbf{A}_{J_0 \cup \Delta_1 \cup \Delta_2} (\mathbf{X}^1 - \mathbf{X}^2)_{(J_0 \cup \Delta_1 \cup \Delta_2)} = \mathbf{0}. \quad (5.23)$$

When  $\text{spark}(\mathbf{A}) > |J_0 \cup \Delta_1 \cup \Delta_2|$ ,  $\mathbf{A}_{J_0 \cup \Delta_1 \cup \Delta_2}$  has full column rank and its null-space is trivial. If (5.22) holds, then  $\text{spark}(\mathbf{A}) > 2k - |J_0| \geq k - 2u \geq |J_0 \cup \Delta_1 \cup \Delta_2|$  such that

$$\mathbf{A}_{J_0 \cup \Delta_1 \cup \Delta_2} (\mathbf{X}^1 - \mathbf{X}^2)_{(J_0 \cup \Delta_1 \cup \Delta_2)} = \mathbf{0} \Leftrightarrow \mathbf{X}^1 = \mathbf{X}^2. \quad (5.24)$$

□

Theorem 6 is an extension to the MMV problem of Proposition 1 of [257] and the upper bound is the same as for the SMV problem. At this point, it would be beneficial to take into account the information contained in  $\mathcal{R}(\mathbf{Y})$  and the partially known support to weaken the uniqueness condition compared to the SMV problem, in a similar way to Theorem 5. This is detailed in Theorem 7.

**Theorem 7.** *The matrix  $\mathbf{X} \in \Sigma_k^{(n, N)}$ , with  $\text{supp}(\mathbf{X}) = J_0 \cup J_1$ ,  $J_0$  known, is the unique solution of (5.21), if  $\mathbf{Y} = \mathbf{A}\mathbf{X}$  and*

$$k < \frac{\text{spark}(\mathbf{A}) + \text{rank}(\mathbf{Y}_a) - 1}{2}, \quad (5.25)$$

where  $\mathbf{Y}_a = [\mathbf{Y}, \mathbf{A}_{J_0}]$ .

*Proof.* Consider the augmented measurement matrix  $\mathbf{Y}_a = [\mathbf{Y}, \mathbf{A}_{J_0}] \in \mathbb{R}^{m \times (N + |J_0|)}$ . Define the corresponding augmented signal matrix  $\mathbf{X}_a = [\mathbf{X}, \mathbf{I}_{J_0}] \in \mathbb{R}^{n \times (N + |J_0|)}$ , where  $\mathbf{I}_{J_0} \in \mathbb{R}^{n \times |J_0|}$  is the identity matrix with columns restricted to  $J_0$ . We can observe that  $\mathbf{Y}_a = \mathbf{A}\mathbf{X}_a$ ,  $\text{supp}(\mathbf{X}_a) =$

$\text{supp}(\mathbf{X})$ , and  $\|\mathbf{X}_a\|_{0,\text{row}} = \|\mathbf{X}\|_{0,\text{row}}$ . Now, define the following augmented MMV problem

$$\min_{\mathbf{X} \in \mathbb{R}^{n \times (N+|J_0|)}} \|\mathbf{X}\|_{0,\text{row}} \text{ subject to } \mathbf{Y}_a = \mathbf{A}\mathbf{X}. \quad (5.26)$$

By applying Theorem 5,  $\mathbf{X}_a$  is the unique solution of (5) if  $\mathbf{Y}_a = \mathbf{A}\mathbf{X}_a$  and

$$k < \frac{\text{spark}(\mathbf{A}) + \text{rank}(\mathbf{Y}_a) - 1}{2}. \quad (5.27)$$

Finally, it is straightforward to show that if  $\mathbf{X}_a$  is the unique solution of (5.26), then  $\mathbf{X}$  is the unique solution of (5.12). Indeed, define  $\mathbf{X}^1 \in \mathbb{K}^{n \times N}$  and  $\mathbf{X}^2 \in \mathbb{K}^{n \times N}$  such that  $\mathbf{X}^1 \neq \mathbf{X}^2$  and both are solutions of (5.21). Consider that the rows of  $\mathbf{X}^1$  (resp.  $\mathbf{X}^2$ ) are supported on  $J_0 \cup \Delta_1$  (resp.  $J_0 \cup \Delta_2$ ). Then,  $\mathbf{X}_a^1 = [\mathbf{X}^1, \mathbf{A}_{J_0}]$  and  $\mathbf{X}_a^2 = [\mathbf{X}^2, \mathbf{A}_{J_0}]$  are solutions of (5.27) and  $\mathbf{X}_a^1 \neq \mathbf{X}_a^2$  which is impossible since  $\mathbf{X}_a$  is unique.  $\square$

Hence, Theorem 7 states that the known support of the measurement model can be used to augment the signal subspace. Indeed, we have that the signal subspace of the augmented measurement matrix,  $\hat{\mathbf{S}}_a$  is defined as

$$\hat{\mathbf{S}}_a = \hat{\mathbf{S}} + \mathcal{R}(\mathbf{A}_{J_0}), \quad (5.28)$$

where  $\hat{\mathbf{S}}$  is the signal subspace associated with  $\mathbf{Y}$ .

We observe that the effect of the partially known support is maximal when  $\mathcal{R}(\mathbf{A}_{J_0})$  is orthogonal to  $\hat{\mathbf{S}}$ .

**MUSIC-based Recovery:** MUSIC-based recovery with partially known support, coined as MUSIC-PKS, is similar to MUSIC algorithm described in Section 5.2.1, except that it is applied to the augmented measurement matrix. The following theorem details the recovery guarantee for MUSIC-PKS.

**Theorem 8** (Recovery guarantee for MUSIC-PKS). *Consider a matrix  $\mathbf{X} \in \Sigma_k^{(n,N)}$ , with  $\text{supp}(\mathbf{X}) = J_0 \cup J_1$ ,  $J_0$  known, such that  $\mathbf{Y} = \mathbf{A}\mathbf{X}$ ,  $\text{rank}(\mathbf{X}) = k + |J_0| - \text{rank}\left(\left(\mathbf{P}_{\mathcal{R}(\mathbf{X})}\right)_{(J_0)}\right)$  and  $k < \text{spark}(\mathbf{A}) - 1$ . Then MUSIC applied to the augmented measurement matrix  $\mathbf{Y}_a = [\mathbf{X}, \mathbf{A}_{J_0}]$  is guaranteed to recover  $\mathbf{X}$ .*

*Proof.* The proof is immediate given Theorem 3 in [244] and the following equality

$$\begin{aligned} \text{rank}([\mathbf{X}, \mathbf{I}_{J_0}]) &= \text{rank}(\mathbf{X}) + \text{rank}(\mathbf{P}_{\mathcal{R}(\mathbf{X})^\perp} \mathbf{I}_{J_0}) \\ &= \text{rank}(\mathbf{X}) + \text{rank}((\mathbf{I} - \mathbf{P}_{\mathcal{R}(\mathbf{X})}) \mathbf{I}_{J_0}) \\ &= \text{rank}(\mathbf{X}) + \text{rank}\left(\mathbf{I}_{(J_0)} - \left(\mathbf{P}_{\mathcal{R}(\mathbf{X})}\right)_{(J_0)}\right) \\ &= \text{rank}(\mathbf{X}) + |J_0| - \text{rank}\left(\left(\mathbf{P}_{\mathcal{R}(\mathbf{X})}\right)_{(J_0)}\right). \end{aligned}$$

$\square$

Hence, take the case where  $\text{rank}(\mathbf{X}_{(J_0)}) = 1$ ,  $\text{rank}(\mathbf{X}_{(J_1)}) = |J_1|$  and  $\text{rank}(\mathbf{X}) = |J_1| + 1$ . We see that

$$\text{rank}(\mathbf{X}_a) = \text{rank}(\mathbf{X}) + |J_0| - \text{rank}\left(\left(\mathbf{P}_{\mathcal{R}(\mathbf{X})}\right)_{(J_0)}\right) = |J_1| + 1 + |J_0| - 1 = k, \quad (5.29)$$

and MUSIC-PKS succeeds in a rank-defective case.

**Greedy Algorithms:** Based on the extension of IHT to partially known support [260], we suggest SNIHT-PKS in which the  $\mathbf{X}$  update step of SNIHT is replaced by the following one:

$$\mathbf{X}^{(i)} = \mathcal{H}_{k-|J_0|}^{J_0}(\mathbf{X}^{(i-1)} + \omega(\mathbf{A}^* \mathbf{R}^{(i-1)})), \quad (5.30)$$

where  $\omega \in \mathbb{R}$  and the non-linear operator  $\mathcal{H}_k^J(\cdot)$  is defined for  $J \subset \{1, \dots, n\}$  as

$$\mathcal{H}_k^J(\mathbf{X}) = \mathbf{X}_{(J)} + \mathcal{H}_k(\mathbf{X}_{(J)}), \quad (5.31)$$

We now state the main result of this section, which provides an upper bound on the discrepancy between the output of SNIHT-PKS and the optimal row-sparse approximation of the solution.

**Theorem 9** (Simultaneous sparse approximation with partially known support). *Consider that  $\mathbf{Y} = \mathbf{A}\mathbf{X}_{(J_0 \cup J_1)} + \tilde{\mathbf{E}}$ . If  $\mathbf{A}$  satisfies the following ARIP conditions:  $2U_{ck} + 2L_{ck} + L_k < 1$  where  $c \in \mathbb{N}$  is such that  $ck \geq 3k - 2|J_0|$ , then the error of SNIHT-PKS at iteration  $i$  is bounded by:*

$$\|\mathbf{X}^{(i)} - \mathbf{X}_{(J)}\|_F \leq \alpha^{(i)} \|\mathbf{X}_{(J)}\|_F + \frac{\beta}{1-\alpha} \|\tilde{\mathbf{E}}\|_F, \quad (5.32)$$

where  $\alpha = 2\frac{U_{ck} + L_{ck}}{1 - L_k}$ ,  $\beta = 2\frac{\sqrt{1 - U_{dk}}}{1 - L_k}$  and  $d \in \mathbb{N}$  is such that  $dk \geq 2k - |J_0|$ .

*Proof.* The proof is close to the one of Blanchard *et al.* [253] and includes contributions from Carrillo *et al.* [260].

As a preliminary, we remind the definition of the asymmetric restricted isometry (ARIP) constants that will be used in the proof.

**Definition 6** (ARIP constants [253]). *Consider  $\mathbf{A} \in \mathbb{K}^{m \times n}$ . The lower and upper ARIP constants of order  $k$  denoted as  $L_k$  and  $U_k$ , respectively, are defined as*

$$L_k = \min_{b \geq 0} b, \text{ subject to } (1 - b) \|\mathbf{x}\|_2^2 \leq \|\mathbf{A}\mathbf{x}\|_2^2, \forall \mathbf{x} \in \Sigma_k$$

$$U_k = \min_{b \geq 0} b, \text{ subject to } (1 - b) \|\mathbf{x}\|_2^2 \geq \|\mathbf{A}\mathbf{x}\|_2^2, \forall \mathbf{x} \in \Sigma_k$$

Recall that  $\|\mathbf{X}\|_{0, \text{row}} = k$  and  $\text{supp}(\mathbf{X}) = J$ ,  $|J| = k$ ,  $J = J_0 \cup J_1$ , where  $|J_0| = r$ , and  $|J_1| = k - r$ . Let  $\mathbf{V}^{(i)} = \mathbf{X}^{(i)} + \omega^{(i)} \mathbf{A}^* (\mathbf{Y} - \mathbf{A}\mathbf{X}^{(i)})$ . By replacing  $\mathbf{Y}$  by its expression, we have that:

$$\mathbf{V}^{(i)} = \mathbf{X}^{(i)} + \omega^{(i)} \mathbf{A}^* \mathbf{A}(\mathbf{X}_{(J)} - \mathbf{X}) + \omega^{(i)} \mathbf{A}^* \tilde{\mathbf{E}}. \quad (5.33)$$

## Chapter 5. Compressive Multiplexing of Ultrasound Signals

Define the update  $\mathbf{X}^{(i+1)} = \mathbf{V}_{(J_0)}^{(i)} + \mathcal{H}_{k-r}(\mathbf{V}_{(J_0)}^{(i)})$ . Also define  $U^{(i)} = \text{supp}(\mathcal{H}_{k-r}(\mathbf{V}_{(J_0)}^{(i)}))$ . It can be easily checked that  $|U^{(i)}| \leq k - r$ , as described in [259].

Now, we can write the following inequality:

$$\|\mathbf{V}^{(i)} - \mathbf{X}^{(i+1)}\|_F^2 = \|\mathbf{V}_{(J_0)}^{(i)} - \mathbf{X}_{(J_0)}^{(i+1)}\|_F^2 + \|\mathbf{V}_{(\bar{J}_0)}^{(i)} - \mathbf{X}_{(\bar{J}_0)}^{(i+1)}\|_F^2, \quad (5.34)$$

$$\leq \|\mathbf{V}_{(J_0)}^{(i)} - \mathbf{X}_{(J_0)}^{(i)}\|_F^2 + \|\mathbf{V}_{(\bar{J}_0)}^{(i)} - \mathbf{X}_{(J_1)}^{(i)}\|_F^2, \quad (5.35)$$

$$= \|\mathbf{V}^{(i)} - \mathbf{X}_{(J)}\|_F^2, \quad (5.36)$$

since  $\mathbf{V}_{(J_0)}^{(i)} = \mathbf{X}_{(J_0)}^{(i+1)}$  and  $\mathbf{X}_{(\bar{J}_0)}^{(i+1)}$  is the best  $(k-r)$ -term approximation of  $\mathbf{V}_{(\bar{J}_0)}^{(i)}$ .

Now, by expanding (5.36) using the Frobenius inner product and bounding the real part of the inner product by its real part, the following inequality holds:

$$\|\mathbf{X}_{(J)} - \mathbf{X}^{j+1}\|_F^2 \leq 2|\langle \mathbf{V}^{(i)} - \mathbf{X}_{(J)}, \mathbf{X}_{(J)} - \mathbf{X}^{(i+1)} \rangle|. \quad (5.37)$$

From (5.33), we have that:

$$\mathbf{V}^{(i)} - \mathbf{X}_{(J)} = (\mathbf{I} - \omega^{(i)} \mathbf{A}^* \mathbf{A})(\mathbf{X}^{(i)} - \mathbf{X}_{(J)}) + \omega^{(i)} \mathbf{A}^* \tilde{\mathbf{E}}, \quad (5.38)$$

which leads to

$$\|\mathbf{X}_{(J)} - \mathbf{X}^{(i+1)}\|_F^2 \leq 2\omega^{(i)} |\langle \tilde{\mathbf{E}}, \mathbf{A}(\mathbf{X}^{(i+1)} - \mathbf{X}_{(J)}) \rangle| + 2|\langle (\mathbf{I} - \omega^{(i)} \mathbf{A}_Q^* \mathbf{A}_Q)(\mathbf{X}^{(i)} - \mathbf{X}_{(J)}), (\mathbf{X}^{(i+1)} - \mathbf{X}_{(J)}) \rangle|, \quad (5.39)$$

where  $Q = J \cup J^{(i)} \cup J^{(i+1)}$  has a cardinality bounded by

$$|Q| = |J_0 \cup J_1 \cup U^{(i)} \cup U^{(i+1)}| \leq 3k - 2r \leq ck, \quad (5.40)$$

where  $c \in \mathbb{N}$  such that  $ck \geq 3k - 2r$ . Now, using Lemma 5 of [253], we can state that if  $\omega^{(i)} \leq \frac{1}{1-L_k}$ , the following inequality holds

$$|\langle (\mathbf{I} - \omega^{(i)} \mathbf{A}_Q^* \mathbf{A}_Q)(\mathbf{X}^{(i)} - \mathbf{X}_{(J)}), (\mathbf{X}^{(i+1)} - \mathbf{X}_{(J)}) \rangle| \leq \varphi(ck) \|\mathbf{X}^{(i)} - \mathbf{X}_{(J)}\|_F \|\mathbf{X}^{(i+1)} - \mathbf{X}_{(J)}\|_F \quad (5.41)$$

where  $\varphi(ck) = \frac{U_{ck} + L_{ck}}{1 - L_k}$ .

In addition, we can bound the first term of (5.39) as:

$$|\langle \tilde{\mathbf{E}}, \mathbf{A}(\mathbf{X}^{(i+1)} - \mathbf{X}_{(J)}) \rangle| \leq \sqrt{1 + U_{dk}} \|\tilde{\mathbf{E}}\|_F \|\mathbf{X}^{(i+1)} - \mathbf{X}_{(J)}\|_F, \quad (5.42)$$

since  $\text{supp}(\mathbf{X}^{(i+1)} - \mathbf{X}_{(J)}) = J \cup U^{(i+1)}$  has its cardinality bounded by  $2k - r \leq dk$ , with  $d \in \mathbb{N}$ .

With (5.39), (5.41), (5.42) and Lemma 2 of [253], we can write

$$\left\| \mathbf{X}_{(J)} - \mathbf{X}^{(i+1)} \right\|_F \leq \alpha^{(i)} \left\| \mathbf{X}_{(J)} \right\|_F + \frac{\beta}{1-\alpha} \left\| \tilde{\mathbf{E}} \right\|_F, \quad (5.43)$$

where  $\alpha = 2\varphi(ck) < 1$  and  $\beta = 2\frac{\sqrt{1+U_{dk}}}{1+L_k}$  since  $\omega^{(i)} \leq \frac{1}{1+L_k}$  (because of (5.41)).  $\square$

It can be seen that the results are closed to the one obtained by Carillo *et al.* [260] for the SMV case, in which the matrix  $\mathbf{A}$  has to meet the RIP property of order  $3k - 2|J_0|$ . In addition, the ARIP conditions provided by Theorem 9 are weaker than the ones of SNIHT, which can be translated into fewer measurements necessary to fulfill (5.32). However, compared to the bound established in Theorem 6, SNIHT-PKS requires  $\mathbf{A}$  to be  $ck$ -RIP which is stronger than  $\text{spark}(\mathbf{A}) > 2k - |J_0|$ .

Regarding OSMP and RA-ORMP, we can use the partially known support in the initial step of the algorithm, right after the estimation of the signal subspace, such that  $J = J_0$ . The algorithms, initialized with the known support, are denoted as RA-ORMP-PKS and OSMP-PKS.

**Subspace Augmented MUSIC:** For subspace augmented MUSIC methods, we can choose to use the partially known support either in the greedy algorithm or in the signal subspace estimation step.

Since greedy algorithms perform better when few indices need to be identified [250], we have chosen to use the partially known support to initialize the greedy algorithm used in the methods. Subspace augmented MUSIC methods with partially known support are denoted as SA-MUSIC-PKS and CS-MUSIC-PKS.

### 5.2.4 Experiments

**Empirical Performance of Recovery Algorithms with Partially Known Support:** We explore the empirical performance of SA-MUSIC-PKS, RA-ORMP-PKS and SNIHT-PKS in a noiseless situation and under additive Gaussian noise with a SNR of 30 dB. The results presented in this section are reproducible and available online<sup>1</sup>. For each experiment, 1000 random trials of the algorithms are run and the recovery probability is computed as the rate of successful support recovery.

We consider a Gaussian random measurement matrix  $\mathbf{A} \in \mathbb{R}^{m \times n}$ , with  $A_{ij} \sim \mathcal{N}(0, 1/\sqrt{m})$  and  $n$  is fixed to 128. The signal matrix  $\mathbf{X} \in \Sigma_k^{(n, N)}$  is built as a random matrix, with  $N = k = 30$ . The impact of the partially known support is first analyzed by comparing the recovery probability of SA-MUSIC-PKS for a fixed rank ( $r = 10$ ), for a number of measurements ranging between 30 and 90, when 0 %, 25 %, 50 % and 75 % of the support is known *a priori*. Then, we compare the methods with their counterpart without known support on two experiments: fixed rank ( $r = 10$ ) for a number of measurements ranging between 30 and 90 and fixed number of measurements ( $m = 51$ ) for a rank varying between 1 and 30. For both experiments, 75 % of the support is assumed to be known.

<sup>1</sup>[https://github.com/AdriBesson/spl2018\\_joint\\_sparse](https://github.com/AdriBesson/spl2018_joint_sparse)

Figure 5.1 displays the results of the different experiments.

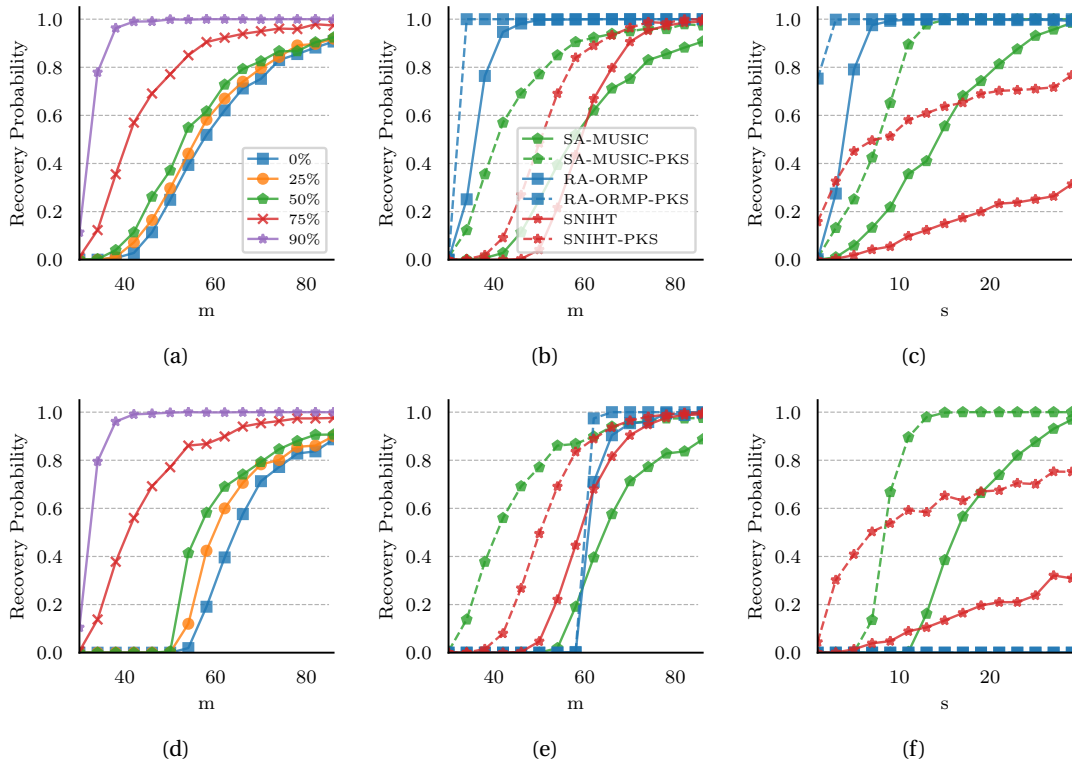


Fig. 5.1. Figures (a) and (d) display the recovery probability of SA-MUSIC-PKS for varying number of measurements and size of the known support in a noiseless and noisy scenarios (SNR = 30 dB). Figures (b) and (e) present the recovery probability of SA-MUSIC-PKS, RA-ORMP-PKS and SNIHT-PKS against SA-MUSIC, RA-ORMP and SNIHT for varying number of measurements in a noiseless and noisy scenarios (SNR = 30 dB). Figures (c) and (f) present the recovery probability of SA-MUSIC-PKS, RA-ORMP-PKS and SNIHT-PKS against SA-MUSIC, RA-ORMP and SNIHT for varying ranks in a noiseless and noisy scenarios (SNR = 30 dB).

On Figures 5.1(a) and 5.1(d), we can see that the accuracy of SA-MUSIC-PKS increases when larger part of the support is known *a priori*, as expected. Similar results are observed both in noiseless case and under additive Gaussian noise. On Figure 5.1(b), we observe that the methods with partially known support achieve significantly better reconstruction than their counterpart without known support in a noiseless scenario which validates the main results of this section. On Figure 5.1(e), we see that the conclusions drawn for the noiseless scenario extend to the noisy scenario for SA-MUSIC and SNIHT, which demonstrates the robustness to noise of the proposed method.

Regarding RA-ORMP, we observe that the results in the noisy scenario are significantly worse than in the noiseless scenario. This is due to the fact that, in the noisy scenario, the measurements  $Y$  are full rank which significantly perturbs the pursuit (it impacts the correlation step). In this case, RA-ORMP-PKS is only slightly better than RA-ORMP since the algorithm fails to recover the unknown part of the support. One way to address such a problem can be to use OSMP in which the noise would affect the estimation of the signal subspace. But, there exists well known methods to tackle the noise in signal subspace estimation [250] such that

the resulting method may be more robust.

Figures 5.1(c) and 5.1(f) show the benefits of partially known support in terms of the minimal value of  $s$  for perfect support recovery. As for Fig. 5.1(b) and 5.1(e), we notice that the partially known support significantly helps the recovery of the different algorithms except for RA-ORMP in the noisy case.

**Empirical Validation of Theorem 7:** Motivated by the fact that the benefits of Theorems 7 and 8 may be quite difficult to quantify at first sight due to the fact that  $\text{rank}(\mathbf{Y}_a)$  intrinsically depends on  $k$  when  $\text{spark}(\mathbf{A}) > k - 1$ , we propose the following illustrative example (For more in depth explanations, please refer to the following iPython notebook<sup>2</sup>).

Consider the signal matrix  $\mathbf{X} \in \mathbb{R}^{n \times N}$  which is designed with  $n = 64$ ,  $N = 128$ ,  $\text{supp}(\mathbf{X}) = J_0 \cup J_1$ , such that  $|J_0| = |J_1| = 8$  and  $J_0$  is known *a priori*.

We also define a Gaussian random measurement matrix  $\mathbf{A} \in \mathbb{R}^{m \times n}$  as before, such that  $\text{rank}(\mathbf{A}) = m \Leftrightarrow \text{spark}(\mathbf{A}) = m + 1$  with probability 1, and the corresponding measurements as  $\mathbf{Y} = \mathbf{A}\mathbf{X}$ .

In a first experiment, we set  $\text{rank}(\mathbf{X}_{(J_0)}) = 1$ ,  $\text{rank}(\mathbf{X}_{(J_1)}) = |J_1|$  such that  $\text{rank}(\mathbf{X}) = |J_1| + 1$ . Since  $|J_1| + 1 < k$ , we are in a rank-defective case in which the MUSIC-based recovery method fails. However, when  $m > k$ ,  $\text{rank}([\mathbf{Y}, \mathbf{A}_{J_0}]) = k$  and we are in the ideal case where  $\mathcal{R}(\mathbf{A}_{J_0})$  augments the signal subspace  $\mathcal{R}(\mathbf{Y})$  such that MUSIC-PKS would succeed. From the point of view of Theorem 8, we are in the case where  $\text{rank}(\left(\mathbf{P}_{\mathcal{R}(\mathbf{X})}\right)_{(J_0)}) = 1$ .

In a second experiment, we set  $\text{rank}(\mathbf{X}_{(J_0)}) = |J_0|$  and  $\text{rank}(\mathbf{X}_{(J_1)}) = 1$  in such a way that we are in the worst case scenario for MUSIC-PKS since  $\mathcal{R}(\mathbf{A}_{J_0}) \subset \mathcal{R}(\mathbf{Y})$ . In this case, MUSIC-PKS does not perform better than MUSIC. From the point of view of Theorem 8, we are in the case where  $\text{rank}(\left(\mathbf{P}_{\mathcal{R}(\mathbf{X})}\right)_{(J_0)}) = |J_0|$ .

Figure 5.2 displays the average recovery probability, computed as the rate of successful support recovery over 1000 random trials of the algorithms.

For the first experiment, we observe that MUSIC-PKS recovers the support of the signal for  $m \geq k + 1 = 17$  which exactly corresponds to the case where the augmented matrix has full rank, as stated in Theorem 2. Concerning the second experiment, both MUSIC and MUSIC-PKS fail as expected.

### 5.3 Low-dimensional Models of Ultrasound Signals

The key aspect in the development of compression methods is the ability to find low-dimensional models of the signals under consideration, expressed in terms of sparsity in the CS framework. In order to develop low-dimensional models of US signals, we rely on few common simplifying assumptions. First, we assume that the medium of interest is homogeneous such that the speed of sound is known and constant. We further neglect the frequency dependent attenuation in such a way that the shape of the pulse-echo waveform does not vary. We also assume that the transducer elements are identical such that we can define a unique pulse-echo waveform which characterizes the experiment.

<sup>2</sup>[https://github.com/AdriBesson/spl2018\\_joint\\_sparse/blob/master/example\\_theorem2.ipynb](https://github.com/AdriBesson/spl2018_joint_sparse/blob/master/example_theorem2.ipynb)

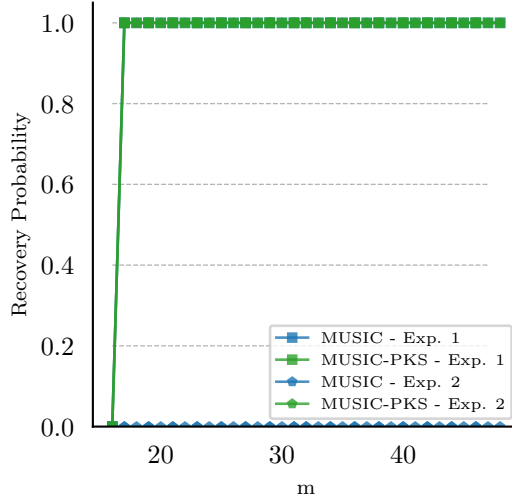


Fig. 5.2. Recovery probability of MUSIC and MUSIC-PKS when  $\text{rank}(\mathbf{X}_{(J_0)}) = |J_0|$  (Exp. 1) and when  $\text{rank}(\mathbf{X}_{(J_0)}) = 1$  (Exp. 2).

Now, consider that we are in the pulse-echo configuration described in Sections 3.5.3 and 3.6.3 where a probe composed of  $N_x^t$  elements, with pulse-echo waveform  $v_{pe}(t)$ , is used to transmit and receive acoustical pulses during a time  $T$ . Suppose that the medium is composed of  $K$  point reflectors located at  $\mathbf{r}_k, k = 1, \dots, K$ . The echo signal  $m_i(t) \in L_2([0, T])$ , received at the  $i$ -th element can be expressed as:

$$m_i(t) = \sum_{k=1}^K a_{ik} v_{pe}(t - t_{ik}), \quad (5.44)$$

where  $a_{ik}$  and  $t_{ik} = t_{Tx}(\mathbf{r}_k) + t_{Rx}(\mathbf{r}_k, \mathbf{p}_i)$  are the amplitude and round-trip TOF of the  $k$ -th point reflector seen by the  $i$ -th transducer element.

Hence, the element raw-data are linear combinations of pulse-echo waveforms, delayed by the round trip TOFs and scaled by the value of the TRF, several parameters related to the propagation and the element directivity. We investigate two low-dimensional models that result from (5.44).

### 5.3.1 The Bandpass Signal Model

A common assumption on the pulse-echo waveform, resulting from the bandpass property of the electro-acoustical impulse response, is that most of its energy is concentrated around the center frequency  $f_c$  of the transducer element, i.e. in the frequency band  $\Xi = [f_c - B, f_c + B] \cup [-f_c - B, -f_c + B]$ , where  $B < f_c$  depends on the bandwidth of the transducer element.

Hence,  $m_i(t)$  is a bandpass signal with frequency concentrated in the same frequency band as the pulse-echo waveform. The echo signals are bandlimited and the WKS theorem states that perfect reconstruction is possible provided that  $f_s > 2(f_c + B)$ .

However, it is well known that bandpass signals can be reconstructed with significantly fewer

samples than dictated by the Nyquist rate, by exploiting the well-known bandpass sampling technique which states that a sufficient condition for perfect reconstruction of a bandpass signal is

$$\frac{2(f_c + B)}{k} \leq f_s \leq \frac{2(f_c - B)}{k-1}, \text{ with } k \leq \frac{f_c + B}{2B}. \quad (5.45)$$

We can interpret the bandpass signal model in a CS-oriented perspective by introducing the normalized discrete Fourier transform (DFT) matrix  $\mathbf{F} \in \mathbb{R}^{N \times N}$  defined element-wise by:

$$F_{ln} = \frac{1}{\sqrt{N}} \exp\left(\frac{-2\pi i n l}{N}\right), \quad n \in \{1, \dots, N\}, \quad l \in \left\{-\frac{N}{2}, \dots, \frac{N}{2} - 1\right\}.$$

Using the above introduced DFT we can express  $\mathbf{M}_i$  as

$$\mathbf{M}_i = \mathbf{F}^* \hat{\mathbf{M}}_i + \boldsymbol{\epsilon}, \quad \|\hat{\mathbf{M}}_i\|_0 \leq |J|, \quad (5.46)$$

where  $\boldsymbol{\epsilon} \in \mathbb{C}^N$  accounts for measurement and modelling noise and  $J$  is the index set defined by

$$J = \left\{ j \in \{1, \dots, N\} \mid \left(\frac{-1}{2} + \frac{j-1}{N}\right) f_s \in \Xi \right\}. \quad (5.47)$$

Hence, depending on the sampling frequency, a bandpass signal can be sparse in the Fourier domain. Interestingly, the quality of a sampling scheme can be interpreted in terms of the sparsity of the spectrum of the resulting signal. In the ideal case of bandpass sampling, i.e. when  $f_c = 2kB$ , with  $k$  an integer, the spectrum is completely dense and  $|J| = N$ .

Back to (5.46), since we assume that the pulse-echo waveform is the same for the different transducer elements, the measurement matrix  $\mathbf{M} = [\mathbf{M}_1, \dots, \mathbf{M}_{N_t}^t] \in \mathbb{R}^{N \times N_t^t}$  is such that

$$\mathbf{M} = \mathbf{F}^* \hat{\mathbf{M}} + \mathbf{E}, \quad \|\hat{\mathbf{M}}\|_{0, \text{row}} \leq |J|, \quad (5.48)$$

where  $\mathbf{E} \in \mathbb{C}^{N \times N_t^t}$  accounts for the noise. Moreover, in many cases, we can have access to an accurate estimate of the pulse-echo waveform and therefore to  $J$ . Thus, we can leverage joint sparse method with partially known support, described in Section 5.2.

#### 5.3.2 The Pulse-stream Model

The bandpass signal model only characterizes the element-raw data but does not account for any prior knowledge on the insonified medium. An alternative approach is to consider  $m_i(t)$ , described in (5.44), as a *pulse stream*. The pulse-stream model has been extensively studied in the signal processing community. Theoretical sampling frameworks for such signals have been developed in the context of FRI [131, 224] and continuous [261] and discrete sparse regularization [262]. Such a model is common in many engineering applications such as US [131, 263, 264], radar [265] and lidar [266] where the objective is to localize strong reflectors.

We exploit a discrete formulation of the pulse-stream model, widely studied in CS [262, 267,

268], where the discrete signal  $\mathbf{M}_i$  follows  $K$ -sparse synthesis model in a convolutional dictionary  $\mathbf{V}_{pe} \in \mathbb{R}^{N \times (N-F+1)}$  made of shifted replicas of the discrete pulse-echo waveform  $\mathbf{v}_{pe} \in \mathbb{R}^F$ , where  $F \ll N$ . Thus, the following equation holds:

$$\mathbf{M}_i = (\mathbf{v}_{pe} * \tilde{\mathbf{M}}_i) + \boldsymbol{\epsilon}' = \mathbf{V}_{pe} \tilde{\mathbf{M}}_i + \boldsymbol{\epsilon}', \quad \|\tilde{\mathbf{M}}_i\|_0 \leq K, \quad \forall i = 1, \dots, N_x^t, \quad (5.49)$$

where  $*$  denotes the discrete convolution and  $\boldsymbol{\epsilon}' \in \mathbb{R}^N$  accounts for model mismatch and measurement noise. An important aspect of the convolution model (5.49) is the boundary condition applied to the discrete convolution. We focus on “full” convolution, i.e. convolution with zero-padding as boundary condition but most of the statements described below may be generalized to other boundary conditions. Hence the measurement matrix can be expressed as

$$\mathbf{M} = \mathbf{V}_{pe} \tilde{\mathbf{M}} + \mathbf{E}', \quad \tilde{\mathbf{M}} = [\tilde{\mathbf{M}}_1, \dots, \tilde{\mathbf{M}}_{N_x^t}], \quad \|\tilde{\mathbf{M}}_i\|_0 \leq K', \quad i = 1, \dots, N_x^t, \quad (5.50)$$

where  $\mathbf{E}' \in \mathbb{R}^{N \times N_x^t}$  accounts for the noise and  $K' \geq K$  is a positive integer. In this case, the coefficients  $\tilde{\mathbf{M}}_i$ ,  $i = 1, \dots, N_x^t$ , do not share a common non-zero support due to propagation effects so we cannot rely on joint-sparse methods. However, we can still exploit sparsity of each representation in the standard CS framework.

The fact that  $m_i(t)$  can be written as a convolution between a sum of  $K$  Dirac delta functions and the pulse-echo waveform does not automatically implies  $K$ -sparsity of the discrete counterpart due to the well-known basis mismatch [269]. Practically, we can think about the discretization as an interpolation of the sum of  $K$  Dirac delta functions on a discrete grid followed by a convolution with a discrete pulse-echo waveform. The interpolation process creates a  $K'$ -sparse signal, with  $K' \geq K$ , and the approximation of the continuous convolution by a discrete one creates noise due to mismatches in the sampling of the pulse-echo waveform. From a CS perspective, the dictionary  $\mathbf{V}_{pe}$  is usually coherent and may not be suited for CS-based reconstruction. To quantify this aspect, we introduce the autocorrelation function associated with a vector  $\mathbf{h} \in \mathbb{R}^M$  as:

$$A_h[n] = \sum_{k=1}^{M-n} \mathbf{h}_k \mathbf{h}_{k+n}, \quad n = 0, \dots, M-1, \quad (5.51)$$

which measures the similarity between  $\mathbf{h}$  and shifted versions of itself.

The following theorem links the value of the coherence of a convolutional dictionary with the autocorrelation of function of the pulse.

**Theorem 10** (Coherence of a convolutional dictionary). *Consider a convolutional dictionary  $\mathbf{H} \in \mathbb{R}^{(N+F-1) \times N}$  composed of shifted replicas of a signal  $\mathbf{h} \in \mathbb{R}^F$ , where  $F \leq N$ . The coherence  $\mu(\mathbf{H})$  of  $\mathbf{H}$  is given by*

$$\mu(\mathbf{H}) = \max_{n=1, \dots, F-1} \frac{|A_h[n]|}{\|\mathbf{h}\|_2^2}$$

*Proof.* Consider two indices  $(i, j) \in \{1, \dots, N\}^2$ , such that  $i < j$ . The inner product  $\langle \mathbf{H}_i, \mathbf{H}_j \rangle$

can be expressed as

$$\langle \mathbf{H}_i, \mathbf{H}_j \rangle = \sum_{k=1}^{N+F-1} \mathbf{H}_{ki} \mathbf{H}_{kj} = \begin{cases} \sum_{k=j+1}^{F+i} \mathbf{h}_{k-j} \mathbf{h}_{k-i} & \text{if } j < i + F \\ 0 & \text{otherwise} \end{cases}.$$

Let us concentrate on the case where  $j < i + F$ , we have that

$$\langle \mathbf{H}_i, \mathbf{H}_j \rangle = \sum_{k=j+1}^{F+i} \mathbf{h}_{k-j} \mathbf{h}_{k-i} = \sum_{K=1}^{F+i-j} \mathbf{h}_K \mathbf{h}_{K+j-i} = A_h[j-i].$$

In addition, we have that  $\|\mathbf{H}_i\|_2 = \|\mathbf{h}\|_2$ ,  $i = 1, \dots, N$ . Hence the coherence  $\mu(\mathbf{H})$  is can be expressed as

$$\mu(\mathbf{H}) = \max_{1 \leq i < j \leq N} \frac{|\langle \mathbf{H}_i, \mathbf{H}_j \rangle|}{\|\mathbf{H}_i\|_2 \|\mathbf{H}_j\|_2} = \max_{1 \leq i < j \leq N} \frac{|\langle \mathbf{H}_i, \mathbf{H}_j \rangle|}{\|\mathbf{h}\|_2^2} = \max_{1 \leq n \leq F-1} \frac{|A_h[n]|}{\|\mathbf{h}\|_2^2},$$

where the last line is obtained by noticing that

$$\max_{1 \leq i < j \leq N} |\langle \mathbf{H}_i, \mathbf{H}_j \rangle| = \max_{\substack{1 \leq i \leq N-F-1 \\ i+1 \leq j \leq F+i-1}} |A_h[j-i]| = \max_{1 \leq n \leq F-1} |A_h[n]|.$$

□

Hence the coherence of a convolutional matrix  $\mathbf{H}$  is nothing else than the normalized auto-correlation of the corresponding signal  $\mathbf{h}$ . This motivates the use of maximally uncorrelated sequences to design the pulse  $\mathbf{v}_{pe}$ , as already discussed in the literature [236, 270].

Unfortunately, the high sampling frequency coupled with the small support of  $\mathbf{v}_{pe}$  induces a high coherence of the matrix  $\mathbf{V}_{pe}$ . For instance, consider a transducer impulse response approximated as convolution between a Gaussian modulated sinusoidal pulse, with a center frequency of 5 MHz, 75 % bandwidth, and a 3-cycle square excitation signal. The coherence of the corresponding dictionary, at 50 MHz, is higher than 0.9.

That means that the proposed dictionary may not be ideal to retrieve the exact sparse matrix  $\tilde{\mathbf{M}}$  that would have generated  $\mathbf{M}$ . Nevertheless, since we are not interested in finding the exact  $\tilde{\mathbf{M}}$  but rather the re-synthesized matrix  $\mathbf{M}$ , we still consider this low-dimensional model as an interesting candidate for the proposed method.

## 5.4 Compressive Multiplexing of Ultrasound Signals

The proposed compression method is based on

- a compression module located in the probe head, which mixes signals in the analog domain in order to reduce the number of necessary coaxial cables;
- a reconstruction module located in the back-end system which recovers the signals from the compressed measurements.

Both modules are detailed in the remainder of this section.

### 5.4.1 Compression Module

The main building block of the proposed compression module is the compressive multiplexer (CMUX), an analog CS architecture introduced by Slavinsky *et al.* [237] for multi-channel signals sparse in the Fourier domain, inspired by the concept of random probes previously introduced for sparse [270] and spectrally sparse [271] signals. More recently, variants of the CMUX have also been studied in the context of ensemble of correlated signals [272].

**The Compressive Multiplexer:** Formally, the CMUX takes as input  $L$  signals  $\{m_i(t)\}_{i=1}^L$ , bandlimited at  $B/2$  Hz, modulates each of them with a chipping sequence  $p_i(t)$  working at  $W$  Hz, and sum them to form a single output signal  $y(t)$ , as described on Figure 5.3. The output

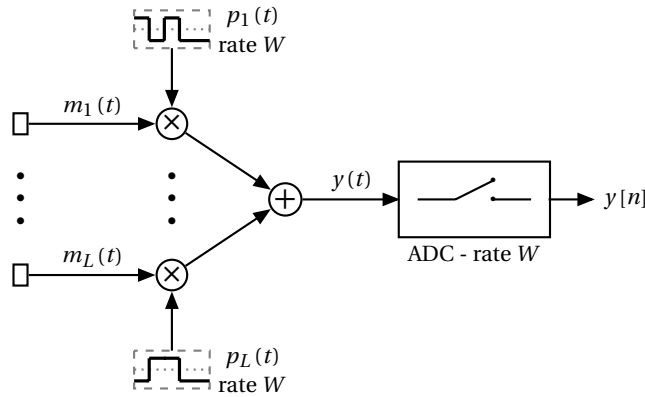


Fig. 5.3. The compressive multiplexer.

signal is carried to the back-end system via a coaxial cable where it is sampled at rate  $W$  by an ADC, to form a discrete vector  $\mathbf{y} \in \mathbb{R}^N$ , where  $\lfloor N = TW \rfloor$ .

The measurement model associated with the CMUX can be expressed as

$$\mathbf{y} = [\boldsymbol{\Sigma}_1, \dots, \boldsymbol{\Sigma}_L] \begin{bmatrix} \mathbf{m}_1 \\ \vdots \\ \mathbf{m}_L \end{bmatrix} = \mathbf{C}\mathbf{m}, \quad (5.52)$$

where  $\boldsymbol{\Sigma}_i = \text{diag}(\mathbf{p}_i) \in \mathbb{R}^{N \times N}$  is the diagonal matrix formed by the  $i$ -th chipping sequence and  $\mathbf{m}_i \in \mathbb{R}^N$  is the  $i$ -th input signal sampled at rate  $W$ . The measurement model can be equivalently formulated as follows:

$$\mathbf{y} = (\mathbf{P} \circ \mathbf{M}) \times \mathbf{1}, \quad (5.53)$$

where  $\mathbf{P} \in \mathbb{R}^{N \times L}$  contains the  $L$  chipping sequences and  $\mathbf{1} \in \mathbb{R}^L$  is a vector of ones. Such a formulation is more suited to problems involving structured sparsity of  $\mathbf{M}$ .

The CMUX architecture has some remarkably nice properties with respect to the Fourier transform, highlighted by the following theorem [237].

**Theorem 11** (Theorem 1 of [237]). *Let  $\mathbf{A}$  be defined as  $\mathbf{A} = [\boldsymbol{\Sigma}_1 \mathbf{F}, \dots, \boldsymbol{\Sigma}_L \mathbf{F}]$ , where  $\boldsymbol{\Sigma}_i$ ,  $i = 1, \dots, L$ ,*

## 5.4. Compressive Multiplexing of Ultrasound Signals

is defined in (5.52),  $\mathbf{F} \in \mathbb{C}^{N \times N}$  is the discrete Fourier basis and fix  $\delta \in [0, 1]$ . Then, there exists a positive constant  $C_0$  such that when

$$W \geq C_1 k \log^4(LW),$$

$\mathbf{A}$  satisfies the RIP property of order  $k$  with probability  $1 - C_0^2 / \delta C_1^2$ , where  $C_1$  is a constant.

Note that the value of the constant  $C_0$  can be found in [236].

Hence, given the available bandwidth  $B = LW$ , the above theorem provides an upper-bound on the number of input signals that can be mixed as  $L \leq \frac{B}{k \log^4(B)}$ .

**The Proposed Compression Module:** Motivated by the properties of the CMUX for multi-channel signals sparse in the Fourier domain, we propose to use  $J = N_x^t / L$  CMUXs to compress the US signals which compose a US probe, as depicted on Figure 5.4.

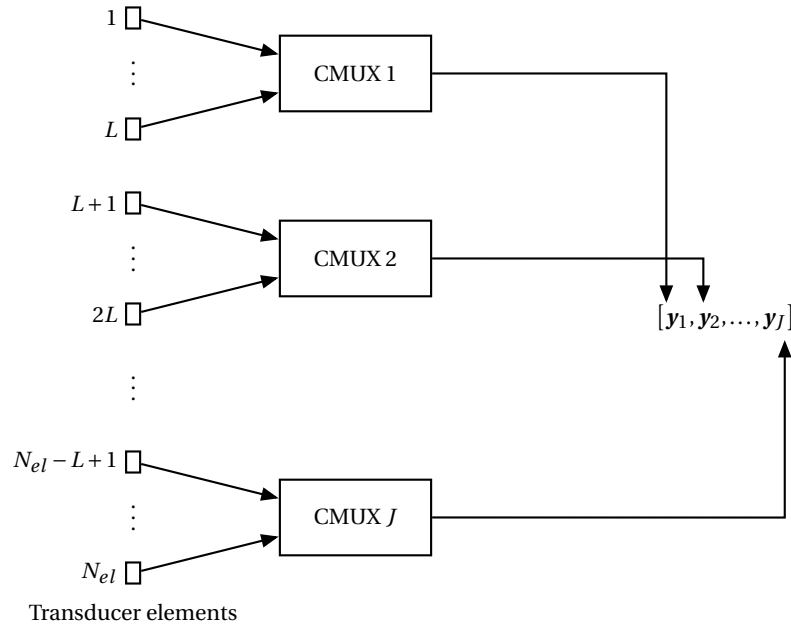


Fig. 5.4. The ultrasound compressive multiplexer architecture.

In the proposed architecture, we concatenate the outputs  $\{\mathbf{y}_j\}_{j=1}^J$  of the CMUXs to create a measurement matrix  $\mathbf{Y} \in \mathbb{R}^{N \times J}$  which is related to  $\mathbf{M} \in \mathbb{R}^{N \times N_x^t}$  by:

$$\mathbf{Y} = ([\mathbf{p}_1, \dots, \mathbf{p}_{N_x^t}] \circ [\mathbf{m}_1, \dots, \mathbf{m}_{N_x^t}]) \times \mathbf{A} = (\mathbf{P} \circ \mathbf{M}) \times \mathbf{A}, \quad (5.54)$$

where  $\mathbf{P} \in \mathbb{R}^{N \times N_x^t}$  is composed of the  $N_x^t$  chipping sequences and  $\mathbf{A} \in \mathbb{R}^{N_x^t \times J}$  performs the summation across the elements.

Alternatively, the problem can be expressed as a matrix-vector product in a similar way

to (5.52):

$$\mathbf{y} = \begin{bmatrix} \boldsymbol{\Sigma}_1, \dots, \boldsymbol{\Sigma}_L, & 0, \dots, 0, & \dots, & 0, \dots, 0, \\ 0, \dots, 0, & \boldsymbol{\Sigma}_{L+1}, \dots, \boldsymbol{\Sigma}_{2L}, & \dots, & 0, \dots, 0 \\ & & \vdots & \\ 0, \dots, 0, & 0, \dots, 0, & \dots, & \boldsymbol{\Sigma}_{N_x^t-L+1}, \dots, \boldsymbol{\Sigma}_{N_x^t} \end{bmatrix} \begin{bmatrix} \mathbf{m}_1 \\ \vdots \\ \mathbf{m}_L \\ \mathbf{m}_{L+1} \\ \vdots \\ \mathbf{m}_{2L} \\ \vdots \\ \mathbf{m}_{N_x^t-L+1} \\ \vdots \\ \mathbf{m}_{N_x^t} \end{bmatrix} = \mathbf{C}\mathbf{m}, \quad (5.55)$$

where  $\mathbf{y} = [\mathbf{y}_1^\top, \dots, \mathbf{y}_J^\top]^\top \in \mathbb{R}^{JN}$  contains the concatenated output signals.

In the proposed architecture, the chipping sequences are chosen as independent Rademacher sequences, i.e.  $\mathbf{p}_i \in \{-1, 1\}^N$ , for  $i = 1, \dots, N_x^t$ .

#### 5.4.2 Reconstruction Module

The reconstruction module which would be implemented in the back-end computer aims to recover the element-raw data  $\mathbf{M}$  from the compressed measurements  $\mathbf{Y}$  by applying CS-based reconstruction algorithms based on the low-dimensional models discussed in Section 5.3.

**Reconstruction based on the Bandpass Signal Model:** We assume that the element raw-data  $\mathbf{M}$  follow the bandpass signal model described in Section 5.3.1. We are therefore interested in solving the following joint-sparse reconstruction problem:

$$\min_{\hat{\mathbf{M}} \in \mathbb{C}^{N \times N_x^t}} \|\mathbf{Y} - (\mathbf{P} \circ \mathbf{F}^* \hat{\mathbf{M}}) \times \mathbf{A}\|_F^2 \text{ s.t. } \|\hat{\mathbf{M}}\|_{0, \text{row}} = |J|, \quad (5.56)$$

where  $\mathbf{F}^*$  is the inverse DFT matrix and  $J$  is defined in (5.47).

Depending on the prior knowledge on the index set  $J$ , different reconstruction techniques may be leveraged. In the vast majority of cases, an accurate estimate  $J_s$  of  $J$  can be found and  $\mathbf{M}$  can be recovered from  $\mathbf{Y}$  by solving the following least-squares problem

$$\min_{\hat{\mathbf{M}}} \|\mathbf{Y} - (\mathbf{P} \circ \mathbf{F}_{J_s}^* \hat{\mathbf{M}}_{(J_s)}) \times \mathbf{A}\|_F^2. \quad (5.57)$$

Problem (5.56) can be solved straightforwardly using any existing least-squares solver, such as LSQR. The main drawback of such a technique is its robustness against measurement noise and modelling errors.

When  $J$  is only partially known, we can leverage methods for joint sparsity with partially known support, described in Section 5.2. Several remarks can be drawn here which would guide our choice of the most suited algorithm. First, we are in a rank-defective situation since

$N_x^t \ll N$  in many imaging scenarios which is not in favor of rank-aware methods. In addition, we may have a non-negligible amount of noise against which the method should be robust. Third, element-raw data can be substantially high-dimensional which can prevent the use of computationally expensive routines such as SVD. Based on these observations, we decide to use SNIHT-PKS. Indeed, Theorem 9 demonstrates its robustness to noise and it does not require any computationally expensive procedure at each iteration.

When  $J$  is completely unknown, we can use joint-sparse algorithms without partially known support, described in Section 5.2.

**Reconstruction based on the Pulse-stream Model:** We suppose that the element-raw data follow the pulse-stream model described in Section 5.3.2. We also assume that we know the pulse-echo waveform  $v_{pe}(t)$  and its discrete counterpart  $\mathbf{v}_{pe} \in \mathbb{R}^F$ . Thus, the reconstruction problem can be expressed as the following weighted  $\ell_1$ -minimization problem on the concatenated measurements:

$$\min_{\tilde{\mathbf{m}} \in \mathbb{R}^{(N-F+1)N_x^t}} \|\mathbf{y} - \mathbf{C}(\mathbf{v}_{pe} * \tilde{\mathbf{m}})\|_2^2 + \|\mathbf{\Lambda}\tilde{\mathbf{m}}\|_1, \quad (5.58)$$

where  $\mathbf{y} \in \mathbb{R}^{JN}$  and  $\mathbf{C} \in \mathbb{R}^{JN \times N_x^t N}$  are the CMUX measurements and measurement matrix and  $\mathbf{\Lambda} \in \mathbb{R}^{N_x^t(N-F+1) \times N_x^t(N-F+1)}$  is a diagonal matrix which may be used to weight differently the element-raw data corresponding to different sensors. In (5.58), there is a slight abuse of notation, for conciseness, since we assume that the discrete convolution is achieved with the appropriate boundary condition.

Problem (5.58) is a standard synthesis-based  $\ell_1$ -minimization problem and can be solved using off-the-shelf convex optimization algorithms, such as FISTA described in Section 4.1.2.

### 5.4.3 Experiments and Results

We propose to compare the following reconstruction methods on various simulations and experiments described in the remaining of this section:

- Least-squares reconstruction on the known support in the frequency domain (LS-F);
- Joint-sparse reconstruction in the frequency domain with SNIHT-PKS (JS-F). Same stopping criterion as described in [253];
- CS reconstruction based on a pulse-stream model with a known pulse (CS-PS). We use FISTA with a maximum number of iterations of 5000 and a stopping criterion based on the relative evolution of the solution. The regularization parameter  $\lambda$  is tuned by grid search.

Regarding the compression strategy, it depends on additional settings, such as the center frequency of the probe and will consequently be discussed for each experiment. After recovery of the element-raw data, the image reconstruction is performed using the DAS algorithm with spline interpolation for delay approximation and apodization weights set to account

for the element directivity. The post-processing step consists of envelope detection (Hilbert transform), normalization and log-compression.

**Simulation Study of Various Compression Strategies for 3D Imaging:** We investigate the behaviour of the proposed methods for various center frequencies, bandwidths, sampling frequencies and compression ratios. More precisely, we simulate four configurations of a phased-array matrix probe composed of 1024 transducer elements, namely two center frequencies of 3 MHz and 5 MHz and two bandwidths of 60 % and 75 %. The electro-acoustical impulse response is modelled as a Gaussian-modulated pulse and the excitation is set as a 2-cycle square signal. We consider a numerical phantom composed of a 6 mm-anechoic inclusion centered at 3 cm embedded in a fully developed speckle background. We insonify the phantom with a single PW with normal incidence. The simulations are run with Field II [89]. Regarding the received signals, we consider the following sampling frequencies: 12.5 MHz, 25 MHz and 50 MHz for 3 MHz and 20.8 MHz, 31.25 MHz and 62.5 MHz for 5 MHz; and the following compression ratios: 2, 4, 8 and 16, corresponding to a total of 12 compression scenarios for each center frequency.

On the reconstruction side, we only consider LS-F and CS-PS since we perfectly know the pulse-echo waveform and therefore the corresponding spectral content. For LS-F, we assume that the frequency content of the signals is concentrated between 2.9 MHz and 6.5 MHz.

The recovery performance is evaluated using the normalized root mean square error (NRMSE) defined for matrices as

$$NRMSE = 1 - \frac{\|M_r - M\|_F}{\|M\|_F},$$

where  $M_r$  are the recovered element raw-data and  $M$  are the reference data, obtained without compression.

The first two plots of Figure 5.5 display the NRMSE for the imaging configurations at 3 MHz where the leftmost plot corresponds to 60 % bandwidth and the other one to 75 % bandwidth. The two rightmost plots correspond to the NRMSE for the two imaging configurations at 5 MHz.

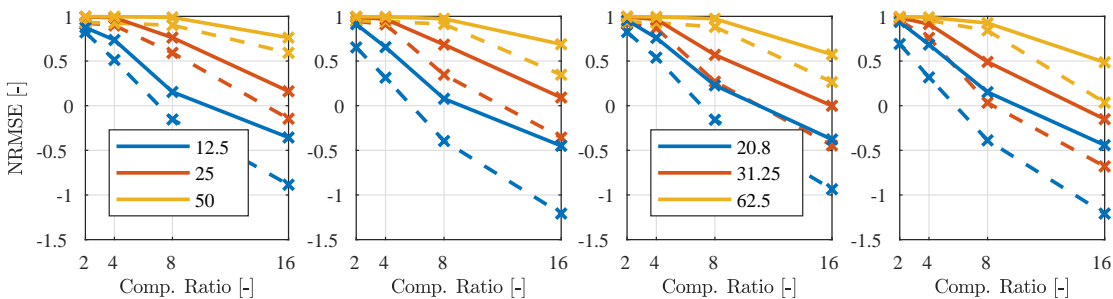


Fig. 5.5. Recovery performance of the proposed compressive multiplexing method on the simulated anechoic-inclusion phantom for JS-F (dashed line) and CS-PS (solid line) and for (from left to right) a 3 MHz probe with 60 % bandwidth, a 3 MHz probe with 75 % bandwidth, a 5 MHz probe with 60 % bandwidth, and a 5 MHz with 75 % bandwidth.

## 5.4. Compressive Multiplexing of Ultrasound Signals

---

We observe that the NRMSE is evidently a decreasing function of the compression ratio. We also notice that CS-PS outperforms LS-F for every compression strategy, which can be justified by the perfect knowledge of the pulse-echo waveform and a possibly higher compressibility of US signals in the pulse-stream model. Regarding the behaviour with respect to the bandwidth, we observe the results of LS-F are significantly worse for a higher bandwidth which is expected since a signal with higher bandwidth would be less sparse in the Fourier domain. For CS-PS, we observe that the results do not depend on the bandwidth.

We can also deduce from these plots that the following two strategies seem to provide a good trade-off between image quality and compression. The first strategy operates at 12 times the center frequency with a compression ratio of 8, and the second strategy works at 6 times the center frequency with a compression ratio of 4. In some cases, depending on the shape of the excitation signals, we can also consider a more aggressive compression strategy which would operate at 12 times the center frequency with a compression ratio of 12.

**Simulation Study on the Numerical PICMUS Phantom:** We use the numerical phantom developed during the PICMUS challenge. We simulate a single PW experiment (normal incidence, no apodization in transmit) using Field II software [89]. The simulation is run at 250 MHz and the data are down-sampled at the desired sampling frequency depending on the compression strategy. The simulated probe is the L11-4v probe (5.208 MHz center frequency, 128 elements, 0.30 mm pitch) whose features are described in details on the website of the challenge.

We evaluate the reconstruction for the two compression strategies mentioned above, i.e. one which operates at 62.5 MHz with a compression ratio of 8 and one working at 31.25 MHz with a compression ratio of 4.

To quantify the quality of the reconstruction, we rely on the following metrics defined in the context of the challenge:

- CNR assessed from the anechoic cyst region and the speckle background;
- axial and lateral resolution computed as the FWHM on the point reflectors located at 14 mm and 45 mm;
- speckle quality assessed as the number of regions, over a total of 6, which pass the “speckle test”. The “speckle test” is a check to see whether a selected region of the image follows a Rayleigh distribution or not by means of the one-sample Kolmogorov-Smirnov test. The main reason for such a test is that pixel intensities of fully developed speckle is supposed to follow a Rayleigh distribution.

Table 5.1 summarizes the values of the metrics for the different methods and the reference obtained on uncompressed data for sampling frequencies of 62.5 MHz and 31.25 MHz. From left to right, Figure 5.6 displays the B-mode images reconstructed with the LS-F, CS-PS and the reference, respectively, for a sampling frequency of 62.5 MHz. We notice that the proposed methods perform well at 62.5 MHz and 31.25 MHz for which the values of the quality metrics are closed to the ones of the reference. Hence, the proposed reconstruction methods manage

## Chapter 5. Compressive Multiplexing of Ultrasound Signals

TABLE 5.1  
COMPARISON OF THE COMPRESSIVE MULTIPLEXING METHODS ON THE NUMERICAL PICMUS PHANTOM

Method	Freq. [MHz]	CNR [dB]	Lat. Res. [mm]		Ax. Res. [mm]		Speckle
			14 mm	45 mm	14 mm	45 mm	
LS-F	62.5	5.90	0.33	0.51	0.38	0.42	6/6
JS-F		5.90	0.33	0.51	0.38	0.42	6/6
CS-PS		6.10	0.33	0.51	0.38	0.42	6/6
Reference		5.90	0.33	0.51	0.37	0.40	6/6
LS-F	31.25	5.90	0.33	0.51	0.38	0.41	4/6
JS-F		5.40	0.33	0.52	0.38	0.41	4/6
CS-PS		6.40	0.34	0.52	0.38	0.41	6/6
Reference		5.90	0.33	0.51	0.37	0.40	6/6

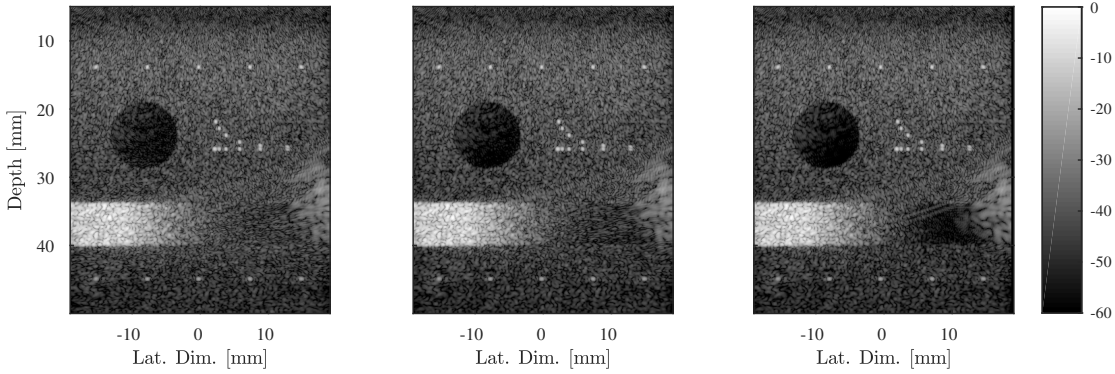


Fig. 5.6. Log-compressed B-mode images of the numerical PICMUS phantom reconstructed (from left to right) with LS-F, CS-PS, and obtained without compression. We consider a sampling frequency of 62.5 MHz and a compression ratio of 8 for LS-F and CS-PS.

to recover accurately both speckle regions, anechoic regions and point reflectors, which confirm the results of the first simulation study. Regarding the performance of JS-F, it can be seen that it is either very similar or slightly lower than LS-F, which can be justified by the absence of measurement noise and the perfect knowledge of the pulse-echo waveform. The variability observed in the values of the CNR is due to the sensitivity of the calculation of the metric and is not observable on the B-mode images.

Concerning Figure 5.6, it can be observed that the most evident degradations are located around the region of linear intensity decay between 35 mm and 40 mm. Indeed, the reconstruction error in the region of high intensity (left part of the strip) induces a slight incoherence in the beamforming process which results in higher sidelobes and additional noise in the anechoic region (right part of the strip).

**Sequence of *In vivo* Carotids:** We acquire two 0.5 s-long sequences (approx. 40 frames) of *in vivo* carotids, one longitudinal and one cross-section, with a Verasonics Vantage 256™ system (Verasonics, WA, USA) equipped with a GE 9L-D probe (linear array, 192 elements, 5.2 MHz center frequency, 75 % bandwidth). We transmit a single PW with normal incidence

## 5.5. Estimation of the Pulse-echo Waveform from Compressed Measurements

with 3-cycle square excitation signal. We acquire the data at 62.5 MHz and we simulate two compression strategies, one with 8 input signals per CMUX and one with 12 input signals per CMUX, performing a compression of  $8\times$  and  $12\times$  on the number of coaxial cables, respectively. We use the same settings as for the simulated experiment for the reconstruction methods, beamforming and post-processing.

Regarding CS-PS, we approximate the impulse response of the transducer elements by a Gaussian modulated sinusoidal pulse centered at 5.208 MHz with 75 % bandwidth. To quantify the image quality, the average PSNR and structural similarity index (SSIM) are computed against the reference sequence reconstructed from element-raw data acquired without compression. Table 5.4 reports the values of SSIM and PSNR for LS-F and CS-PS for the two considered compression strategies.

TABLE 5.2  
COMPARISON OF THE COMPRESSIVE MULTIPLEXING METHODS ON THE IN VIVO CAROTIDS

Method	Acquisition	Compression Ratio [-]	PSNR [dB]	SSIM [-]
LS-F	Longitudinal	8	44.5	0.96
CS-PS			42.2	0.96
LS-F		12	33.2	0.79
CS-PS			38.7	0.91
LS-F	Cross-section	8	42.6	0.95
CS-PS			40.3	0.95
LS-F		12	34.3	0.82
CS-PS			37.1	0.90

We observe that both methods lead to high-quality reconstructions for a compression ratio of 8, with slightly better results for LS-F. This may be explained by the imperfect knowledge of the pulse shape which impacts the quality of the reconstruction with CS-PS. Regarding the reconstruction with a compression ratio of 12, we observe that CS-PS significantly outperforms LS-F, which can be explained by a potentially sparser representation of US signals in the pulse-stream model than with the bandlimited signal model, especially when the bandwidth is relatively high.

Figure 5.7 displays the log-compressed B-mode images of a single frame of the sequence of longitudinal carotids for the compression ratio of 8. Visual assessment of the images corroborates the above analysis of the metrics and shows the remarkable quality of the reconstruction with the proposed approaches.

## 5.5 Estimation of the Pulse-echo Waveform from Compressed Measurements

In many realistic situations, the pulse-echo waveform is unknown and only approximated with a Gaussian modulated pulse. Such an approximation results in a decrease of the performance compared to cases where it is perfectly known, as shown in Section 5.4.3

In order to address this problem, we propose to estimate the pulse-echo waveform directly from the compressed measurements  $y$ .

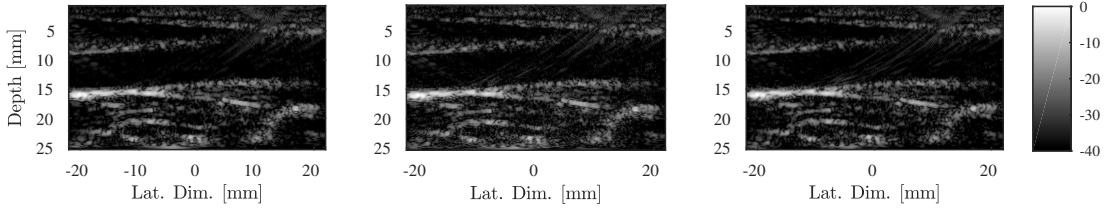


Fig. 5.7. Log-compressed B-mode images of the *in vivo* carotid reconstructed (from left to right) with LS-F, CS-PS, and obtained without compression. We consider a sampling frequency of 62.5 MHz and a compression ratio of 8 for CS-PS and LS-F.

### 5.5.1 Estimation of Pulse-echo Waveform as a Blind Deconvolution Problem

In order to estimate the pulse-echo waveform, we propose to solve the following blind deconvolution problem:

$$\min_{\substack{\mathbf{v} \in \mathbb{R}^F \\ \tilde{\mathbf{m}} \in \mathbb{R}^{(N-F+1)N_x^t}}} \|\mathbf{y} - \mathbf{C}(\mathbf{v} * \tilde{\mathbf{m}})\|_2^2 + \mathcal{R}(\mathbf{v}, \tilde{\mathbf{m}}), \quad (5.59)$$

where  $\mathcal{R}$  is a regularizer which encodes prior knowledge on  $\mathbf{v}$  and  $\tilde{\mathbf{m}}$ . Let us define the following functional:

$$\mathcal{L}(\mathbf{v}, \tilde{\mathbf{m}}) = \|\mathbf{y} - \mathbf{C}(\mathbf{v} * \tilde{\mathbf{m}})\|_2^2 + \mathcal{R}(\mathbf{v}, \tilde{\mathbf{m}}). \quad (5.60)$$

Problem (5.59) is non-convex and has been extensively studied in the literature. Apart from its non-convexity, a well-known pitfall of such a problem is the scaling ambiguity which states that if scale variant norms are used as regularizers and if  $(\mathbf{v}, \tilde{\mathbf{m}})$  is a global minimum of (5.59), then  $(\lambda \mathbf{v}, \frac{1}{\lambda} \tilde{\mathbf{m}})$  is also a global minimum of (5.59) [273–275]. More specifically, we have two well-known illustrations of such a phenomenon:

- if the regularizer has the following form  $\mathcal{R}(\mathbf{v}, \tilde{\mathbf{m}}) = C \|\tilde{\mathbf{m}}\|$ , for any norm, then there exists  $\tilde{\mathbf{m}}_k$  and  $\mathbf{v}_k$  such that  $\tilde{\mathbf{m}}_k \xrightarrow[k \rightarrow \infty]{} \mathbf{0}$  and  $\mathcal{L}(\mathbf{v}_k, \tilde{\mathbf{m}}_k) \xrightarrow[k \rightarrow \infty]{} 0$  and the global minimum is never reached;
- if the regularizer has the following form  $\mathcal{R}(\mathbf{v}, \tilde{\mathbf{m}}) = C \|\tilde{\mathbf{m}}\| + \|\mathbf{v}\|_p$ , with  $p < 1$ , then there exists a positive number  $\mu$  and two vectors  $\mathbf{v}_s$  and  $\tilde{\mathbf{m}}_s$  such that  $(\mu \delta, \frac{1}{\mu} \mathbf{v}_s * \tilde{\mathbf{m}}_s)$  is a global minimum of (5.59) (Corollary 1 of [273]), where  $\delta$  is such that  $\delta * \mathbf{y} = \mathbf{y}$ .

Hence, the regularizer has to be carefully chosen in order to avoid such pitfalls.

A key aspect relies on the fact that the support of the pulse-echo waveform  $\mathbf{v}$  is of size  $F$  small compared to the size of the measurements. Hence, a possible way to recover  $\mathbf{v}$  is by MAP estimation from the measurements. The MAP estimate would be obtained by maximizing the posterior probability  $p(\mathbf{v}|\mathbf{y})$  and would be successful with high probability [274]. However, evaluating the posterior probability may be unfeasible in the general case.

Instead, we propose to use the taxicab-Euclidean norm ratio ( $\ell_1/\ell_2$  ratio) for the regularization term on  $\tilde{\mathbf{m}}$ . This scale-invariant sparsity measure prevents the method from the scaling ambiguity and has been used in several blind deconvolution methods [276–278].

## 5.5. Estimation of the Pulse-echo Waveform from Compressed Measurements

Regarding the pulse-echo waveform, since it is well approximated by Gaussian modulated pulses, we suggest to use the  $\ell_2$ -norm as a regularizer, leading to the following optimization problem

$$\min_{\substack{\mathbf{v} \in \mathbb{R}^F \\ \tilde{\mathbf{m}} \in \mathbb{R}^{(N-F+1)N_x^t}}} \|\mathbf{y} - \mathbf{C}(\mathbf{v} * \tilde{\mathbf{m}})\|_2^2 + \lambda \frac{\|\tilde{\mathbf{m}}\|_1}{\|\tilde{\mathbf{m}}\|_2} + \beta \|\mathbf{v}\|_2^2, \quad (5.61)$$

where  $\lambda, \beta \in \mathbb{R}_+$  are regularization parameters.

Consider that we know the excitation signal  $\mathbf{e} \in \mathbb{R}^E$ , which is the case in US imaging, we can express the pulse-echo waveform as a convolution between the two-way impulse response  $\mathbf{v}_{tw} \in \mathbb{R}^{F-E+1}$  and the excitation signal such that (5.59) is formulated on  $\mathbf{v}_{tw}$  as

$$\min_{\substack{\mathbf{v} \in \mathbb{R}^{F-E+1} \\ \tilde{\mathbf{m}} \in \mathbb{R}^{(N-F+1)N_x^t}}} \|\mathbf{y} - \mathbf{C}(\mathbf{e} * \mathbf{v} * \tilde{\mathbf{m}})\|_2^2 + \lambda \frac{\|\tilde{\mathbf{m}}\|_1}{\|\tilde{\mathbf{m}}\|_2} + \beta \|\mathbf{v}\|_2^2, \quad (5.62)$$

Additionally, assume that we have a prior knowledge on the bandpass signal property of the two-way impulse response. Such a prior knowledge can be interpreted in terms of low and high cutoff frequencies of a bandpass filter  $\mathbf{h}_f$ , which can be taken into account in the problem as follows

$$\min_{\substack{\mathbf{v} \in \mathbb{R}^{F-E+1} \\ \tilde{\mathbf{m}} \in \mathbb{R}^{(N-F+1)N_x^t}}} \|\mathbf{y} - \mathbf{C}(\mathbf{e} * \mathbf{h}_f * \mathbf{v} * \tilde{\mathbf{m}})\|_2^2 + \lambda \frac{\|\tilde{\mathbf{m}}\|_1}{\|\tilde{\mathbf{m}}\|_2} + \beta \|\mathbf{v}\|_2^2, \quad (5.63)$$

which can be used in conjunction with the prior on the excitation signal.

### 5.5.2 Solving the Blind Deconvolution Problem

The different instances of Problem (5.61) described in the previous section are all non-convex due to the convolution and the taxicab-Euclidean norm. A common way to solve such a problem is by alternating minimization (AM), in which, at each iteration, we alternatively update each variable while keeping the other quantities constant [279].

While convergence to a critical point is not guaranteed theoretically, a careful initialization may lead to convergence to local minima of interest.

Without loss of generality, we focus on Problem (5.61) but the same reasoning can be applied to (5.62) and (5.63). Formally, we perform the following sequential minimization:

$$\begin{cases} \tilde{\mathbf{m}}^{(k+1)} & \in \operatorname{argmin}_{\tilde{\mathbf{m}} \in \mathbb{R}^{(N-F+1)N_x^t}} \|\mathbf{y} - \mathbf{C}(\mathbf{v}^{(k)} * \tilde{\mathbf{m}})\|_2^2 + \lambda \frac{\|\tilde{\mathbf{m}}\|_1}{\|\tilde{\mathbf{m}}\|_2} \\ \mathbf{v}^{(k+1)} & = \operatorname{argmin}_{\mathbf{v} \in \mathbb{R}^F} \|\mathbf{y} - \mathbf{C}(\mathbf{v} * \tilde{\mathbf{m}}^{(k+1)})\|_2^2 + \beta \|\mathbf{v}\|_2^2 \end{cases}, \quad (5.64)$$

where  $k \in \mathbb{N}_+$ .

**Update of  $\tilde{\mathbf{m}}$ :** Because of the  $\ell_1/\ell_2$ -norm term, the update of  $\tilde{\mathbf{m}}$  involves solving a challenging non-convex optimization problem. Several approaches have been proposed to address such a problem. Repetti *et al.* [276] propose to use a smooth approximation of the ratio and

derive convergence results when using a proximal-gradient algorithm. In this work, we use the trick introduced by Krishnan *et al.* [277] in which we transform the  $\ell_1/\ell_2$  minimization into a reweighted- $\ell_1$  minimization problem.

More precisely, to update  $\tilde{\mathbf{m}}$ , we solve a sequence of  $\ell_1$ -minimization problems, where, at each iteration, the  $\ell_1$ -norm is weighted by  $1/\|\tilde{\mathbf{m}}\|_2$ , where  $\|\tilde{\mathbf{m}}\|_2$  is calculated from  $\tilde{\mathbf{m}}$  obtained at the last iterate, as described in Algorithm 7. Each  $\ell_1$ -minimization problem is solved using FISTA.

---

### Algorithm 7 $\tilde{\mathbf{m}}$ Update

---

**Require:**  $\mathbf{y}, \mathbf{v}, \mathbf{C}, \tilde{\mathbf{m}}_0, \lambda, M$   
**for**  $j = 1 \dots M$  **do**  
 $\lambda^{(j)} = \lambda \|\tilde{\mathbf{m}}^{(j-1)}\|_2$   
 $\tilde{\mathbf{m}}^{(j)} \in \underset{\tilde{\mathbf{m}}}{\operatorname{argmin}} \|\mathbf{y} - \mathbf{C}(\mathbf{v} * \tilde{\mathbf{m}})\|_2^2 + \lambda^{(j)} \|\tilde{\mathbf{m}}\|_1$   
**end for**  
**return**  $\tilde{\mathbf{m}}^{(M)}$

---

While the convergence of such a procedure has not been deeply investigated, it appears to be quite efficient in practice [277].

**Update of  $\mathbf{v}$ :** The update of  $\mathbf{v}$  is significantly simpler than the update of  $\tilde{\mathbf{m}}$ . Formally, we can express the problem as:

$$\min_{\mathbf{v} \in \mathbb{R}^F} \|\mathbf{y} - \Phi^{(k+1)} \mathbf{v}\|_2^2 + \beta \|\mathbf{v}\|_2^2, \quad (5.65)$$

where  $\Phi^{(k+1)} = \mathbf{C} \tilde{\mathbf{M}}^{(k+1)} \mathbf{P}_F \in \mathbb{R}^{NN_x^t \times F}$ , with  $\mathbf{P}_F \in \mathbb{R}^{N_x^t(N-F+1) \times F}$  the identity restricted to the first  $F$  coefficients and  $\tilde{\mathbf{M}}^{(k+1)} \in \mathbb{R}^{NN_x^t \times N_x^t(N-F+1)}$  is the convolution matrix associated with  $\tilde{\mathbf{m}}^{(k+1)}$ .

Problem (5.65) is a standard ridge regression problem and  $\mathbf{v}^{(k+1)}$  is recovered by solving the following linear problem:

$$\Phi^{(k+1)\top} \mathbf{y} = \left( \Phi^{(k+1)\top} \Phi^{(k+1)} + \beta \mathbf{I} \right) \mathbf{v}, \quad (5.66)$$

which has a closed-form expression of the following form:

$$\mathbf{v}^{(k+1)} = \left( \Phi^{(k+1)\top} \Phi^{(k+1)} + \beta \mathbf{I} \right)^{-1} \Phi^{(k+1)\top} \mathbf{y}. \quad (5.67)$$

In practice, rather than computing the inverse  $\left( \Phi^{(k+1)\top} \Phi^{(k+1)} + \beta \mathbf{I} \right)^{-1}$ , we solve the normal equations (5.66) using state-of-the-art techniques e.g. conjugate gradient method.

**Overall Pulse-echo Waveform Estimation Algorithm:** The overall AM algorithm computes sequentially the two update steps described above. It is detailed in Algorithm 8.

---

**Algorithm 8** Pulse-echo Waveform Estimation Algorithm

---

**Require:**  $\mathbf{y}, \mathbf{C}, \tilde{\mathbf{m}}^0, \mathbf{v}^0, \lambda, \beta, M$   
**Initialization:**  $k = 1$   
**repeat**  
     $\boldsymbol{\alpha}^{(0)} \leftarrow \tilde{\mathbf{m}}^{(k-1)}$   
    **for**  $j = 1 \dots M$  **do**  
         $\lambda^{(j)} = \lambda \left\| \boldsymbol{\alpha}^{(j-1)} \right\|_2$   
         $\boldsymbol{\alpha}^{(j)} \in \underset{\boldsymbol{\alpha}}{\operatorname{argmin}} \left\| \mathbf{y} - \mathbf{C} (\mathbf{v}^{(k-1)} * \boldsymbol{\alpha}) \right\|_2^2 + \lambda^{(j)} \left\| \boldsymbol{\alpha} \right\|_1$   
    **end for**  
     $\tilde{\mathbf{m}}^{(k)} \leftarrow \boldsymbol{\alpha}^{(M)}$   
     $\mathbf{v}^{(k)} \leftarrow (\boldsymbol{\Phi}^{(k)\top} \boldsymbol{\Phi}^{(k)} + \beta \mathbf{I})^{-1} \boldsymbol{\Phi}^{(k)\top} \mathbf{y}$   
     $k \leftarrow k + 1$   
**until** a stopping criterion is met  
**return**  $\mathbf{v}$

---

### 5.5.3 Validation of the Algorithm

We propose to validate the pulse-echo waveform estimation algorithm on two simulated examples, namely a point-reflector phantom composed of 5 point reflectors and an anechoic inclusion of 4 mm diameter centered at a depth of 45 mm and embedded in a fully developed speckle background.

The idea is to evaluate the algorithm on two different scenarios, one with a very sparse image on which the sparsity assumption in the pulse-stream model should readily apply and one on a dense image where the the sparsity assumption is not very accurate.

The L11-4v probe is used and the phantoms are insonified with a single PW with normal incidence. The excitation is a 2-cycle square signal and the impulse response of the transducer elements is set to be a Gaussian modulated sinusoidal pulse. The simulations are performed with Field II [89].

We propose to evaluate the influence of the modeling assumptions on the pulse-echo waveform described above, i.e. the bandlimited (BL) assumption and the convolution model (CM). More precisely, we test the following configurations: no BL-no CM, BL-no CM, no BL-CM and BL-CM, where “no BL” (resp. “no CM”) accounts for “no bandlimited assumption” (resp. “no convolution model”). We evaluate the estimation algorithm for the two compression strategies described in Section 5.4.3.

Regarding the estimation technique, we fix the maximum number of iterations of Algorithm 8 to 50. We also set a stopping criterion on the relative evolution of the pulse between consecutive iterations to a tolerance of  $5 \times 10^{-3}$ . The regularization parameter  $\beta$  is set manually by grid search.

Regarding Algorithm 7, we set a maximum of 5 iterations for the reweighted- $\ell_1$  algorithm, and 10 iterations for the  $\ell_1$ -minimization algorithm involved in each step of the algorithm.

The quality of the estimation is evaluated using the NRMSE between the estimated pulse and the reference pulse. Table 5.3 reports the values of the NRMSE.

First, it can be observed that the proposed methods work well for both strategies and for

## Chapter 5. Compressive Multiplexing of Ultrasound Signals

TABLE 5.3  
COMPARISON OF THE PULSE-ESTIMATION METHODS ON THE SIMULATED ANECHOIC AND POINT-REFLECTOR PHANTOMS

Method	Freq. [MHz]	NRMSE [-]	
		Anechoic	Point-Reflector
noBL-noCM	62.5	0.87	<b>0.96</b>
BL-noCM		0.90	<b>0.96</b>
noBL-CM		<b>0.92</b>	0.94
BL-CM		0.91	<b>0.96</b>
noBL-noCM	31.25	0.86	<b>0.96</b>
BL-noCM		0.88	<b>0.96</b>
noBL-CM		<b>0.90</b>	0.94
BL-CM		<b>0.90</b>	<b>0.96</b>

every model assumption, with a minimum value of the NRMSE of 0.86. We can see that the results are slightly better on the point-reflector phantom which makes sense since it has a significantly sparser representation in the pulse-stream model than the anechoic-inclusion phantom. The surprisingly good results on the anechoic-inclusion phantom, which is dense in the pulse-stream model, can be explained the fact that the pulse estimation problem is highly over-determined and regularized.

Figure 5.8 shows the estimated pulse-echo waveforms for the point-reflector and anechoic-inclusion phantoms respectively, for the considered compression strategies.

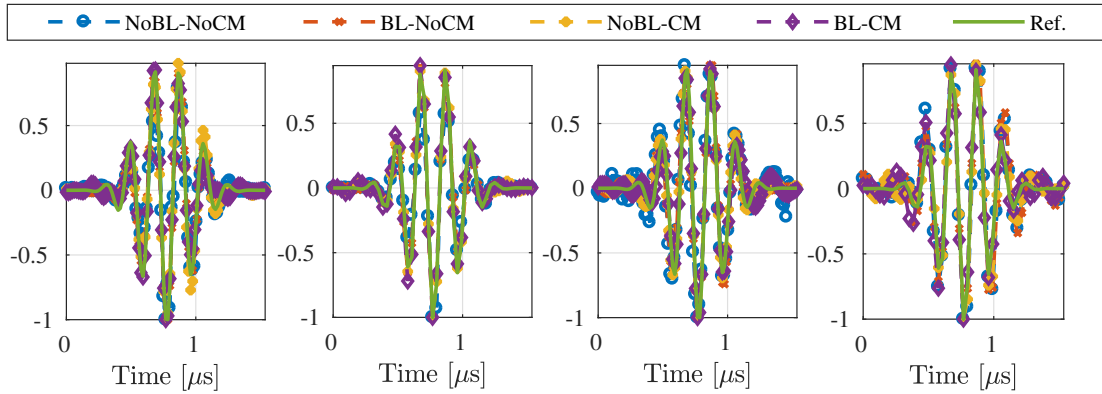


Fig. 5.8. From left to right: Pulse-echo waveform estimated on the point-reflector phantom for the first and second compression strategy; pulse-echo waveform estimated on the anechoic phantom for the first and second compression strategy.

Visual assessment corroborates the results on the NRMSE. The estimated pulse-echo waveforms are remarkably similar to the reference (green solid line). The main difference between the shape of the waveform estimated on the anechoic phantom and on the point-reflector phantom are the oscillations at the very beginning and the very end of the pulse.

Regarding the modeling assumptions, we notice that every assumption leads to slightly improved performance compared to the case with no assumption. This improvement is barely visible on the pulse-echo waveform. We also observe empirically that such assumptions

## 5.5. Estimation of the Pulse-echo Waveform from Compressed Measurements

significantly stabilize and accelerate the AM procedure.

### 5.5.4 Reconstruction of *In Vivo* Carotids from Compressed Measurements and Unknown Pulse-echo Waveform

We acquire two 0.5 s-long sequences (approx. 40 frames) of *in vivo* carotids, one longitudinal and one cross-section, with a Verasonics Vantage 256™ (Verasonics, WA, USA) equipped with a GE 9L-D probe (linear array, 192 elements, 5.2 MHz center frequency, 75 % bandwidth). We transmit a single PW with normal incidence with 3-cycle square excitation signal.

We acquire the data at 62.5 MHz and we simulate two US-CMUX strategies, one with 8 input signals per CMUX and one with 12 input signals per CMUX, resulting in a compression equivalent to 8× and 12× on the number of coaxial cables, respectively.

We use the same settings as in Section 5.5.3 for the reconstruction methods, beamforming and post-processing. Regarding CS-PS, we approximate the impulse response of the transducer elements by a Gaussian modulated sinusoidal pulse centered at 5.2 MHz with 75 % bandwidth. Concerning CS-PSE, we learn the pulse-echo waveform of the first frame on the sequence and use it for the remaining frames.

Table 5.4 reports the values of SSIM and PSNR for LS-F, JS-F, CS-PS, and CS-PSE for the considered compression strategies.

TABLE 5.4  
COMPARISON OF THE COMPRESSIVE MULTIPLEXING METHODS WITH PULSE-ESTIMATION ON THE *IN VIVO* CAROTIDS

	Method	Compression Ratio [-]	PSNR [dB]	SSIM [-]
Longitudinal	LS-F	8	44.3	0.96
	JS-F		44.2	0.96
	CS-PS		42.0	0.95
	CS-PSE		42.7	0.96
	LS-F	12	34.4	0.83
	JS-F		34.3	0.81
	CS-PS		38.2	0.90
	CS-PSE		39.9	0.93
Cross-section	LS-F	8	43.4	0.96
	JS-F		42.8	0.96
	CS-PS		40.2	0.95
	CS-PSE		40.9	0.96
	LS-F	12	33.6	0.79
	JS-F		34.7	0.82
	CS-PS		36.7	0.89
	CS-PSE		38.0	0.92

We observe that all the methods lead to high-quality reconstructions for a compression ratio of 8, with slightly better results for the methods based on the bandpass signal model. We notice that LS-F always outperforms JS-F due to our strong knowledge of the index set  $J$ . We also observe that CS-PSE always outperforms CS-PS which was expected due to a reduced mismatch of the pulse-echo waveform. This shows the importance of an accurate pulse-echo

waveform estimation in *in vivo* configurations.

Regarding the reconstruction with a compression ratio of 12, we observe that CS-PS and CS-PSE significantly outperform LS-F and JS-F, which can be explained by a potentially sparser representation of US signals in the pulse-stream model than under the bandlimited signal model, especially in this case where the bandwidth is relatively high.

Figure 5.9 displays, from left to right, the B-mode images reconstructed with the LS-F, CS-PS and CS-PSE and the reference, respectively, for a sampling frequency of 62.5 MHz and a compression ratio of 8.

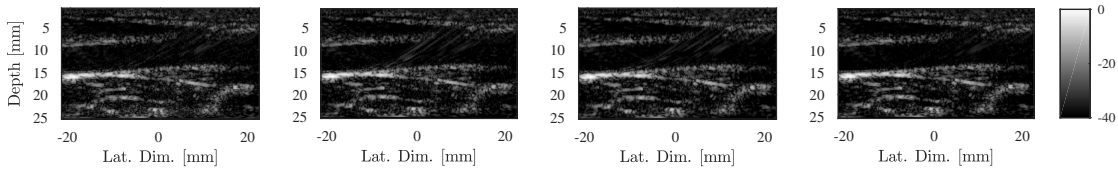


Fig. 5.9. Log-compressed B-mode images of the *in-vivo* carotid reconstructed (from left to right) with LS-F, CS-PS, CS-PSE and obtained without compression. We consider a sampling frequency of 62.5 MHz and a compression ratio of 8 for LS-F, CS-PS and CS-PSE.

We notice that the proposed methods lead to reconstructed images remarkably similar to the reference. We can nevertheless observe sidelobe artefacts related to high-intensity reflections at the carotid walls and at the interface with tissue fibers between 20 mm and 25 mm.

## 5.6 Discussion on the Proposed Compressive Multiplexing Strategy

From a signal processing perspective, one may question the relevance of the US-CMUX in the sense that the considered sampling frequencies are significantly higher than the Nyquist frequency. This is true but, in a system designer perspective, working at a higher sampling frequency is not problematic in US imaging since there is no critical power or data-rate requirements in the back-end system. ADCs of most current US imaging systems operate at higher rates than the Nyquist frequency and decimation, if necessary, is performed by a dedicated digital module.

On the contrary, the number of coaxial cables connecting the probe to the US acquisition system is critical. Hence, the US-CMUX exploits the additional budget offered by the high ADC rate to reduce the number of coaxial cables. It is nevertheless interesting to note that the overall data-rate reduction of the US-CMUX strategy is of the order of 75 % compared to uncompressed RF data sampled at Nyquist frequency.

A remarkable feature of the proposed strategy resides in its compatibility with micro-beamforming techniques. Indeed, the US-CMUX only exploits temporal characteristics of the signals while micro-beamforming methods perform spatial compression across channels. Hence, one can imagine that the US-CMUX can be applied on pre-beamformed signals which would combine the effects of the two methods resulting in a significantly lower number of coaxial cables.

A natural question concerns the realizability of the proposed US-CMUX strategies in a US system. While the objective of this chapter is not to provide a detailed study on this aspect, we can give some guidelines towards a possible implementation. First, hardware implementations

## 5.6. Discussion on the Proposed Compressive Multiplexing Strategy

---

of the CMUX schemes have been suggested by Slavinsky *et al.* [237] and Kim *et al.* [248]. An important observation is that both implementations require active components that are not desirable in the head of the probe, due to thermal effects induced by the dissipated power.

Kim *et al.* [248] have proposed a circuit-level realization of the CMUX based on sample and hold (SH) circuits and switch-capacitors which works at similar range of frequencies than in US imaging. Thus, we can think about adapting such an architecture for the US-CMUX, where the SH circuits are settled in the head of the probe, and the quantizer is settled in the back-end system.

Alternatively, one can think about using the passive averager CMUX described in [237] where the  $\pm 1$  modulation is achieved with two banks of resistors towards which the input signals are directed depending on the output of a linear-feedback shift register. In this case, two output cables per CMUX may be required to transfer the outputs of the two banks, which may increase the number of coaxial cables.

Regarding the modulation, pseudo-random sequences such as Kasami, Gold, maximum length and Hadamard can be used. See [248] for a more complete discussion on this topic.



# 6 Ultrasound Localization at the Rate of Innovation

Pluralitas non est ponenda sine  
necessitate

---

*Quaestiones et decisiones in quatuor  
libros Sententiarum cum centilogio  
theologico*  
Guillaume d'Ockham

In this chapter, we address the problem of recovering the exact locations of a finite number of point reflectors from the echo signals recorded by several transducer elements. Such a problem is common in several applications of US imaging, e.g. flaws detection in NDE and microbubble localization in contrast-enhanced US imaging.

We question the degrees of freedom related to such a problem, i.e. the minimum number of samples required for perfect localization, in terms of the number of transducer elements and the number of samples collected per element. This allows us to define a critical sampling rate associated with the localization of a finite number of strong reflectors.

We also detail a localization method that is able to operate at the critical rate. The technique is based on three steps, namely a TOF-recovery step, a TOF-labeling step and a localization step. In the TOF-recovery step, we leverage the FRI framework to retrieve the TOFs of the pulses corresponding to the different reflectors. In the TOF-labeling step, we associate the recovered TOFs to a given reflector using the concept of EDM. Finally, we use the labeled TOFs to localize the point reflectors by multilateration.

We validate the different steps of the proposed approach as well as the overall technique on simulated and *in vitro* data from an NDE experiment.

## 6.1 Existing Approaches and Proposed Localization Method

### 6.1.1 Existing Localization Approaches in Ultrasound Imaging

The localization of strong reflectors in an insonified medium is of significant interest in several applications, e.g. flaws detection in NDE [280], underwater acoustics [281].

In medical US imaging, microbubbles contrast agents localization is a key step in the well-known US localization microscopy [282, 283], which exploits localizations of contrast agents

to reveal the finest vasculature of the body, with applications to the diagnosis of cancer, arteriosclerosis and diabete.

The main obstacle for the localization of strong reflectors is the limited axial and lateral resolution due to the finite aperture of the probe and the bandlimited properties of transducer elements.

Several localization methods have been investigated in the literature. Couture *et al.* [284] have developed a technique to localize an isolated microbubble based on parabola fitting whose resolution limit, discussed in several studies [283, 285], depends on the number of elements, the aperture size, and the timing resolution of the system.

Another technique has been developed by Prada and Clement [286], based on the SVD of the time-reversal operator, interpreted as a covariance matrix used for standard source separation. The localization of the sources is based on fitting the singular vectors of the covariance matrix with the corresponding Green vectors, using maximum likelihood or MUSIC. Such a method requires the number of transducer elements to be higher than the number of strong reflectors and the medium of interest to be gridded.

The vast majority of localization approaches solve a  $\ell_1$ -minimization problem, in which the medium is discretized and sparsity is imposed on the image [287–290]. These approaches require a gridding of the medium, which significantly impacts the accuracy of the localization and they are only feasible under strict coherence conditions of the measurement matrix, which require the pulse to be localized in time and the point reflectors to be sufficiently spaced [291].

### 6.1.2 Measurement Setup and Problem Statement

As in previous chapters, we consider a standard UFUS imaging setup where a US probe, composed of  $N_x^t$  transducer elements located at  $\{\mathbf{p}_i\}_{i=1}^{N_x^t}$ , is used to transmit a PW or a DW inside a medium  $\Omega$ . On receive, we record backscattered echoes as echo-signals  $m_i(t) \in L_2([0, T])$ ,  $i = 1, \dots, N_x^t$ , during a time  $T$ .

In this chapter, we further consider that the medium is composed of  $K$  point reflectors, located at  $\{\mathbf{r}_k\}_{k=1}^K$ , and we assume that the element-raw data follow the previously introduced pulse-stream model, such that the following holds

$$m_i(t) = \sum_{k=1}^K a_{ik} v_{pe}(t - \tau(\mathbf{r}_k, \mathbf{p}_i)) = \sum_{k=1}^K a_{ik} v_{pe}(t - t_{ik}), \quad (6.1)$$

where  $a_{ik}$  designates the amplitude of the pulse originating from the  $k$ -th point reflector and received by the  $i$ -th transducer element, and  $\tau(\mathbf{r}_k, \mathbf{p}_i)$  is the round-trip TOF between the  $k$ -th point reflector and the  $i$ -th transducer element.

We put ourselves in a discrete setting where we assume that we have access to  $N$  uniform samples of the element-raw data, acquired at the rate  $f_s$ , which form a matrix  $\mathbf{M} \in \mathbb{R}^{N \times N_x^t}$ .

From such a measurement setup, the localization problem can be formulated as follows.

**Problem 1** (Ultrasound Localization Problem). *Given the measurements  $\mathbf{M} \in \mathbb{R}^{N \times N_x^t}$  obtained from (6.1) at locations  $\{\mathbf{p}_i\}_{i=1}^{N_x^t}$ , estimate the locations of the point reflectors  $\{\mathbf{r}_k\}_{k=1}^K$ .*

### 6.1.3 Proposed Localization Approach

In order to address the above introduced localization problem, we propose a threefold localization approach as shown in Figure 6.1.

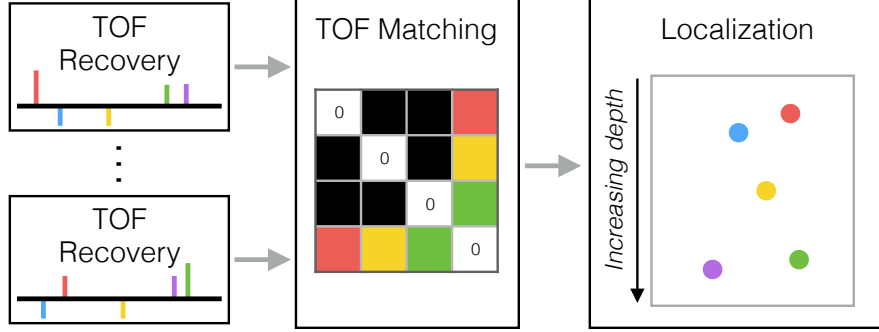


Fig. 6.1. Diagram of the proposed localization approach: (1) time-of-flight recovery for each channel, (2) time-of-flight matching across channels, (3) localization.

**TOF-recovery step:** In the TOF-recovery step, the TOFs,  $\mathbb{T}_i = \{\tau(\mathbf{r}_k, \mathbf{p}_i)\}_{k=1}^K$ , of each transducer element are recovered from the corresponding element-raw data  $\mathbf{M}_i$ ,  $i = 1, \dots, N_x^t$ . Such a problem amounts to retrieving a parametric model (stream of pulses), from a set of discrete measurements. Two group of approaches may be considered for such a task, namely continuous deconvolution of pulse streams, recently investigated by Bendory *et al.* [261, 263], and FRI [224] extended to pulse streams in several studies [131, 292, 293].

In this work, we focus on the latter and the proposed TOF-recovery approach is described in Section 6.2.

**Localization step:** Assuming a perfect recovery of the TOFs for each transducer element, the localization of the  $K$  point reflectors amounts to solving a problem similar to the well-known uDGP [294]. Mathematically, consider a bipartite graph  $G = (U, V, E)$ , as shown in Figure 6.2, where  $U$  corresponds to the set of transducer elements and  $V$  is the set of point reflectors.

Although  $\mathbb{T}_i$  represents the recovered TOFs between a given element  $u_i \in U$  and the set of point reflectors  $V = \{v_k\}_{k=1}^K$ , we do not know the correspondence between a TOF  $t \in \mathbb{T}_i$  and one of the  $K$  edges in  $E_i = \{u_i, v_k\}_{k=1}^K$ .

Hence the localization problem can be recast as the following problem.

**Problem 2** (uDGP-like Localization Problem). *Determine  $N_x^t$  assignment functions  $\alpha_i : \{1, \dots, K\} \rightarrow E_i$ ,  $i = 1, \dots, N_x^t$  and an embedding  $r : V \rightarrow \mathbb{R}^2$ , such that*

$$\alpha_i(k) = \{u_i, v_k\} \in E_i \text{ and } \tau(r(v_k), \mathbf{p}_i) = \tau(\mathbf{r}_k, \mathbf{p}_i), \forall (k, i) \in \{1, \dots, K\} \times \{1, \dots, N_x^t\}. \quad (6.2)$$

This can be expressed as the following minimization problem

$$\min_{\{\alpha_i\}_{i=1}^{N_x^t}} \left[ \min_{r: V \rightarrow \mathbb{R}^2} \sum_{i=1}^{N_x^t} \sum_{k=1}^K J(\tau(r(v_k), \mathbf{p}_i) - \tau(\mathbf{r}_k, \mathbf{p}_i)) \right], \quad (6.3)$$

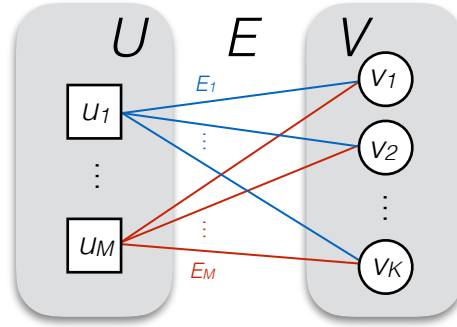


Fig. 6.2. Bipartite graph associated with the proposed localization approach.

where  $J$  is a suitable cost function, typically the squared Euclidean distance, and the minimization is over all the possible assignments.

To solve such a problem, we propose an approach where we first recover the optimal assignment functions  $\{\alpha_i^*\}_{i=1}^{N_t^x}$  (TOF-matching step) and then the optimal embedding  $r^*$  (localization step).

The TOF-matching step relies on the concept of EDM and is detailed in Section 6.3. The localization step from the assigned TOFs is performed by multilateration, as described in Section 6.4.

#### 6.1.4 Critical Sampling Rate of the Proposed Localization Approach

We are interested in the critical sampling rate associated with the localization of  $K$  reflectors which corresponds to the minimum number of samples required to perform such a task.

Intuitively, a signal composed of echoes originating from  $K$  point reflectors has  $2K$  degrees of freedom, namely the TOFs and amplitudes of the echoes. Hence, in cases where there is a one-to-one correspondence between the TOFs and the locations of the reflectors, the localization may be performed with at least  $2K + 1$  samples [293].

In US imaging, there is no such a one-to-one correspondence due to diffraction effects and another critical sampling rate has to be devised, related to the problem defined hereafter.

**Problem 3** (Minimum Number of Samples for the Localization Task). *Find the minimum number of transducer elements  $N_t^c$  and the number of samples  $N^c$  per element required to successfully perform the localization of  $K$  point reflectors.*

Hence, we define the critical sampling rate of our localization method as

$$\rho_{loc} = \frac{N_t^c N^c}{T}, \tag{6.4}$$

by analogy with the critical sampling rate defined in the context of signal sampling. In the following sections, we detail the three steps of the proposed approach and show that there exists a critical sampling rate associated with each of them. More precisely, we show in Section 6.2 that the proposed TOF-recovery step requires  $2K + 1$  samples per transducer element. Then, we demonstrate in Section 6.3 that the TOF-labeling step necessitates at least 3 transducer elements to succeed with probability 1.

Hence the critical sampling rate of the localization approach is  $\rho_{loc} = \frac{3(2K+1)}{T}$ , which corresponds to a reduction of the data rate by several order of magnitudes compared to existing methods.

## 6.2 Sampling Along Channels with Finite Rate of Innovation

### 6.2.1 From Bandlimited Signal Sampling to Finite Rate of Innovation

**Shannon Theorem in the Light of Hilbert Spaces:** As described in Section 5.1.2, the theory of signal sampling was born in 1949, when Claude Shannon published his seminal paper “Communication in the Presence of Noise” [220]. Associated with the WKS theorem, the following reconstruction formula is presented

$$f(t) = \sum_{k \in \mathbb{Z}} f(kT) \operatorname{sinc}\left(\frac{t}{T} - k\right). \quad (6.5)$$

Equation (6.5) is one of the most beautiful results in signal processing and information theory. It gives us the recipe to convert an analog signal into vectors that can be stored in a computer. Since then, the work of Shannon has been significantly extended and the field is now quite mature [295].

In particular, an enlightening interpretation of (6.5) is in terms of projections in Hilbert spaces. Indeed, consider that we work in the Hilbert space of square integrable functions  $L_2(\mathbb{C})$ , equipped with the standard inner product. In such a space, the set of shifted sinc kernels  $\{\phi_k = \operatorname{sinc}(\frac{\cdot}{T} - k)\}_{k \in \mathbb{Z}}$  is an orthonormal family. More precisely, it is the orthonormal basis of the subspace of the functions bandlimited to  $\omega_{max}$  which can therefore be defined as

$$V(\phi) = \left\{ \sum_{k \in \mathbb{Z}} \langle f, \phi_k \rangle \phi_k \mid f \in L_2(\mathbb{C}) \right\}. \quad (6.6)$$

The associated orthogonal projection operator  $P_{V(\phi)} : L_2(\mathbb{C}) \rightarrow V(\phi)$  is defined as

$$P_{V(\phi)} f = \operatorname{argmin}_{g \in V(\phi)} \|f - g\|^2 = \sum_{k \in \mathbb{Z}} \langle f, \phi_k \rangle \phi_k, \quad (6.7)$$

where the computation of the inner-product  $\langle f, \phi_k \rangle$  can be performed by low-pass filtering followed by sampling [295].

Hence, we can conclude that the standard signal processing pipeline, which consists of low-pass filtering and sampling of a signal  $f$  actually performs the orthogonal projection of  $f$  onto the space of bandlimited signals  $V(\phi)$ . From such a statement, it is evident to observe that if  $f$  is bandlimited by  $\omega_{max}$ , then  $P_V f = f$  and the process of sampling is invertible.

Starting from this analysis, we can extend the process of sampling to other shift invariant spaces characterized by different generating functions. More precisely, given a generic family of non-necessarily orthogonal functions  $\{\phi_k = \phi(\cdot - k)\}_{k \in \mathbb{Z}}$  which nevertheless satisfy several mathematical conditions detailed in [295], we can express the orthogonal projection on  $V(\phi)$ , the space generated by such functions, as

$$P_{V(\phi)} f = \operatorname{argmin}_{g \in V(\phi)} \|f - g\|^2 = \sum_{k \in \mathbb{Z}} \langle f, \tilde{\phi}_k \rangle \phi_k, \quad (6.8)$$

where  $\tilde{\phi}_k$  is the dual basis function of  $\phi_k$  [295].

Hence, using the same principle of pre-filtering and sampling as detailed in the WKS theorem, but with a slightly different function than the one used for reconstruction, we can generalize the sampling theorem to other classes of signals, such as polynomials.

**Finite Rate of Innovation as Another Extension of the WKS Theorem:** In FRI, we are interested in another extension of the WKS theorem, where we allow arbitrary shifts of the generating functions. Formally, we consider signals of the following form

$$f(x) = \sum_{k \in \mathbb{Z}} c[k] \phi\left(\frac{t - t_k}{T}\right), \quad (6.9)$$

where  $t_k \in \mathbb{R}$  is not necessarily equal to  $kT$ .

A central notion of FRI is the rate of innovation of a signal denoted by  $\rho$ , which corresponds to the number of degrees of freedom of this signal per unit of time. For instance, our signal bandlimited to  $\omega_{max}$  has a rate of innovation  $\rho = \omega_{max}/\pi$ . According to the WKS theorem, we need samples spaced  $\pi/\omega_{max}$  seconds apart for perfect reconstruction. Hence, the WKS theorem provides us a way to sample bandlimited signals at their rate of innovation.

Inspired by this idea, FRI answers the following questions: Is there a way to sample certain classes of signals of form (6.9) at their rate of innovation? What classes of signals? What is the corresponding sampling process? How do we reconstruct these signals from the discrete measurements?

The initial paper of Vetterli *et al.* [224] addresses the problem of sampling several classes of signals, e.g. periodic and finite-length streams of Diracs, derivative of Diracs, piecewise polynomials, in a noiseless scenario. The problem of FRI in a noisy scenario has been tackled slightly later with a second publication from the same group [296].

### 6.2.2 Proposed Finite Rate of Innovation Sampling of Ultrasound Signals

We consider the periodic extension of the pulse stream model described in (6.1) as

$$m_i(t) = \sum_{m \in \mathbb{Z}} \sum_{k=1}^K a_k v_{pe}(t - t_{ik} - mT) \in L_2(\mathbb{R}), \quad i = 1, \dots, N_x^t, \quad (6.10)$$

where  $m_i(t)$  is now a  $T$ -periodic signal defined for  $t \in \mathbb{R}$ .

Given that the pulse-echo waveform is known, we observe that the signal (6.10) is characterized

## 6.2. Sampling Along Channels with Finite Rate of Innovation

by  $2K$  degrees of freedom per period  $T$ , corresponding to the delays and amplitudes of the  $K$  pulses, therefore by a finite rate of innovation  $\rho = \frac{2K}{T}$ .

In the remainder of this section, we derive a strategy which allows us to reconstruct the element-raw data  $m_i(t)$  from measurements acquired at critical sampling, i.e. at the rate of innovation, in a noiseless scenario and we propose techniques which address the problem of noise. The proposed sampling strategy is inspired from the work of Kusuma *et al.* [292], which have extended FRI to communications signals.

**Sampling Requirements:** We consider that we have access to  $N$  uniform samples acquired via the following sampling operation

$$y_n = \left\langle m_i(t) e^{-2i\pi f_c t}, \text{sinc}(B(nT_s - t)) \right\rangle, n = 1, \dots, N, \quad (6.11)$$

where  $T_s$  denotes the sampling period and  $f_c$  corresponds to the center frequency of the pulse-echo waveform.

To obtain such measurements, we first perform an IQ-demodulation of the element-raw data followed by a convolution with a standard low-pass filter with bandwidth  $B$ . We require the following for successful recovery of the element-raw data  $m_i(t)$  from the measurements  $(y_n)_{n=1}^N$ :

- The bandwidth of the sampling kernel must be greater than or equal to the rate of innovation, i.e.  $B \geq \rho$ ;
- The number of uniform samples must satisfy the following inequality:  $N \geq 2M + 1$ , where  $M = \lfloor \frac{BT}{2} \rfloor$ , such that  $T_s = \frac{T}{N}$ .

In a noiseless scenario, we can set  $B$  and  $N$  to their lower bounds, i.e.  $B = \rho$  and  $N = 2K + 1$  such that the sampling period becomes  $T_s = \frac{T}{2K+1}$  which corresponds to sampling at the rate of innovation.

**Signal Reconstruction in Noiseless Scenarios:** The central idea of signal reconstruction in FRI relies on the ability to transform the signal of interest into a weighted sum of sinusoids whose frequencies depend on the signal parameters. This allows us to exploit the annihilation property, a result known since Prony's work two centuries ago [297], which states that there exists a finite length discrete filter, called the annihilating filter, whose discrete convolution with the weighted sum of sinusoids is always 0 [225].

Mathematically, consider the following discrete signal, which corresponds to the Fourier series coefficients of a  $T$ -periodic stream of Diracs

$$\hat{\mathbf{x}}_m = \frac{1}{T} \sum_{k=1}^K \mathbf{a}_k e^{-2\pi i m \frac{t_k}{T}}, m = -K, \dots, K, \quad (6.12)$$

where the signal parameters are  $(\mathbf{a}, \mathbf{t}) \in \mathbb{C}^K \times \mathbb{C}^K$ .

We observe that (6.12) is effectively a weighted sum of sinusoids and we build the discrete filter  $\mathbf{h} \in \mathbb{C}^{K+1}$  whose  $z$ -transform is given by

$$H(z) = \sum_{k=0}^K \mathbf{h}_k z^{-k} = \prod_{k=1}^K (1 - \mathbf{u}_k z^{-1}), \quad (6.13)$$

where  $\mathbf{u}_k = e^{-2\pi i \frac{t_k}{T}}$ ,  $k = 1, \dots, K$ .

With few calculations, we can demonstrate that [225]

$$\sum_{k=0}^K \mathbf{h}_k \hat{\mathbf{x}}_{m-k} = 0, \quad \forall m \in \{0, \dots, K-1\}, \quad (6.14)$$

which can alternatively be expressed as the following Toeplitz system

$$T_K(\hat{\mathbf{x}}) \mathbf{h} = 0, \quad (6.15)$$

where  $\hat{\mathbf{x}} \in \mathbb{C}^{2K+1}$  are the signal coefficients, and  $T_K: \mathbb{C}^{2K+1} \rightarrow \mathbb{C}^{K \times K}$  such that

$$T_K(\hat{\mathbf{x}}) = \begin{pmatrix} \hat{\mathbf{x}}_0 & \hat{\mathbf{x}}_{-1} & \cdots & \hat{\mathbf{x}}_{-K} \\ \hat{\mathbf{x}}_1 & \hat{\mathbf{x}}_0 & \cdots & \hat{\mathbf{x}}_{-K+1} \\ \vdots & \vdots & \ddots & \vdots \\ \hat{\mathbf{x}}_{K-1} & \hat{\mathbf{x}}_{K-2} & \cdots & \hat{\mathbf{x}}_{-1} \end{pmatrix}. \quad (6.16)$$

Hence, given that we have access to  $2K + 1$  consecutive Fourier coefficients  $\hat{\mathbf{x}}_k$ ,  $k = -K, \dots, K$ , we recover the parameters  $\mathbf{a}$  and  $\mathbf{t}$  by performing the following steps:

1. Form the Toeplitz matrix  $T_K(\hat{\mathbf{x}})$  and solve (6.15) to retrieve the coefficients  $\mathbf{h} \in \mathbb{C}^{K+1}$ ;
2. Build the polynomial  $H(z) = \sum_{k=0}^K \mathbf{h}_k z^{-k}$  and find its roots to recover the coefficients  $\mathbf{u}$  and therefore the delays  $\mathbf{t}$ ;
3. Consider  $K$  consecutive Fourier coefficients  $\hat{\mathbf{x}}_k$ ,  $k = 1, \dots, K$  and solve the following Vandermonde system to recover the amplitudes  $\mathbf{a}$ :

$$\begin{pmatrix} \hat{\mathbf{x}}_1 \\ \hat{\mathbf{x}}_2 \\ \vdots \\ \hat{\mathbf{x}}_K \end{pmatrix} = \begin{pmatrix} \mathbf{u}_1 & \mathbf{u}_2 & \cdots & \mathbf{u}_K \\ \mathbf{u}_1^2 & \mathbf{u}_2^2 & \cdots & \mathbf{u}_K^2 \\ \vdots & \vdots & \ddots & \vdots \\ \mathbf{u}_1^K & \mathbf{u}_2^K & \cdots & \mathbf{u}_K^K \end{pmatrix} \begin{pmatrix} \mathbf{a}_1 \\ \mathbf{a}_2 \\ \vdots \\ \mathbf{a}_K \end{pmatrix}. \quad (6.17)$$

We now show that we can transform the measurements (6.11) into a weighted sum of sinusoids as in (6.12). Indeed, we can express the stream of pulses (6.10) as a convolution  $m_i = x \circledast \nu_{pe}$  where  $x$  is defined as the following stream of Diracs:

$$x(t) = \sum_{m \in \mathbb{Z}} \sum_{k=1}^K a_k \delta(t - t_{ik} - mT). \quad (6.18)$$

## 6.2. Sampling Along Channels with Finite Rate of Innovation

Hence, the Fourier coefficients  $\hat{\mathbf{y}} \in \mathbb{C}^N$  obtained by taking the DFT of the uniform samples  $\mathbf{y}$ , are given by

$$\hat{\mathbf{y}}_m = \frac{1}{B} \hat{\mathbf{x}}_m \hat{v}_{pe} \left( f_c + \frac{m}{T} \right) \Leftrightarrow \hat{\mathbf{x}}_m = \frac{B \hat{\mathbf{y}}_m}{\hat{v}_{pe} \left( f_c + \frac{m}{T} \right)}, \quad m = -\frac{N}{2}, \dots, \frac{N}{2} - 1, \quad (6.19)$$

where we assume an ideal low-pass filter  $s_B(f) = \frac{1}{B} \text{rect}\left(\frac{f}{B}\right)$  and  $\hat{v}_{pe}(f) = \hat{e}(f) \hat{h}_{ae}(f) \hat{h}_{ea}(f)$ . Thus, we can relate the Fourier coefficients of the measurements  $\hat{\mathbf{y}}_m$  to coefficients  $\hat{\mathbf{x}}_m$  that can be annihilated by simple division by the Fourier transform of the pulse-echo waveform (assumed to be known), in a process usually called equalization [292].

The overall signal reconstruction algorithm is described in Algorithm 9.

---

**Algorithm 9** Noiseless FRI pulse-stream reconstruction.

---

**Require:**  $\mathbf{y} \in \mathbb{C}^N, K, T, N, f_c, \hat{v}_{pe}$

Estimate the Fourier coefficients  $\hat{\mathbf{y}} \in \mathbb{C}^N$  by DFT of the measurements;

Perform equalization:  $\hat{\mathbf{x}}_m = \frac{\hat{\mathbf{y}}_m}{\hat{v}_{pe}(f_c + \frac{m}{T})}, m = -K, \dots, K$ ;

Build the Toeplitz matrix  $T_K(\hat{\mathbf{x}})$  and solve (6.15) to retrieve the coefficients  $\{h_k\}_{k=0}^K$ ;

Build the polynomial  $H(z) = \sum_{k=0}^K h_k z^{-k}$  and find its roots to recover the delays  $\{t_{ik}\}_{k=1}^K$ ;

Consider  $K$  consecutive Fourier coefficients  $\hat{\mathbf{x}}_k, k = 1, \dots, K$  and solve the corresponding Vandermonde system to recover the amplitudes  $\{a_k\}_{k=1}^K$ ;

**return**  $\{a_k, t_{ik}\}_{k=1}^K$

---

**Signal Reconstruction in Noisy Scenarios:** In realistic scenarios, we always have to deal with noise which can be of several forms. First, we can have additive noise due to an imperfect measurement system. Such a noise is usually incorporated after the sampling process and is uncorrelated across different channels and acquisitions. We can also have noise due to modeling errors, which accounts for the discrepancy between the mathematical model of the signal of interest and its real nature. In the case of US imaging, the discrepancy can be due to an inexact estimate of the pulse-echo waveform or to a wrong model order.

Noise is problematic in Algorithm 9 since it may lead to solve an inexact Toeplitz system that would result in inaccuracies in the estimation of the signal parameters.

A common way to deal with noise is by maximum likelihood estimation of the parameters given the measurements [298]. Under the assumption of additive Gaussian noise, the maximum likelihood estimation amounts to solving the following problem [299]

$$(\mathbf{a}, \mathbf{t}) = \underset{\mathbf{t} \in [0, T]^K, \mathbf{a} \in \mathbb{R}^K}{\text{argmin}} \sum_{m=-M}^M \left| \hat{\mathbf{x}}_m - \sum_{k=1}^K \mathbf{a}_k e^{-2\pi i m \frac{t_k}{T}} \right|^2, \quad (6.20)$$

where  $N = 2M + 1$ . The main drawback of this approach in the context of FRI is that it may lead to non-linear least squares problems that can be challenging to solve due to the multimodal shape of the involved cost function [299].

## Chapter 6. Ultrasound Localization at the Rate of Innovation

---

A more common way to address the noisy FRI reconstruction is by exploiting the annihilation property. Indeed, consider an integer  $P \in \{K, \dots, M\}$  and build the Toeplitz matrix  $T_P(\hat{\mathbf{x}}) \in \mathbb{C}^{(N-P) \times (P+1)}$ . The annihilation equation (6.15) enforces the following rank constraint on  $T_P(\hat{\mathbf{x}})$

$$\text{rank}(T_P(\hat{\mathbf{x}})) \leq K. \quad (6.21)$$

Hence, we can recast the maximum likelihood estimation as the following structured low-rank approximation problem [299]

$$\min_{\mathbf{T} \in \mathbb{C}^{(N-P) \times (P+1)}} \|\mathbf{T} - T_P(\hat{\mathbf{x}})\|_F^2 \text{ subject to } \mathbf{T} \in \mathcal{H}_K \cap \mathcal{T}, \quad (6.22)$$

where  $\mathcal{T}$  is the subspace of Toeplitz matrices of  $\mathbb{C}^{(N-P) \times (P+1)}$  and  $\mathcal{H}_K$  is the manifold of  $\mathbb{C}^{(N-P) \times (P+1)}$  composed of matrices with rank lower than  $K$ .

Problem (6.22) is non-convex and the convergence to a unique solution cannot be guaranteed. However, since both  $\mathcal{H}_K$  and  $\mathcal{T}$  are closed, we define the corresponding orthogonal projectors onto the two sets as  $P_{\mathcal{H}_K}$  and  $P_{\mathcal{T}}$ , respectively. The common heuristic to solve (6.22) consists in performing the following iteration

$$\mathbf{T}^{(p+1)} = P_{\mathcal{T}} \left( P_{\mathcal{H}_K} \left( \mathbf{T}^{(p)} \right) \right), \quad (6.23)$$

in a procedure called Cadzow denoising [225, 299].

Once we obtain a solution  $\tilde{\mathbf{T}}$  of (6.22), we reshape  $\tilde{\mathbf{T}}$  as  $\tilde{\mathbf{T}}_K \in \mathbb{C}^{(N-K) \times (K+1)}$ , we compute the SVD of  $\tilde{\mathbf{T}}_K$  and we keep the eigenvector corresponding to the smallest eigenvalue. Such a vector corresponds to the coefficients of the annihilating filter.

The overall algorithm is summarized in Algorithm 10.

---

### Algorithm 10 Noisy FRI pulse-stream reconstruction.

---

**Require:**  $\mathbf{y} \in \mathbb{C}^N, K, P, T, N, f_c, \hat{v}_{pe}$

Estimate the Fourier coefficients  $\hat{\mathbf{y}} \in \mathbb{C}^N$  by DFT of the measurements;

Perform equalization:  $\hat{\mathbf{x}}_m = \frac{\hat{y}_m}{\hat{v}_{pe}(f_c + \frac{m}{T})}$ ,  $m = -K, \dots, K$ ;

Build the Toeplitz matrix  $T_P(\hat{\mathbf{x}})$  and solve the structured low-rank approximation problem (6.22) to obtain  $\tilde{\mathbf{T}}$ ;

Reshape  $\tilde{\mathbf{T}}$  into  $\tilde{\mathbf{T}}_K \in \mathbb{C}^{(N-K) \times (K+1)}$  and identify the eigenvector corresponding to the smallest eigenvalue  $\mathbf{h}$ ;

Build the polynomial  $H(z) = \sum_{k=0}^K h_k z^{-k}$  and find its roots to recover the delays  $\{t_{ik}\}_{k=1}^K$ ;

Consider  $K$  consecutive Fourier coefficients  $\hat{\mathbf{x}}_k$ ,  $k = 1, \dots, K$  and solve the corresponding Vandermonde system to recover the amplitudes  $\{a_k\}_{k=1}^K$ ;

**return**  $(a_k, t_{ik})_{k=1}^K$

---

### 6.2.3 Experiments and Results

In this section, we validate the proposed algorithms with an extensive number of simulations. We consider a pulse-echo waveform built as a convolution between a 2-cycle square excitation and a Gaussian modulated sinusoidal pulse, with center frequency  $f_c = 5.2$  MHz and bandwidth of 67 %.

**Single-channel Noiseless Recovery:** In a first step, we validate Algorithm 9 for a pulse-stream composed of  $K = 10$  pulses. We consider a period  $T$  of  $64 \mu\text{s}$ , which corresponds to an imaging depth of 5 cm. The pulses are randomly placed in  $[0, T[$  and have random amplitudes, distributed according to a normal distribution with zero mean and variance 1. Since we are in a completely noiseless scenario, we sample at the critical rate, i.e. we acquire  $N = 21$  uniform samples of the demodulated element-raw data, which corresponds to a sampling rate of 323 kHz and a compression ratio of 64 compared to the uncompressed element-raw data.

On the left plot of Figure 6.3, we observe the element-raw data sampled at 20.8 MHz with the corresponding pulse-stream parameters. On the right plot, we report the parameters recovered with Algorithm 9 as well as the true parameters.

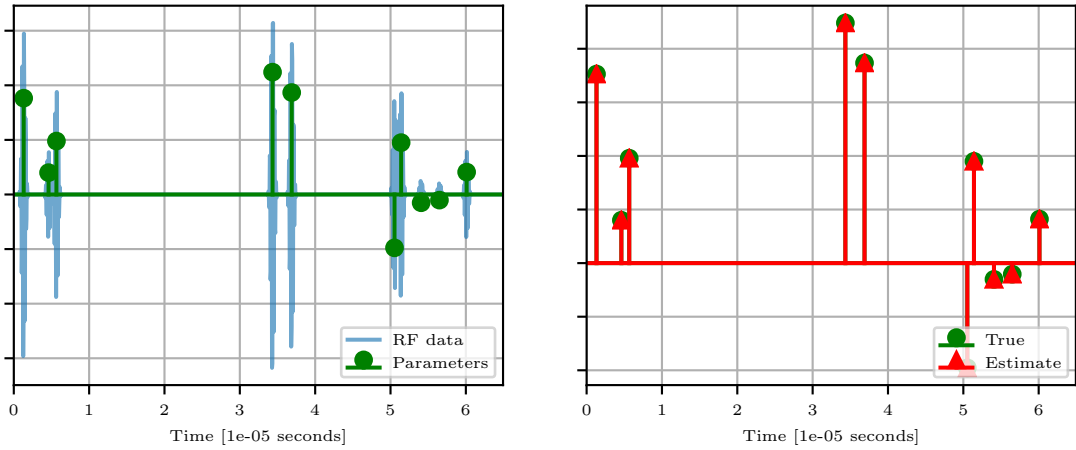


Fig. 6.3. The leftmost figure presents the element-raw data sampled at 20.8 MHz with overlaid pulse-stream parameters. The rightmost figure reports the recovered pulse-stream parameters (red) as well as the reference parameters (green) for  $K = 10$  pulses.

We notice that the pulse-stream parameters are perfectly recovered with the proposed approach.

**Single-channel Noiseless Recovery for an Increasing Number of Parameters:** In the context of US imaging, we may encounter cases where the number of pulses can be of the order of thousands. Thus, it would be interesting to test the robustness of the proposed technique for an increasing number of parameters.

From a signal processing perspective, we can define an upper bound on the model order as  $K_u = \lfloor \frac{f_s T - 1}{2} \rfloor$  after which the data rate of FRI is higher than the one provided by bandlimited

sampling. In the proposed experiment, we have  $K_u = 675$ . At first sight, such a value is far from the thousands values that we would need in medical imaging. Nevertheless, it may be sufficient for some applications, e.g. microbubbles tracking or flaws detection in NDE.

Hence, we suggest to quantify the quality of the reconstruction not on the parameters themselves but on the re-synthesized pulse-stream (See [300] for more details). As a metric, we use the signal-to-residual ratio (SRR) defined as

$$SRR = 20 \log \left( \frac{\|\mathbf{m}\|_2}{\|\mathbf{m} - \hat{\mathbf{m}}\|_2} \right), \quad (6.24)$$

where  $\mathbf{m}$  is the reference signal and  $\hat{\mathbf{m}}$  is the re-synthesized signal.

The left plot of Figure 6.4 displays the evolution of the SRR for an increasing number of parameters. Each value of the SRR is obtained as an average over 50 random trials, with the red bar indicating the standard deviation. On the right plot, we report the parameters recovered with Algorithm 9 as well as the true parameters for  $K = 30$ .

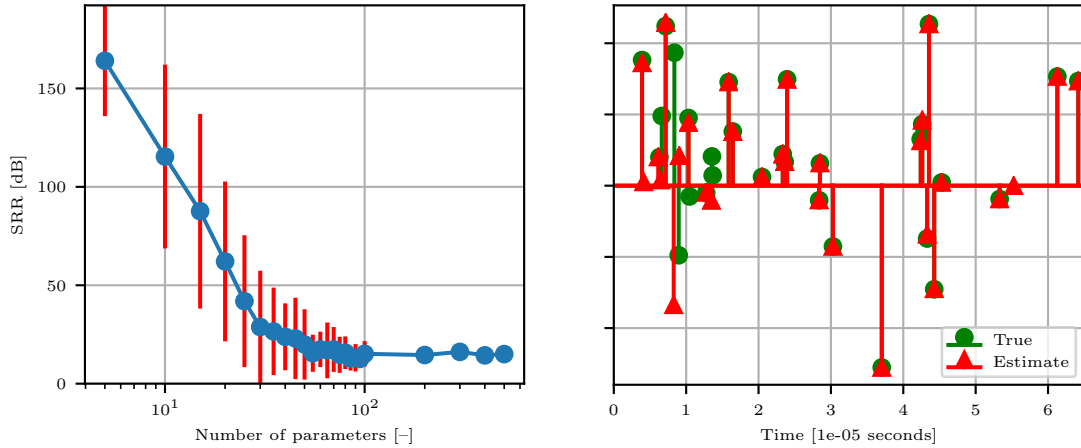


Fig. 6.4. The leftmost figure reports the signal-to-residuals ratio for an increasing number of pulse-stream parameters. The rightmost figure presents the recovered pulse-stream parameters (red) as well as the reference parameters (green) for  $K = 30$  pulses.

We observe that the SRR decreases relatively fast until it reaches a saturation which corresponds to the state where a random guess would be as good as the algorithm. The main reasons for such a decline are twofold. First, we notice that the root-finding operation required to obtain the coefficients  $\mathbf{u}$  from the annihilating filter becomes numerically challenging for high-degree polynomials. We have noticed that off-the-shelf methods fail for polynomials with degree higher than 20. In addition, FRI becomes unstable when it comes to discriminate closely spaced pulses due to the ill-conditioned Vandermonde system (See Appendix A8 of [300] for more details). This can be seen on the right plot of Figure 6.4, where the algorithm fails to recover closely spaced pulses.

**Single-channel Recovery with Additive Gaussian Noise:** We corrupt the measurements  $\mathbf{y}$  with an additive white Gaussian noise, whose variance depends on the SNR which varies

### 6.3. Sampling Across Channels with Euclidean Distance Matrices

between 0 dB and 50 dB. To address the problem of noise, we acquire  $P = \beta(2K + 1)$  measurements, where  $\beta$  is the oversampling ratio, and we simultaneously increase the bandwidth of the sampling kernel  $B = \beta \frac{2K}{T}$ . We then apply Algorithm 10, where we use Cadzow denoising (20 iterations) to solve the structured low-rank approximation problem.

Figure 6.5 reports the SRR against the SNR for two experiments, one with  $K = 10$  pulses and oversampling ratios  $\beta \in [2, 4, 6, 8, 10]$  (left plot) and one with  $K = 20$  pulses and oversampling ratios  $\beta \in [2, 3, 4, 5]$  (right plot).

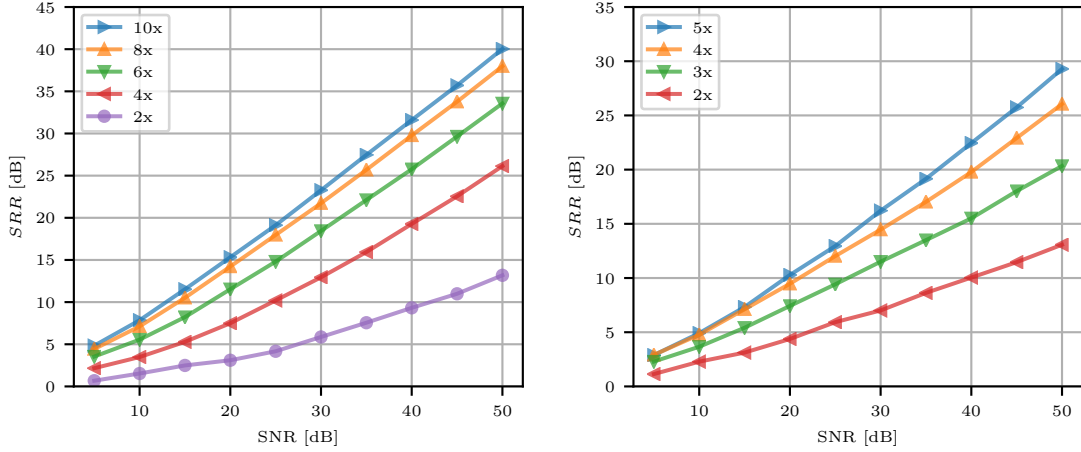


Fig. 6.5. Signal-to-residuals ratio as a function of the signal-to-noise ratio for 10 pulses (left figure) and 20 pulses (right plot) and several oversampling ratios.

As expected, we observe that the SRR is an increasing function of both the SNR and the oversampling factor. We also notice that the SRR deteriorates for a higher number of pulses, which is consistent with the results obtained in the noiseless case.

### 6.3 Sampling Across Channels with Euclidean Distance Matrices

In US imaging, we do not have a one-to-one correspondence between the TOFs and the locations of the point reflectors due to diffraction effects. In this Section, we devise a method to label the TOFs, i.e. to assign each TOF to the strong reflector from which it originates, based on the concept of EDM [301].

#### 6.3.1 Time-of-flight Labeling with Euclidean Distance Matrices

**A Short Tour on EDMs:** EDMs are matrices constructed by distances between a set of points. Mathematically, consider  $n$  points  $\mathbf{x}_i \in \mathbb{R}^d$  in a  $d$ -dimensional Euclidean space such that they form a matrix  $\mathbf{X} = [\mathbf{x}_1, \dots, \mathbf{x}_n] \in \mathbb{R}^{d \times n}$ . The EDM matrix  $\mathbf{D} \in \mathbb{R}^{n \times n}$  is defined element-wise by

$$D_{ij} = \|\mathbf{x}_i - \mathbf{x}_j\|_2^2, (i, j) \in \{1, \dots, n\}^2. \quad (6.25)$$

By expanding the squared  $\ell_2$ -norm, we deduce that

$$D_{ij} = \mathbf{x}_i^\top \mathbf{x}_i - 2\mathbf{x}_i^\top \mathbf{x}_j + \mathbf{x}_j^\top \mathbf{x}_j, (i, j) \in \{1, \dots, n\}^2, \quad (6.26)$$

from which we can define the EDM as

$$\mathbf{D} = \text{edm}(\mathbf{X}) = \mathbf{1} \text{diag}(\mathbf{X}^\top \mathbf{X})^\top - 2\mathbf{X}^\top \mathbf{X} + \text{diag}(\mathbf{X}^\top \mathbf{X}) \mathbf{1}^\top. \quad (6.27)$$

Equation (6.27), while being very simple, leads us to a powerful result about EDMs stated in the theorem hereafter.

**Theorem 12** (Rank of EDMs. Theorem 1 of [301].). *The rank of an EDM corresponding to points in a  $d$ -dimensional Euclidean space is at most  $d + 2$ .*

*Proof.* The proof is straightforward using (6.27). Indeed, we have that

$$\text{rank}(\mathbf{1} \text{diag}(\mathbf{X}^\top \mathbf{X})^\top) = 1 \text{ and } \text{rank}(\mathbf{X}^\top \mathbf{X}) \leq d,$$

such that

$$\text{rank}(\mathbf{D}) \leq \text{rank}(\mathbf{1} \text{diag}(\mathbf{X}^\top \mathbf{X})^\top) + \text{rank}(\mathbf{X}^\top \mathbf{X}) + \text{rank}(\text{diag}(\mathbf{X}^\top \mathbf{X}) \mathbf{1}^\top) \leq d + 2.$$

□

This is a strong result since it states that the rank of an EDM does not depend on the number of points but only on the dimension of the affine subspace that contains the points.

Such a property is used for many practical applications reviewed in [301], e.g. distance denoising, determining missing distances and distance labeling. The latter is of interest to us and will be developed in the remainder of the Section.

Another interesting property of the EDM is that it can be related to the Gram matrix of the set of points  $\mathbf{X}^\top \mathbf{X}$ . Indeed, consider the point  $\mathbf{x}_1$  as the origin, such that  $\mathbf{x}_1 = \mathbf{0}$ . Then, we immediately have that

$$\mathbf{D}_1 \mathbf{1}^\top = \text{diag}(\mathbf{X}^\top \mathbf{X}) \mathbf{1}^\top, \quad (6.28)$$

such that

$$\mathbf{G} = \mathbf{X}^\top \mathbf{X} = \frac{1}{2} (\mathbf{D}_1 \mathbf{1}^\top + \mathbf{1} \mathbf{D}_1^\top - \mathbf{D}). \quad (6.29)$$

In addition, the following inequality holds by construction

$$\text{rank}(\mathbf{G}) \leq d. \quad (6.30)$$

**Proposed TOFs-labeling Algorithm:** The proposed method, described in Algorithm 12 is inspired from the echo-sorting algorithm developed for room-shape recovery by Dokmanic *et al.* [33, 301].

The idea is based on two observations:

1. We know the locations of the transducer elements such that we can build a valid EDM from those locations;

2. The TOF on receive between the  $i$ -th transducer element and the  $k$ -th point reflector is related to their Euclidean distance as follows:

$$t_{Rx}(\mathbf{r}_k) = \frac{\|\mathbf{r}_k - \mathbf{p}_i\|_2}{c}. \quad (6.31)$$

Suppose that we have access to the round-trip TOFs,  $\mathbb{T}_i$ ,  $i = 1, \dots, M$ , and consider the first transducer element as the reference element. Take a candidate TOF  $t_1 \in \mathbb{T}_1$ . We can build  $K^{M-1}$  candidate vectors  $\mathbf{t} = [t_1, \dots, t_M]^\top$ , where  $t_i \in \mathbb{T}_i$ , from which only one corresponds to a valid combination, i.e. an echo that must be labeled.

To check whether a candidate vector corresponds to a valid combination, we rely on the second point mentioned above. First, we devise a method that estimates the vector of TOFs on receive  $\mathbf{t}_{Rx} \in \mathbb{R}^M$  from the candidate vector  $\mathbf{t}$ . We describe the method in the 2D-case but it can be easily extended to 3D. The round-trip TOF between the  $i$ -th transducer element and the  $k$ -th point reflector can be expressed as

$$\tau_i = \tau(\mathbf{r}_k, \mathbf{p}_i) = \frac{x_k \sin(\theta) + z_k \cos(\theta)}{c} + \frac{\|\mathbf{r}_k - \mathbf{p}_i\|_2}{c} = \frac{z'_k}{c} + \frac{\|\mathbf{r}'_k - \mathbf{p}'_i\|_2}{c}, \quad (6.32)$$

where  $\mathbf{r}'_k = \mathbf{R}_\theta \mathbf{r}_k$  and  $\mathbf{p}'_i = \mathbf{R}_\theta \mathbf{p}_i$ , with  $\mathbf{R}_\theta$  the rotation matrix of angle  $\theta$ .

Using (6.32), we can express the following parametric equation for the  $z$ -coordinate in the rotated domain:

$$z'_k = \frac{1}{2(c\tau_i - x_i \sin(\theta))} ((c\tau_i)^2 - (x'_k - x_i \cos(\theta))^2 - x_i^2 \sin^2(\theta)), \quad \forall i = 1, \dots, M. \quad (6.33)$$

Consider two different transducer elements located at  $\mathbf{p}_i$  and  $\mathbf{p}_j$ , we have that

$$\begin{aligned} \frac{(c\tau_i)^2 - (x'_k - x_i \cos(\theta))^2 - x_i^2 \sin^2(\theta)}{2(c\tau_i - x_i \sin(\theta))} &= \frac{(c\tau_j)^2 - (x'_k - x_j \cos(\theta))^2 - x_j^2 \sin^2(\theta)}{2(c\tau_j - x_j \sin(\theta))} \\ \Leftrightarrow \alpha_{ij} x'_k{}^2 + \beta_{ij} x'_k - \nu_{ij} &= 0, \end{aligned} \quad (6.34)$$

where the coefficients of the polynomial are given by

$$\begin{cases} \alpha_{ij} &= c(\tau_i - \tau_j) + \sin(\theta)(x_j - x_i) \\ \beta_{ij} &= 2 \cos(\theta) c(\tau_j x_i - \tau_i x_j) \\ \nu_{ij} &= c^3 \tau_i \tau_j (\tau_i - \tau_j) + c^2 \sin(\theta) (x_i \tau_j^2 - x_j \tau_i^2) + c(\tau_i x_j^2 - \tau_j x_i^2) \end{cases}.$$

Solving (6.34) leads to two possible values of  $x'_k$  and two possible values of  $z'_k$  by plugging them in (6.33), among which only one, denoted as  $z'_{kij}$  is on the feasible set of values of  $z'_k$ .

This allows us to compute the transmit time corresponding to the transducer elements  $i$  and  $j$  as  $z'_{kij}$ . Now, if we consider  $M$  couples of transducer elements  $\{i, j\}$ , forming a set  $E$ , we

compute the average transmit time as

$$t_{Tx}(\mathbf{r}'_k) = \frac{1}{M} \sum_{\{i,j\} \in E} \frac{z'_{kij}}{c}. \quad (6.35)$$

The overall estimation algorithm is described in Algorithm 11.

---

**Algorithm 11** Estimation of the transmit time

---

**Require:**  $\mathbf{t} \in \mathbb{R}^M, \mathbf{P}, E, c, \theta$

$t_{Tx} \leftarrow 0$

**for all**  $\{i, j\} \in E$  **do**

Find  $(x^-, x^+)$  solutions of  $\alpha_{ij} x_k'^2 + \beta_{ij} x_k' - v_{ij} = 0$

Compute  $(z^-, z^+)$  using (6.33) and select the valid solution  $z^*$

$t_{Tx} \leftarrow t_{Tx} + \frac{z^*}{c}$

**end for**

$t_{Tx} \leftarrow \frac{t_{Tx}}{|E|}$

**return**  $t_{Tx}$

---

Now that we can estimate the TOF on transmit corresponding to our candidate vector, we compute the vector of TOFs on receive (and consequently the distance) by deducing the transmit TOF to  $\mathbf{t}$  such that

$$\mathbf{t}_{Rx} = \mathbf{t} - t_{Tx} \Rightarrow \mathbf{d} = c(\mathbf{t}_{Rx} \circ \mathbf{t}_{Rx}).$$

At this stage, we have a candidate distance vector at our disposal and we can check whether it is a valid vector using the standard echo-sorting algorithm [301]. We rely on the fact that we know the location of  $M$  transducer elements to build the matrix  $\mathbf{P} = [\mathbf{p}'_1, \dots, \mathbf{p}'_M] \in \mathbb{R}^{d \times M}$ , from which we construct the corresponding EDM  $\mathbf{D} = \text{edm}(\mathbf{P}) \in \mathbb{R}^{M \times M}$ .

We build an augmented EDM with the proposed candidate vector as

$$\mathbf{D}_a = \begin{pmatrix} \mathbf{D} & \mathbf{d} \\ \mathbf{d}^\top & 0 \end{pmatrix} \in \mathbb{R}^{(M+1) \times (M+1)}, \quad (6.36)$$

from which we compute the Gram matrix  $\mathbf{G}_a$  using (6.29).

Finally, we check whether  $\mathbf{G}_a$  is a valid Gram matrix with the following rank test

$$\text{rank}(\mathbf{G}_a) \stackrel{?}{\leq} d. \quad (6.37)$$

To do so, we perform an eigenvalue decomposition (EVD) of  $\mathbf{G}_a = \mathbf{U}\mathbf{\Lambda}\mathbf{U}^\top$  where  $\mathbf{\Lambda} \in \mathbb{R}^{M \times M}$  is a diagonal matrix,  $\mathbf{U}$  is an orthonormal matrix, and we check whether  $\mathbf{\Lambda}_{dd} = 0$  or not.

The overall algorithm is detailed in Algorithm 12.

Once a valid candidate vector is identified, we assign a label,  $k \in \{1, \dots, K\}$ , to the corresponding TOFs and we repeat the process for another TOF  $t_1 \in \mathbb{T}_1$ .

---

**Algorithm 12** Proposed TOF-labeling algorithm
 

---

**Require:**  $\mathbf{P}, t_0, \theta, c, \mathbb{T}_1, \dots, \mathbb{T}_{M-1}, E$   
 $\mathbf{D} \leftarrow \text{edm}(\mathbf{P})$   
 $s_b \leftarrow +\infty$   
**for all**  $\mathbf{t} = [t_1, \dots, t_{M-1}]^\top$ , such that  $t_i \in \mathbb{T}_i$ , **do**  
 $\mathbf{t}_{TxRx} \leftarrow [t_0, \mathbf{t}^\top]^\top$   
 $t_{Tx} \leftarrow \text{EstimateTransmitTime}(\mathbf{t}_{TxRx}, \mathbf{P}, E, c, \theta)$   
 $\mathbf{t}_{Rx} \leftarrow \mathbf{t}_{TxRx} - t_{Tx}$   
 $\mathbf{d} \leftarrow c^2(\mathbf{t}_{Rx} \circ \mathbf{t}_{Rx})$   
 $\mathbf{D}_a \leftarrow \begin{pmatrix} \mathbf{D} & \mathbf{d} \\ \mathbf{d}^\top & 0 \end{pmatrix}$   
 $\mathbf{G}_a \leftarrow \frac{1}{2}(\mathbf{D}_{a1}\mathbf{1}^\top + \mathbf{1}\mathbf{D}_{a1}^\top - \mathbf{D}_a)$   
**if**  $\lambda_{d+1}(\mathbf{G}_a) < s_b$  **then**  
 $s_b \leftarrow \lambda_{d+1}(\mathbf{G}_a)$   
 $\mathbf{t}_b \leftarrow \mathbf{t}_{Rx}$   
**end if**  
**end for**  
**return**  $\mathbf{t}_b$

---

### 6.3.2 Pruning Methods to Reduce the Number of Combinations

Algorithm 12 requires to check  $K^M$  combinations in a configuration with  $M$  transducer elements and  $K$  point reflectors. In addition, checking the validity of a candidate vector requires to perform an EVD of a Gram matrix that can be computationally costly.

A first way of reducing the number of combination is by discarding previously labeled TOFs. Hence, once a valid combination is identified, the identification of a new candidate vector would require to search over  $(K-1)^M$  instead of  $K^M$  candidate vectors.

In addition, we can introduce the following pruning method based on geometrical constraints induced by the UFUS configuration.

**Maximal Difference Between TOFs:** Consider two transducer elements located at  $\mathbf{p}_i$  and  $\mathbf{p}_j$ , with corresponding sets of estimated TOFs  $\mathbb{T}_i$  and  $\mathbb{T}_j$ . Given  $t_i \in \mathbb{T}_i$ , it can be easily demonstrated, using maximal distance between the sensors, that the valid  $t_j$  lies in the following interval [302]

$$t_j \in \left[ t_i - \frac{\|\mathbf{p}_i - \mathbf{p}_j\|_2}{c}, t_i + \frac{\|\mathbf{p}_i - \mathbf{p}_j\|_2}{c} \right]. \quad (6.38)$$

Using this interval on the TOF of one channel given another, we can prune the  $t_i \in \mathbb{T}_i$  on line 4 of Algorithm 12 as follows

$$\mathbf{t} = [t_1, \dots, t_M]^\top, \text{ such that } t_i \in \mathbb{T}_i \text{ and } t_i \in \left[ t_1 - \frac{\|\mathbf{p}_i - \mathbf{p}_1\|_2}{c}, t_1 + \frac{\|\mathbf{p}_i - \mathbf{p}_1\|_2}{c} \right].$$

### 6.3.3 Conditions for Unique Recovery of the Time-of-flight Labeling Method

So far, we did not provide any recovery guarantee for the proposed TOF-labeling method. In this section, we discuss this aspect based on the work of Dokmanic *et al.* [33].

First, we detail the concept of feasible region in Definition 7, which allows us to put some restriction on the set of points in order to prove uniqueness of the recovery.

**Definition 7** (Feasible Region). *Consider a UFUS configuration composed of  $M$  transducer elements in receive, located at  $\{\mathbf{p}_i = [x_i, 0]^\top\}_{i=1}^M$ , which record backscattered echoes from a medium  $\Omega \subset \mathbb{R}^2$  in the time interval  $[0, T]$ .*

*The feasible region  $\Omega_f \subset \Omega$  is such that the echoes from each point of the region are recorded by all the transducer elements during the time interval  $[0, T]$ .*

Equipped with the above definition, we can state the main result of this section.

**Theorem 13** (Uniqueness). *Consider a UFUS configuration composed of  $M \geq 3$  transducer elements in receive, located at  $\{\mathbf{p}_i = [\lambda_i p, 0]^\top\}_{i=1}^M$ , where  $\lambda_i \in \{0, \dots, N_x^t - 1\}$  and  $p \in \mathbb{R}_+$ , which record backscattered echoes from a medium  $\Omega \subset \mathbb{R}^2$  in the time interval  $[0, T]$ . Consider also that the medium is composed of  $K$  point reflectors randomly placed in the feasible region. The TOF-labeling from the corresponding TOFs  $\mathbb{T}_i$ ,  $i = 1, \dots, M$ , based on Algorithm 12, will be successful with probability 1.*

*Proof.* The proof is based on the fact that the Gram matrix obtained from  $M \geq 3$  transducer elements using the EDM-based procedure, is of rank 1.

We show the result for 3 transducer elements and it can be easily extended to more than 3 elements. Consider that the first transducer element is positioned at the origin, which is always feasible, and that the two remaining elements are placed at  $[\lambda_1 p, 0]^\top$  and  $[\lambda_2 p, 0]^\top$ . Then, the corresponding Gram matrix is given by

$$\mathbf{G} = p^2 \begin{pmatrix} 0 & 0 & 0 \\ 0 & \lambda_1^2 & \lambda_1 \lambda_2 \\ 0 & \lambda_1 \lambda_2 & \lambda_2^2 \end{pmatrix}, \quad (6.39)$$

which is of rank 1, since  $\mathbf{G}_2 = \frac{\lambda_1}{\lambda_2} \mathbf{G}_3$ .

At this stage, consider a valid candidate vector  $\mathbf{t} = [t_1, t_2, t_3]^\top$ , where  $t_i \in \mathbb{T}_i$ , from which we compute the distance vector  $\mathbf{d} \in \mathbb{R}^3$  as in Algorithm 12. Assume that the vector  $\mathbf{t}$  corresponds to a point reflector located at  $[x, z]^\top$ , where  $x$  and  $z$  are random variables. The corresponding augmented Gram matrix can be expressed as

$$\mathbf{G}_a = \begin{pmatrix} 0 & 0 & 0 & 0 \\ 0 & \lambda_1^2 p^2 & \lambda_1 \lambda_2 p^2 & \lambda_1 p x \\ 0 & \lambda_1 \lambda_2 p^2 & \lambda_2^2 p^2 & \lambda_2 p x \\ 0 & \lambda_1 p x & \lambda_2 p x & x^2 \end{pmatrix}, \quad (6.40)$$

which has rank 2 with probability 1 since  $x$  is random.

### 6.3. Sampling Across Channels with Euclidean Distance Matrices

In the case where the candidate vector  $\mathbf{t} = [t_1, \dots, t_M]^\top$  is not valid, the augmented Gram matrix has the following form

$$\mathbf{G}_a = \begin{pmatrix} 0 & 0 & 0 & 0 \\ 0 & \lambda_1^2 p^2 & \lambda_1 \lambda_2 p^2 & a \\ 0 & \lambda_1 \lambda_2 p^2 & \lambda_2^2 p^2 & b \\ 0 & a & b & c \end{pmatrix}, \quad (6.41)$$

where  $a, b, c$  are random numbers due to the random locations of the scatterers.

Such a matrix is of rank 3 except in the specific case where we have a valid candidate vectors. Indeed, the set of vectors such that  $\text{rank}(\mathbf{G}_a) = 2$  is of measure 0 since it corresponds to the case where two roots of the characteristic polynomial are equal.

Hence, the rank test is successful with probability 1.  $\square$

#### 6.3.4 Time-of-flight Labeling in Noisy Scenarios

In realistic scenarios, we may face two main types of noise:

1. Noisy TOFs when the estimate in the TOF-recovery step is not perfect;
2. Missing TOFs for echoes that do not belong to the feasible region.

Noisy TOFs may come from model inaccuracies in the TOF-recovery step and will impact the performance of the rank test since even the valid candidates may lead to an augmented Gram matrix with a rank of 3. Since the test in Algorithm 12 selects the combination that leads to an augmented Gram matrix whose third eigenvalue is minimal (not necessarily 0), we believe that it may be robust to noisy TOFs up to some values of the SNR. To make the proposed method more robust to noise, a solution consists in increasing the number of transducer elements used in receive.

Missing distances may occur due to the limited directivity of the transducer elements, that can significantly reduce the feasible region. In order to deal with such a case, we can increase the number of transducer elements used in receive and select a subset of these elements which have recorded the appropriate number of echoes.

#### 6.3.5 Validation of the Proposed Approach with Simulations

In this section, we consider a linear array composed of 128 transducer elements (wavelength pitch) which operates at 5.208 MHz. We neglect the element-directivity and approximate the transducer elements as point-sources such that the size of the feasible region is maximized. On transmit, we simulate a PW insonification with normal incidence. On receive, we select a subset of  $M$  elements uniformly across the aperture and we simulate a medium with  $K$  reflectors.

**Noiseless TOF-labeling:** In this experiment, we simulate  $K = 20, 30, 40, 50$  randomly placed point reflectors and  $M = 3$  transducer elements in receive. We assume that the TOF-recovery step has successfully recovered the TOFs corresponding to the  $K$  pulses. We apply the proposed TOF-labeling algorithm and validate whether the labeling is accurate.

We draw 50 runs of simulations with different randomly placed scatterers and we quantify the accuracy of the proposed method by computing the average misclassification error between the true and estimated labels.

For all of them, Algorithm 12 has a 0 misclassification error which means that the proposed method always succeeds in a noiseless scenario.

**Noisy TOF-labeling:** In this experiment, we simulate  $K = 20, 30, 40, 50$  randomly placed point reflectors and  $M = 3, 4, 5$  transducer elements in receive. In order to simulate a noisy scenario, we add a white Gaussian noise on the TOFs, with different SNR values of 50 dB, 40 dB, 30 dB and 20 dB, respectively. We apply the proposed TOF-labeling algorithm and validate whether the labeling is accurate using the misclassification error.

Figure 6.6 displays the misclassification error of the TOF-labeling as a function of the SNR.

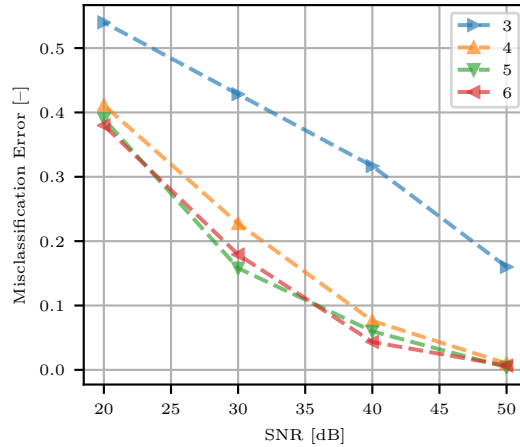


Fig. 6.6. Average misclassification error (10 draws) of the proposed time-of-flight labeling algorithm for different values of the signal-to-noise ratio.

As expected, we observe that the misclassification error decreases with a higher number of transducer elements in receive and for a higher SNR. This validates our strategy which consists in increasing the number of transducer elements to deal with noisy TOFs.

**Impact of the Pruning Methods:** In this experiment, we show the impact of the pruning methods described in Section 6.3.2 on the number of combinations and processing time. Figure 6.7 displays the number of combinations (left plot) as well as the average processing times (over 100 draws) on a 2.6 GHz Intel Core i5 processor (right plot) as a function of the number of reflectors for 3 transducer elements in receive.

We observe that the proposed method drastically reduces the number of combinations to test and consequently the processing time.

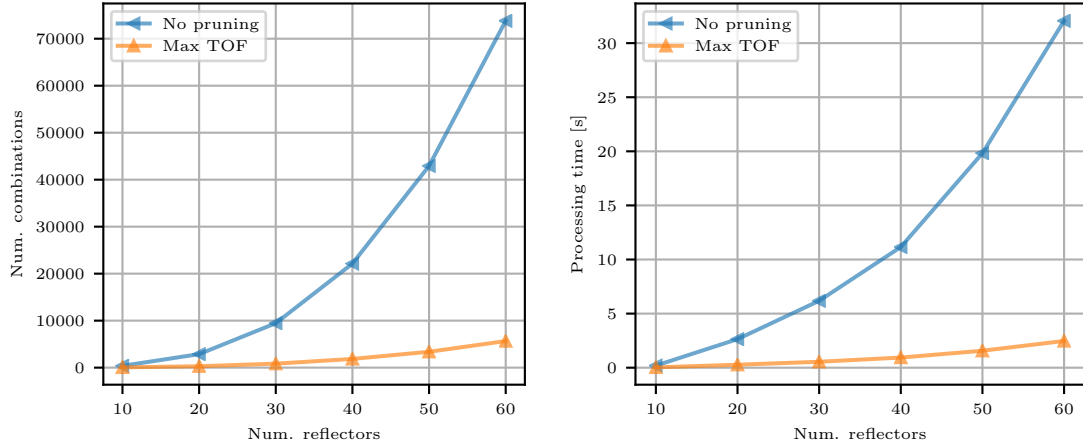


Fig. 6.7. Impact of the proposed pruning method on (left figure)-the number of combinations and (right figure)-the processing time of the time-of-flight labeling method; “No pruning” removes the already used combinations and “Max TOF” exploits the method described in Section 6.3.2.

## 6.4 Localization from Labeled Time-of-flights

In this section, we describe the technique used to localize the  $K$  point reflectors from a set of at least  $M \geq 3$  TOFs per point reflector, recorded by  $M$  transducer elements. We assume, without loss of generality, that one of the transducer elements is located at the origin.

### 6.4.1 Multidimensional Scaling

A first technique consists in building the EDM matrix  $\mathbf{D} \in \mathbb{R}^{(K+M) \times (K+M)}$  corresponding to the  $M$  transducer elements and  $K$  point reflectors based on their TOF as described in Section 6.3. We then deduce the gram matrix  $\mathbf{G}$  from the EDM using (6.29).

Based on the Gram matrix, we exploit the multidimensional scaling approach [301, 303] which consists in performing an EVD of the Gram matrix:

$$\mathbf{G} = \mathbf{U}\mathbf{\Lambda}\mathbf{U}^T, \quad \mathbf{\Lambda} = \text{diag}(\lambda_1, \dots, \lambda_{M+K}), \quad (6.42)$$

where  $|\lambda_1| > \dots > |\lambda_{M+K}|$ . Then we construct the estimate of the locations  $\hat{\mathbf{X}} \in \mathbb{R}^{2 \times (M+K)}$  as

$$\hat{\mathbf{X}} = \left[ \text{diag}(\sqrt{\lambda_1}, \sqrt{\lambda_2}), \mathbf{0}_{2 \times (M+K-2)} \right] \mathbf{U}^T. \quad (6.43)$$

More advanced techniques to deal with noisy distances has also been developed and are reviewed in [301].

### 6.4.2 Multilateration

Another technique, inspired from multilateration [304, 305], relies directly on the TOFs in order to determine the locations of the point reflectors.

In this section, we derive the formulations for PW with normal incidence. It can be easily extended to steered PW by considering the appropriate rotation matrix.

Consider a point reflector located at  $\mathbf{r} = [x, z]^\top \in \Omega$ , such that  $z > 0$ . The corresponding round-trip TOFs are given by

$$\begin{aligned} \tau_i &= \frac{z}{c} + \frac{\sqrt{(x-x_i)^2 + z^2}}{c}, \quad i = 1, \dots, M, \\ \Leftrightarrow z^2 &= (c\tau_i - z)^2 - (x-x_i)^2. \end{aligned} \quad (6.44)$$

Consider the transducer elements  $i$  and  $j$ , we deduce from (6.44) that

$$\begin{aligned} (c\tau_i - z)^2 - (x-x_i)^2 &= (c\tau_j - z)^2 - (x-x_j)^2 \\ \Leftrightarrow [x_j - x_i, c(\tau_j - \tau_i)] \begin{bmatrix} x \\ z \end{bmatrix} &= \frac{c^2(\tau_j^2 - \tau_i^2) + x_j^2 - x_i^2}{2}. \end{aligned} \quad (6.45)$$

Using (6.45) for all possible combinations of transducer elements, we come up with the following linear system of equations

$$\mathbf{A}\mathbf{r} = \mathbf{b} \Rightarrow \mathbf{r} = \mathbf{A}^\dagger \mathbf{b}, \quad (6.46)$$

where  $\mathbf{A} \in \mathbb{R}^{N_c \times 2}$ ,  $\mathbf{b}^{N_c}$ , with  $N_c = \frac{M(M-1)}{2}$ .

## 6.5 Experiments and Results

In this section, we validate the proposed localization approach on Field II simulations as well as on measured NDE data.

### 6.5.1 Field II Simulations

We consider a linear-array composed of 128 transducer elements with the following parameters: center frequency of 5.208 MHz, 67% bandwidth, wavelength pitch. We assume that the pulse-echo waveform is a Gaussian sinusoidal pulse and the excitation is a 1-cycle square signal. We transmit a single PW with normal incidence in a medium composed of 15 point reflectors. On receive, the element-raw data are sampled at 20.8 MHz.

White Gaussian noise is added to the element-raw data such that the SNR is 11.4 dB, as it can be seen on the left plot of Figure 6.8.

Using the element-raw data from three transducer elements spanning the whole array, we are able to localize the point reflectors, with a SRR equal to 45.7 dB. For the TOF-recovery approach, we perform 20 iterations of Cadzow denoising and we use a  $5\times$  oversampling compared to the critical sampling rate.

The overall data rate is reduced by a factor of 485 compared to existing localization methods that rely on data acquired at Nyquist rate on every transducer element.

### 6.5.2 Non-destructive Evaluation Experiment

In this experiment, we work with an example measurement for NDE. The phantom consists of an aluminum block with 7 holes drilled at different depths. Using an open phased-array

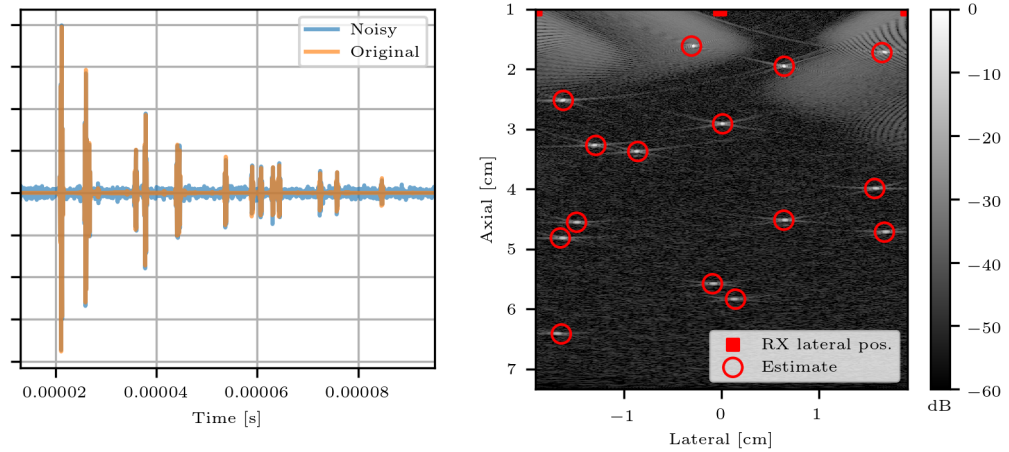


Fig. 6.8. The leftmost figure displays the original (orange) and noisy element-raw data (blue); The rightmost figure presents the localizations of the 15 point-reflectors recovered with the proposed approach with 3 transducer elements in receive and 5 times oversampling compared to critical sampling rate (20 iterations of Cadzow denoising for time-of-flight recovery).

platform (OEM-PA, by Advanced OEM Solutions), we insonify the phantom with a single PW with normal incidence. The linear probe (by Imasonic SAS) is composed of 64 transducer elements, with a center frequency of 5 MHz, bandwidth of 100 % and a pitch of 0.93 mm. The excitation signal is a half-cycle square wave and we assume the impulse response of the transducer elements to be a Gaussian modulated sinusoidal pulse. The speed of sound in aluminum is approximately  $6300 \text{ m s}^{-1}$ .

In order to deal with missing TOFs that are due to the limited directivity of the elements, we apply the proposed method on 7 elements that span the whole aperture. Regarding the TOF-recovery step, we run 20 iterations of Cadzow denoising with an oversampling factor of 9.5 to deal with modeling errors on the pulse-echo waveform. By visual assessment of the localized points, displayed on Figure 6.9, we observe that the proposed technique manages to accurately recover the locations of the holes. Since we do not have their exact locations, a more quantitative assessment is impossible.

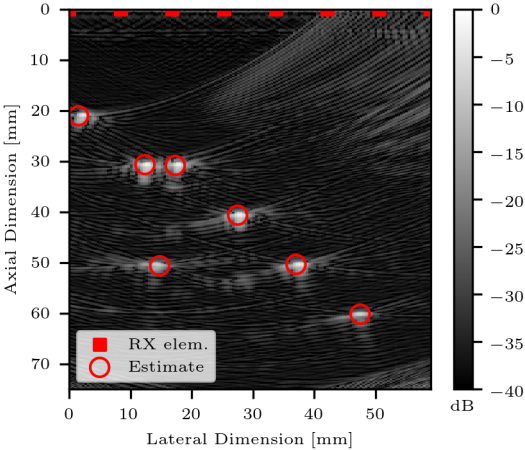


Fig. 6.9. Localization of the 7 drilled holes. The localization results are overlaid on the log-compressed B-mode image reconstructed with the delay-and-sum algorithm.

## 7 Concluding Remarks

Passons passons puisque tout passe  
Je me retournerai souvent  
Les souvenirs sont cors de chasse  
Dont meurt le bruit parmi le vent.

---

*Cors de Chasse, Alcools*  
Guillaume Apollinaire

We conclude this thesis with a few remarks. First, we propose to time-reverse this work and summarize the various contributions. Then, we briefly discuss future lines of research.

### 7.1 Time-reversing the Thesis

Our work explores several inverse problems related to US imaging and localization and aims to solve two main challenges:

1. performing high-quality imaging with few insonifications;
2. reducing the data collected per insonification.

The different technical contributions are described hereafter in an order that illustrates the story behind the thesis.

**Modeling the Pulse-echo Imaging Process** The first part of this thesis has been dedicated to model the US imaging process. We revisited pulse-echo US imaging as a linear inverse problem relating the echo signals recorded by the transducer elements to local variations of acoustic impedance, denoted as the TRF. We showed that the measurement model involved in the inverse problem consists of projections onto quadric surfaces whose shapes depend on the configuration, e.g. prolate spheroids in DW imaging and paraboloid in PW imaging. Hence, measurements gather many of these projections in a similar way to CT. Standard imaging, performed via the well-known DAS algorithm, can be interpreted as a backprojection of the proposed model under several assumptions.

Moreover, we have demonstrated that the composition of the measurement model and the DAS operator, the linear operator underpinning the DAS algorithm, models non-stationary blur in US imaging.

## Chapter 7. Concluding Remarks

---

We have suggested efficient matrix-free evaluation strategies of the proposed measurement model, and of its adjoint, based on a parameterization of the corresponding quadric surfaces. Such formulations were used inside regularization methods to

- perform high-quality imaging with fewer insonifications and fewer data collected per insonification than existing techniques;
- enhance already formed images by MAP estimation based on our model of non-stationary blur.

We have illustrated the benefits of the proposed approaches through an extensive number of simulated, *in vitro* and *in vivo* experiments.

**Take a Step Back: Modeling Echo-signals Rather than RF Images?** Because of the propagation of US waves, we realized that pulse-echo US imaging is inherently incompatible with CS. On the one hand, CS requires the signal of interest to be as spread as possible across the measurements. On the other hand, US imaging confines the signal onto quadric surfaces of isochronous loci.

We thought about two potential ways to tackle this problem. A first one consists in hacking the propagation in order to steer the measurement model towards a random matrix, as proposed by Kruizinga *et al.* [143]. An alternative, far easier to realize but maybe less elegant, was to get rid of the measurement model and concentrate on the element-raw data.

We have adopted the second solution in Chapters 5 and 6 of this thesis.

In Chapter 5, we have developed a CS-based multiplexing method for US signals which permits to perform imaging with significantly fewer coaxial cables than existing approaches. The compression is based on the CMUX architecture and performed in the head of the probe. The reconstruction is achieved in the back-end system with CS-based algorithms, where sparsity is expressed in models specifically suited to the element-raw data. We demonstrated through simulated and *in vivo* experiments that the proposed method was able to perform high-quality reconstruction with 8 to 12 times fewer coaxial cables.

In Chapter 6, we have devised a technique that is capable of localizing  $K$  reflectors with only 3 transducer elements and  $2K + 1$  samples collected per element, allowing for a significant reduction of the data rate compared to existing approaches. We modeled the element-raw data as a pulse stream and recovered the TOFs with the FRI framework. Then, we performed localization from the recovered TOFs in two steps. First, we assigned the TOFs to a given point-reflector using an echo-sorting algorithm based on EDM. Then, we performed localization from the labeled echoes using multilateration. We have evaluated the approach with simulated and *in vitro* NDE experiments.

**Some Theory Along the Way: Joint Sparsity with Partially-known Support** This thesis also contributes to the field of CS by extending joint sparsity to cases where partial support of the signal under scrutiny is known *a priori*. We have demonstrated that the knowledge of such a support is beneficial since it permits to have a unique solution of the CS problem under

weaker conditions than existing results on joint sparsity. Indeed, knowing part of the support allows us to benefit from additional information contained in the span of the columns of the measurement matrix. We augment the signal subspace correspondingly and the dimension of such a space is of major importance for joint-sparse recovery. In addition, we have extended MUSIC-based methods, subspace pursuit algorithms, augmented MUSIC methods and SNIHT to the case with partially known support. We have derived recovery guarantees for the different algorithms and compared them with the case without known support. We have validated empirically the benefits of partially known support through extensive simulations.

## 7.2 Future Prospects

**Towards DNN-based Image Reconstruction** In this thesis, we have described several methods for enhanced US imaging based on regularization approaches. These techniques suffer from two major drawbacks, already discussed in Section 4.5.1, namely the number of iterations necessary for reconstruction and the fine tuning of the regularization parameter. As discussed in Section 4.5.1, I believe that the next step consists in investigating DNN-based beamformers since they are compatible with real-time implementations and do not require any fine tuning of hyper-parameters. Future research should study the benefit of using a DNN inside an optimization algorithm, as in [198], compared to the simple approach where the DAS algorithm is followed by an inference from a DNN, as described in Section 4.5.3.

**Towards High-quality Portable Ultrasound** In the introduction, we mention portable US imaging as a key factor in the mutation of US imaging. We believe that the proposed methods, even though they are more computationally costly than the DAS algorithm, may be compatible with mobile commodity devices, especially if a DNN approach is used. Indeed, we can benefit from the GPUs that equip some of the mobile commodity devices and from several deep learning frameworks, such as TensorFlow Lite, that are dedicated to mobile platforms.

**Validation of the Proposed Methods on Advanced Imaging Modes** In order to emphasize the potential of the proposed methods for clinical applications, they should be tested within advanced imaging modes that are/will be used in clinics. Applications that would benefit from the proposed methods are the ones which require high frame rates and where coherent compounding cannot be performed. Two possible applications are vector-flow imaging and elastography.

We can also think about testing the proposed localization method in the context of US localization microscopy.

**Quantitative Imaging and Inverse Scattering** Additionally, I see quantitative imaging as a natural extension of this thesis. Indeed, there is no major issue towards the use of the proposed model to solve inverse scattering problems where we want to recover maps of speed of sound or TRF from the scattered pressure fields in a similar way to transmission-mode US tomography. At first sight, this may be feasible with the proposed optimization framework, by setting an appropriate prior for the quantity under scrutiny.

## Chapter 7. Concluding Remarks

---

But, we can consider more advanced problems in which, for instance, we relax the first-order Born approximation and perform non-linear inverse scattering via a recursive Born approach, similar to [306].

# A Generalized Radon Transforms

## A.1 Linear Radon Transform

### A.1.1 Definition of the Linear Radon Transform

Consider a function  $f(\mathbf{x}) \in \mathcal{S}(\mathbb{R}^m)$ , where  $\mathcal{S}(\mathbb{R}^m)$  denotes the set of test functions of  $\mathbb{R}^m$ , i.e. the set of all rapidly decreasing (faster than any inverse power of  $|\mathbf{x}|$ )  $\mathcal{C}^\infty$  functions on  $\mathbb{R}^m$ . Consider a line perpendicular to the hyperplane given by the equation  $p = \langle \boldsymbol{\xi}, \mathbf{x} \rangle$ , in which  $\boldsymbol{\xi} = [\xi_1, \dots, \xi_m] \in \mathbb{R}^m$  and  $p \in \mathbb{R}$ .

We define the *linear projection* of  $f$  in the direction perpendicular to  $\boldsymbol{\xi}$  by

$$\mathcal{R}[f](p, \boldsymbol{\xi}) = \int_{\mathbf{x} \in \mathbb{R}^m} f(\mathbf{x}) \delta(p - \langle \boldsymbol{\xi}, \mathbf{x} \rangle) d\mathbf{x}. \quad (\text{A.1})$$

The LRT is defined by the set of all the linear projections for  $p \in \mathbb{R}$  and  $\boldsymbol{\xi} \in \mathbb{R}^m$  such that  $\|\boldsymbol{\xi}\|_2 = 1$ .

Historically, the LRT has been introduced by Johann Radon in 1917 who also provided an inverse transform [307] in  $\mathcal{S}(\mathbb{R}^2)$ . In  $\mathbb{R}^2$ , the LRT can be expressed using polar coordinates as

$$\mathcal{R}[f](p, \theta) = \int_{s \in \mathbb{R}} f(s \sin(\theta) + p \cos(\theta), -s \cos(\theta) + p \sin(\theta)) ds, \quad (\text{A.2})$$

where  $p$  is the perpendicular distance from the line to the origin and  $\theta$  is the angle formed by the distance vector.

The most famous application of the LRT is in the area of X-ray transmission CT. Indeed, in the 1960s, Cormack showed that if one transmits a narrow X-ray beam inside the human body, the intensity received by an X-ray detector can be linked to the spatially varying attenuation by means of a linear Radon transform [308].

### A.1.2 Inversion of the Linear Radon Transform in 2D

The first inversion formula of the LRT has been derived by Radon itself in its seminal work, and is given by

$$f(x, y) = \iint_{\boldsymbol{\xi} \in S^1, p \in \mathbb{R}} \frac{\partial \mathcal{R}[f](p, \boldsymbol{\xi})}{\partial p} \frac{dp d\boldsymbol{\xi}}{\langle \boldsymbol{\xi}, \mathbf{x} \rangle - p}, \quad (\text{A.3})$$

## Appendix A. Generalized Radon Transforms

---

where  $S^1$  denotes the unit-sphere in  $\mathbb{R}^2$ . The main problem of such a formulation is that it may be very difficult to compute the integral, and the problem is technically ill-posed.

A neat way to invert the Radon transform relies on the projection-slice theorem (also known as Fourier slice theorem), which states that the 1D Fourier transform (FT) of any projection  $p_\theta(s)$  of a function  $f(x, y)$  along a line of angle  $\theta$  is equal to the 2D FT of  $f$  along the line parallel to the projection line and passing through the origin. Puts formally, we state the following theorem

**Theorem 14** (Fourier-slice theorem). *For any  $\theta \in [0, \pi]$ , the Fourier transform of the linear projection  $\mathcal{R}[f](\cdot, \theta)$  satisfies*

$$\int_{p \in \mathbb{R}} \mathcal{R}[f](p, \theta) e^{-ikp} dp = F(k \cos(\theta), k \sin(\theta)), \quad (\text{A.4})$$

where  $F$  is the 2D Fourier transform of  $f$ .

Hence, measuring the Radon transform is equivalent to acquiring the Fourier transform of  $f$  along radial lines. This relationship is fundamental in the derivation of the inverse Radon transform, also called filtered backprojection, given in the theorem hereafter.

**Theorem 15** (Inverse by filtered backprojection). *The following equality holds*

$$f(\mathbf{x}) = \frac{1}{4\pi^2} \int_0^\pi (\mathcal{R}[f](\cdot, \theta) \otimes h)(\langle \mathbf{x}, \mathbf{n}_\theta \rangle) d\theta, \quad (\text{A.5})$$

where  $h$  is such that  $\mathcal{F}[h](k) = |k|$  and  $\mathbf{n}_\theta = [\cos(\theta), \sin(\theta)]^\top$ .

Hence, we recover  $f$  from its Radon transform by performing a convolution with the kernel  $h$ , which corresponds to a high-pass filter, followed by standard backprojection.

## A.2 Generalized Radon Transform

### A.2.1 Definition of the Generalized Radon Transform

The generalized Radon transform (GRT) extends the LRT to other shapes than simple lines, e.g. circles and conics.

Formally, we introduce a real-valued function  $\Phi \in \mathcal{C}^\infty(\mathbb{R}^m \times \mathbb{R}^n)$  and a set of corresponding hypersurfaces  $\Omega_{\mathbf{s}, c} = \{\mathbf{x} \in \mathbb{R}^m \mid \Phi(\mathbf{x}, \mathbf{s}) = c\}$ , parameterized by  $c \in \mathbb{R}$  and  $\mathbf{s} \in \mathbb{R}^n$ .

The GRT projects the function  $f(\mathbf{x}) \in \mathcal{S}(\mathbb{R}^m)$  on one of the above defined hypersurfaces. Puts formally, we define the *projection* on the hypersurface  $\Omega_{\mathbf{s}, c}$  as [309]

$$\mathcal{R}[f](\mathbf{s}, c) = \int_{\mathbf{x} \in \mathbb{R}^m} f(\mathbf{x}) \delta(c - \Phi(\mathbf{x}, \mathbf{s})) d\mathbf{x}. \quad (\text{A.6})$$

It can be seen that the function  $\Phi(\mathbf{x}, \mathbf{s}) - c$  corresponds to the implicit function of the hypersurface  $\Omega_{\mathbf{s}, c}$ . The GRT is defined by the set of projections onto all the hypersurfaces.

We can also note that the LRT is a special instance of the GRT when  $\Phi(\mathbf{x}, \mathbf{s}) = \langle \mathbf{x}, \mathbf{s} \rangle$ .

Although GRTs have been studied in their general form (A.6) by many authors [310–315], richer theories have been defined for specific applications [316]. Some of them are listed in the remaining sections.

### A.2.2 The Spherical Radon Transform

The spherical Radon transform is a GRT where projections are achieved along spheres in  $\mathbb{R}^m$ . When  $m = 1$ , it is often referred as the circular Radon transform [316]. Formally, the *spherical projection* of  $f$  at center  $\mathbf{s} \in S$ ,  $S \subset \mathbb{R}^m$  being an hypersurface of  $\mathbb{R}^m$ , or alternatively the spherical average over  $B(\mathbf{s}, c)$  is defined as [316–318]:

$$\begin{aligned} \mathcal{R}[f](\mathbf{s}, c) &= \int_{\mathbf{x} \in B(\mathbf{s}, c)} f(\mathbf{x}) dA(\mathbf{x}), \quad (\mathbf{s}, c) \in S \times \mathbb{R}_+, \\ B(\mathbf{s}, c) &= \{\mathbf{y} \in \mathbb{R}^m \mid \|\mathbf{y} - \mathbf{s}\|_2 = c\}, \end{aligned} \quad (\text{A.7})$$

where  $dA(\mathbf{x})$  is the area measure on the sphere.

The integral transform that maps  $f$  to the complete set of spherical projections is the spherical Radon transform. Such a transform is useful in many applications such as thermoacoustic tomography [317, 319], photoacoustic imaging [320], sonar [318] and radar [321].

Many interesting properties of the spherical Radon transform have been derived for specific shapes of  $S$ . When  $S$  is an hyperplane of  $\mathbb{R}^m$  and  $\mathcal{R}[f](\mathbf{s}, c)$  is known for every  $c$  and every  $\mathbf{s}$ , Courant and Hilbert showed that any even function is uniquely determined by the corresponding complete set of projections [322]. Exact inversion techniques have been derived in the case where  $S$  is a sphere [69, 70, 323, 324] or a cylinder [69] and approximate back-projection methods have also been proposed [319, 320].

### A.2.3 The Elliptical Radon Transform

Elliptical Radon transforms, where the projections are achieved along ellipsoids, have been particularly studied because of their potential application in seismic imaging [325], bistatic SAR [326] imaging and ultrasound reflection tomography [104]. They are not very well known mathematical objects and most of the studies have been achieved in  $\mathbb{R}^3$  or  $\mathbb{R}^2$  under some restrictions on the focal points of the ellipses. The extension of the elliptical Radon transform to  $\mathbb{R}^m$  have been proposed very recently by Moon and Joonghyeok [327].

In this Section, we restrict our attention to  $\mathbb{R}^3$ . We can define an elliptical projection of the function  $f \in \mathcal{S}(\mathbb{R}^3)$  as follows

$$\begin{aligned} \mathcal{R}[f](\mathbf{s}, \mathbf{r}, c) &= \int_{\mathbf{x} \in E(\mathbf{s}, \mathbf{r}, c)} f(\mathbf{x}) dA(\mathbf{x}), \quad (\mathbf{s}, \mathbf{r}, c) \in S \times S \times \mathbb{R}_+, \\ E(\mathbf{s}, \mathbf{r}, c) &= \{\mathbf{y} \in \mathbb{R}^3 \mid \|\mathbf{y} - \mathbf{s}\|_2 + \|\mathbf{y} - \mathbf{r}\|_2 = c\}, \end{aligned} \quad (\text{A.8})$$

where  $\mathbf{s} \in S$  and  $\mathbf{r} \in S$  correspond to the foci of the ellipsoid and  $S$  is an hyperplane.

The integral transform that maps  $f$  to the complete set of elliptical projections is the elliptical Radon transform. Very little is known about the inversion of such a transform. Inversion techniques for family of ellipsoids with foci along a line [326, 328], on a circle [104, 329] and on a plane [327] have been studied.

### A.2.4 The Parabolic Radon Transform

Parabolic Radon transforms have been even less studied than elliptical Radon transforms, maybe because applications can only be found in seismic imaging, where it is known as the slant slack transform [325, 330, 331]. It has mainly been studied in  $\mathbb{R}^2$ , where the parabolic projection of a function  $f(x, y) \in \mathcal{S}(\mathbb{R}^2)$  is defined as [327]

$$\begin{aligned} \mathcal{R}[f](s, l, c) &= \int_{\mathbf{x} \in P(s, l, c)} f(x, y) dA(x, y), \quad (s, l, c) \in S \times S \times \mathbb{R}_+, \\ P(s, l, c) &= \left\{ [x, y]^T \in \mathbb{R}^2 \mid y - \frac{(x-s)^2}{2l} = c \right\}, \end{aligned} \quad (\text{A.9})$$

where  $S \subset \mathbb{R}$ .

The parabolic Radon transform is composed of the complete set of parabolic projections over parabola with apex  $(s, c)$ . Inversion techniques have been recently proposed by Moon [327] for a fixed axis direction and by Denecker *et al.* [309] for isofocal parabolas.

# B Expression of the Parametric Equations in Ultrafast Ultrasound Imaging

## B.1 Parametric Equations in Diverging Wave Imaging

### B.1.1 3D Imaging

In this section, we suppose that the transducer elements are arranged into a matrix probe located in the plane  $z = 0$ , with spacing  $\Delta_x^t$  and  $\Delta_y^t$  in the lateral and elevation dimension, respectively. We therefore consider the following uniform grid of transducer elements:

$$\mathbf{p}_{ij} = \left[ i\Delta_x^t, j\Delta_y^t, 0 \right]^\top, (i, j) \in \{1, \dots, N_x^t\} \times \{1, \dots, N_y^t\},$$

where  $N_x^t$  and  $N_y^t$  are the number of transducer elements in lateral and elevation dimension, respectively, such that  $N_t = N_x^t N_y^t$ .

We assume that the virtual point is positioned at  $\mathbf{r}_n = [x_n, y_n, z_n]^\top$  behind the probe. We are interested in finding a set of parametric equations of the points that belong to the following interface

$$\partial\Omega(\mathbf{p}_{ij}, \mathbf{r}_n, t) = \{\mathbf{r} \in \Omega \mid \|\mathbf{r} - \mathbf{p}_{ij}\|_2 + \|\mathbf{r} - \mathbf{r}_n\|_2 = c(t + t_0)\},$$

Using a dedicated computing software such as Wolfram Mathematica, we can demonstrate the following equivalence

$$\mathbf{r} = [x, y, z]^\top \in \partial\Omega(\mathbf{p}_{ij}, \mathbf{r}_n, t) \Leftrightarrow \begin{cases} x(\alpha, \beta, \mathbf{p}_{ij}, \mathbf{r}_n, t) = \alpha \\ y(\alpha, \beta, \mathbf{p}_{ij}, \mathbf{r}_n, t) = \beta \\ z(\alpha, \beta, \mathbf{p}_{ij}, \mathbf{r}_n, t) = \frac{A \pm \sqrt{\Delta}}{2(4(c t_0)^2 + 8c^2 t t_0 + 4c^2 t^2 - 4z_n^2)} \end{cases}, \quad (\text{B.1})$$

## Appendix B. Expression of the Parametric Equations in Ultrafast Ultrasound Imaging

where  $(\alpha, \beta) \in [x_{min}, x_{max}] \times [y_{min}, y_{max}]$ ,  $\Delta$  is given by

$$\begin{aligned} \Delta = & z_n^2 \left( -4\mathbf{p}_{ij_x}^2 + 8\alpha\mathbf{p}_{ij_x} - 4\mathbf{p}_{ij_y}^2 - 4(ct_0)^2 - 4c^2 t^2 + 4x_n^2 + 4y_n^2 + 4z_n^2 - 8c^2 t t_0 - 8x_n\alpha \right. \\ & \left. + 8\mathbf{p}_{ij_y}\beta - 8y_n\beta \right)^2 - 4 \left( 4(ct_0)^2 + 8c^2 t t_0 + 4c^2 t^2 - 4z_n^2 \right) \left( -\mathbf{p}_{ij_x}^4 + 4\alpha\mathbf{p}_{ij_x}^3 - 2\mathbf{p}_{ij_y}^2\mathbf{p}_{ij_x}^2 \right. \\ & \left. + 2(ct_0)^2\mathbf{p}_{ij_x}^2 + 2c^2 t^2\mathbf{p}_{ij_x}^2 + 2x_n^2\mathbf{p}_{ij_x}^2 + 2y_n^2\mathbf{p}_{ij_x}^2 + 2z_n^2\mathbf{p}_{ij_x}^2 - 4\alpha^2\mathbf{p}_{ij_x}^2 + 4c^2 t t_0\mathbf{p}_{ij_x}^2 \right. \\ & \left. - 4x_n\alpha\mathbf{p}_{ij_x}^2 + 4\mathbf{p}_{ij_y}\beta\mathbf{p}_{ij_x}^2 - 4y_n\beta\mathbf{p}_{ij_x}^2 + 8x_n\alpha^2\mathbf{p}_{ij_x} + 4\mathbf{p}_{ij_y}^2\alpha\mathbf{p}_{ij_x} - 4(ct_0)^2\alpha\mathbf{p}_{ij_x} \right. \\ & \left. - 4c^2 t^2\alpha\mathbf{p}_{ij_x} - 4x_n^2\alpha\mathbf{p}_{ij_x} - 4y_n^2\alpha\mathbf{p}_{ij_x} - 4z_n^2\alpha\mathbf{p}_{ij_x} - 8c^2 t t_0\alpha\mathbf{p}_{ij_x} - 8\mathbf{p}_{ij_y}\alpha\beta\mathbf{p}_{ij_x} \right. \\ & \left. + 8y_n\beta\beta\mathbf{p}_{ij_x} - \mathbf{p}_{ij_y}^4 - (ct_0)^4 - c^4 t^4 - x_n^4 - y_n^4 - z_n^4 - 4c^4 t^3 t_0 + 2\mathbf{p}_{ij_y}^2(ct_0)^2 + 2\mathbf{p}_{ij_y}^2 c^2 t^2 \right. \\ & \left. - 6c^2 t^2 (ct_0)^2 + 2\mathbf{p}_{ij_y}^2 x_n^2 + 2(ct_0)^2 x_n^2 + 2c^2 t^2 x_n^2 + 4c^2 t t_0 x_n^2 + 2\mathbf{p}_{ij_y}^2 y_n^2 + 2(ct_0)^2 y_n^2 + 2c^2 t^2 y_n^2 \right. \\ & \left. - 2x_n^2 y_n^2 + 4c^2 t t_0 y_n^2 + 2\mathbf{p}_{ij_y}^2 z_n^2 + 2(ct_0)^2 z_n^2 + 2c^2 t^2 z_n^2 - 2x_n^2 z_n^2 - 2y_n^2 z_n^2 + 4c^2 t t_0 z_n^2 + 4(ct_0)^2 \alpha^2 \right. \\ & \left. + 4c^2 t^2 \alpha^2 - 4x_n^2 \alpha^2 + 8c^2 t t_0 \alpha^2 - 4\mathbf{p}_{ij_y}^2 \beta^2 + 4(ct_0)^2 \beta^2 + 4c^2 t^2 \beta^2 - 4y_n^2 \beta^2 + 8c^2 t t_0 \beta^2 \right. \\ & \left. + 8\mathbf{p}_{ij_y} y_n \beta^2 - 4ct(ct_0)^3 + 4\mathbf{p}_{ij_y}^2 c^2 t t_0 + 4x_n^3 \alpha + 4x_n y_n^2 \alpha + 4x_n z_n^2 \alpha - 4\mathbf{p}_{ij_y}^2 x_n \alpha - 4(ct_0)^2 x_n \alpha \right. \\ & \left. - 4c^2 t^2 x_n \alpha - 8c^2 t t_0 x_n \alpha + 4\mathbf{p}_{ij_y}^3 \beta + 4y_n^3 \beta - 4\mathbf{p}_{ij_y} (ct_0)^2 \beta - 4\mathbf{p}_{ij_y} c^2 t^2 \beta - 4\mathbf{p}_{ij_y} x_n^2 \beta \right. \\ & \left. - 4\mathbf{p}_{ij_y} y_n^2 \beta - 4\mathbf{p}_{ij_y} z_n^2 \beta + 4y_n z_n^2 \beta - 8\mathbf{p}_{ij_y} c^2 t t_0 \beta - 4\mathbf{p}_{ij_y}^2 y_n \beta - 4(ct_0)^2 y_n \beta \right. \\ & \left. - 4c^2 t^2 y_n \beta + 4x_n^2 y_n \beta - 8c^2 t t_0 y_n \beta + 8\mathbf{p}_{ij_y} x_n \beta^2 - 8x_n y_n \beta^2 \right), \end{aligned}$$

and  $A$  is given by

$$\begin{aligned} A = & -z_n \left( -4\mathbf{p}_{ij_x}^2 + 8\alpha\mathbf{p}_{ij_x} - 4\mathbf{p}_{ij_y}^2 - 4(ct_0)^2 - 4c^2 t^2 \right. \\ & \left. + 4x_n^2 + 4y_n^2 + 4z_n^2 - 8c^2 t t_0 - 8x_n\alpha + 8\mathbf{p}_{ij_y}\beta - 8y_n\beta \right). \end{aligned}$$

### B.1.2 2D Imaging

In this section, we suppose that the transducer elements are arranged into a linear probe located in the plane  $z = 0$ , with spacing  $\Delta_x^t$  in the lateral dimension. We assume that the virtual point is positioned at  $\mathbf{r}_n = [x_n, z_n]^\top$  behind the probe. We are interested in finding a set of parametric equations of the points that belong to the following interface

$$\partial\Omega(\mathbf{p}_i, \mathbf{r}_n, t) = \{ \mathbf{r} \in \Omega \mid \|\mathbf{r} - \mathbf{p}_i\|_2 + \|\mathbf{r} - \mathbf{r}_n\|_2 = c(t + t_0) \},$$

Using a dedicated computing software such as Wolfram Mathematica, we can demonstrate the following equivalence

$$\mathbf{r} = [x, z]^\top \in \partial\Omega(\mathbf{p}_i, \mathbf{r}_n, t) \Leftrightarrow \begin{cases} x(\alpha, \mathbf{p}_i, \mathbf{r}_n, t) & = \alpha \\ z(\alpha, \mathbf{p}_i, \mathbf{r}_n, t) & = \frac{-z_n(-4\mathbf{p}_{i_x}^2 + 8\mathbf{p}_{i_x}\alpha - 4c^2 t^2 - 8c^2 t t_0 - 4(ct_0)^2 + 4x_n^2 - 8x_n\alpha + 4z_n^2) \pm \sqrt{\Delta}}{8c^2 t^2 + 16c^2 t t_0 + 8(ct_0)^2 - 8z_n^2} \end{cases}, \quad (\text{B.2})$$

where  $\alpha \in [x_{min}, x_{max}]$  and  $\Delta$  is given by

$$\begin{aligned} \Delta = & z_n^2 (-4\mathbf{p}_{i_x}^2 + 8\mathbf{p}_{i_x}\alpha - 4c^2 t^2 - 8c^2 t t_0 - 4(ct_0)^2 + 4x_n^2 - 8x_n\alpha + 4z_n^2)^2 - 4(4c^2 t^2 + 8c^2 t t_0 \\ & + 4(ct_0)^2 - 4z_n^2) (-\mathbf{p}_{i_x}^4 + 4\mathbf{p}_{i_x}^3\alpha + 2\mathbf{p}_{i_x}^2 c^2 t^2 + 4\mathbf{p}_{i_x}^2 c^2 t t_0 + 2\mathbf{p}_{i_x}^2 (ct_0)^2 + 2\mathbf{p}_{i_x}^2 x_n^2 - 4\mathbf{p}_{i_x}^2 x_n\alpha \\ & + 2\mathbf{p}_{i_x}^2 z_n^2 - 4\mathbf{p}_{i_x}^2 \alpha^2 - 4\mathbf{p}_{i_x} c^2 t^2 \alpha - 8\mathbf{p}_{i_x} c^2 t t_0 \alpha - 4\mathbf{p}_{i_x} (ct_0)^2 \alpha - 4\mathbf{p}_{i_x} x_n^2 \alpha + 8\mathbf{p}_{i_x} x_n \alpha^2 \\ & - 4\mathbf{p}_{i_x} z_n^2 \alpha - c^4 t^4 - 4c^4 t^3 t_0 - 6c^2 t^2 (ct_0)^2 + 2c^2 t^2 x_n^2 - 4c^2 t^2 x_n \alpha + 2c^2 t^2 z_n^2 + 4c^2 t^2 \alpha^2 \\ & - 4ct(ct_0)^3 + 4c^2 t t_0 x_n^2 - 8c^2 t t_0 x_n \alpha + 4c^2 t t_0 z_n^2 + 8c^2 t t_0 \alpha^2 - (ct_0)^4 + 2(ct_0)^2 x_n^2 \\ & - 4(ct_0)^2 x_n \alpha + 2(ct_0)^2 z_n^2 + 4(ct_0)^2 \alpha^2 - x_n^4 + 4x_n^3 \alpha - 2x_n^2 z_n^2 - 4x_n^2 \alpha^2 + 4x_n z_n^2 \alpha - z_n^4). \end{aligned} \quad (\text{B.3})$$

## B.2 Parametric Equations in Plane Wave Imaging

### B.2.1 3D Imaging

In this section, we suppose that the transducer elements are arranged into a matrix probe located in the plane  $z = 0$ , with spacing  $\Delta_x^t$  and  $\Delta_y^t$  in the lateral and elevation dimension, respectively. We therefore consider the following uniform grid of transducer elements:

$$\mathbf{p}_{ij} = [i\Delta_x^t, j\Delta_y^t, 0]^\top, \quad (i, j) \in \{1, \dots, N_x^t\} \times \{1, \dots, N_y^t\},$$

where  $N_x^t$  and  $N_y^t$  are the number of transducer elements in lateral and elevation dimension, respectively, such that  $N_t = N_x^t N_y^t$ .

We are interested in finding a set of parametric equations of the points that belong to the following interface

$$\partial\Omega(\mathbf{p}_{ij}, \boldsymbol{\theta}, t) = \{\mathbf{r} \in \Omega \mid \|\mathbf{r} - \mathbf{p}_{ij}\|_2 + \langle \mathbf{r}, \mathbf{e}_\theta \rangle = ct\}, \quad (\text{B.4})$$

**Plane Wave With Normal Incidence** When  $\theta_x = \theta_y = 0$ , the parameterization is directly obtained from (B.4) and we have the following equivalence:

$$\mathbf{r} = [x, y, z]^\top \in \partial\Omega(\mathbf{p}_{ij}, \mathbf{0}, t) \Leftrightarrow \begin{cases} x(\alpha, \beta, \mathbf{p}_{ij}, t) = \alpha \\ y(\alpha, \beta, \mathbf{p}_{ij}, t) = \beta \\ z(\alpha, \beta, \mathbf{p}_{ij}, t) = \frac{1}{2ct} \left( (ct)^2 - (\alpha - \mathbf{p}_{ij_x})^2 - (\beta - \mathbf{p}_{ij_y})^2 \right) \end{cases}.$$

**Steered Plane Wave** When  $\theta_x \neq 0$ , significantly more calculations are involved. Using a dedicated computing software such as Wolfram Mathematica, we can demonstrate the following equivalence

$$\mathbf{r} = [x, y, z]^\top \in \partial\Omega(\mathbf{p}_{ij}, \boldsymbol{\theta}, t) \Leftrightarrow \begin{cases} x(\alpha, \beta, \mathbf{p}_{ij}, \boldsymbol{\theta}, t) = \alpha \\ y(\alpha, \beta, \mathbf{p}_{ij}, \boldsymbol{\theta}, t) = \beta \\ z(\alpha, \beta, \mathbf{p}_{ij}, \boldsymbol{\theta}, t) = \frac{2\cos(\theta_x)(ct - \alpha \sin(\theta_x)) \pm \sqrt{\Delta}}{2(\cos(\theta_x)^2 - 1)} \end{cases},$$

## Appendix B. Expression of the Parametric Equations in Ultrafast Ultrasound Imaging

where  $\Delta$  is given by

$$\Delta = \cos^2(\theta_x) (2\alpha \sin(\theta_x) - 2ct)^2 - 4(\cos^2(\theta_x) - 1) (-\mathbf{p}_{ij_x}^2 + 2\mathbf{p}_{ij_x}\alpha - \mathbf{p}_{ij_y}^2 + 2\mathbf{p}_{ij_y}\beta - 2ct\alpha \sin(\theta_x) + \alpha^2 \sin^2(\theta_x) + (ct)^2 - \alpha^2 - \beta^2).$$

The parametric equations for the case  $\theta_y \neq 0$  can be easily obtained by switching the variables  $\alpha$  and  $\beta$  in the above equations.

### B.2.2 2D Imaging

In this section, we suppose that the transducer elements are arranged into a linear probe located in the plane  $z = 0$ , with spacing  $\Delta_x^t$  in the lateral dimension. We are interested in finding a set of parametric equations of the points that belong to the following interface:

$$\partial\Omega(\mathbf{p}_i, \theta, t) = \{\mathbf{r} \in \Omega \mid \|\mathbf{r} - \mathbf{p}_i\|_2 + x \sin(\theta) + z \sin(\theta) = ct\}. \quad (\text{B.5})$$

**Plane Wave With Normal Incidence** When  $\theta = 0$ , the parameterization is directly obtained from (B.5) and we have the following equivalence:

$$\mathbf{r} = [x, z]^\top \in \partial\Omega(\mathbf{p}_i, 0, t) \Leftrightarrow \begin{cases} x(\alpha, \mathbf{p}_i, t) = \alpha \\ z(\alpha, \mathbf{p}_i, t) = \frac{1}{2ct} \left( (ct)^2 - (\alpha - \mathbf{p}_{i_x})^2 \right) \end{cases}.$$

**Steered Plane Wave** When  $\theta \neq 0$ , significantly more calculations are involved. Using a dedicated computing software such as Wolfram Mathematica, we can demonstrate the following equivalence

$$\mathbf{r} = [x, z]^\top \in \partial\Omega(\mathbf{p}_i, \theta, t) \Leftrightarrow \begin{cases} x(\alpha, \mathbf{p}_i, \theta, t) = \alpha \\ z(\alpha, \mathbf{p}_i, \theta, t) = \frac{2ct \cos(\theta) - \alpha \sin(2\theta) \pm 2\sqrt{\Delta}}{\cos(2\theta) - 1} \end{cases}, \quad (\text{B.6})$$

where  $\Delta$  is defined as

$$\Delta = -\mathbf{p}_{i_x}^2 \sin^2(\theta) + 2\mathbf{p}_{i_x}\alpha \sin^2(\theta) + c^2 t^2 - 2ct\alpha \sin(\theta).$$

# C Proximity Operators of Several Regularization Terms

## C.1 Proximity Operators Associated with the $\ell_1$ -norm

### C.1.1 $\ell_1$ -norm in the Image Domain

The proximity operator associated with the  $\ell_1$ -norm in  $\mathbb{K}^n$  is defined as follows

$$\text{prox}_{\lambda \|\cdot\|_1}(\mathbf{x}) = \min_{\mathbf{z} \in \mathbb{K}^n} \lambda \|\mathbf{z}\|_1 + \frac{1}{2} \|\mathbf{x} - \mathbf{z}\|_2^2, \lambda > 0. \quad (\text{C.1})$$

In case of real vectors, (C.1) has a closed form solution known as the *soft-thresholding* operator [222] defined by

$$\mathbf{z} = \max(0, |\mathbf{x}| - \lambda) \text{sgn}(\mathbf{x}). \quad (\text{C.2})$$

When dealing with complex vectors, the sign function is not defined and the proximal operator is slightly modified as follows [332]

$$\mathbf{z} = \max(0, |\mathbf{x}| - \lambda) \frac{\mathbf{x}}{|\mathbf{x}|}. \quad (\text{C.3})$$

### C.1.2 $\ell_1$ -norm in the Transform Domain

Consider the proximity operator associated with the  $\ell_1$ -norm in the transform domain, with associated transform  $\Psi: \mathbb{K}^m \rightarrow \mathbb{K}^n$  defined as follows

$$\text{prox}_{\lambda \|\Psi^* \cdot\|_1}(\mathbf{x}) = \min_{\mathbf{z} \in \mathbb{K}^n} \lambda \|\Psi^* \mathbf{z}\|_1 + \frac{1}{2} \|\mathbf{x} - \mathbf{z}\|_2^2, \lambda > 0. \quad (\text{C.4})$$

If  $\Psi$  is a tight frame with bound  $c \in \mathbb{R}_+$ , then the following relationship holds [333]

$$\text{prox}_{\lambda \|\Psi^* \cdot\|_1}(\mathbf{x}) = \mathbf{x} + c^{-1} \Psi \left( \text{prox}_{\lambda c \|\cdot\|_1}(\Psi^* \mathbf{x}) - \Psi^* \mathbf{x} \right). \quad (\text{C.5})$$

If  $\Psi$  is a general frame with bound  $c_1 < c_2 \in \mathbb{R}_+$ , there is no closed-form expression of the proximity operator and the following iteration needs to be performed [333]:

$$\begin{cases} \mathbf{u}^{(t+1)} &= \mathbf{u}^{(t)} + \mu \left( \Psi^* \mathbf{p}^{(t)} - \text{prox}_{\frac{\lambda}{\mu} \|\cdot\|_1} \left( \frac{\mathbf{u}^{(t)}}{\mu} + \Psi^* \mathbf{p}^{(t)} \right) \right), \\ \mathbf{p}^{(t+1)} &= \mathbf{x} - \Psi \mathbf{u}^{(t+1)} \end{cases},$$

where  $\mu \in [0, 2/c_2]$ . Then, when  $t \rightarrow \infty$ ,  $\mathbf{p}^{(t)}$  tends to the desired proximity operator.

## C.2 Proximity Operators Associated with the $\ell_p$ -norm

In this section, we are interested in the proximity operator associated with the  $\ell_p$ -norm to the power  $p$ , for  $p \in ]1, 2]$ , defined as follows

$$\text{prox}_{\lambda \|\cdot\|_1}(\mathbf{x}) = \min_{\mathbf{z} \in \mathbb{R}^n} \lambda \|\mathbf{z}\|_p^p + \frac{1}{2} \|\mathbf{x} - \mathbf{z}\|_2^2, \lambda > 0. \quad (\text{C.6})$$

Thanks to the separability of the two functions involved in (C.6), the problem can be solved element-wise. According to Table 10.2 of [113], the following equivalence holds:

$$\begin{aligned} z_i &= \underset{z_i \in \mathbb{R}}{\text{argmin}} \lambda |z_i|^p + \frac{1}{2} (z_i - x_i)^2, \forall (x_i, z_i) \in \mathbb{R} \times \mathbb{R}, \lambda > 0 \\ \Leftrightarrow z_i &= \text{sign}(x_i) q, q \geq 0, q + p\lambda q^{p-1} = |x_i|. \end{aligned} \quad (\text{C.7})$$

Thus, in order to derive the desired proximity operator, we have to solve (C.7), which involves finding the roots of a polynomial with arbitrarily high degree. In the general case, this can be achieved using any off-the-shelf root finding algorithm, e.g. using the companion matrix or the Newton's method.

For specific values of  $p$ , the polynomial may have a degree lower or equal to 3. In such cases, (C.7) has an analytical solution. This is the case for the values of  $p$  considered in the thesis and described below.

### C.2.1 Case $p = 3/2$

The solution of (C.7) involves to find the positive root of the following polynomial of order 2:

$$\begin{aligned} 0 &= q + \frac{3}{2} \lambda q^{1/2} - |x_i| \\ \Leftrightarrow 0 &= q^2 - \left( 2|x_i| + \frac{9}{4} \lambda^2 \right) q + x_i^2, |x_i| \geq q \\ \Leftrightarrow q &= |x_i| + \frac{9}{8} \lambda \left( \lambda - \sqrt{\frac{16}{9} |x_i| + \lambda^2} \right). \end{aligned}$$

### C.2.2 Case $p = 4/3$

The solution of (C.7) involves to find the positive root of the following polynomial of order 3:

$$0 = q + \frac{4}{3} \lambda q^{1/3} - |x_i| \quad (\text{C.8})$$

$$\Leftrightarrow 0 = q^3 - 3|x_i|q^2 + \left( 3|x_i|^2 + \frac{64}{27} \lambda^3 \right) q - |x_i|^3. \quad (\text{C.9})$$

Using Cardano's method and after several calculations not detailed here, one may obtain the

following value of  $q$ :

$$q = |x_i| + \frac{1}{9} \left( -\frac{16 \cdot 2^{1/3} \cdot \lambda^2}{(z - 27|x_i|)^{1/3}} + 2^{5/3} \lambda (z - 27|x_i|)^{1/3} \right)$$
$$z = \sqrt{256\lambda^3 + 729|x_i|^2}.$$



# Bibliography

- [1] T. Rossing, “A Brief History of Acoustics”, in *Springer Handb. Acoust.* 2007, pp. 9–24.
- [2] P. Curie, *Oeuvres de Pierre Curie*, Gauthier-Villars, Ed. Paris, 1908.
- [3] T. L. Szabo, “Introduction”, in *Diagnostic Ultrasound Imaging Insid. Out*, 2014, ch. 1, pp. 1–37.
- [4] I. Edler, “Early echocardiography”, *Ult. Med. Biol.*, vol. 17, pp. 425–431, 1991.
- [5] K. T. Dussik, “Weitere ergebnisse der ultraschalluntersuchung bei gehirnerkrankungen”, *Acta Neurochir. (Wien)*., vol. 2, pp. 379–401, 1952.
- [6] G. B. Devey and P. N. T. Wells, “Ultrasound in medical diagnosis”, *Scientific American*, vol. 238, pp. 98–113, 1978.
- [7] O. T. von Ramm and F. L. Thurstone, “Thaumascan: design considerations and performance characteristics”, in *Ultrasound Med.* 1975, pp. 373–378.
- [8] J. A. Jensen, S. Nikolov, A. C. Yu, *et al.*, “Ultrasound vector flow imaging: I: Sequential systems”, *IEEE Trans. Ultrason. Ferroelectr. Freq. Control*, vol. 63, pp. 1704–1721, 2016.
- [9] J. M. Thijssen, “Ultrasonic tissue characterization”, in *Acoust. Imaging*, 2002, pp. 9–25.
- [10] T. L. Szabo, “Elastography”, in *Diagnostic Ultrasound Imaging Insid. Out*, 2014, ch. 16, pp. 699–733.
- [11] M. Tanter and M. Fink, “Ultrafast imaging in biomedical ultrasound”, *IEEE Trans. Ultrason. Ferroelectr. Freq. Control*, vol. 61, pp. 102–119, 2014.
- [12] D. Gabor, “A new microscopic principle”, *Nature*, vol. 161, pp. 777–778, 1948.
- [13] M. Fink, “Time reversal of ultrasonic fields. I. Basic principles”, *IEEE Trans. Ultrason. Ferroelectr. Freq. Control*, vol. 39, pp. 555–566, 1992.
- [14] C. Bruneel, R. Torguet, K. M. Rouvaen, *et al.*, “Ultrafast echotomographic system using optical processing of ultrasonic signals”, *Appl. Phys. Lett.*, vol. 30, pp. 371–373, 1977.
- [15] B. Delannoy, R. Torguet, C. Bruneel, *et al.*, “Acoustical image reconstruction in parallel-processing analog electronic systems”, *J. Appl. Phys.*, vol. 50, pp. 3153–3159, 1979.
- [16] J. A. Jensen, S. I. Nikolov, K. L. Gammelmark, *et al.*, “Synthetic aperture ultrasound imaging”, *Ultrasonics*, vol. 44, e5–e15, 2006.
- [17] S. I. Nikolov, J. Kortbek, and J. A. Jensen, “Practical applications of synthetic aperture imaging”, in *2010 IEEE Int. Ultrason. Symp.*, 2010, pp. 350–358.
- [18] G. Lockwood, J. Talman, and S. Brunke, “Real-time 3-D ultrasound imaging using sparse synthetic aperture beamforming”, *IEEE Trans. Ultrason. Ferroelectr. Freq. Control*, vol. 45, pp. 980–988, 1998.
- [19] C. Hazard and G. Lockwood, “Theoretical assessment of a synthetic aperture beamformer for real-time 3-D imaging”, *IEEE Trans. Ultrason. Ferroelectr. Freq. Control*, vol. 46, pp. 972–980, 1999.
- [20] J.-Y. Lu and J. F. Greenleaf, “Ultrasonic nondiffracting transducer for medical imaging”, *IEEE Trans. Ultrason. Ferroelectr. Freq. Control*, vol. 37, pp. 438–447, 1990.
- [21] J.-Y. Lu and J. F. Greenleaf, “Pulse-echo imaging using a nondiffracting beam transducer.”, *Ultrasound Med. Biol.*, vol. 17, pp. 265–81, 1991.

## Bibliography

---

- [22] J.-Y. Lu and J. F. Greenleaf, "Experimental verification of nondiffracting X waves", *IEEE Trans. Ultrason. Ferroelectr. Freq. Control*, vol. 39, pp. 441–446, 1992.
- [23] J.-Y. Lu, "2D and 3D high frame rate imaging with limited diffraction beams", *Ultrason. Ferroelectr. Freq. Control. IEEE Trans.*, vol. 44, pp. 839–856, 1997.
- [24] M. Tanter, J. Bercoff, L. Sandrin, *et al.*, "Ultrafast compound imaging for 2-D motion vector estimation: application to transient elastography", *IEEE Trans. Ultrason. Ferroelectr. Freq. Control*, vol. 49, pp. 1363–1374, 2002.
- [25] L. Sandrin, M. Tanter, S. Catheline, *et al.*, "Shear modulus imaging with 2-D transient elastography", *IEEE Trans. Ultrason. Ferroelectr. Freq. Control*, vol. 49, pp. 426–435, 2002.
- [26] J. Bercoff, M. Tanter, and M. Fink, "Supersonic shear imaging: a new technique for soft tissue elasticity mapping.", *IEEE Trans. Ultrason. Ferroelectr. Freq. Control*, vol. 51, pp. 396–409, 2004.
- [27] J. Bercoff, G. Montaldo, T. Loupas, *et al.*, "Ultrafast compound doppler imaging: providing full blood flow characterization", *IEEE Trans. Ultrason. Ferroelectr. Freq. Control*, vol. 58, pp. 134–147, 2011.
- [28] G. Montaldo, M. Tanter, J. Bercoff, *et al.*, "Coherent plane-wave compounding for very high frame rate ultrasonography and transient elastography", *IEEE Trans. Ultrason. Ferroelectr. Freq. Control*, vol. 56, pp. 489–506, 2009.
- [29] C. Papadacci, M. Pernot, M. Couade, *et al.*, "High-contrast ultrafast imaging of the heart", *IEEE Trans. Ultrason. Ferroelectr. Freq. Control*, vol. 61, pp. 288–301, 2014.
- [30] J. A. Jensen, H. Holten-Lund, R. T. Nilsson, *et al.*, "SARUS: A synthetic aperture real-time ultrasound system", *IEEE Trans. Ultrason. Ferroelectr. Freq. Control*, vol. 60, pp. 1838–1852, 2013.
- [31] J. Provost, C. Papadacci, C. Demene, *et al.*, "3-D ultrafast Doppler imaging applied to the noninvasive mapping of blood vessels in vivo", *IEEE Trans. Ultrason. Ferroelectr. Freq. Control*, vol. 62, pp. 1467–1472, 2015.
- [32] L. Petrusca, F. Varray, R. Souchon, *et al.*, "Fast volumetric ultrasound B-mode and Doppler imaging with a new high-channels density platform for advanced 4D cardiac imaging/therapy", *Appl. Sci.*, vol. 8, p. 200, 2018.
- [33] I. Dokmanic, R. Parhizkar, A. Walther, *et al.*, "Acoustic echoes reveal room shape", *Proc. Natl. Acad. Sci.*, vol. 110, pp. 12 186–12 191, 2013.
- [34] M. A. Flower, *Webb's physics of medical imaging*. CRC Press, 2012.
- [35] M. Fink, W. A. Kuperman, J.-P. Montagner, *et al.*, *Imaging of Complex Media with Acoustic and Seismic Waves*. Berlin, Heidelberg: Springer Berlin Heidelberg, 2002, vol. 84.
- [36] T. L. Szabo, "Transducers", in *Diagnostic Ultrasound Imaging Insid. Out*, 2014, ch. 5, pp. 121–165.
- [37] ———, "Beamforming", in *Diagnostic Ultrasound Imaging Insid. Out*, 2014, ch. 6, pp. 167–207.
- [38] J. Goodman, *Introduction to Fourier Optics*. New York: McGraw-Hill, 1968, p. 441.
- [39] T. L. Szabo, "Array beamforming", in *Diagnostic Ultrasound Imaging Insid. Out*, 2014, ch. 7, pp. 209–255.
- [40] J. F. Greenleaf, "Acoustical Medical Imaging Instrumentation", in *Encycl. Acoust.* 2007, pp. 1751–1760.
- [41] M. C. Van Wijk and J. M. Thijssen, "Performance testing of medical ultrasound equipment: Fundamental vs. harmonic mode", *Ultrasonics*, vol. 40, pp. 585–591, 2002.
- [42] J. Abbott, "Acoustic speckle: Theory and experimental analysis", *Ultrason. Imaging*, vol. 1, pp. 303–324, 1979.
- [43] T. L. Szabo, "Wave scattering and imaging", in *Diagnostic Ultrasound Imaging Insid. Out*, 2014, ch. 8, pp. 257–294.

- [44] H. B. Kim, J. R. Hertzberg, and R. Shandas, "Development and validation of echo PIV", *Exp. Fluids*, vol. 36, pp. 455–462, 2004.
- [45] J.-L. Gennisson, T. Deffieux, M. Fink, *et al.*, "Ultrasound elastography: Principles and techniques", *Diagn. Interv. Imaging*, vol. 94, pp. 487–495, 2013.
- [46] J. W. Goodman, "Some fundamental properties of speckle", *J. Opt. Soc. Am.*, vol. 66, p. 1145, 1976.
- [47] E. Jakeman and W. Welford, "Speckle statistics in imaging systems", *Opt. Commun.*, vol. 21, pp. 72–79, 1977.
- [48] E. Jakeman and R. J. A. Tough, "Generalized K distribution: a statistical model for weak scattering", *J. Opt. Soc. Am. A*, vol. 4, p. 1764, 1987.
- [49] L. Weng, J. M. Reid, P. M. Shankar, *et al.*, "Ultrasound speckle analysis based on the K distribution", *J. Acoust. Soc. Am.*, vol. 89, pp. 2992–2995, 1991.
- [50] M. F. Insana, R. F. Wagner, B. S. Garra, *et al.*, "Analysis of ultrasound image texture via generalized Rician statistics", *Opt. Eng.*, vol. 25, p. 256 743, 1986.
- [51] C. B. Burckhardt, "Speckle in ultrasound B-mode scans", *IEEE Trans. Sonics Ultrason.*, vol. 25, pp. 1–6, 1978.
- [52] R. F. Wagner, S. Smith, J. Sandrik, *et al.*, "Statistics of speckle in ultrasound B-scans", *IEEE Trans. Sonics Ultrason.*, vol. 30, pp. 156–163, 1983.
- [53] T. L. Szabo, "Attenuation", in *Diagnostic Ultrasound Imaging Insid. Out*, 2014, ch. 4, pp. 167–207.
- [54] —, "Time domain wave equations for lossy media obeying a frequency power law", *J. Acoust. Soc. Am.*, vol. 96, pp. 491–500, 1994.
- [55] D. E. Goldman and T. F. Hueter, "Tabular data of the velocity and absorption of high-frequency sound in mammalian tissues", *J. Acoust. Soc. Am.*, vol. 28, pp. 35–37, 1956.
- [56] P. N. T. Wells, "The medical applications of ultrasonics", *Reports Prog. Phys.*, vol. 33, p. 302, 1970.
- [57] T. L. Szabo, "Causal theories and data for acoustic attenuation obeying a frequency power law", *J. Acoust. Soc. Am.*, vol. 97, pp. 14–24, 1995.
- [58] B. Denarie, T. A. Tangen, I. K. Ekroll, *et al.*, "Coherent plane wave compounding for very high frame rate ultrasonography of rapidly moving targets", *IEEE Trans. Med. Imaging*, vol. 32, pp. 1265–1276, 2013.
- [59] P. S. Green, L. F. Schaefer, E. D. Jones, *et al.*, "A New, High-Performance Ultrasonic Camera", in *Acoust. Hologr.* 1974, pp. 493–503.
- [60] A. H. Andersen and A. C. Kak, "Digital ray tracing in two-dimensional refractive fields", *J. Acoust. Soc. Am.*, vol. 72, pp. 1593–1606, 1982.
- [61] R. Mueller, M. Kaveh, and G. Wade, "Reconstructive tomography and applications to ultrasonics", *Proc. IEEE*, vol. 67, pp. 567–587, 1979.
- [62] R. K. Mueller, M. Kaveh, and R. D. Iverson, "A New Approach to Acoustic Tomography Using Diffraction Techniques", in 1980, pp. 615–628.
- [63] E. Wolf, "Three-dimensional structure determination of semi-transparent objects from holographic data", *Opt. Commun.*, vol. 1, pp. 153–156, 1969.
- [64] A. Devaney, "A filtered backpropagation algorithm for diffraction tomography", *Ultrason. Imaging*, vol. 4, pp. 336–350, 1982.
- [65] T. D. Mast, "Wideband quantitative ultrasonic imaging by time-domain diffraction tomography", *J. Acoust. Soc. Am.*, vol. 106, pp. 3061–3071, 1999.
- [66] S. Kenue and J. F. Greenleaf, "Limited angle multifrequency diffraction tomography", *IEEE Trans. Sonics Ultrason.*, vol. 29, pp. 213–216, 1982.
- [67] S. A. Johnson and M. L. Tracy, "Inverse scattering solutions by a sinc basis, multiple source, moment method – Part I: Theory", *Ultrason. Imaging*, vol. 5, pp. 361–375, 1983.

## Bibliography

---

- [68] P. M. van den Berg and A. Abubakar, "Contrast source inversion method: State of art", *Prog. Electromagn. Res.*, vol. 34, pp. 189–218, 2001.
- [69] S. J. Norton, "Reconstruction of a two-dimensional reflecting medium over a circular domain: Exact solution", *J. Acoust. Soc. Am.*, vol. 67, pp. 1266–1273, 1980.
- [70] S. J. Norton and M. Linzer, "Ultrasonic reflectivity imaging in three dimensions: exact inverse scattering solutions for plane, cylindrical, and spherical apertures.", *IEEE Trans. Biomed. Eng.*, vol. 28, pp. 202–220, 1981.
- [71] J. A. Jensen, "A model for the propagation and scattering of ultrasound in tissue", *J. Acoust. Soc. Am.*, vol. 89, pp. 182–190, 1991.
- [72] G. E. Tupholme, "Generation of acoustic pulses by baffled plane pistons", *Mathematika*, vol. 16, pp. 209–224, 1969.
- [73] P. R. Stepanishen, "The time-dependent force and radiation impedance on a piston in a rigid infinite planar baffle", *J. Acoust. Soc. Am.*, vol. 49, pp. 841–849, 1971.
- [74] M. F. Schiffner and G. Schmitz, "Fast image acquisition in pulse-echo ultrasound imaging using compressed sensing", in *Ultrason. Symp. (IUS), 2012 IEEE Int.*, 2012, pp. 1944–1947.
- [75] M. F. Schiffner and G. Schmitz, "Compensating the combined effects of absorption and dispersion in plane wave pulse-echo ultrasound imaging using sparse recovery", *IEEE Int. Ultrason. Symp. IUS*, pp. 573–576, 2013.
- [76] M. F. Schiffner and G. Schmitz, "Pulse-echo ultrasound imaging combining compressed sensing and the fast multipole method", *2014 IEEE Int. Ultrason. Symp.*, pp. 2205–2208, 2014.
- [77] Bo Zhang, J.-L. Robert, and G. David, "Dual-domain compressed beamforming for medical ultrasound imaging", in *2015 IEEE Int. Ultrason. Symp.*, 2015, pp. 1–4.
- [78] G. David, J.-L. Robert, B. Zhang, *et al.*, "Time domain compressive beam forming of ultrasound signals", *J. Acoust. Soc. Am.*, vol. 137, pp. 2773–2784, 2015.
- [79] G. David, J.-L. Robert, B. Zhang, *et al.*, "Time domain compressive beamforming: Application to in-vivo echocardiography", in *2015 IEEE Int. Ultrason. Symp.*, 2015, pp. 1–4.
- [80] E. Ozkan, V. Vishnevsky, and O. Goksel, "Inverse problem of ultrasound beamforming with sparsity constraints and regularization", *IEEE Trans. Ultrason. Ferroelectr. Freq. Control*, vol. 65, pp. 356–365, 2018.
- [81] C. Wang, X. Peng, D. Liang, *et al.*, "Plane-wave ultrasound imaging based on compressive sensing with low memory occupation", in *2015 IEEE Int. Ultrason. Symp.*, 2015, pp. 1–4.
- [82] P. M. Morse and K. U. Ingard, *Theoretical Acoustics*. New York: McGraw-Hill, 1968.
- [83] A. D. Pierce and R. T. Beyer, "Acoustics: An introduction to its physical principles and applications", *J. Acoust. Soc. Am.*, vol. 87, pp. 1826–1827, 1990.
- [84] J. C. Lockwood and J. G. Willette, "High-speed method for computing the exact solution for the pressure variations in the nearfield of a baffled piston", *J. Acoust. Soc. Am.*, vol. 53, pp. 735–741, 1973.
- [85] J. L. San Emeterio and L. G. Ullate, "Diffraction impulse response of rectangular transducers", *J. Acoust. Soc. Am.*, vol. 92, pp. 651–662, 1992.
- [86] J. A. Jensen, "Ultrasound fields from triangular apertures", *J. Acoust. Soc. Am.*, vol. 100, pp. 2049–2056, 1996.
- [87] M. Arditi, F. S. Foster, and J. W. Hunt, "Transient fields of concave annular arrays", *Ultrason. Imaging*, vol. 3, pp. 37–61, 1981.
- [88] A. Penttinen and M. Luukkala, "The impulse response and pressure nearfield of a curved ultrasonic radiator", *J. Phys. D. Appl. Phys.*, vol. 9, pp. 1547–1557, 1976.

- [89] J. A. Jensen and N. B. Svendsen, "Calculation of pressure fields from arbitrarily shaped, apodized, and excited ultrasound transducers", *IEEE Trans. Ultrason. Ferroelectr. Freq. Control*, vol. 39, pp. 262–267, 1992.
- [90] O. V. Michailovich and D. Adam, "A novel approach to the 2-D blind deconvolution problem in medical ultrasound", *IEEE Trans. Med. Imaging*, vol. 24, pp. 86–104, 2005.
- [91] K. Nagai, "A new synthetic-aperture focusing method for ultrasonic B-scan imaging by the Fourier transform", *IEEE Trans. Sonics Ultrason.*, vol. 32, pp. 531–536, 1985.
- [92] P. Corl, P. Grant, and G. Kino, "A digital synthetic focus acoustic imaging system for NDE", in *1978 Ultrason. Symp.*, 1978, pp. 263–268.
- [93] M. Martorella, J. Homer, J. Palmer, *et al.*, "Inverse synthetic aperture radar", *EURASIP J. Adv. Signal Process.*, vol. 2006, p. 063 465, 2006.
- [94] M. Soumekh, "Bistatic synthetic aperture radar inversion with application in dynamic object imaging", *IEEE Trans. Signal Process.*, vol. 39, pp. 2044–2055, 1991.
- [95] D. A. Ausherman, A. Kozma, J. L. Walker, *et al.*, "Developments in radar imaging", *IEEE Trans. Aerosp. Electron. Syst.*, vol. AES-20, pp. 363–400, 1984.
- [96] C. Cafforio, C. Prati, and F. Rocca, "SAR data focusing using seismic migration techniques", *IEEE Trans. Aerosp. Electron. Syst.*, vol. 27, pp. 194–207, 1991.
- [97] D. Turnbull and F. Foster, "Fabrication and characterization of transducer elements in two-dimensional arrays for medical ultrasound imaging", *IEEE Trans. Ultrason. Ferroelectr. Freq. Control*, vol. 39, pp. 464–475, 1992.
- [98] S. Osher and R. Fedkiw, *Level Set Methods and Dynamic Implicit Surfaces*. New York, NY: Springer New York, 2003, vol. 153.
- [99] K. Langenberg, M. Berger, T. Kreutter, *et al.*, "Synthetic aperture focusing technique signal processing", *NDT Int.*, vol. 19, pp. 177–189, 1986.
- [100] K. Mayer, R. Marklein, K. Langenberg, *et al.*, "Three-dimensional imaging system based on Fourier transform synthetic aperture focusing technique", *Ultrasonics*, vol. 28, pp. 241–255, 1990.
- [101] D. Zwillinger, *CRC Standard Mathematical Tables and Formulas*. New York: Chapman and Hall/CRC, 2018, p. 872.
- [102] R. Arthur and S. Broadstone, "Imaging via inversion of ellipsoidal projections of solutions to the linear acoustic wave equation (medical ultrasound)", *IEEE Trans. Med. Imaging*, vol. 8, pp. 89–95, 1989.
- [103] F. Anderson and F. Morgan, "Active imaging analysis via ellipsoidal projections", in 1995, pp. 171–182.
- [104] G. Ambartsoumian, J. Boman, V. Krishnan, *et al.*, "Microlocal analysis of an ultrasound transform with circular source and receiver trajectories", in *Geometric Analysis and Integral Geometry*, vol. 598, 2013, pp. 45–58.
- [105] A. Quarteroni, F. Saleri, and P. Gervasio, "Numerical differentiation and integration", in 2010, ch. 4, pp. 107–128.
- [106] M. O'Donnell, "Coded excitation system for improving the penetration of real-time phased-array imaging systems", *IEEE Trans. Ultrason. Ferroelectr. Freq. Control*, vol. 39, pp. 341–351, 1992.
- [107] H. W. Engl, M. Hanke, and A. Neubauer, *Regularization of inverse problems*. Springer Science & Business Media, 1996, vol. 375.
- [108] O. Scherzer, M. Grasmair, H. Grossauer, *et al.*, "Variational regularization methods for the solution of inverse problems", in *Variational Methods in Imaging*. 2009, pp. 53–113.

## Bibliography

---

- [109] R. Tibshirani, “Regression shrinkage and selection via the Lasso”, *J. R. Stat. Soc. Ser. B (Statistical Methodol.)*, vol. 58, pp. 267–288, 1996.
- [110] S. Osher, M. Burger, D. Goldfarb, *et al.*, “An iterative regularization method for total variation-based image restoration”, *Multiscale Model. Simul.*, vol. 4, pp. 460–489, 2005.
- [111] S. Boyd and L. Vandenberghe, *Convex Optimization*. Cambridge: Cambridge University Press, 2004.
- [112] N. Parikh and S. Boyd, “Proximal algorithms”, *Found. Trends Optim.*, vol. 1, pp. 123–231, 2014.
- [113] P. L. Combettes and J.-C. Pesquet, “Proximal splitting methods in signal processing”, in *Fixed-Point Algorithms Inverse Probl. Sci. Eng.* 2011, ch. 10, pp. 185–212.
- [114] J. J. Moreau, “Fonctions convexes duales et points proximaux dans un espace hilbertien.”, *Comptes Rendus de l’Académie des Sciences (Paris), Série A*, vol. 255, pp. 2897–2899, 1962.
- [115] A. M. Thompson and J. Kay, “On some Bayesian choices of regularization parameter in image restoration”, *Inverse Probl.*, vol. 9, pp. 749–761, 1993.
- [116] P. L. Combettes and V. R. Wajs, “Signal recovery by proximal forward-backward splitting”, *Multiscale Model. Simul.*, vol. 4, pp. 1168–1200, 2005.
- [117] B. Eicke, “Iteration methods for convexly constrained ill-posed problems in hilbert space”, *Numer. Funct. Anal. Optim.*, vol. 13, pp. 413–429, 1992.
- [118] A. Beck and M. Teboulle, “A fast iterative shrinkage-thresholding algorithm for linear inverse problems”, *SIAM J. Imaging Sci.*, vol. 2, pp. 183–202, 2009.
- [119] T. Szasz, A. Basarab, and D. Kouame, “Beamforming through regularized inverse problems in ultrasound medical imaging”, *IEEE Trans. Ultrason. Ferroelectr. Freq. Control*, vol. 63, pp. 2031–2044, 2016.
- [120] T. Szasz, A. Basarab, M.-F. Vaida, *et al.*, “Elastic-net based beamforming in medical ultrasound imaging”, in *2016 IEEE 13th Int. Symp. Biomed. Imaging*, 2016, pp. 477–480.
- [121] A. R. Selfridge, G. S. Kino, and B. T. Khuri-Yakub, “A theory for the radiation pattern of a narrow-strip acoustic transducer”, *Appl. Phys. Lett.*, vol. 37, pp. 35–36, 1980.
- [122] R. E. Carrillo, J. D. McEwen, D. Van De Ville, *et al.*, “Sparsity averaging for compressive imaging”, *IEEE Signal Process. Lett.*, vol. 20, pp. 591–594, 2013.
- [123] R. E. Carrillo, J. D. McEwen, and Y. Wiaux, “Sparsity averaging reweighted analysis (SARA): A novel algorithm for radio-interferometric imaging”, *Mon. Not. R. Astron. Soc.*, vol. 426, pp. 1223–1234, 2012.
- [124] H. Liebgott, A. Rodriguez-Molares, F. Cervenansky, *et al.*, “Plane-wave imaging challenge in medical ultrasound”, in *2016 IEEE Int. Ultrason. Symp.*, 2016, pp. 1–4.
- [125] A. Besson, M. Zhang, F. Varray, *et al.*, “A Sparse Reconstruction Framework for Fourier-Based Plane-Wave Imaging”, *IEEE Trans. Ultrason. Ferroelectr. Freq. Control*, vol. 63, pp. 2092–2106, 2016.
- [126] F. Varray, M. Azizian Kalkhoran, and D. Vray, “Adaptive minimum variance coupled with sign and phase coherence factors in IQ domain for plane wave beamforming”, in *2016 IEEE Int. Ultrason. Symp.*, 2016, pp. 1–4.
- [127] A. M. Deylami, J. A. Jensen, and B. M. Asl, “An improved minimum variance beamforming applied to plane-wave imaging in medical ultrasound”, in *2016 IEEE Int. Ultrason. Symp.*, 2016, pp. 1–4.
- [128] A. Besson, R. E. Carrillo, D. Perdios, *et al.*, “Morphological component analysis for sparse regularization in plane wave imaging”, in *2016 IEEE Int. Ultrason. Symp.*, 2016, pp. 1–4.
- [129] M. F. Duarte, M. A. Davenport, D. Takhar, *et al.*, “Single-pixel imaging via compressive sampling”, *IEEE Signal Process. Mag.*, vol. 25, pp. 83–91, 2008.

- [130] E. J. Candes, “Compressive sampling”, in *Proc. Int. Congr. Math. Madrid, August 22–30, 2006*, 2006, pp. 1433–1452.
- [131] R. Tur, Y. C. Eldar, and Z. Friedman, “Innovation rate sampling of pulse streams with application to ultrasound imaging”, *IEEE Trans. Signal Process.*, vol. 59, pp. 1827–1842, 2011.
- [132] N. Wagner, Y. C. Eldar, and Z. Friedman, “Compressed beamforming in ultrasound imaging”, *IEEE Trans. Signal Process.*, vol. 60, pp. 4643–4657, 2012.
- [133] T. Chernyakova and Y. C. Eldar, “Fourier-domain beamforming: the path to compressed ultrasound imaging”, *IEEE Trans. Ultrason. Ferroelectr. Freq. Control*, vol. 61, pp. 1252–1267, 2014.
- [134] A. Burshtein, M. Birk, T. Chernyakova, *et al.*, “Sub-Nyquist sampling and Fourier domain beamforming in volumetric ultrasound imaging”, *IEEE Trans. Ultrason. Ferroelectr. Freq. Control*, vol. 63, pp. 703–716, 2016.
- [135] H. Liebgott, R. Prost, and D. Friboulet, “Pre-beamformed RF signal reconstruction in medical ultrasound using compressive sensing”, *Ultrasonics*, vol. 53, pp. 525–533, 2013.
- [136] C. Quinsac, A. Basarab, and D. Kouame, “Frequency domain compressive sampling for ultrasound imaging”, *Adv. Acoust. Vib.*, vol. 2012, pp. 1–16, 2012.
- [137] A. Basarab, H. Liebgott, O. Bernard, *et al.*, “Medical ultrasound image reconstruction using distributed compressive sampling”, in *2013 IEEE 10th Int. Symp. Biomed. Imaging*, 2013, pp. 628–631.
- [138] O. Lorintiu, H. Liebgott, M. Alessandrini, *et al.*, “Compressed sensing reconstruction of 3D ultrasound data using dictionary learning and line-wise subsampling”, *IEEE Trans. Med. Imaging*, vol. 34, pp. 2467–2477, 2015.
- [139] C. Quinsac, N. Dobigeon, A. Basarab, *et al.*, “Bayesian compressed sensing in ultrasound imaging”, in *2011 4th IEEE Int. Work. Comput. Adv. Multi-Sensor Adapt. Process.*, 2011, pp. 101–104.
- [140] N. Dobigeon, A. Basarab, D. Kouame, *et al.*, “Regularized Bayesian compressed sensing in ultrasound imaging”, in *Eur. Signal Process. Conf.*, 2012, pp. 2600–2604.
- [141] A. Achim, B. Buxton, G. Tzagkarakis, *et al.*, “Compressive sensing for ultrasound RF echoes using  $\alpha$ -stable distributions”, in *2010 Annu. Int. Conf. IEEE Eng. Med. Biol.*, 2010, pp. 4304–4307.
- [142] A. Achim, A. Basarab, G. Tzagkarakis, *et al.*, “Reconstruction of compressively sampled ultrasound images using dual prior information”, in *2014 IEEE Int. Conf. Image Process.*, 2014, pp. 1283–1286.
- [143] P. Kruizinga, P. van der Meulen, A. Fedjajevs, *et al.*, “Compressive 3D ultrasound imaging using a single sensor”, *Sci. Adv.*, vol. 3, e1701423, 2017.
- [144] K. Melde, A. G. Mark, T. Qiu, *et al.*, “Holograms for acoustics”, *Nature*, vol. 537, pp. 518–522, 2016.
- [145] M. Lustig, D. L. Donoho, and J. M. Pauly, “Sparse MRI: The application of compressed sensing for rapid MR imaging”, *Magn. Reson. Med.*, vol. 58, pp. 1182–95, 2007.
- [146] L. Welch, “Lower bounds on the maximum cross correlation of signals (Corresp.)”, *IEEE Trans. Inf. Theory*, vol. 20, pp. 397–399, 1974.
- [147] H. Gomersall, D. Hodgson, R. Prager, *et al.*, “Efficient implementation of spatially-varying 3-D ultrasound deconvolution”, *IEEE Trans. Ultrason. Ferroelectr. Freq. Control*, vol. 58, pp. 234–238, 2011.
- [148] L. Roquette, M. Simeoni, P. Hurley, *et al.*, “On an analytical, spatially-varying, formulation of the point-spread-function with an application to deconvolution”, in *2017 IEEE Int. Ultrason. Symp.*, 2017, pp. 1–4.

## Bibliography

---

- [149] G. S. Alberti, H. Ammari, F. Romero, *et al.*, “Mathematical analysis of ultrafast ultrasound imaging”, *SIAM J. Appl. Math.*, vol. 77, pp. 1–25, 2017.
- [150] W. Vollmann, “Resolution enhancement of ultrasonic B-scan images by deconvolution”, *IEEE Trans. Sonics Ultrason.*, vol. 29, pp. 78–82, 1982.
- [151] C. N. Liu, M. Fatemi, and R. C. Waag, “Digital processing for improvement of ultrasonic abdominal images”, *IEEE Trans. Med. Imaging*, vol. 2, pp. 66–75, 1983.
- [152] T. Loupas, S. D. Pye, and W. N. McDicken, “Deconvolution in medical ultrasonics: practical considerations”, *Phys. Med. Biol.*, vol. 34, pp. 1691–1700, 1989.
- [153] Z. Chen, A. Basarab, and D. Kouame, “Compressive deconvolution in medical ultrasound imaging”, *IEEE Trans. Med. Imaging*, vol. 35, pp. 728–737, 2016.
- [154] O. V. Michailovich, “Non-stationary blind deconvolution of medical ultrasound scans”, in *Prog. Biomed. Opt. Imaging - Proc. SPIE*, vol. 10139, 2017, p. 101391C.
- [155] N. Zhao, A. Basarab, D. Kouame, *et al.*, “Joint segmentation and deconvolution of ultrasound images using a hierarchical Bayesian model based on generalized Gaussian priors”, *IEEE Trans. Image Process.*, vol. 25, pp. 3736–3750, 2016.
- [156] J. Duan, H. Zhong, B. Jing, *et al.*, “Increasing axial resolution of ultrasonic imaging with a joint sparse representation model”, *IEEE Trans. Ultrason. Ferroelectr. Freq. Control*, vol. 63, pp. 2045–2056, 2016.
- [157] U. R. Abeyratne, A. P. Petropulu, and J. M. Reid, “Higher order spectra based deconvolution of ultrasound images”, *IEEE Trans. Ultrason. Ferroelectr. Freq. Control*, vol. 42, pp. 1064–1075, 1995.
- [158] T. Taxt, “Comparison of cepstrum-based methods for radial blind deconvolution of ultrasound images”, *IEEE Trans. Ultrason. Ferroelectr. Freq. Control*, vol. 44, pp. 666–674, 1997.
- [159] T. Taxt and J. Strand, “Two-dimensional noise-robust blind deconvolution of ultrasound images”, *IEEE Trans. Ultrason. Ferroelectr. Freq. Control*, vol. 48, pp. 861–867, 2001.
- [160] O. V. Michailovich and D. Adam, “Robust estimation of ultrasound pulses using outlier-resistant de-noising”, *IEEE Trans. Med. Imaging*, vol. 22, pp. 368–381, 2003.
- [161] M. Alessandrini, S. Maggio, J. Poree, *et al.*, “A restoration framework for ultrasonic tissue characterization”, *IEEE Trans. Ultrason. Ferroelectr. Freq. Control*, vol. 58, pp. 2344–2360, 2011.
- [162] J. A. Jensen, “Estimation of in vivo pulses in medical ultrasound”, *Ultrason. Imaging*, vol. 16, pp. 190–203, 1994.
- [163] J. A. Jensen and S. Leeman, “Nonparametric estimation of ultrasound pulses”, *IEEE Trans. Biomed. Eng.*, vol. 41, pp. 929–936, 1994.
- [164] T. Taxt, “Radial homomorphic deconvolution of B-mode medical ultrasound images”, in *Proc. 12th IAPR Int. Conf. Pattern Recognit.*, 1994, pp. 149–152.
- [165] G. Demoment, R. Reynaud, and A. Herment, “Range resolution improvement by a fast deconvolution method”, *Ultrason. Imaging*, vol. 6, pp. 435–451, 1984.
- [166] R. Demirli and J. Saniie, “Model-based estimation of ultrasonic echoes part I: Analysis and algorithms”, *IEEE Trans. Ultrason. Ferroelectr. Freq. Control*, vol. 48, pp. 787–802, 2001.
- [167] D. Iraca, L. Landini, and L. Verrazzani, “Power spectrum equalization for ultrasonic image restoration”, *IEEE Trans. Ultrason. Ferroelectr. Freq. Control*, vol. 36, 1989.
- [168] O. V. Michailovich and A. Tannenbaum, “Blind deconvolution of medical ultrasound images: a parametric inverse filtering approach”, *IEEE Trans. Image Process.*, vol. 16, pp. 3005–3019, 2007.
- [169] N. Zhao, Q. Wei, A. Basarab, *et al.*, “Blind deconvolution of medical ultrasound images using a parametric model for the point spread function”, in *2016 IEEE Int. Ultrason. Symp.*, 2016, pp. 1–4.

- [170] C. Yu, C. Zhang, and L. Xie, "A blind deconvolution approach to ultrasound imaging", *IEEE Trans. Ultrason. Ferroelectr. Freq. Control*, vol. 59, pp. 271–280, 2012.
- [171] R. Jirik and T. Taxt, "Two-dimensional blind Bayesian deconvolution of medical ultrasound images", *IEEE Trans. Ultrason. Ferroelectr. Freq. Control*, vol. 55, pp. 2140–2153, 2008.
- [172] R. Morin, S. Bidon, A. Basarab, *et al.*, "Semi-blind deconvolution for resolution enhancement in ultrasound imaging", in *2013 IEEE Int. Conf. Image Process.*, 2013, pp. 1413–1417.
- [173] F. Sroubek, J. Kamenicky, and Y. M. Lu, "Decomposition of space-variant blur in image deconvolution", *IEEE Signal Process. Lett.*, vol. 23, pp. 346–350, 2016.
- [174] L. Denis, E. Thiebaud, F. Soulez, *et al.*, "Fast approximations of shift-variant blur", *Int. J. Comput. Vis.*, vol. 115, pp. 253–278, 2015.
- [175] M. Hirsch, S. Sra, B. Schölkopf, *et al.*, "Efficient filter flow for space-variant multiframe blind deconvolution", in *Proc. IEEE Comput. Soc. Conf. Comput. Vis. Pattern Recognit.*, 2010, pp. 607–614.
- [176] J. G. Nagy and D. P. O'Leary, "Restoring images degraded by spatially variant blur", *SIAM J. Sci. Comput.*, vol. 19, pp. 1063–1082, 1998.
- [177] C. Preza and J.-A. Conchello, "Depth-variant maximum-likelihood restoration for three-dimensional fluorescence microscopy", *J. Opt. Soc. Am. A*, vol. 21, p. 1593, 2004.
- [178] J. Bardsley, S. Jefferies, J. Nagy, *et al.*, "A computational method for the restoration of images with an unknown, spatially-varying blur.", *Opt. Express*, vol. 14, pp. 1767–1782, 2006.
- [179] M. I. Florea, A. Basarab, D. Kouame, *et al.*, "An axially variant kernel imaging model applied to ultrasound image reconstruction", *IEEE Signal Process. Lett.*, vol. 25, pp. 961–965, 2018.
- [180] D. Miraut and J. Portilla, "Efficient shift-variant image restoration using deformable filtering (Part I)", *EURASIP J. Adv. Signal Process.*, vol. 2012, pp. 1–20, 2012.
- [181] R. C. Flicker and E. J. Rigaut, "Anisoplanatic deconvolution of adaptive optics images.", *J. Opt. Soc. Am.*, vol. 22, pp. 504–513, 2005.
- [182] H. Deng, W. Zuo, H. Zhang, *et al.*, "An additive convolution model for fast restoration of nonuniform blurred images", *Int. J. Comput. Math.*, vol. 91, pp. 2446–2466, 2014.
- [183] T. Hrycak, S. Das, G. Matz, *et al.*, "Practical estimation of rapidly varying channels for OFDM systems", *IEEE Trans. Commun.*, vol. 59, pp. 3040–3048, 2011.
- [184] P. Escande and P. Weiss, "Approximation of integral operators using product-convolution expansions", *J. Math. Imaging Vis.*, vol. 58, pp. 333–348, 2017.
- [185] ———, "Sparse wavelet representations of spatially varying blurring operators", *SIAM J. Imaging Sci.*, vol. 8, pp. 2976–3014, 2015.
- [186] J. Wei, C. A. Bouman, and J. P. Allebach, "Fast space-varying convolution using matrix source coding with applications to camera stray light reduction", *IEEE Trans. Image Process.*, vol. 23, pp. 1965–1979, 2014.
- [187] A. Besson, D. Perdios, F. Martinez, *et al.*, "USSR: An ultrasound sparse regularization framework", in *2017 IEEE Int. Ultrason. Symp.*, 2017, pp. 1–4.
- [188] A. Besson, D. Perdios, F. Martinez, *et al.*, "Ultrafast ultrasound imaging as an inverse problem: Matrix-free sparse image reconstruction", *IEEE Trans. Ultrason. Ferroelectr. Freq. Control*, vol. 65, pp. 339–355, 2018.
- [189] Y. Yankelevsky, Z. Friedman, and A. Feuer, "Component-based modeling and processing of medical ultrasound signals", *IEEE Trans. Signal Process.*, vol. 65, pp. 5743–5755, 2017.
- [190] J.-L. Starck, Y. Moudden, J. Bobin, *et al.*, "Morphological component analysis", in *IEEE Trans. Image Process.*, vol. 16, 2005, 59140Q.
- [191] K. Gregor and Y. LeCun, "Learning fast approximations of sparse coding", in *Proc. 27th Int. Conf. Mach. Learn.*, 2010, pp. 399–406.

## Bibliography

---

- [192] A. Liutkus, D. Martina, S. Popoff, *et al.*, “Imaging with nature: Compressive imaging using a multiply scattering medium”, *Sci. Rep.*, vol. 4, p. 5552, 2015.
- [193] J. Schwab, S. Antholzer, and M. Haltmeier, “Deep null space learning for inverse problems: Convergence analysis and rates”, pp. 1–13, 2018. arXiv: 1806.06137.
- [194] J. Adler and O. Öktem, “Solving ill-posed inverse problems using iterative deep neural networks”, *Inverse Probl.*, vol. 33, p. 124 007, 2017.
- [195] M. T. McCann, K. H. Jin, and M. Unser, “Convolutional neural networks for inverse problems in imaging: A review”, *IEEE Signal Process. Mag.*, vol. 34, pp. 85–95, 2017.
- [196] K. H. Jin, M. T. McCann, E. Froustey, *et al.*, “Deep convolutional neural network for inverse problems in imaging”, *IEEE Trans. Image Process.*, vol. 26, pp. 4509–4522, 2017.
- [197] G. Wang, “A perspective on deep imaging”, *IEEE Access*, vol. 4, pp. 8914–8924, 2016.
- [198] H. Gupta, K. H. Jin, H. Q. Nguyen, *et al.*, “CNN-based projected gradient descent for consistent CT image reconstruction”, *IEEE Trans. Med. Imaging*, vol. 37, pp. 1440–1453, 2018.
- [199] H. Chen, Y. Zhang, W. Zhang, *et al.*, “Low-dose CT via convolutional neural network”, *Biomed. Opt. Express*, vol. 8, p. 679, 2017.
- [200] S. Wang, Z. Su, L. Ying, *et al.*, “Accelerating magnetic resonance imaging via deep learning”, in *2016 IEEE 13th Int. Symp. Biomed. Imaging*, vol. 36, 2016, pp. 514–517.
- [201] M. Gasse, F. Millioz, E. Roux, *et al.*, “High-quality plane wave compounding using convolutional neural networks”, *IEEE Trans. Ultrason. Ferroelectr. Freq. Control*, vol. 64, pp. 1637–1639, 2017.
- [202] A. C. Luchies and B. C. Byram, “Deep neural networks for ultrasound beamforming”, *IEEE Trans. Med. Imaging*, vol. 37, pp. 2010–2021, 2018.
- [203] D. Perdios, M. Volanthen, A. Besson, *et al.*, “Deep convolutional neural network for ultrasound image enhancement”, in *2018 IEEE Int. Ultrason. Symp.*, 2018, pp. 1–4.
- [204] A. Mousavi and R. G. Baraniuk, “Learning to invert: Signal recovery via deep convolutional networks”, 2017. arXiv: 1701.03891.
- [205] U. S. Kamilov, H. Mansour, and B. Wohlberg, “A plug-and-play priors approach for solving nonlinear imaging inverse problems”, *IEEE Signal Process. Lett.*, vol. 24, pp. 1872–1876, 2017.
- [206] J. Yen, J. Steinberg, and S. Smith, “Sparse 2-D array design for real time rectilinear volumetric imaging”, *IEEE Trans. Ultrason. Ferroelectr. Freq. Control*, vol. 47, pp. 93–110, 2000.
- [207] D. Turnbull and F. Foster, “Beam steering with pulsed two-dimensional transducer arrays”, *IEEE Trans. Ultrason. Ferroelectr. Freq. Control*, vol. 38, pp. 320–333, 1991.
- [208] R. E. Davidsen, J. A. Jensen, and S. W. Smith, “Two-dimensional random arrays for real time volumetric imaging”, *Ultrason. Imaging*, vol. 16, pp. 143–163, 1994.
- [209] G. Lookwood and F. Foster, “Optimizing the radiation pattern of sparse periodic two-dimensional arrays”, *IEEE Trans. Ultrason. Ferroelectr. Freq. Control*, vol. 43, pp. 15–19, 1996.
- [210] C. Morton and G. Lockwood, “Theoretical assessment of a crossed electrode 2-D array for 3-D imaging”, in *2003 IEEE Symp. Ultrason.*, 2003, pp. 968–971.
- [211] C. H. Seo and J. T. Yen, “A  $256 \times 256$  2-D array transducer with row-column addressing for 3-D rectilinear imaging”, *IEEE Trans. Ultrason. Ferroelectr. Freq. Control*, vol. 56, pp. 837–847, 2009.
- [212] H. Bouzari, M. Engholm, C. Beers, *et al.*, “Curvilinear 3-D imaging using row-column-addressed 2-D arrays with a diverging lens: feasibility study”, *IEEE Trans. Ultrason. Ferroelectr. Freq. Control*, vol. 64, pp. 978–988, 2017.
- [213] S. W. Hughes, T. J. D’Arcy, D. J. Maxwell, *et al.*, “Volume estimation from multiplanar 2D ultrasound images using a remote electromagnetic position and orientation sensor”, *Ultrasound Med. Biol.*, vol. 22, pp. 561–572, 1996.
- [214] S. Tong, D. Downey, H. Cardinal, *et al.*, “A three-dimensional ultrasound prostate imaging system”, *Ultrasound Med. Biol.*, vol. 22, pp. 735–746, 1996.

- [215] K. Hara, J. Sakano, M. Mori, *et al.*, “A new 80V 32x32ch low loss multiplexer LSI for a 3D ultrasound imaging system”, in *Power Semicond. Devices ICs, 2005. Proceedings. ISPSD '05. 17th Int. Symp.*, 2005, pp. 359–362.
- [216] J. Yen and S. Smith, “Real-time rectilinear volumetric imaging”, *IEEE Trans. Ultrason. Ferroelectr. Freq. Control*, vol. 49, pp. 114–124, 2002.
- [217] J. T. Yen and S. W. Smith, “Real-time rectilinear 3-D ultrasound using receive mode multiplexing”, *IEEE Trans. Ultrason. Ferroelectr. Freq. Control*, vol. 51, pp. 216–226, 2004.
- [218] B. Savord and R. Solomon, “Fully sampled matrix transducer for real time 3D ultrasonic imaging”, in *2003 IEEE Symp. Ultrason.*, 2003, pp. 945–953.
- [219] H. Nyquist, “Certain topics in telegraph transmission theory”, *Trans. Am. Inst. Electr. Eng.*, vol. 47, pp. 617–644, 1928.
- [220] C. Shannon, “Communication in the presence of noise”, in *Proc. Inst. Radio Eng.*, vol. 39, 1949, pp. 10–21.
- [221] G. K. Wallace, “The JPEG still picture compression standard”, *Commun. ACM*, vol. 34, pp. 31–44, 1991.
- [222] D. L. Donoho, “De-noising by soft-thresholding”, *IEEE Trans. Inf. Theory*, vol. 41, pp. 613–627, 1995.
- [223] ———, “Compressed sensing”, *IEEE Trans. Inf. Theory*, vol. 52, pp. 1289–1306, 2006.
- [224] M. Vetterli, P. Marziliano, and T. Blu, “Sampling signals with finite rate of innovation”, *IEEE Trans. Signal Process.*, vol. 50, pp. 1417–1428, 2002.
- [225] T. Blu, P.-L. Dragotti, M. Vetterli, *et al.*, “Sparse sampling of signal innovations”, *IEEE Signal Process. Mag.*, vol. 25, pp. 31–40, 2008.
- [226] Y. Lu and M. Do, “A theory for sampling signals from a union of subspaces”, *IEEE Trans. Signal Process.*, vol. 56, pp. 2334–2345, 2008.
- [227] B. K. Natarajan, “Sparse approximate solutions to linear systems”, *SIAM J. Comput.*, vol. 24, pp. 227–234, 1995.
- [228] S. S. Chen, D. L. Donoho, and M. A. Saunders, “Atomic decomposition by basis pursuit”, *SIAM J. Sci. Comput.*, vol. 20, pp. 33–61, 1998.
- [229] M. A. Davenport, M. F. Duarte, Y. C. Eldar, *et al.*, “Introduction to compressed sensing”, in *Compress. Sens.* 2012, pp. 1–64.
- [230] D. L. Donoho and M. Elad, “Optimally sparse representation in general (nonorthogonal) dictionaries via  $\ell^1$  minimization”, *Proc. Natl. Acad. Sci.*, vol. 100, pp. 2197–2202, 2003.
- [231] E. J. Candes and T. Tao, “Decoding by linear programming”, *IEEE Trans. Inf. Theory*, vol. 51, pp. 4203–4215, 2005.
- [232] W. B. Johnson and J. Lindenstrauss, “Extensions of Lipschitz mappings into a Hilbert space”, *Contemp. Math.*, vol. 26, p. 1, 1984.
- [233] E. J. Candes, “The restricted isometry property and its implications for compressed sensing”, *Comptes Rendus Math.*, vol. 346, pp. 589–592, 2008.
- [234] D. L. Donoho, M. Elad, and V. Temlyakov, “Stable recovery of sparse overcomplete representations in the presence of noise”, *IEEE Trans. Inf. Theory*, vol. 52, pp. 6–18, 2006.
- [235] H. Rauhut, *Compressive sensing with structured random matrices*, 2012.
- [236] J. Romberg, “Compressive sensing by random convolution”, *SIAM J. Imaging Sci.*, vol. 2, pp. 1098–1128, 2009.
- [237] J. P. Slavinsky, J. N. Laska, M. A. Davenport, *et al.*, “The compressive multiplexer for multi-channel compressive sensing”, in *2011 IEEE Int. Conf. Acoust. Speech Signal Process.*, 2011, pp. 3980–3983.

## Bibliography

---

- [238] S. Becker, “Practical compressed sensing: Modern data acquisition and signal processing”, PhD thesis, 2011, pp. 1–306.
- [239] G. Puy, J. P. Marques, R. Gruetter, *et al.*, “Spread spectrum magnetic resonance imaging”, *IEEE Trans. Med. Imaging*, vol. 31, pp. 586–598, 2012.
- [240] S. Kirolos, J. Laska, M. Wakin, *et al.*, “Analog-to-information conversion via random demodulation”, in *2006 IEEE Dallas/CAS Work. Des. Appl. Integr. Softw.*, 2006, pp. 71–74.
- [241] M. Mishali and Y. C. Eldar, “Expected RIP: Conditioning of the modulated wideband converter”, in *2009 IEEE Inf. Theory Work.*, 2009, pp. 343–347.
- [242] S. M. Popoff, G. Lerosey, R. Carminati, *et al.*, “Measuring the transmission matrix in optics: An approach to the study and control of light propagation in disordered media”, *Phys. Rev. Lett.*, vol. 104, pp. 100601-1–100601-4, 2010.
- [243] J. Chen and X. Huo, “Theoretical results on sparse representations of multiple measurement vectors”, *IEEE Trans. Signal Process.*, vol. 54, pp. 4634–4643, 2006.
- [244] M. E. Davies and Y. C. Eldar, “Rank awareness in joint sparse recovery”, *IEEE Trans. Inf. Theory*, vol. 58, pp. 1135–1146, 2012.
- [245] J. A. Tropp, “Algorithms for simultaneous sparse approximation. Part II: Convex relaxation”, *Signal Processing*, vol. 86, pp. 589–602, 2006.
- [246] M. Hyder and K. Mahata, “A robust algorithm for joint-sparse recovery”, *IEEE Signal Process. Lett.*, vol. 16, pp. 1091–1094, 2009.
- [247] Y. C. Eldar and M. Mishali, “Robust recovery of signals from a structured union of subspaces”, *IEEE Trans. Inf. Theory*, vol. 55, pp. 5302–5316, 2009.
- [248] J. M. Kim, O. K. Lee, and J. C. Ye, “Compressive MUSIC: Revisiting the link between compressive sensing and array signal processing”, *IEEE Trans. Inf. Theory*, vol. 58, pp. 278–301, 2012.
- [249] P. Feng and Y. Bresler, “Spectrum-blind minimum-rate sampling and reconstruction of multi-band signals”, in *1996 IEEE Int. Conf. Acoust. Speech, Signal Process. Conf. Proc.*, vol. 3, 1996, pp. 1688–1691.
- [250] K. Lee, Y. Bresler, and M. Junge, “Subspace methods for joint sparse recovery”, *IEEE Trans. Inf. Theory*, vol. 58, pp. 3613–3641, 2012.
- [251] J. A. Tropp, A. C. Gilbert, and M. J. Strauss, “Algorithms for simultaneous sparse approximation. Part I: Greedy pursuit”, *Signal Processing*, vol. 86, pp. 572–588, 2006.
- [252] J.-F. Determe, J. Louveaux, L. Jacques, *et al.*, “On the exact recovery condition of simultaneous orthogonal matching pursuit”, *IEEE Signal Process. Lett.*, vol. 23, pp. 164–168, 2016.
- [253] J. D. Blanchard, M. Cermak, D. Hanle, *et al.*, “Greedy algorithms for joint sparse recovery”, *IEEE Trans. Signal Process.*, vol. 62, pp. 1694–1704, 2014.
- [254] Z. Wen, B. Hou, and L. Jiao, “Joint sparse recovery with semisupervised MUSIC”, *IEEE Signal Process. Lett.*, vol. 24, pp. 629–633, 2017.
- [255] R. von Borries, C. J. Miosso, and C. Potes, “Compressed sensing using prior information”, in *2007 2nd IEEE Int. Work. Comput. Adv. Multi-Sensor Adapt. Process.*, 2007, pp. 121–124.
- [256] M. A. Khajehnejad, W. Xu, A. S. Avestimehr, *et al.*, “Weighted  $\ell_1$ -minimization for sparse recovery with prior information”, in *2009 IEEE Int. Symp. Inf. Theory*, 2009, pp. 483–487.
- [257] N. Vaswani and W. Lu, “Modified-CS: Modifying compressive sensing for problems with partially known support”, *IEEE Trans. Signal Process.*, vol. 58, pp. 4595–4607, 2010.
- [258] M. P. Friedlander, H. Mansour, R. Saab, *et al.*, “Recovering compressively sampled signals using partial support information”, *IEEE Trans. Inf. Theory*, vol. 58, pp. 1122–1134, 2012.
- [259] R. E. Carrillo, L. F. Polania, and K. E. Barner, “Iterative algorithms for compressed sensing with partially known support”, in *2010 IEEE Int. Conf. Acoust. Speech Signal Process.*, 2010, pp. 3654–3657.

- [260] ———, “Iterative hard thresholding for compressed sensing with partially known support”, in *2011 IEEE Int. Conf. Acoust. Speech Signal Process.*, 2011, pp. 4028–4031.
- [261] T. Bendory, S. Dekel, and A. Feuer, “Robust recovery of stream of pulses using convex optimization”, *J. Math. Anal. Appl.*, vol. 442, pp. 511–536, 2016.
- [262] C. Hegde and R. G. Baraniuk, “Sampling and recovery of pulse streams”, *IEEE Trans. Signal Process.*, vol. 59, pp. 1505–1517, 2011.
- [263] T. Bendory, A. Bar-Zion, D. Adam, *et al.*, “Stable support recovery of stream of pulses with application to ultrasound imaging”, *IEEE Trans. Signal Process.*, vol. 64, pp. 3750–3759, 2016.
- [264] E. F. Bezzam, A. Besson, H. Pan, *et al.*, “Sparse recovery of strong reflectors with an application to non-destructive evaluation”, in *2018 IEEE Int. Ultrason. Symp.*, 2018, pp. 1–4.
- [265] O. Bar-Ilan and Y. C. Eldar, “Sub-Nyquist radar via Doppler focusing”, *IEEE Trans. Signal Process.*, vol. 62, pp. 1796–1811, 2014.
- [266] A. Bhandari and R. Raskar, “Signal processing for time-of-flight imaging sensors: An introduction to inverse problems in computational 3-D imaging”, *IEEE Signal Process. Mag.*, vol. 33, pp. 45–58, 2016.
- [267] F. M. Naini, R. Gribonval, L. Jacques, *et al.*, “Compressive sampling of pulse trains: Spread the spectrum!”, in *2009 IEEE Int. Conf. Acoust. Speech Signal Process.*, 2009, pp. 2877–2880.
- [268] G. Tsagkatakis, P. Tsakalides, A. Woiselle, *et al.*, “Compressed sensing reconstruction of convolved sparse signals”, in *2014 IEEE Int. Conf. Acoust. Speech Signal Process.*, 2014, pp. 3340–3344.
- [269] Y. Chi, L. L. Scharf, A. Pezeshki, *et al.*, “Sensitivity to basis mismatch in compressed sensing”, *IEEE Trans. Signal Process.*, vol. 59, pp. 2182–2195, 2011.
- [270] J. Romberg and R. Neelamani, “Sparse channel separation using random probes”, *Inverse Probl.*, vol. 26, 2010.
- [271] J. Romberg, “Multiple channel estimation using spectrally random probes”, in *SPIE Wavelets XIII*, vol. 744606, 2009, p. 744 606.
- [272] A. Ahmed and J. Romberg, “Compressive multiplexing of correlated signals”, *IEEE Trans. Inf. Theory*, vol. 61, pp. 479–498, 2015.
- [273] A. Benichoux, E. Vincent, and R. Gribonval, “A fundamental pitfall in blind deconvolution with sparse and shift-invariant priors”, in *2013 IEEE Int. Conf. Acoust. Speech Signal Process.*, 2013, pp. 6108–6112.
- [274] A. Levin, Y. Weiss, F. Durand, *et al.*, “Understanding and evaluating blind deconvolution algorithms”, in *2009 IEEE Conf. Comput. Vis. Pattern Recognit.*, vol. 33, 2009, pp. 1964–1971.
- [275] S. Choudhary and U. Mitra, “Sparse blind deconvolution: What cannot be done”, in *IEEE Int. Symp. Inf. Theory*, 2014, pp. 3002–3006.
- [276] A. Repetti, M. Q. Pham, L. Duval, *et al.*, “Euclid in a taxicab: Sparse blind deconvolution with smoothed  $\ell_1/\ell_2$  regularization”, *IEEE Signal Process. Lett.*, vol. 22, pp. 539–543, 2015.
- [277] D. Krishnan, T. Tay, and R. Fergus, “Blind deconvolution using a normalized sparsity measure”, in *2011 IEEE Conf. Comput. Vis. Pattern Recognit.*, 2011, pp. 233–240.
- [278] X. Jia, M. Zhao, M. Buzza, *et al.*, “A geometrical investigation on the generalized  $\ell_p/\ell_q$  norm for blind deconvolution”, *Signal Processing*, vol. 134, pp. 63–69, 2017.
- [279] T. F. Chan and C. Wong, “Convergence of the alternating minimization algorithm for blind deconvolution”, *Linear Algebra Appl.*, vol. 316, pp. 259–285, 2000.
- [280] M. Li and G. Hayward, “Ultrasound nondestructive evaluation (NDE) imaging with transducer arrays and adaptive processing”, *Sensors*, vol. 12, pp. 42–54, 2011.
- [281] H.-P. Tan, R. Diamant, W. K. Seah, *et al.*, “A survey of techniques and challenges in underwater localization”, *Ocean Eng.*, vol. 38, pp. 1663–1676, 2011.

## Bibliography

---

- [282] O. Couture, V. Hingot, B. Heiles, *et al.*, “Ultrasound localization microscopy and super-resolution: A state of the art”, *IEEE Trans. Ultrason. Ferroelectr. Freq. Control*, vol. 65, pp. 1304–1320, 2018.
- [283] C. Errico, J. Pierre, S. Pezet, *et al.*, “Ultrafast ultrasound localization microscopy for deep super-resolution vascular imaging”, *Nature*, vol. 527, pp. 499–502, 2015.
- [284] O. Couture, B. Besson, G. Montaldo, *et al.*, “Microbubble ultrasound super-localization imaging (MUSLI)”, in *2011 IEEE Int. Ultrason. Symp.*, 2011, pp. 1285–1287.
- [285] Y. Desailly, J. Pierre, O. Couture, *et al.*, “Resolution limits of ultrafast ultrasound localization microscopy”, *Phys. Med. Biol.*, vol. 60, pp. 8723–8740, 2015.
- [286] C. Prada and J.-L. Thomas, “Experimental subwavelength localization of scatterers by decomposition of the time reversal operator interpreted as a covariance matrix”, *J. Acoust. Soc. Am.*, vol. 114, pp. 235–243, 2003.
- [287] M. S. O’Brien, A. N. Sinclair, and S. M. Kramer, “Recovery of a sparse spike time series by L1 norm deconvolution”, *IEEE Trans. Signal Process.*, vol. 42, pp. 3353–3365, 1994.
- [288] T. Olofsson and T. Stepinski, “Minimum entropy deconvolution of pulse-echo signals acquired from attenuative layered media”, *J. Acoust. Soc. Am.*, vol. 109, pp. 2831–2839, 2001.
- [289] E. Carcreff, S. Bourguignon, J. Idier, *et al.*, “Inverse problems with attenuation and dispersion”, *IEEE Trans. Ultrason. Ferroelectr. Freq. Control*, vol. 61, pp. 1191–1203, 2014.
- [290] G. Guarneri, D. Pipa, F. Junior, *et al.*, “A sparse reconstruction algorithm for ultrasonic images in nondestructive testing”, *Sensors*, vol. 15, pp. 9324–9343, 2015.
- [291] C. Dossal and S. Mallat, “Sparse spike deconvolution with minimum scale”, in *Signal Process. with Adapt. Sparse Struct. Represent.*, 2005, pp. 123–126.
- [292] J. Kusuma, A. Ridolfi, and M. Vetterli, “Sampling of communication systems with bandwidth expansion”, *IEEE Int. Conf. Commun.*, vol. 3, pp. 1601–1605, 2002.
- [293] A. Bhandari, A. M. Wallace, and R. Raskar, “Super-resolved time-of-flight sensing via FRI sampling theory”, in *2016 IEEE Int. Conf. Acoust. Speech Signal Process.*, 2016, pp. 4009–4013.
- [294] P. Duxbury, L. Granlund, S. Gujarathi, *et al.*, “The unassigned distance geometry problem”, *Discret. Appl. Math.*, vol. 204, pp. 117–132, 2016.
- [295] M. Unser, “Sampling-50 years after Shannon”, *Proc. IEEE*, vol. 88, pp. 569–587, 2000.
- [296] I. Maravic and M. Vetterli, “Sampling and reconstruction of signals with finite rate of innovation in the presence of noise”, *IEEE Trans. Signal Process.*, vol. 53, pp. 2788–2805, 2005.
- [297] R. Prony, “Essai expérimental et analytique sur les lois de la dilatabilité des fluides élastiques et sur celles de la force expansive de la vapeur de l’alcool, à différentes températures”, *Journal de l’École Polytechnique Floréal et Plairial*, 1795.
- [298] A. Hirabayashi, T. Iwami, S. Maeda, *et al.*, “Reconstruction of the sequence of Diracs from noisy samples via maximum likelihood estimation”, in *2012 IEEE Int. Conf. Acoust. Speech Signal Process.*, 2012, pp. 3805–3808.
- [299] L. Condat, A. Hirabayashi, L. Condat, *et al.*, “Cadow denoising upgraded : A new projection method for the recovery of Dirac pulses from noisy linear measurements”, 2015.
- [300] E. F. Bezzam, “Sampling at the rate of innovation for ultrasound imaging and localization”, Tech. Rep., 2018, Unpublished Master’s thesis.
- [301] I. Dokmanic, R. Parhizkar, J. Ranieri, *et al.*, “Euclidean distance matrices: Essential theory, algorithms, and applications”, *IEEE Signal Process. Mag.*, vol. 32, pp. 12–30, 2015.
- [302] A. Besson, D. Perdios, Y. Wiaux, *et al.*, “Pulse-stream models in time-of-flight imaging”, in *2018 IEEE Int. Conf. Acoust. Speech Signal Process.*, 2018, pp. 3389–3393.
- [303] “Multidimensional scaling: I. Theory and method”, *Psychometrika*, vol. 17, pp. 401–419, 1952.
- [304] B. Fang, “Simple solutions for hyperbolic and related position fixes”, *IEEE Trans. Aerosp. Electron. Syst.*, vol. 26, pp. 748–753, 1990.

- [305] D. E. Manolakis, "Efficient solution and performance analysis of 3-D position estimation by trilateration", *IEEE Trans. Aerosp. Electron. Syst.*, vol. 32, pp. 1239–1248, 1996.
- [306] H.-Y. Liu, D. Liu, H. Mansour, *et al.*, "SEAGLE: Sparsity-driven image reconstruction under multiple scattering", *IEEE Trans. Comput. Imaging*, vol. 4, pp. 73–86, 2018.
- [307] J. Radon, "On the determination of functions from their integral values along certain manifolds", *IEEE Trans. Med. Imaging*, vol. 5, pp. 170–176, 1986.
- [308] A. M. Cormack, "Representation of a function by its line integrals, with some radiological applications", *J. Appl. Phys.*, vol. 34, pp. 2722–2727, 1963.
- [309] K. Denecker, J. V. Overloop, and F. Sommen, "The general quadratic Radon transform", *Inverse Probl.*, vol. 14, pp. 615–633, 1998.
- [310] I. M. Gel'fand, M. I. Graev, and Z. Y. Shapiro, "Differential forms and integral geometry", *Funct. Anal. Its Appl.*, vol. 3, pp. 101–114, 1969.
- [311] A. M. Cormack, "The Radon transform on a family of curves in the plane", *Proc. Am. Math. Soc.*, vol. 83, p. 325, 1981.
- [312] D. A. Popov, "The generalized Radon transform on the plane, the inverse transform, and the Cavalieri conditions", *Funct. Anal. its Appl.*, vol. 35, pp. 270–283, 2001.
- [313] —, "The Paley-Wiener theorem for the generalized Radon transform on the plane", *Funct. Anal. its Appl.*, vol. 37, pp. 215–220, 2003.
- [314] E. T. Quinto, "The dependence of the generalized Radon transform on defining measures", *Trans. Am. Math. Soc.*, vol. 257, p. 331, 1980.
- [315] G. Beylkin, "Inversion of the generalized Radon transform", 1983, pp. 32–39.
- [316] P. Kuchment, "Generalized transforms of Radon type and their applications", *Proc. Symp. Appl. Math.*, vol. 0000, pp. 1–32, 2006.
- [317] O. Scherzer, M. Grasmair, H. Grossauer, *et al.*, "Case examples of imaging", in *Variational Methods in Imaging*. 2009, pp. 3–25.
- [318] A. K. Louis and E. T. Quinto, "Local tomographic methods in sonar", in *Surv. Solut. Methods Inverse Probl.* Vol. 2, 2000, pp. 147–154.
- [319] M. Xu and L. V. Wang, "Time-domain reconstruction for thermoacoustic tomography in a spherical geometry", *IEEE Trans. Med. Imaging*, vol. 21, pp. 814–822, 2002.
- [320] R. A. Kruger, P. Liu, Y. " Fang, *et al.*, "Photoacoustic ultrasound (PAUS)-reconstruction tomography", *Med. Phys.*, vol. 22, pp. 1605–1609, 1995.
- [321] L.-E. Andersson, "On the determination of a function from spherical averages", *SIAM J. Math. Anal.*, vol. 19, pp. 214–232, 1988.
- [322] R. Courant and D. Hilbert, Eds., *Methods of Mathematical Physics*. Weinheim, Germany: Wiley-VCH Verlag GmbH, 1989.
- [323] J. A. Fawcett, "Inversion of N-dimensional spherical averages", *SIAM J. Appl. Math.*, vol. 45, pp. 336–341, 1985.
- [324] D. Finch and S. K. Patch, "Determining a function from its mean values over a family of spheres", *SIAM J. Math. Anal.*, vol. 35, pp. 1213–1240, 2004.
- [325] D. Miller, M. Oristaglio, and G. Beylkin, "A new slant on seismic imaging: Migration and integral geometry", *GEOPHYSICS*, vol. 52, pp. 943–964, 1987.
- [326] V. P. Krishnan, H. Levinson, and E. T. Quinto, "Microlocal analysis of elliptical Radon transforms with foci on a line", in *The mathematical legacy of Leon Ehrenpreis*, vol. 16, 2012, pp. 163–182.
- [327] S. Moon and J. Heo, "Inversion of the elliptical Radon transform arising in migration imaging using the regular Radon transform", *J. Math. Anal. Appl.*, vol. 436, pp. 138–148, 2016.
- [328] J. D. Coker and A. H. Tewfik, "Multistatic SAR image reconstruction based on an elliptical-geometry radon transform", *2007 Int. Waveform Divers. Des. Conf.*, pp. 204–208, 2007.

## Bibliography

---

- [329] R. Gouia-Zarrad and G. Ambartsoumian, “Approximate inversion algorithm of the elliptical Radon transform”, in *2012 8th Int. Symp. Mechatronics its Appl.*, 2012, pp. 1–4.
- [330] E. Maeland, “Focusing aspects of the parabolic Radon transform”, *GEOPHYSICS*, vol. 63, pp. 1708–1715, 1998.
- [331] S. Moon, “Inversion of the seismic parabolic Radon transform and the seismic hyperbolic Radon transform”, *Inverse Probl. Sci. Eng.*, vol. 24, pp. 317–327, 2016.
- [332] J. Yang and Y. Zhang, “Alternating direction algorithms for  $\ell_1$ -problems in compressive sensing”, *SIAM J. Sci. Comput.*, vol. 33, pp. 250–278, 2011.
- [333] M. Fadili and J.-L. Starck, “Monotone operator splitting for optimization problems in sparse recovery”, in *2009 16th IEEE Int. Conf. Image Process.*, 2009, pp. 1461–1464.

## Adrien Besson

---

CONTACT INFORMATION	Signal Processing Laboratory (LTS 5) EPFL-STI-IEL-LTS5, Station 11 CH-1015 Lausanne	Tel: +41 21 69 35672 adrien.besson@epfl.ch <a href="https://adribesson.github.io/">https://adribesson.github.io/</a>
RESEARCH INTERESTS	Ultrasound imaging, compressed sensing, convex optimization, inverse problems, deep learning	
EDUCATION	<b>Ecole Polytechnique Fédérale de Lausanne</b> , Lausanne, Switzerland	
	Ph.D., Ultrasound imaging, <i>Expected</i> : Mar 2019	
	<ul style="list-style-type: none"><li>• Thesis Topic: <i>Model-based Ultrasound Imaging</i></li><li>• Advisors: Prof. Jean-Philippe Thiran and Prof. Yves Wiaux</li></ul>	
	M.Sc., Electrical Engineering, Aug 2013	
	<ul style="list-style-type: none"><li>• Thesis: <i>Development of an anti-fraud module for a fingerprint sensor</i></li><li>• Advisors: Prof. Pascal Frossard and Jérôme Lorenzi (Morpho)</li></ul>	
	<b>Supélec</b> , Gif-sur-Yvette, France	
	Engineering Diploma, Electrical Engineering, Aug 2013	
RESEARCH AND PROFESSIONAL EXPERIENCE	<b>Research Assistant</b> Signal Processing Laboratory (LTS 5), Ecole Polytechnique Fédérale de Lausanne	January 2015 to present
	<b>R&amp;D engineer</b> Center for Excellence of Terminals, Morpho S.A. <b>Mission:</b> Operational research for the design of the checkpoint of the future	June 2013 to Jan 2015
	<b>Engineering intern</b> Center for Excellence of Terminals, Morpho S.A. <b>Mission:</b> Development of an anti-fraud module for a fingerprint sensor	January 2013 to June 2013
	<b>Research Intern</b> Multimedia Signal Processing Group (MMSPG), Ecole Polytechnique Fédérale de Lausanne <b>Mission:</b> Objective quality metrics for scalable video coding	January 2012 to June 2012
HONORS AND AWARDS	<ul style="list-style-type: none"><li>• First prize at the PICMUS challenge</li><li>• LEM prize for student excellence</li><li>• Anna Barbara Reinhard prize for student excellence</li></ul>	Sep 2016 Sep 2013 Sep 2013
PRESENTATIONS	International Conferences	
	<ul style="list-style-type: none"><li>• International Conference on Image Processing, Phoenix, USA</li><li>• International Ultrasonics Symposium, Tours, France</li><li>• European Signal Processing Conference, Budapest, Hungary</li><li>• International Ultrasonics Symposium, Taipei, Taiwan</li></ul>	Sep 2016 Sep 2016 Aug 2016 Sep 2015
	Workshops	
	<ul style="list-style-type: none"><li>• International BASP Frontiers workshop, Villars sur Ollon, Switzerland</li><li>• 2<sup>nd</sup> Swiss Medical Image Computing Day, Bern, Switzerland</li></ul>	Jan 2017 Nov 2016

TEACHING EXPERIENCE	Students supervised at EPFL (co-supervised with Prof. Jean-Philippe Thiran)	
	Lucas Mayrhofer (with IIS at ETHZ)	Fall 2017
	• Compressed Sensing Algorithms for Hand-held Ultrasound Medical Imaging Devices	
	Malo Grisard	Fall 2017
	• Deep Learning for Enhanced Ultrasound Image Reconstruction	
	Yuliang Zheng	Fall 2017
	• Image Reconstruction with Generative Models	
	Julie Delacroix	Spring 2017
	• Extension of the Experimental Demonstrator With a Doppler Ultrasound Method	
	Saleh Bagher	Spring 2017
	• Deep Learning for Block Compressed Sensing of Images	
	Philippe Rossinelli	Fall 2016
	• Learning Optimal Thresholding Parameters	
	Marc Beusch (with TIK at ETHZ)	Fall 2016
	• Parallelization of Compressed Sensing Based Ultrasound Imaging	
	Benjamin Beck	Fall 2016
	• Extension of the Compressed-Sensing based Demonstrator to Diverging Wave Imaging	
Florian Martinez	Spring 2016	
• Methods for Accelerated Reconstruction of Ultrasound Images Based on Compressed Sensing on GPU		
Eric F. Bezzam	Spring 2016	
• Development of a Compressive Sensing Based Demonstrator for 2D Ultrasound Plane Wave Imaging		
Louis Sarazin	Fall 2015	
• Optimization of Compressed Sensing Based Ultrafast Ultrasound Imaging Algorithms		
Teaching Assistant		
EE-350 - Signal Processing	Falls 2015–16	
Instructors: Prof. Frossard and Prof. Thiran		
Electrical and Electronics Engineering, Ecole Polytechnique Fédérale de Lausanne		
EE-451 - Image Analysis and Pattern Recognition	Spring 2015	
Instructor: Prof. Thiran		
Electrical and Electronics Engineering, Ecole Polytechnique Fédérale de Lausanne		

PROFESSIONAL  
ACTIVITIES AND  
SERVICE

- Professional societies
- Institute of Electrical and Electronic Engineers (IEEE)  
Student Member (2015-present)
- Reviewing Activities
- Journals
    - IEEE Signal Processing Letters
    - IEEE Transactions on Ultrasonics, Ferroelectrics, and Frequency Control
    - Elsevier Ultrasonics
  - International Conferences
    - EUSIPCO 2016
    - IEEE ICASSP 2017, IEEE ICASSP 2018

1. **A. Besson**, D. Perdios, M. Arditi, Y. Wiaux and J.-Phi. Thiran "Compressive Multiplexing and Reconstruction of Ultrasound Signals," In preparation.
2. **A. Besson**, L. Roquette, D. Perdios, M. Simeoni, M. Arditi, P. Hurley, Y. Wiaux and J.-Phi. Thiran "A Physical Model of Non-stationary Blur in Ultrasound Imaging," submitted to *IEEE Transactions on Computational Imaging*.
3. **A. Besson**, D. Perdios, Y. Wiaux and J.-Phi. Thiran "Joint Sparsity with Partially Known Support and Application to Ultrasound Imaging," *IEEE Signal Processing Letters*, vol. 26, no. 1, pp. 84-88, jan 2019.
4. **A. Besson**, D. Perdios, F. Martinez, Z. Chen, R. E. Carrillo, M. Arditi, Y. Wiaux and J.-Phi. Thiran "Ultrafast Ultrasound Imaging as an Inverse Problem: Matrix-free Sparse Image Reconstruction," *IEEE Transactions on Ultrasonics, Ferroelectrics, and Frequency Control*, vol. 65, no. 3, pp. 339-355, mar 2018.
5. **A. Besson**, M. Zhang, F. Varray, H. Liebgott, D. Friboulet, Y. Wiaux, J.-Phi. Thiran, R. E. Carrillo and O. Bernard "A Sparse Reconstruction Framework for Fourier-Based Plane-Wave Imaging," *IEEE Transactions on Ultrasonics, Ferroelectrics, and Frequency Control*, vol. 63, no. 12, pp. 2092-2106, dec 2016.
6. M. Zhang, F. Varray, **A. Besson**, R. E. Carrillo, M. Viallon, D. Garcia, J.-Phi. Thiran, D. Friboulet, H. Liebgott and O. Bernard "Extension of Fourier-Based Techniques for Ultrafast Imaging in Ultrasound With Diverging Waves," *IEEE Transactions on Ultrasonics, Ferroelectrics, and Frequency Control*, vol. 63, no. 12, pp. 2125-2137, dec 2016.

## Conference, symposium and workshop

1. E. F. Bezzam, **A. Besson** and J.-Phi. Thiran "An Echo-nomic Approach to Localization," *International Biomedical and Astronomical Signal Processing Frontiers workshop (BASP)*, jan 2019.
2. **A. Besson**, D. Perdios, Y. Wiaux and J.-Phi. Thiran "Compressive Multiplexing of Ultrasound Signals," *2018 IEEE International Ultrasonics Symposium (IUS)*, oct 2018.
3. E. F. Bezzam, **A. Besson**, H. Pan, D. Perdios, J.-Phi. Thiran and M. Vetterli "Sparse Recovery of Strong Reflectors With an Application to Non-Destructive Evaluation," *2018 IEEE International Ultrasonics Symposium (IUS)*, oct 2018.
4. **A. Besson**, D. Perdios, Y. Wiaux and J.-Phi. Thiran "Pulse-stream Models in Time-of-flight imaging," *2018 IEEE International Conference on Acoustics, Speech and Signal Processing*, apr 2018.
5. L. Roquette, M. Simeoni, P. Hurley and **A. Besson** "On an Analytical, Spatially-varying, Point-spread-function," *2017 IEEE International Ultrasonics Symposium (IUS)*, sep 2017.
6. D. Perdios, **A. Besson**, M. Arditi and J.-Phi. Thiran "A Deep Learning Approach to Ultrasound Image Recovery," *2017 IEEE International Ultrasonics Symposium (IUS)*, sep 2017.
7. **A. Besson**, D. Perdios, F. Martinez, M. Arditi, Y. Wiaux and J.-Phi. Thiran "USSR: An Ultrasound Sparse Regularization Framework," *2017 IEEE International Ultrasonics Symposium (IUS)*, sep 2017.

8. D. Perdios, **A. Besson**, P. Rossinelli and J.-Phi. Thiran "Learning the Weight Matrix for Sparsity Averaging in Compressive Imaging," *2017 IEEE International Conference on Image Processing (ICIP)*, sep 2017.
9. **A. Besson**, R. E. Carrillo, D. Perdios, M. Arditi, Y. Wiaux and J.-Phi. Thiran "A compressed-sensing approach for ultrasound imaging", *2017 Signal Processing with Adaptive Sparse Structured Representations (SPARS) workshop*, jun 2017.
10. Z. Chen, **A. Besson**, J.-Phi. Thiran and Y. Wiaux "Beamforming-deconvolution: A novel concept of deconvolution for ultrasound imaging," *International Biomedical and Astronomical Signal Processing Frontiers workshop (BASP)*, jan 2017.
11. **A. Besson**, R. E. Carrillo, O. Bernard, Y. Wiaux and J.-Phi. Thiran "Compressed delay-and-sum beamforming for ultrafast ultrasound imaging," *2016 IEEE International Conference on Image Processing (ICIP)*, sep 2016.
12. **A. Besson**, R. E. Carrillo, D. Perdios, M. Arditi, O. Bernard, Y. Wiaux and J.-Phi. Thiran "A compressed beamforming framework for ultrafast ultrasound imaging," *2016 IEEE International Ultrasonics Symposium (IUS)*, sep 2016.
13. **A. Besson**, R. E. Carrillo, D. Perdios, E. F. Bezzam, M. Arditi, Y. Wiaux and J.-Phi. Thiran "Morphological component analysis for sparse regularization in plane wave imaging," *2016 IEEE International Ultrasonics Symposium (IUS)*, sep 2016.
14. **A. Besson**, R. E. Carrillo, M. Zhang, D. Friboulet, O. Bernard, Y. Wiaux and J.-Phi. Thiran "Sparse regularization methods in ultrafast ultrasound imaging," *2016 24th European Signal Processing Conference (EUSIPCO)*, aug 2016.
15. M Zhang, **A. Besson**, R. E. Carrillo, F. Varray, M. Viallon, H. Liebgott, J.-Phi. Thiran, D. Friboulet and O. Bernard "Extension of Ultrasound Fourier Slice Imaging theory to sectorial acquisition," *2015 IEEE International Ultrasonics Symposium (IUS)*, oct 2015.
16. R. E. Carrillo, **A. Besson**, M. Zhang, D. Friboulet, Y. Wiaux, J.-Phi. Thiran and O. Bernard "A Sparse regularization approach for ultrafast ultrasound imaging" *2015 IEEE International Ultrasonics Symposium (IUS)*, oct 2015.
17. **A. Besson**, F. De Simone and T. Ebrahimi "Objective quality metrics for video scalability," *2013 IEEE International Conference on Image Processing*, sep 2013.

#### Patent

1. D. Perdios, **A. Besson**, F. Martinez, M. Arditi and J.-Phi. Thiran "Image Reconstruction Based on a Trained Non-linear Mapping," submitted, 2018.
2. **A. Besson**, D. Perdios, M. Arditi and J.-Phi. Thiran "Model Based Image Reconstruction," *PCT/EP2018/072579*, 2018.
3. **A. Besson**, A. Thiebot, D. Dumont and J. Lorenzi "Method of validation intended to validate that an element is covered by a true skin," *WO 2015091701 A1*, 2015.

LANGUAGE SKILLS      French (native), English (advanced), and Spanish (basic)

PROGRAMMING SKILLS      MATLAB, Python (scipy, numpy, sklearn, Tensorflow, Jupyter), Linux (Ubuntu), Windows, LaTeX



